Trinity College Dublin
the University of Dublin

School of Physics

The Effects of Rotation on the Evolution of the First Stars in the Universe

---

Author:

Laura Murphy

Supervisor:

Prof. Jose Groh

A thesis submitted for the degree of

Philosophiæ Doctor (PhD) in Astrophysics

2022

Declaration

I declare that this thesis has not been submitted as an exercise for a degree at this or any other university and it is entirely my own work.

I agree to deposit this thesis in the University's open access institutional repository or allow the Library to do so on my behalf, subject to Irish Copyright Legislation and Trinity College Library conditions of use and acknowledgement.

I consent to the examiner retaining a copy of the thesis beyond the examining period, should they so wish.

Laura Murphy

Signature:

Laura Murphy

Date:

16/02/2022

Summary

More than 13 billion years ago the first stars brought light to our Universe, and set in motion the formation of the first galaxies, first stellar systems, first planets, and eventually our own solar system. They were the nuclear engines where the first heavy elements formed, their ionizing radiation heated and transformed their surroundings, and their explosive deaths as Supernovae determined the nature of their stellar descendants including our Sun. Understanding the nature of the first stars is therefore fundamental in understanding the evolution of the Universe.

With new observational facilities such as the James Webb Space Telescope we may soon have the first detections of the first stellar populations, but to interpret these observations we require detailed theoretical models. Stellar evolution models will allow us to understand what sort of evolutionary behaviour could lead to observed properties of the earliest stars, and in doing so can allow us to trace back in time to the formation of the first stars from observations of later stages of their evolution.

With this in mind we have developed a new state-of-the-art grid of stellar evolution models of zero-metallicity stars with and without rotation, and used it to investigate how rotation impacts the evolution of the first stars. In particular we have studied how rotation impacts the surface properties, stellar structure, metal enrichment and ionizing photon production of the first stars throughout their evolution.

Our stellar evolution models are produced using the Geneva code, and we provide background to the physics of the code and the treatment of properties such as rotation, convection and mass loss, as well as how our models are used to calculate ionizing photon production rates, both for individual stars and for zero-metallicity populations. We present our model grid in its entirety for initial masses of $1.7\,\mathrm{M}_\odot \leq M_\mathrm{ini} \leq 120\,\mathrm{M}_\odot$ and explain key features of the grid. We then discuss our analysis of the massive models ($M_\mathrm{ini} \geq 9\,\mathrm{M}_\odot$) in the grid, and our results on how rotation affects their evolution and ionizing photon production.

The three prinicipal findings of this work pertain to the effects of rotation on the surface properties, metal enrichment, and ionizing photon production of the first stars. We find that rotation impacts the surface properties in different ways depending on the initial mass of the star, which determines whether rotational mixing predominantly impacts the stellar core or the nuclear burning shells in the post main sequence evolution. In general, the main effect of rotation across the evolution is to increase the luminosity and decrease the surface temperature of the star. The increase in luminosity arises from the increased core size due to rotational mixing, and the decrease in surface temperature arises from changes in energy generation in the envelope which drive an increase to the stellar radius.

In terms of the chemical enrichment of the star, we focus on the production of nitrogen and how it is impacted by rotational mixing. We find that rotation can increase nitrogen production, but can also hinder it due to sudden changes in energy generation and stellar structure brought about by rotational mixing in the early stages of He burning. For ionizing photon production, the impact of rotation reflects the rotational effects on the surface properties. For individual stars we find that rotation impacts ionizing photon production by up to 25%. We have also found that higher convective overshooting increases ionizing photon production by approximately 20% for the change in overshooting considered in this work. For stellar populations, we explore how the production of ionizing photons varies as a function of the initial mass function (IMF) slope, and minimum and maximum initial masses. For a fixed population mass we have found changes of the order of 20-30% through varying the nature of the IMF. This work is useful for many future studies of reionization since it presents ionizing photon production predictions for the most up-to-date Geneva stellar evolution models of Population III stars, and provides insight into how key evolutionary parameters impact the contribution of the first stars to reionization.

This new Geneva model grid of zero-metallicity stars and our detailed analysis of it will be helpful for a variety of future studies on the first stars and the early Universe, including radiative transfer modelling, 3-D hydrodynamic simulations, and population synthesis.

Acknowledgements

I'll begin by expressing my immense gratitude to my supervisor, Jose Groh. I have been incredibly lucky to have had such a supportive and encouraging mentor throughout my PhD and my undergraduate project where I first became interested in the evolution of massive stars. So much of my knowledge of Astrophysics is because of our conversations and your enthusiasm for massive stars research. Thank you for inspiring me to continue despite obstacles and for all of your feedback and kind words. Thank you also to the other senior members of the Astrophysics group and the School of Physics in Trinity, who have helped to create an engaging and supportive environment for all of us.

Probably the greatest part of my PhD has been the people I've met and the friends I've made. Having to spend the last 18 months without the support of my pals in the office, a.k.a. 'Astroffice', has been heartbreaking but I'm so grateful for all the memories we made. Pearse, Brendan, and Ciara, thanks for sharing the start of this journey with me and for your continued friendship after the great solar group departure of 2019. I can't wait to be reunited with you to celebrate this thing that we did and to reminisce over some Pav pratzky. To the other solar group members who welcomed us with open arms into the office, Laura, Aoife Mc. and Aoife R., thank you for the laughs and the madness and for being such inspirations to me. I could only hope to be as knowledgeable and fabulous as you queens. Thank you Dúalta for being a dear friend throughout this experience, for the pints and the chats and the advice, I can't imagine it without you. To the newer additions, Stephen, Rob, Amanda, thanks for making the office even more fun and for making me laugh every day. Thanks also Maxime for brightening the place up even with only one week before a global pandemic tore us apart! To all the more recent recruits who I haven't been able to share the office with, I hope you enjoy the place as much as I did.

To my fellow group members Ioana, Eoin and Andrew, I am particularly grateful. Thanks Andrew for being such a great addition to the group and for your continued support and feedback throughout remote working. Thanks Eoin for your enthusiasm for stellar evolution and for so often sparking my interest in stars. I'm really grateful that we could share the CCA experience and have such great chats, thanks for being so supportive always. Lastly thank you Ioana, you have been my other half throughout this experience and made it easier at every step. I'm eternally grateful for your encouragement and reassurance, and thankful to have made an amazing friend in the process.

I must also thank my friends Kate and Holly who have always supported me and been my rocks since our early days in Physics. To all my friends I am grateful, Clodagh, Lynda, Jess, Erin, Síofra, Dara, Anna, Elisa, Ro, Liam, Sarah, Ross, Seán, and everyone in between, thank you for always having my back and cheering me on.

I want to share my gratitude for my collaborators and friends in the Geneva Observatory, especially Sylvia Ekström, Georges Meynet, Cyril Georgy, Raphael Hirschi, Arthur Choplin, Camilla Pezzotti, Sébastien Martinet, and Sophie Tsiatsiou. I want to also thank everyone I met through Women in Technology and Science (WITS), the friends I made in the Trinity Postgraduate Worker's Alliance (TPGWA), and during my time at the Centre for Computational Astrophysics (CCA) in New York, in particular thank you to my mentors Orsola De Marco, Matteo Cantiello, and Pascale Garaud. I must also recognise the Student Counselling Services in Trinity for the wonderful work that they do and the support that they provide. Finally, thank you to the Irish Research Council (IRC) for funding my research, ChETEC for funding my collaborative visits to Geneva, and the Simmons Foundation for funding my research visit to CCA.

On a more personal note, thank you Robbie. I'm so grateful that I met you and that I had you by my side through so much of my PhD. You have been an incredible support to me, you have encouraged and congratulated me and you make everything feel easier. Thanks for being a big ray of sunshine in my life, even in times of stress.

Lastly, I want to thank my family. To my grandparents, my granduncle, my aunts and uncles, and my cousins, thank you for your support. In particular, Mairtín, Betty, Lorcan, Siobhán, Fr. Seamus, and Ceola, you have inspired and supported me my whole life and I'm forever grateful for it. To my brother and sister, Conor and Ríon, you are my best friends and you are always there for me when I need you. I feel so lucky to have your constant love and support. We celebrated my last graduation together, and I can't imagine this one without you either. To my parents, Martina and James, everything I have and everything I have achieved is because of you. From a young age I remember your encouragement and how you inspired me to be curious about the world. I remember every opportunity you have given me and how much you have believed in me. This thesis is dedicated to you.

For my parents

List of Publications

First-authored publications

1. **Murphy, L.J.**, Groh, J.H., Ekström, S., Meynet, G., Pezzotti, C., Georgy, C., Choplin, A., Eggenberger, P., Farrell, E., Haemmerlé, L., Hirschi, R., Maeder, A., Martinet, S., *Grids of stellar models with rotation - V. Models from 1.7 to 120* $M_\odot$ *at zero metallicity*, Monthly Notices of the Royal Astronomical Society, Vol. 501, Issue 2, pp.2745-2763, February 2021
2. **Murphy, L.J.**, Groh, J.H., Farrell, E., Meynet, G., Ekström, S., Tsiatsiou, S., Hackett, A., Martinet, S., *Ionizing photon production of Population III stars: effects of rotation, convection, and initial mass function*, Monthly Notices of the Royal Astronomical Society, Vol. 506, Issue 4, pp.5731-5749, October 2021

Co-authored publications

1. Groh, J.H., Ekström, S., Georgy, C., Meynet, G., Choplin, A., Eggenberger, P., Hirschi, R., Maeder, A., **Murphy, L.J.**, Boian, I., Farrell, E., *Grids of stellar models with rotation - IV. Models from 1.7 to 120* $M_\odot$ *at Z=0.0004*, Astronomy & Astrophysics, Vol. 627, id.A24, 19 pp., July 2019
2. Groh, J.H., Farrell, E., Meynet, G., Smith, N., **Murphy, L.J.**, Allan, A., Georgy, C., Ekström, S., *Massive Black Holes Regulated by Luminous Blue Variable Mass Loss and Magnetic Fields*, The Astrophysical Journal, Vol. 900, Issue 2, id.98, 5 pp., September 2020
3. Farrell, E., Groh, J.H., Hirschi, R., **Murphy, L.J.**, Kaiser, E., Ekström, S., Georgy, C., Meynet, G., *Is GW190521 the merger of black holes from the first stellar generations?*, Monthly Notices of the Royal Astronomical Society, Vol. 502, Issue 1, pp.L40-L44, March 2021
4. Martinet, S., Meynet, G., Ekström, S., Simón-Díaz, S., Holgado, G., Castro, N., Georgy, C., Eggenberger, P., Buldgen, G., Salmon, S., Hirschi, R., Groh, J.H., Farrell, E., **Murphy, L.J.**, *Convective core sizes in rotating massive stars. I. Constraints from solar metallicity OB field stars*, Astronomy & Astrophysics, Vol. 648, id.A126, 13 pp., April 2021
5. Eggenberger, P., Ekström, S., Georgy, C., Martinet, S., Pezzotti, C., Nandal, D., Meynet, G., Buldgen, G., Salmon, S., Haemmerlé, L., Maeder, A., Hirschi,

R., Yusof, N., Groh, J.H., Farrell, E., **Murphy, L.J.**, Choplin, A., *Grids of stellar models with rotation - VI. Models from 0.8 to 120* $M_\odot$ *at a metallicity Z=0.006*, Astronomy & Astrophysics, Vol. 652, id.A137, 11 pp., August 2021

6. Yusof, N., Hirschi, R., Abu Kassim, H., Eggenberger, P., Ekström, S., Georgy, C., Meynet, G., Crowther, P.A., Maeder, A., Groh, J.H., Farrell, E., **Murphy, L.J.**, *Grids of stellar models with rotation - VII. Models from 0.8 to 300* $M_\odot$ *at super-solar metallicity (Z=0.020)*, in preparation

List of Presentations

Scientific oral presentations

1. **Murphy, L.J.**, Groh, J.H., *The First Stellar Explosions and their Progenitors*, Geneva Observatory Seminar, Switzerland, March 2018
2. **Murphy, L.J.**, Groh, J.H., *The Effects of Rotation on the First Stars in the Universe*, Irish National Astronomy Meeting, Birr, Co. Offaly, Ireland, September 2018
3. **Murphy, L.J.**, Cantiello, M., Garaud, P., De Marco, O., *Thermohaline Mixing in Magnetized Red Giant Cores*, Flatiron Institute, New York, USA, August 2019
4. **Murphy, L.J.**, Groh, J.H., Ekström, S., Pezzotti, C., Meynet, G., Georgy, C., Hirschi, R., Choplin, A., *A new grid of Geneva stellar evolution models for Population III stars*, Irish National Astronomy Meeting, Armagh Observatory & Planetarium, Co. Armagh, Ireland, September 2019
5. **Murphy, L.J.**, Groh, J.H., Ekström, S., Pezzotti, C., Meynet, G., Georgy, C., Hirschi, R., Choplin, A., *A new grid of Geneva stellar evolution models for Population III stars*, CEMP Stars as Probes of First Star Nucleosynthesis, the IMF, and Galactic Assembly, Université de Geneve, Geneva, Switzerland, September 2019
6. **Murphy, L.J.**, Groh, J.H., Ekström, S., Pezzotti, C., Meynet, G., Georgy, C., Hirschi, R., Choplin, A., *The Effects of Rotation on the Evolution and Observable Signatures of Population III Stars*, The European Astronomical Society Annual Meeting, held virtually from Leiden, Netherlands, July 2020
7. **Murphy, L.J.**, Groh, J.H., Ekström, S., Meynet, G., Pezzotti, C., Georgy, C., Choplin, A., Eggenberger, P., Farrell, E., Haemmerle, L., Hirschi, R., Maeder, A., Martinet, S., *The Effects of Rotation on the Evolution and Observable Signatures of Population III Stars*, Irish National Astronomy Meeting, Virtual, September 2020
8. **Murphy, L.J.**, Groh, J.H., Ekström, S., Meynet, G., Pezzotti, C., Georgy, C., Choplin, A., Eggenberger, P., Farrell, E., Haemmerle, L., Hirschi, R., Maeder, A., Martinet, S., Tsiatsiou, S., *The Effects of Rotation on the Evolution and Observable Signatures of Population III Stars*, TCD Postgraduate Seminar, held virtually from Trinity College Dublin, October 2020
9. **Murphy, L.J.**, Groh, J.H., Ekström, S., Meynet, G., Pezzotti, C., Georgy, C., Choplin, A., Eggenberger, P., Farrell, E., Haemmerle, L., Hirschi, R., Maeder,

A., Martinet, S., Tsiatsiou, S., *The Effects of Rotation on the Evolution and Observable Signatures of Population III Stars*, IAUS 361 - Massive Stars Virtual Preview Meeting, held virtually from Ireland, May 2021

10. **Murphy, L.J.**, Groh, J.H., Ekström, S., Meynet, G., Pezzotti, C., Georgy, C., Choplin, A., Eggenberger, P., Farrell, E., Haemmerle, L., Hirschi, R., Maeder, A., Martinet, S., Tsiatsiou, S., Hackett, A., *The Effects of Rotation on the Evolution and Observable Signatures of Population III Stars*, invited seminar for ULB Astrophysics group, held virtually from Brussels, Belgium, May 2021

11. **Murphy, L.J.**, Groh, J.H., Ekström, S., Meynet, G., Pezzotti, C., Georgy, C., Choplin, A., Eggenberger, P., Farrell, E., Haemmerle, L., Hirschi, R., Maeder, A., Martinet, S., Tsiatsiou, S., Hackett, A., *The Effects of Rotation on the Evolution and Observable Signatures of Population III Stars*, The European Astronomical Society Annual Meeting, held virtually from Leiden, Netherlands, June 2021

Scientific poster presentations

1. **Murphy, L.J.**, Groh, J.H., Ekström, S., Meynet, G., *The Effects of Rotation on the Observable Signatures of Population III Stars and their Supernovae*, The European Week of Astronomy and Space Science, Liverpool, UK, April 2018

2. **Murphy, L.J.**, Groh, J.H., Ekström, S., Meynet, G., Pezzotti, C., Georgy, C., Choplin, A., Eggenberger, P., Farrell, E., Haemmerle, L., Hirschi, R., Maeder, A., Martinet, S., Tsiatsiou, S., *The Effects of Rotation on the First Stars*, Royal Astonomical Society Early Career poster competition, Virtual, August 2020

Public presentations

1. **Murphy, L.J.**, *The First Stars in the Universe*, invited lecture for Irish Astronomical Association, Queen's University, Belfast, Ireland, February 2020

2. **Murphy, L.J.**, *First Light: The First Stars in the Universe*, Soapbox Science Dublin, Virtual, July 2020

3. **Murphy, L.J.**, *The First Stars in the Universe*, invited talk for the Centre for Talented Youth Ireland (CTYI), Virtual, July 2020

4. **Murphy, L.J.**, *The First Stars in the Universe*, invited talk for I-LOFAR Astro camp, Virtual, July 2020

5. **Murphy, L.J.**, *First Light: The First Stars in the Universe*, invited lecture for Galway Astrofest, Virtual, January 2021

6. **Murphy, L.J.**, *First Light: The First Stars in the Universe*, invited lecture for Astronomy Ireland, Virtual, March 2021

Contents

List of Figures

List of Tables

Chapter 1

Introduction

The first generation of stars, otherwise known as Population III (Pop III) stars, are unique because they are just that, the first. They formed from the metal-free gas produced in the Big Bang, and as the very first stars they play a crucial role in the history of the Universe. Pop III stars are defined by their metal content as stars with an initial metallicity of $Z \leq 10^{-8}$ (e.g. Iocco et al. 2007), meaning that the mass fraction of metals (elements heavier than helium) in their initial composition is less than 10^{-8}. The first stars in the Universe are generally referred to as Pop III, zero-metallicity, primordial, or metal-free stars. To understand the evolution of these first stars, we must understand massive star evolution, and what makes the first stars different in how they evolved and impacted their environments. In this introduction we provide background to this topic by summarising massive star evolution in Section 1.1, discussing how this evolution differs for the first stars in Section 1.2, and finally we discuss how the first stars impacted their environments and why they are so important in understanding the evolution of the early Universe in Section 1.3.

1.1 Massive Star Evolution

Typically defined as having initial masses of $M_{\mathrm{ini}} \geq 8\,\mathrm{M}_{\odot}$, massive stars play a crucial role in the evolution of the Universe. These stars are unlike lower mass stars because they can produce iron in their cores, and many end their lives in large explosive events known as supernovae (SNe). Through these large explosions they can chemically enrich their surroundings by ejecting the heavy elements that they produce during their lifetimes into the Universe. Elements such as oxygen, sodium, and magnesium, which are required for life to exist, are mainly produced by massive stars and their explosive deaths (see nucleosynthesis review: Johnson 2019). Therefore, without massive stars and their explosions, our world would look very different today. Massive stars are important for many other reasons including ultraviolet (UV) feedback, stellar winds, and ionization, as we will discuss in Section 1.1.1. The evolution of massive stars is complex and subject to the effects of rotation, mass loss, convection, and binary interaction. We will provide background on key aspects of massive star evolution throughout different burning phases and systems in Sections 1.1.2 to 1.1.5, where we will discuss massive star evolution in the context with which it is most frequently studied, solar-metallicity massive stars. A solar-metallicity star shares the same initial composition as the Sun, that is, approximately 72% hydrogen, 26.6% helium and 1.4% heavier elements (by mass) such as carbon and oxygen (Asplund et al. 2005; Ekström et al. 2012). We later describe how the evolution is affected at other initial compositions of lower metallicities in Section 1.1.6.

1.1.1 Importance of Massive Stars

Massive stars are rare in the local Universe. According to the Salpeter (1955) initial mass function (IMF) and its revisions (Scalo 1986; Kroupa 2001; Chabrier 2003), at solar metallicity massive stars are significantly rarer than low-mass stars. This is partly due to the physics of star formation, since the radiation pressure of massive stars is expected to hinder accretion (see reviews: Tan et al. 2014; Krumholz 2015; Motte et al. 2018). However, massive stars also have shorter lifetimes than stars of lower initial masses due to their high luminosities, which further contributes to their scarcity.

Despite the rarity of massive stars, their impact on the Universe is substantial. One of the most important impacts of massive stars is their role in nucleosynthesis and the chemical enrichment of the Universe. In order to counteract their immense gravitational force, massive stars must produce a lot of energy throughout their lives. They do so through nuclear fusion in their cores. Massive stars have larger and hotter cores than stars of lower masses, which allows them to fuse heavier elements and produce important elements such as iron, silicon, and nickel. Shown in Figure 1.1 is a schematic of the structure of burning regions in a massive star before its death. The right side of the figure shows a basic illustration of a massive star at the beginning of its evolution, with a nuclear burning convective core, and a radiative envelope. The left side of the figure then depicts the final structure of the original convective core, having evolved through each of the nuclear burning stages. Stars typically begin the first phase of their evolution when the core has reached the required temperature for H fusion, which is $\sim 10^7\,$K. Following the depletion of hydrogen in the core, there is a second nuclear burning phase of He fusion if the core can reach the temperature necessary for He burning, which is $\sim 10^8\,$K. The subsequent burning phases are C burning, Ne photodisintegration*, O burning, and Si burning; which occur at increasingly short timescales, as the central

---

*Unlike 'burning' phases where nuclei fuse together, Ne nuclei are disintegrated by photons which at high temperatures have enough energy to break the Ne nuclei.

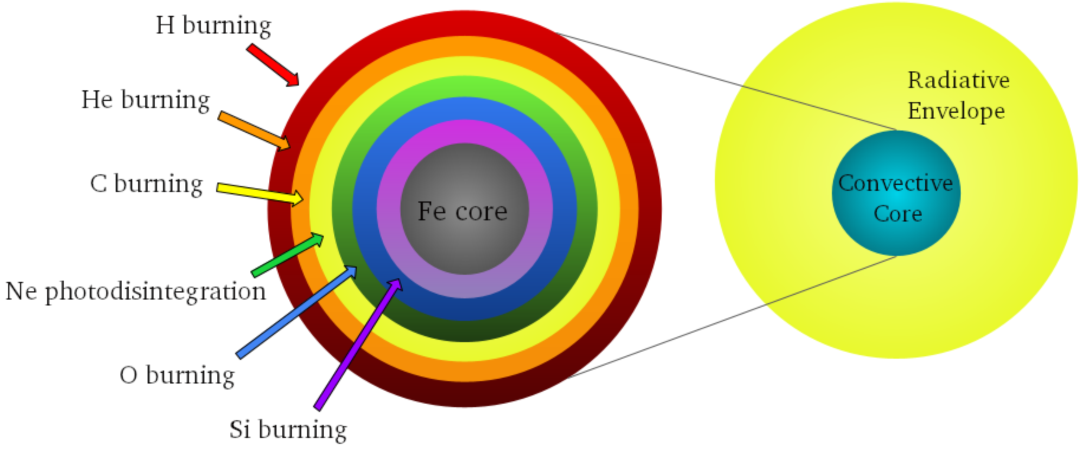

Figure 1.1: Schematic of the structure of a massive star, prior to the end of its evolution. The right side illustrates the radiative envelope and convective core, while the left side shows the interior structure of what was originally the H-burning core. Shown are the burning phases from H fusion to the formation of the Fe core, with nuclear burning shells having developed.

temperature increases to the required temperatures to overcome the binding energy of each successive species. These late nuclear burning phases distinguish massive stars from other stars, since cores of lower mass stars cannot reach the necessary temperatures to continue nuclear burning until the formation of an Fe core. The evolution of massive stars ceases with the formation of this Fe core at the end of Si burning, as illustrated by Figure 1.1. Nuclear burning ceases at this point because Fe burning is endothermic, which means that it requires more energy than it produces, and so the star no longer has an energy source to counteract the force of its own gravity. This triggers a collapse of the star which, depending on the mass of the core, compactness, and remaining burning regions in the envelope (e.g. Burrows & Goshy 1993; Heger et al. 2003; Fryer et al. 2012; Sukhbold & Woosley 2014; Roberts et al. 2016; Vartanyan et al. 2021), may produce a SN explosion. For more information on nuclear burning phases of massive stars in late evolution see Chapter 28 of Maeder (2009), and Chapter 35 of Kippenhahn et al. (2012), in particular their Figure 35.1.

The picture of the evolution of a massive star that we have described here is a simplification of the complexity of the structural evolution of massive stars. In reality convection and nucleosynthesis are not restricted to the stellar core, and convective burning zones can develop in different regions of massive stars as their evolution continues. The diagram used to study how convective regions and stellar structure vary over time is known as the Kippenhahn diagram. A Kippenhahn diagram for a $15\,\mathrm{M}_\odot$ non-rotating model at

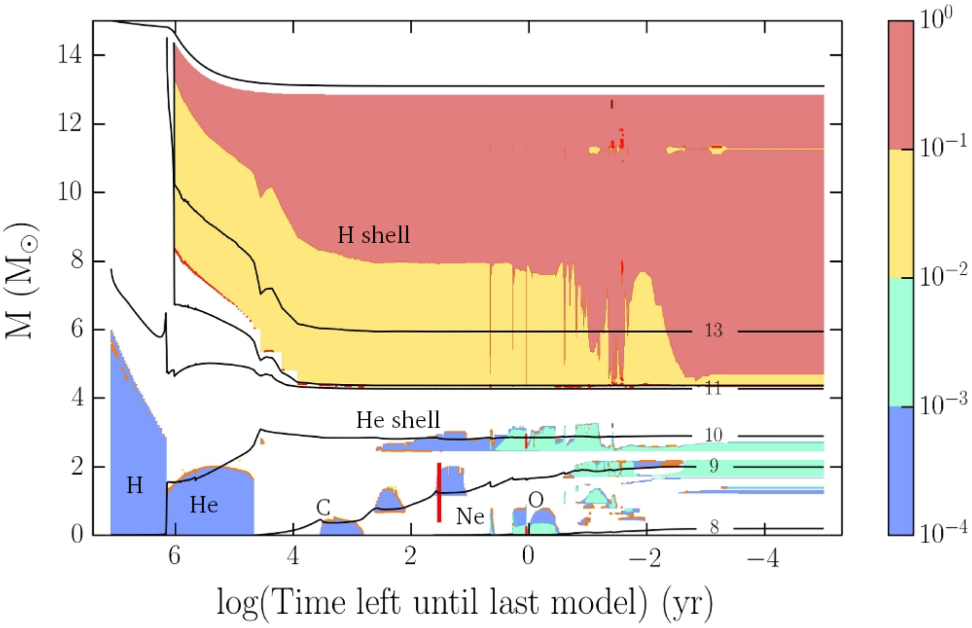

Figure 1.2: Kippenhahn diagram of a $15\,M_\odot$ solar-metallicity non-rotating model. Taken from Cristini et al. (2017), Figure 1, and adapted by the author to include labels of various key burning regions. The horizontal axis is a logarithmic scale of the time left before the predicted collapse of the star in years and the vertical axis is the stellar mass coordinate. The total mass and radial contours (in the form log(r) in cm), are drawn as solid black lines. Shaded areas correspond to convective regions. The colour indicates the value of the Mach number, which is the ratio of the convective velocity to the speed of sound. The red vertical bar around log[time left in years]$\sim$1.5 represents the domain simulated in 3-D, and the time at which the 3-D simulations start, relative to the evolution of the star.

solar metallicity is given in Figure 1.2, originally Figure 1 of Cristini et al. (2017), where 3-D simulations were carried out to investigate the nature of the C-burning convective shell in massive stars. This figure illustrates the complexity of the structural evolution of massive stars and how their nuclear-burning processes change over time. We see the original H-burning core, followed by a He-burning core with a new H-burning convective zone in the envelope. In later burning stages we see the development of convective cores burning heavier elements, and new nuclear burning shells above the stellar core. The structural evolution of massive stars varies depending on evolutionary properties such as initial mass, mass loss, and rotational velocity. It is important that we understand this structural evolution if we are to understand their chemical enrichment, and the nature of their explosive deaths as SNe.

These explosive deaths of massive stars play a crucial role in the chemical evolution of galaxies and the Universe. Their high velocities ($\sim 10000 - 15000\,\mathrm{km\,s^{-1}}$) transport ejecta to large distances. For example, the Crab nebula, which is a nearly 1000 year old SN remnant, has a diameter of $\sim$ 3.4 pc (11 light yr; Hester 2008; Bühler & Blandford 2014). These powerful explosions can therefore enrich their surroundings up to great distances, making them a very efficient source of heavy elements in the Universe. There are different types of SNe depending on the nature of the explosion, and each contribute to chemical enrichment in different ways. Most massive stars explode as core-collapse SNe (CCSNe), which typically produce H-rich ejecta with significant amounts of carbon, oxygen, and nitrogen. The stellar core left behind in a CCSN explosion will become either a neutron star or a black hole depending on its mass, and most of the heavier elements (e.g. iron, nickel) remain in this extremely dense remnant (CCSNe reviews: Janka et al. 2007; Smartt 2009; Janka 2012). Another type of explosion, which may occur for very massive stars, is a pair-instability SN (PISN), in which pulsations trigger an explosion of the whole star including the core. These dramatic explosions are therefore important sources of iron and very heavy elements in the Universe, although their existence is yet to be observationally confirmed (Dessart et al. 2013). PISNe can be understood as follows. In high mass domains, stars which have finished He burning enter a temperature and density regime in which electron-positron pair creation occurs. This leads to an instability which triggers the gravitational collapse of the CO core. For certain mass ranges explosive O burning occurs during the collapse, the thermal pressure from which halts the collapse and the whole star is disrupted by nuclear-powered explosions, producing a PISN. For higher mass cases nuclear burning isn't enough to halt the collapse and the result is the formation of a black hole. According to Heger & Woosley (2002) the expected initial mass range for PISNe is 140-260 $\mathrm{M}_\odot$ for Pop III stars. We will discuss pair-instability events and stellar remnants further in Section 1.3.3. The energy produced by SN explosions can be destructive in their immediate vicinity, since they produce such strong shock waves and ionizing radiation. However at large distances these shock waves can trigger the collapse of molecular clouds, and thus star formation (e.g. Chevalier 1977; McKee & Ostriker 2007), which means that stars can be born from the remnants of a previous explosion. Therefore, the evolution and explosive deaths of massive stars are imperative for understanding the nature of the generations of stars that follow them.

While SNe are extremely important for chemical enrichment, massive stars can also pollute their environments through mass loss during their evolution. Massive stars experience strong mass loss throughout their lives through stellar winds, which are driven by the large radiation pressure of massive stars and heavy elements at the surface (Kudritzki & Puls 2000; Vink et al. 2001; Smith 2014). The ejecta from this mass loss provides the interstellar medium (ISM) with the elements produced during the star's lifetime and in doing so can chemically enrich the regions around the star. In some cases, mass lost through stellar winds of massive stars can produce circumstellar material (CSM) around the star, which may dramatically alter the nature of the subsequent final explosion, producing what is known as interacting SNe (Chevalier & Fransson 1985; Chugai & Danziger 1994; Boian & Groh 2019, 2020). Interaction of SN shock waves with a dense CSM may even drive an extremely powerful event known as a superluminous SN (e.g. SN2006gy; Ofek et al. 2007; Dessart et al. 2015). Therefore, the substantial mass loss of massive stars not only impacts their evolution, but also their environments and the nature of their explosions. Massive stars are also an important source of UV and ionizing radiation in the Universe due to their high luminosities and temperatures. This strong radiation ionizes their surroundings (e.g. Whitworth 1979) and may be largely responsible for the reionization era as we will discuss in Section 1.3.2. In light of how important massive stars are in the evolution of the Universe, it is crucial that we have a strong understanding of their evolution, and how they are impacted by fundamental properties such as rotation, mass loss, and metallicity.

1.1.2 Main Sequence Evolution

The main sequence (MS) phase is the first phase in a star's evolution, where H fusion in the core is powering the star's radiation (see Figure 1.2). The MS is the longest evolutionary phase, and stars will spend approximately 90% of their lifetimes on the MS (e.g. Ekström et al. 2012) until they have exhausted all of their central hydrogen. The MS is therefore very important in understanding how stars evolve, and their evolution during this phase will determine their structure in later burning phases and subsequent final fate. Unlike lower mass stars, massive stars have large convective cores and radiative envelopes (Figures 1.1 and 1.2). While low mass stars are dominated by gas pressure, massive stars are dominated by radiation pressure, which gives a much stronger temperature dependence. To understand this we take Equation 1.1, which is the equation for the total pressure produced by the star.

$$P_{total} = \frac{\rho k T}{\mu m_H} + \frac{1}{3} a T^4 \tag{1.1}$$

Gas pressure is given by the first term with density ρ, Boltzmann constant k, temperature T, mean molecular weight μ, and hydrogen atomic mass m_H. Radiative pressure is given by the second term with radiative constant a and the stronger temperature dependence, T^4. Since radiation pressure dominates, the ratio of radiation to gas pressure, $\frac{P_{rad}}{P_{gas}} \propto \frac{T^3}{\rho}$, is enhanced. This favors stellar winds and enhances rotational mixing, which both have significant effects on stellar evolution. Strong stellar winds provide heavy mass loss, while rotational mixing can lead to enrichment of the stellar surface, changes to stellar structure, and may even result in chemically homogeneous evolution (CHE) where the star is fully mixed. Another consequence of the dominant radiation pressure in massive stars is the effect on the luminosity-mass relation. From energy conservation we find $L \propto M\epsilon$ where ϵ gives energy generation and varies depending on the nuclear reactions in question. In low mass stars where energy generation is less efficient, luminosity depends on mass as $L \propto \mu^4 M^3$. Since massive stars are dominated by radiation pressure and have more efficient energy generation, this relation changes, and the luminosity-mass relation becomes $L \propto M$. This then has a crucial impact on the luminosity evolution of massive stars and how much variation is seen in surface properties across their lifetimes.

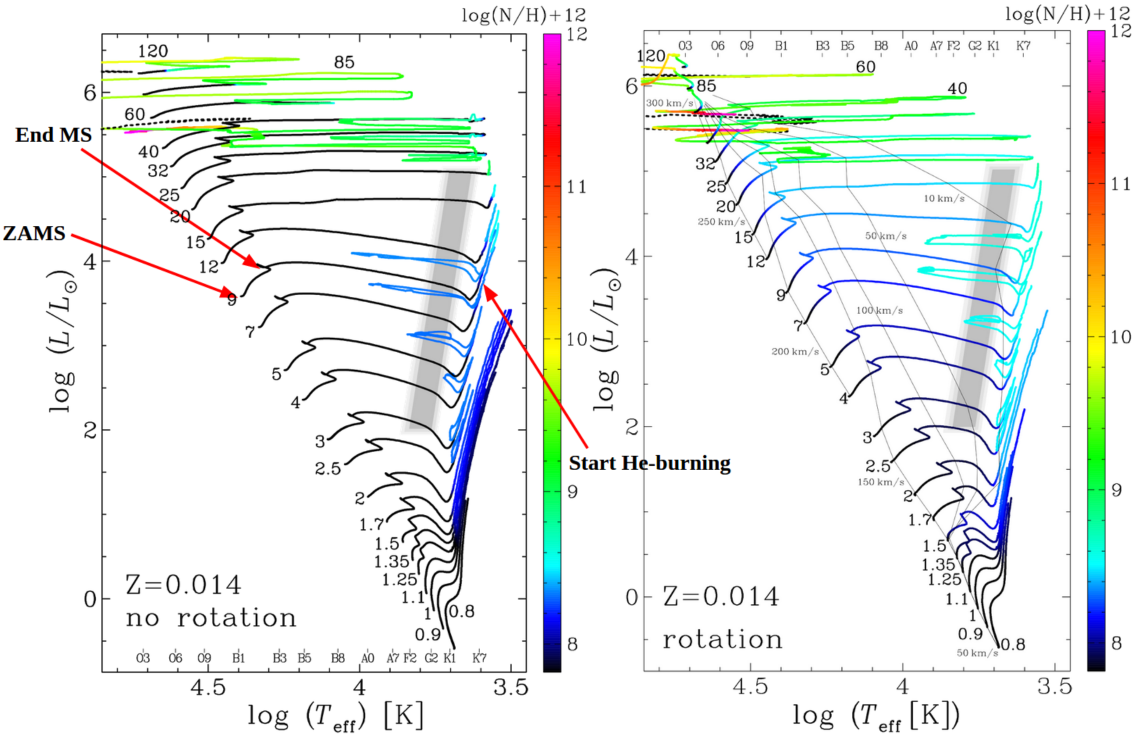

Figure 1.3: Hertzsprung-Russell (HR) diagram for non-rotating (left panel) and rotating (right panel) models, with initial masses in the range $0.8\,\mathrm{M}_\odot \leq M_{\rm ini} \leq 120\,\mathrm{M}_\odot$, at solar metallicity, from Ekström et al. (2012), Figures 4 and 9. The figure is edited by the author to show the beginning (ZAMS) and end of the H-burning phase, and the start of the He-burning phase for the $9\,\mathrm{M}_\odot$ model. The colour scale indicates the surface number abundance of nitrogen on a log scale as a fraction of hydrogen abundance, i.e. where $N = H$, $\log(N/H) + 12 = 12$. The grey shaded area represents the Cepheid instability strip where pulsations are expected (Tammann et al. 2003).

One of the most common ways to study stellar evolution is to observe how stellar models evolve on the Hertzsprung-Russell (HR) diagram. One such diagram is shown in Figure 1.3. Taken from Ekström et al. (2012), this allows us to view the key differences in stellar evolution for a variety of initial masses, $0.8\,\mathrm{M}_\odot \leq M_{\rm ini} \leq 120\,\mathrm{M}_\odot$, at solar metallicity. We will first discuss the models without rotation, therefore focusing on the left panel of Figure 1.3. Indicated in the figure are the start and end points of the MS stage, and the start of the He-burning phase, for the $9\,\mathrm{M}_\odot$ model. The zero age main sequence (ZAMS) phase signals the beginning of H burning in the core, and the stellar mass here ($M_{\rm ZAMS}$) is taken as the initial mass ($M_{\rm ini}$) of the star. The end of the MS is the point in the evolution when there is a fraction of less than 10^{-3} hydrogen remaining in the core and H-burning ceases. This end MS stage can be observed in Figure 1.3 as the point where the effective temperature, $T_{\rm eff}$, begins to increase (e.g. $log(T_{\rm eff}/\mathrm{K}) \approx 4.3$

for the non-rotating $9\,\mathrm{M}_\odot$ model), which we will discuss in Section 1.1.3. The HR diagram enables us to track the evolution of the surface properties of a star based on its bolometric luminosity and effective temperature. A star evolving towards higher temperatures may indicate a contraction of the envelope or mass loss. The opposite is true as it moves to lower temperatures, a decrease in effective temperature may indicate an expansion of the envelope or mass gained from a companion in a binary system. In terms of luminosity evolution, an increase typically indicates higher energy generation, but is also strongly correlated with mass loss. During the MS, the evolution of the surface properties for all initial masses is such that the luminosity increases while the surface temperature decreases. These changes to the surface properties result from the increase in average mean molecular weight in the stellar interior, as H fusion converts hydrogen atoms into helium. This is discussed in detail in Farrell et al. (2021a), which uses a new stellar modelling technique, SNAPSHOT (Farrell et al. 2020), to isolate the cause and effect between interior and surface properties in stellar evolution.

It can be observed from Figure 1.3, that massive stars are much more luminous than lower mass models, owing to their larger nuclear burning cores and subsequent higher energy generation. On the other hand, models of lower initial mass increase more in luminosity during their lifetime. As we have discussed, luminosity varies differently with mass for massive stars compared to low mass stars, due to their dominant radiation pressure. Therefore in low mass stars, where their luminosity-mass relation is $L \propto \mu^4 M^3$, L will increase sharply as μ increases, which happens as hydrogen is fused into helium. Meanwhile the luminosity of massive stars sees less variation, since it is less sensitive to changes in composition. Massive stars are also much hotter than lower mass stars for the majority of their life and are spectroscopically classified as OB stars, as can be seen in Figure 1.3 where higher mass stars spend their main sequence (MS) lifetimes in the blue ($T_\mathrm{eff} \gtrsim 10^4\,\mathrm{K}$). In addition to having higher effective temperatures, massive stars also have higher central temperatures which allows them to burn hydrogen more efficiently than lower mass stars. This is because they are hot enough to achieve H fusion through the CNO cycle[†], while the temperatures of lower mass cores must rely only on the proton-proton chain reaction. The use of the CNO cycle explains the higher energy generation of massive stars and hence why they are significantly more luminous than lower mass stars. Their higher energy generation rates also explain their shorter lifetimes, since they burn through their hydrogen supply more quickly than lower mass stars. While Figure 1.3 shows that massive stars see less variation in luminosity than lower mass stars on the MS,

---

[†] H fusion can occur through two different sets of reactions. The first are the proton-proton (pp) chain reactions which occur at lower temperatures and require only hydrogen elements to begin fusion. The second set of reactions are referred to as the CNO cycle which require higher temperatures and the presence of carbon, nitrogen and oxygen for H fusion. The CNO cycle can produce more energy than the pp chain reactions by several orders of magnitude at higher temperatures (see Maeder 2009, Chapter 25), hence why massive stars are dominated by the CNO cycle to counteract their high gravitational pressure.

the opposite is true for their surface temperatures. From the figure it can be seen that as initial mass increases, so too does the variation in temperature on the MS. According to the findings of Ekström et al. (2012), this is mainly due to increased mass loss at higher initial masses which results from their increased radiation pressure. Envelope inflation may also play a role in the higher temperature variance however, where the high luminosities of massive stars cause an expansion of the envelope and a subsequent decrease in surface temperature (e.g. Gräfener et al. 2012, Section 5.5.4).

The evolution of massive stars is also highly dependent on initial properties such as convection, mass loss, and rotation. Increased convective mixing provides the burning core with more hydrogen which increases the lifetime of the star, and also impacts the energy generation rate, luminosity, and surface temperature. Convective overshooting also changes the location of the end of the MS in the HR diagram, otherwise known as the terminal age main sequence (TAMS), and studies such as Castro et al. (2014); Martinet et al. (2021) have used this feature to constrain the parameters that describe convective overshooting. Another important property in the evolution of massive stars is mass loss. Mass loss is not only important for understanding massive stars in terms of their contribution to chemical enrichment of the ISM or how their ejected material affects their final fate (see Section 1.1.1), but it is also important because of how it impacts the structure and subsequent evolution of the star itself. Strong stellar winds can alter the structure of the star significantly on the MS, for example, by altering the temperature profile which can change the size of the convective core. Strong mass loss also impacts the surface properties. Shedding the outer layers of the star can be observed in the HR diagram as a bluewards evolution, however, this is more commonly observed in the post MS stages as we will discuss in Section 1.1.3. Rotational effects can be more difficult to understand than convection or mass loss because of the complexities in how rotation impacts mixing of the stellar interior, energy generation rates, and mass loss. The right panel of Figure 1.3 shows the evolutionary tracks of the models with rotation from Ekström et al. (2012). The most obvious difference with rotation from this figure is the increased chemical enrichment due to rotational mixing, with significant increases in nitrogen abundance even on the MS for more massive models. As well as increasing the production of heavy elements within the star, rotational mixing increases the stellar lifetime, for the same reason as convective mixing in that more hydrogen can be mixed inwards to the burning core from the envelope. Rotation may also boost stellar winds and drive mass loss if the angular momentum transport within the star is efficient enough. These effects on the structure of the star during the MS strongly impact the evolution during the post MS phases, and will subsequently determine the nature of the final fate of the star. We discuss rotation and its effects on stellar structure in detail in Section 1.1.4.

1.1.3 Post Main Sequence Evolution

At the end of the MS the lack of energy generation in the nearly exhausted H-burning core allows gravity to dominate, and the whole star briefly contracts. This leads to the feature seen at the end of the MS in Figure 1.3, where $T_{\rm eff}$ begins to increase. Once fully exhausted of hydrogen the contraction of the now inactive core increases greatly. The core grows hotter and hotter throughout this strong contraction until the temperature required for He burning is reached. During this contraction a H-burning shell develops which triggers an expansion of the stellar envelope. In Figure 1.3 this expansion is evident from the large decrease in effective temperature between the end of H burning and He ignition. This expansion ceases when He burning begins in the core and the star regains hydrostatic equilibrium, therefore the extent of this 'contracting core, expanding envelope' phase depends on the central temperature increase required for He fusion from the end of the MS. As we will see in Section 1.2.5 this behaviour varies with metallicity.

Although the MS covers $\sim$90% of the lifetime of a star, the post MS stages are also hugely impactful on the evolution. These later phases can see large increases in mass loss, significant variation in surface properties, and substantial chemical enrichment, all of which influence the final fate of the star. There are a number of different scenarios which categorise stars in their post MS evolution based on observational definitions. As a star evolves redwards in the HR diagram and their surface temperature decreases they can be categorised as blue supergiants (BSGs), yellow supergiants/hypergiants (YSGs/YHGs), or red supergiants (RSGs), for different ranges of effective temperature. This typically represents an expansion of the stellar envelope, and will impact mass loss (e.g. van Loon et al. 2005; Mauron & Josselin 2011; Smith 2014) and the observational signatures of SNe (e.g. Groh et al. 2013a,b) accordingly. Evolution towards the red part of the HR diagram impacts mass-loss rates and the nature of the mass loss, and it impacts the observational signatures of SNe in how the inflated envelope affects the light curve, for example in powering a plataeu phase and producing a Type II-P SN (classification from Barbon et al. 1979). For certain values of luminosity and temperature stars can also become unstable and experience pulsations, they are then known as luminous blue variables (LBVs; see reviews, Humphreys & Davidson 1994; Smith 2014; Weis & Bomans 2020), although it should be noted that this is a definition based on observed photometric and spectral variability. Stars which evolve to LBVs lose large amounts of mass during these pulsations, with mass-loss rates $> 10^{-5}\,{\rm M_{\odot}yr^{-1}}$ and even up to a few solar masses during large eruptions. If enough mass is lost and the outer layers of the star are stripped, the star will evolve to much higher effective temperatures. The star now becomes a Wolf-Rayet (WR; see review, Crowther 2007) star, a scenario distinguished through spectral signatures of strong, broad emission lines. There are further classifications for WR stars based on their chemical composition which can indicate the chemical enrichment of the star. These are, WN stars that show evidence of helium and nitrogen content, WC stars which contain helium and carbon, and WO stars which contain helium and oxygen.

Understanding what drives the star to evolve to lower or higher effective temperature in the post MS phases is complex because of the interdependent nature of interior properties such as mass loss, rotation, and convective mixing. A new way to investigate the connection between interior and surface properties is presented in Farrell et al. (2020) to address this question. Through their SNAPSHOT technique, which systematically computes stellar structure models in hydrostatic and thermal equilibrium based on specific structural properties, four main factors have been discovered to drive the evolution to lower effective temperatures during central He-burning. These are, an increase in He abundance in the H-burning shell; an increase in the core-mass ratio in the regime of $M_{\text{core}}/M_{\text{total}} > 0.6$; an increase in the CNO abundance in the H-burning shell; and a decrease in the central He abundance (Y_{c}) during the latter half of core He burning. Based on these changes to the interior structure, as well as shedding of the outer layers through mass loss, massive stars can evolve back and forth on the HR diagram and pass through these different phases multiple times. Through linking observations of these objects with stellar evolution modelling predictions, we can better understand the true nature of massive stars and how they impact the Universe.

As shown in Figure 1.3, massive models can experience substantial changes to their surface properties as they evolve through these different phases. By comparing the left and right panels of Figure 1.3 we can observe how rotation can impact the post MS evolution. Similarly to the MS evolution described in Section 1.1.2, the most obvious change from the figure with rotation is an increase to the production of nitrogen, which is indicative of the increased chemical mixing in rotating models. However, we can also observe changes to the evolution towards RSG or BSG phases, with rotation hindering the redwards evolution of massive stars and promoting evolution to higher effective temperatures. The changes to surface properties in these late stages with rotation are not straightforward, and are evidence for the sensitivity of the surface properties to changes to interior mixing in the models. Given the impact that the final surface properties have on the nature of the stellar explosion (e.g. Groh et al. 2013a,b; Boian & Groh 2018), it is crucial that we understand the impact of rotation on stellar structure if we are to understand the nature of the late burning stages and the final fate.

1.1.4 Rotation

Stars rotate because of the nature in which they form. As molecular gas clouds clump together they rotate, then as these clouds collapse to form stars, the law of conservation of angular momentum ($\Omega r^2 =$ constant) states that their decreasing radius amplifies this rotation. Therefore, even a small rotation of the molecular cloud can result in significant rotation of the subsequent protostars. Observational surveys have confirmed the ubiquity of rotating stars in the Universe, with a report of 496 OB stars by Huang & Gies (2006) showing a velocity distribution of up to $400\,\mathrm{km\,s^{-1}}$, peaking at $200\,\mathrm{km\,s^{-1}}$ (see their Figure 5). Their later report of 441 field B stars and 557 cluster B stars (Huang et al. 2010a) showed that the highest probability density for the rotational velocity of newborn B stars is $\upsilon_{\mathrm{eq}}/\upsilon_{\mathrm{crit}} = 0.49$, with $\sim$52% of B stars born with $0.4 \leq \upsilon_{\mathrm{eq}}/\upsilon_{\mathrm{crit}} \leq 0.8$. However for massive stars in the sample ($M_{\mathrm{ini}}/\mathrm{M}_{\odot} \geq 8.6$) the maximum rotational velocity found was $\upsilon_{\mathrm{eq}}/\upsilon_{\mathrm{ini}} \sim 0.63$. Here, υ_{eq} refers to the velocity at the stellar equator, and υ_{crit} refers to the critical, or 'break-up', velocity where the centrifugal force equals the gravitational attraction at the equator (see Chapter 2, Maeder 2009). The critical velocity, υ_{crit}, is defined as

$$\upsilon_{\mathrm{crit}} = \sqrt{\frac{GM}{R_{\mathrm{eq}}}} \tag{1.2}$$

where G is the gravitational constant, M is the stellar mass, and R_{eq} is the stellar radius at the equator. More recently, Ramírez-Agudelo et al. (2013) studied the rotational velocities of a sample of 216 O stars in the Large Magellanic Cloud (LMC). It was found that 80% of the observed stars rotate with initial velocities $\upsilon_{\mathrm{ini}} \leq 300\,\mathrm{km\,s^{-1}}$, peaking at $80\,\mathrm{km\,s^{-1}}$, while the remaining 20% are fast rotators with $300\,\mathrm{km\,s^{-1}} < \upsilon_{\mathrm{ini}} \lesssim 600\,\mathrm{km\,s^{-1}}$. Since rotation appears to be an innate property of stars, it is crucial that its effects on stellar evolution are well studied.

There are two main treatments of rotation in stellar evolution modelling, differential rotation ($\Omega = \Omega(r)$), and rigid rotation ($\Omega =$constant). The former refers to shellular rotation where the inner regions and the core rotate faster than the outer layers. This leads to what is known as the shear instability, in which differential rotation induces a shear force between layers which have different angular velocities, and this shear drives turbulent mixing between different layers. The shear instability therefore increases chemical mixing within the star. Rigid rotation, or solid-body rotation, arises through coupling of the core and the envelope which can be achieved through magnetic fields. This coupling of the outer layers to the inner regions increases rotation closer to the surface and increases mixing throughout the star. However, the star may also lose angular momentum through a process known as magnetic braking. This refers to the process whereby particles in the stellar wind are trapped by the magnetic field and rotate with the star up to large distances, which by the law of conservation of angular momentum causes the star to spin down.

A crucial impact of rotation is that the star cannot be in thermal equilibrium. This is because, except at the equator, the centrifugal force is not parallel to the gravitational force. As a result, the effective gravity is no longer radial, and is lower at the equator than at the poles. Fast-rotating stars therefore have an ellipsoidal-like shape with a bigger equatorial than polar radius, thus the effective temperature is lower at the equator than at the poles. The lack of thermal equilibrium in rotating stars leads to an instability known as the Eddington-Sweet circulation, or the meridional circulation, which are large scale currents in the star acting to restore thermal equilibrium. These currents are very important for the transport of chemical species and angular momentum, and vary depending on the density of the star, as we will discuss in Sections 1.2.4 and 1.2.6.

Rotation can act as a sustaining force against the gravitational pressure of stars. The centrifugal force produced by rotation weakens the gravitational force as stars form and get closer to H-ignition on the ZAMS. This impact on gravitational pressure changes the density structure, and subsequently leads to a steeper temperature profile within the star. The size of the nuclear burning core is determined by the temperature gradients and a steeper temperature profile leads to a smaller core, which in turn reduces the luminosity and surface temperature on the ZAMS. However, rotational mixing allows the star to increase its core mass throughout the evolution which can increase surface temperature and luminosity, and, by providing more fuel to continue nuclear burning, can also increase the stellar lifetime.

In addition to the effect on chemical transport and stellar structure, rotation can impact mass loss during the evolution. This occurs if the rotational velocity is high near the stellar surface, which decreases gravity and strengthens mass loss. If mass is lost due to rotation, then the mass is expected to be lost at the equator. This can then lead to the formation of a so-called decretion disk (Lee et al. 1991; Owocki 2005; Krtička et al. 2011). These disks impact the observable signatures of the star by producing strong emission lines in the stellar spectrum. Stars with these signatures are known as Oe stars (e.g. Li et al. 2018), or Be stars depending on their original spectral class (reviews: Porter & Rivinius 2003; Rivinius et al. 2013). If a star experiences significant mass loss, then this also impacts the rotation of the star by removing large proportions of their angular momentum. This is an example of the interdependent nature of evolutionary effects in massive stars. To understand rotational effects and how they change other evolutionary properties such as mass loss, we therefore need to self-consistently model rotation in stellar evolution models. From this we can better understand how rotation impacts a star throughout its evolution, and how these changes impact the evolution of our Universe. For a detailed review on the impact of rotation on stellar evolution see Maeder & Meynet (2000b).

1.1.5 Binaries

Through observational research it has been found that roughly 20-60% of massive stars are part of a binary system, and this increases to even higher rates of 80% for stars of initial masses $\geq 16\,\mathrm{M}_\odot$ (Kobulnicky & Fryer 2007). In reality these fractions are probably even higher since spectroscopic binaries can be missed due to factors such as low inclination, long orbital periods, high eccentricity, or low-mass companions that are difficult to detect. Of those that are missed in binary surveys some will be close binaries that interact and exchange mass, these missing binaries must therefore be accounted for in order for the observational fraction to be representative. In recent research it has been estimated that the fraction of massive stars in binary systems whose orbital period is so short that the stars must exchange mass or merge is approximately 75% (Kobulnicky & Fryer 2007; Kiminki & Kobulnicky 2012; Sana et al. 2012). Of the total population of massive stars, it is estimated that 24% will merge, 33% will have their H envelopes stripped before death, 14% will be spun up by accretion, and only about 29% of massive stars are effectively single, which includes wide binaries (Sana et al. 2012). More recently, Moe & Di Stefano (2017) reported a single star frequency of $16 \pm 9\%$ for stars of initial masses $9\,\mathrm{M}_\odot \leq M_\mathrm{ini} \leq 16\,\mathrm{M}_\odot$ and $6 \pm 6\%$ for stars of initial masses $M_\mathrm{ini} \geq 16\,\mathrm{M}_\odot$. It follows from these high binary fractions that Roche lobe overflow[‡] must dominate the observed effects of mass loss and mixing seen in massive stars.

Binary interaction may also impact rotation and has been linked to the formation of Be stars (Porter & Rivinius 2003; de Mink et al. 2013; Rivinius et al. 2013). Additionally, the exchange of mass in the system can have interesting implications for the observational signatures of the mass gaining companion star (e.g. Hellings 1983). If the companion gains significant mass and settles into equilibrium they can appear on the HR diagram as more massive younger stars. This has been found to be the case for binary mergers, where the two stars in the system coalesce to form a larger star which is then ‘rejuvinated’ and classified as a ‘blue straggler’ star, such as τ Sco (Schneider et al. 2016, 2019), which with an inferred age of $< 5\,\mathrm{Myr}$ appears anomalously young compared to other stars of $\sim 11\,\mathrm{Myr}$ which are thought to have formed together in the Upper Scorpius association. Studies such as Eldridge et al. (2008); de Mink et al. (2013); Yoon et al. (2017); and Farrell et al. (2019) have modelled the stellar evolution of binary stars and looked in detail at how binary interaction can impact mass loss, rotation, and observational signatures of massive stars. Among the key results of these works are increased fractions of stripped WR stars (Eldridge et al. 2008) and higher rotational velocities due to binary interaction (de Mink et al. 2013). Given the prevalence of binaries among massive stars, such works are crucial in understanding how binary interaction impacts stellar evolution and final fates.

1.1.6 Evolution at Lower Metallicities

So far we have discussed massive star evolution at solar metallicity. However, as we move to higher redshifts and earlier epochs in the Universe, the metallicity of stars decreases. To understand the evolution of stars in the distant Universe then, we need to understand how changing the initial composition impacts the evolution. We have

---

[‡] Roche lobe overflow refers to the exchange of mass between stars in a binary system when the stars are close enough such that the gravity of the companion star can remove mass from the primary star. This typically occurs in late stages of the evolution when the primary star expands.

discussed the complexity of how massive star evolution is impacted by properties such as mass loss, rotation, convection, and binarity at solar metallicity. The uncertainty of these evolutionary effects is further increased at lower metallicity where we have less observations, and thus less constraints for our models. However, with the help of theoretical models and improving observational facilities we can predict how these evolutionary effects differ as we go to lower metallicity. One of the most significant effects of a lower initial metallicity is the impact on mass loss. The outcome of the evolution of a massive star is largely a function of their stellar wind and mass-loss rate (Section 1.1.3). However, the strength of the stellar wind is strongly dependent on the metallicity. The relationship between mass loss and metallicity is based on the CAK theory (named after Castor, Abbott and Klein) which describes the acceleration of the stellar wind by line opacities (Lucy & Solomon 1970; Castor et al. 1975; Abbott 1982). In simple terms, the absorption of photons by heavy elements at the stellar surface transfers momentum to the gas and produces a force on the stellar material which accelerates the stellar wind. On this basis mass-loss prescriptions were derived by de Jager et al. (1988) and Vink et al. (2000, 2001) showing that the mass-loss rate ($\dot{M}$) is inversely proportional to metallicity, Z. Now widely used in stellar evolution modelling, the relation $\dot{M} \propto Z^{0.85} \nu_{\infty}^{p}$ was developed by Vink et al. (2001), where ν_{∞} is the terminal wind velocity with $p = -1.23$ for $T_{\rm eff} \gtrsim 25000\,$K, and $p = -1.60$ for $T_{\rm eff} \lesssim 25000\,$K. The effective temperature $T_{\rm eff} = 25000\,$K is significant because it is at approximately this temperature that the bi-stability jump[§] is expected. The stark dependence of mass loss on metallicity leads to significant changes to the evolution of lower-metallicity stars. A particularly important effect is the change to the final stellar mass which directly impacts the final fate and the nature of the explosion.

An initial composition of lower metallicity not only impacts mass loss but also the fundamental stellar structure. The opacity (absorption coefficient, κ) of stellar matter determines the speed at which a star spends its energy, therefore the luminosity of a star is set by its opacity (see Chapter 8, Maeder 2009). The opacity is determined by density and temperature, $\kappa = \kappa(\rho, T)$, but also depends on the chemical composition, and through changes to metallicity can impact temperature and density. It has previously been assumed, therefore, that as we move to lower metallicities, stars become hotter and more luminous because of lower opacities. However, massive stars are dominated by electron-scattering opacity which is metallicity independent. Recent work by Farrell et al. (2021a) has provided an explanation for the increase in surface temperature and luminosity at lower metallicities. Through their SNAPSHOT technique they have found that a lower CNO abundance in the core favours higher luminosities, smaller stellar radii, and higher effective temperature. This is due to the impact of the central CNO abundance on nuclear reaction rates, whereby increased CNO increases the energy generation

---

[§] The bi-stability jump refers to a sharp increase in radiative mass-loss rates due to recombination of Fe IV to Fe III at a critical temperature of $\sim 25000\,$K (Vink et al. 1999).

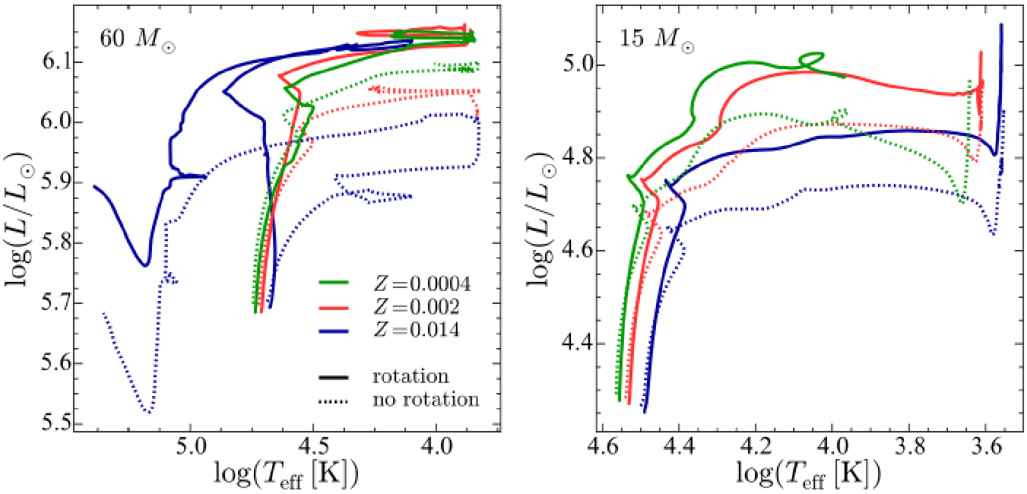

Figure 1.4: Evolutionary tracks in the HR diagram for models of initial masses $M_{\text{ini}} = 15\,\text{M}_\odot$ and $M_{\text{ini}} = 60\,\text{M}_\odot$ at various metallicities, $Z = 0.0004, 0.002, 0.014$, with (solid lines) and without (dotted lines) rotation. This figure is taken from Groh et al. (2019), Figure 8.

rates of H burning through the CNO cycle. Therefore, as the central CNO abundance decreases, the star becomes more compact to compensate for their energy deficit from the CNO cycle. This explains the higher effective temperature of low-metallicity stars. The reason for their higher luminosities then is that their compact nature produces a flatter temperature and density profile, which increases energy generation in the outer parts of the nuclear burning region in the core. These changes to the initial stellar structure impact the behaviour of low-metallicity stars throughout their evolution with respect to their energy generation, chemical mixing, and rotational effects.

The impact of metallicity on stellar evolution was studied extensively in Groh et al. (2019). In that work a new stellar evolution model grid was presented with initial metallicity Z=0.0004 (1/35 solar), comparable to the metallicities of the most metal poor galaxies observed so far, such as I Zw 18 (Zwicky 1966; Searle & Sargent 1972; Izotov et al. 1999). This grid followed earlier Geneva stellar evolution model grids (Ekström et al. 2012; Georgy et al. 2013a) and provided an opportunity to study metallicity effects because of consistent physical inputs with these earlier grids at solar and SMC (Small Magellanic Cloud; $Z = 0.002$) metallicities. Figure 1.4 is taken from that work and shows the HR diagram for models with initial masses $M_{\text{ini}} = 15\,\text{M}_\odot$ and $M_{\text{ini}} = 60\,\text{M}_\odot$, at $Z = 0.0004, 0.002, 0.014$, corresponding to the metallicities of the different Geneva stellar evolution grids. The figure also shows models with and without rotation for an initial rotational velocity of $\upsilon_{\text{ini}} = 0.4\,\upsilon_{\text{crit}}$, so the impact of rotation as well as metallicity can be observed. The effect of metallicity on the ZAMS location in the HR diagram can be clearly seen from the figure, confirming the hotter and more luminous nature of lower metallicity stars. Looking at the right panel of Figure 1.4 we see that this trend holds throughout the evolution for the $15\,\text{M}_\odot$ models, with the lower metallicity models remaining hotter and more luminous than the solar metallicity case. However this is not the case for the 60 $\mathrm{M}_\odot$ models (left panel Figure 1.4), where strong rotational mixing and mass loss cause the rotating, solar-metallicity, 60 $\mathrm{M}_\odot$ model to evolve towards the blue. It is also apparent from the figure that the post MS trends with metallicity are more complex than that of the MS, as instabilities due to mass loss, rotation, and shell burning (burning regions in the envelope) become more prevalent. However, there are some trends which have been identified in that work due to changes in dominance of mass loss and rotation at lower metallicities. For example, due to reduced mass-loss rates low-metallicity stars are less likely to become stripped WR stars. It was also found that their increased compactness and reduced mass-loss rates can increase the rotational velocities of low-metallicity stars, which subsequently increases their chemical enrichment. Furthermore, low-metallicity stars with masses $M_{\rm ini} \gtrsim 5\,\mathrm{M}_\odot$ were found to spend most of their core He-burning lifetime as BSGs, which reduces the number of RSGs expected in low-metallicity populations and thus impacts the nature of SNe from these populations (see Section 1.1.3). It is clear that metallicity significantly impacts the structure and subsequent evolution of massive stars. It can therefore be assumed that the first stars with an initially metal-free composition would have evolved very differently to massive stars today. In the next section we will discuss some of these differences, and summarise what is known thus far about the evolution of the first stars in the Universe.

1.2 Evolution at Zero Metallicity

Despite previous and ongoing surveys a metal-free star is yet to be observed (Beers et al. 1992; McWilliam et al. 1995; Ryan et al. 1996; Cayrel et al. 2004; Christlieb et al. 2008; Roederer et al. 2014; Howes et al. 2016; Starkenburg et al. 2017). However, this may change in the coming decade with new facilities such as the James Webb Space Telescope (JWST), the Wide Field Infrared Survey Telescope (WFIRST), and the Square Kilometre Array (SKA). Ahead of this new era of high-redshift observations there is increased research on the observability of Pop III stars (Zackrisson et al. 2011, 2015; Windhorst et al. 2018) and the likelihood for JWST and other new instruments to observe the first stellar populations. Previous studies have addressed the detectability of SNe and PISNe from the early universe (Tanaka et al. 2013; Whalen et al. 2013a,b,c, 2014; de Souza et al. 2013, 2014; Moriya et al. 2019), suggesting that these events will be easily observed by the next generation of optical space telescopes up to a redshift $z = 15 - 30$. In order to understand these observations we will require detailed theoretical models. We must therefore continue to improve our knowledge of stellar evolution at zero metallicity, and develop a broad range of models that can prepare us for the coming decade of groundbreaking observations and discovery.

1.2.1 Formation of the First Stars

The Big Bang signalled the beginning of our Universe, approximately 13.8 billion years ago, followed by a period of 'Inflation' lasting only a fraction of a second (Liddle 2003). In the minutes that followed this dramatic explosion the temperature decreased from $\gtrsim 10^{15}\,$K to $\sim 10^{8}\,$K and the first nucleosynthesis in the Universe occurred. For approximately 350000 years the Universe was so hot that the gas would have been fully ionized, filling space with a plasma so opaque that photons could not travel. The remnant of this epoch is the cosmic microwave background, which allows us to observe our Universe at this young age. The Universe expanded and continued to cool during this time until neutral atoms were able to form through recombination. The now matter-dominated Universe then became transparent, beginning a period known as the 'Dark Ages'. It is believed that throughout this epoch, clouds of hydrogen began to collapse very slowly in denser regions of the early Universe. The first stars formed from this collapsing metal-free primordial gas at a redshift of $z \approx 20-30$, a few hundred million years after the Big Bang (Bromm 2013; Klessen 2019). It is well accepted that their formation ended the epoch known as the Dark Ages and brought light into the Universe, but the question of how they formed remains somewhat unknown.

Since the advent of new numerical methods and supercomputers, there has been much research regarding this question, with sophisticated simulations of star formation in the early Universe gradually bringing us closer to understanding the formation of the first stars. The early Universe was very different to modern day star formation regions. Initially it was assumed that the first star formation depended only on the initial Gaussian density perturbations of material at very high-redshift, which are well understood from measuring the cosmic microwave background (Planck Collaboration et al. 2016, 2020), the growth of cosmological structures, and the heating and cooling processes of primordial gas, which were thought to be simple because of the lack of elements heavier than helium. Potentially the most significant reason for how the first star formation differed from star formation at present day, is the absence of these heavier elements prior to the existence of Pop III stars. Without these heavier elements, the only efficient cooling process during the collapse of primordial haloes is that of molecular hydrogen. At present day, the dominant cooling process in star formation is that of dust, which is significantly more efficient at cooling than molecular hydrogen. As a result, the temperature in the first star forming regions was expected to cool down to only $\sim$200 K (Abel et al. 2002; Bromm et al. 2002), as opposed to $\sim 10-20\,$K which is expected for star formation regions of solar-metallicity stars. Based on these assumptions, it was believed that Pop III stars would form in isolation with only one extremely massive star ($\geq 100\,\mathrm{M}_{\odot}$) forming in each dark matter halo (Bromm et al. 1999; Omukai & Palla 2001; Abel et al. 2002; Bromm et al. 2002; O'Shea & Norman 2007). However, as simulations improved and the effects of protostellar feedback were included, it was found that accretion disks

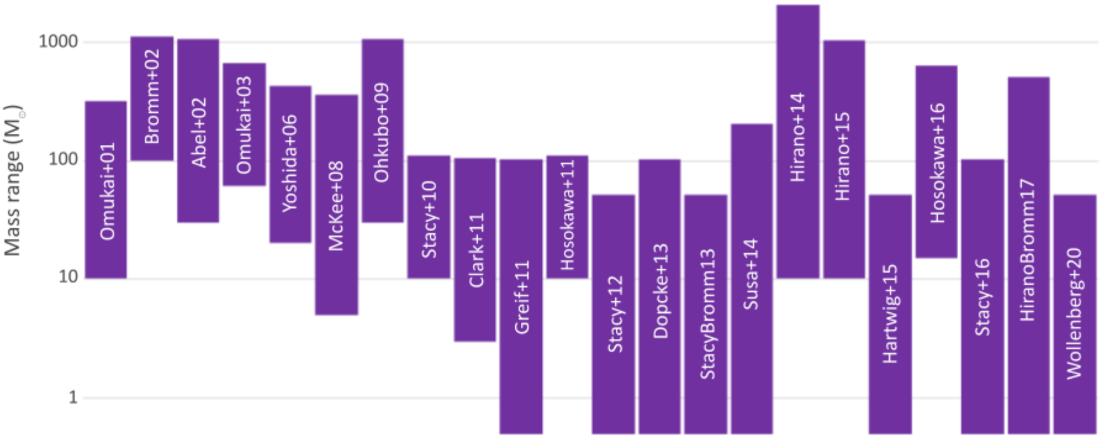

Figure 1.5: Overview of predicted mass ranges of the first stars from different publications in chronological order. This figure is adapted by the author from earlier versions by N. Yoshida and T. Hartwig.

around the first stars are highly susceptible to fragmentation (Turk et al. 2009; Stacy et al. 2010; Clark et al. 2011a,b; Greif et al. 2011; Smith et al. 2011; Greif et al. 2012; Stacy et al. 2012; Dopcke et al. 2013; Stacy & Bromm 2013; Stacy et al. 2016). This led to the current understanding of primordial star formation that there is widespread fragmentation with Pop III stars forming in multiple stellar systems. This discovery has been a significant development in our understanding of the early Universe, and has greatly changed our understanding of the initial mass function of the first stars. Recent simulations have also changed our perspective of the initial evolutionary properties of the first stars, suggesting for example that the first stars formed with rapid rotation (Stacy et al. 2011, 2013; Hirano & Bromm 2018). This indicates that Pop III stars likely experienced strong rotational mixing, which impacts their chemical yields and final fates. Therefore, understanding how the first stars formed is a crucial piece in the puzzle of uncovering how the first stars lived and died.

1.2.2 Initial Mass Function

Current stellar evolution models (see Section 1.2.6) indicate that the nature of the first explosions at high redshift is determined by the final masses of the first stars (Marigo et al. 2001; Ekström et al. 2008; Yoon et al. 2012) which are largely unknown. As described in Section 1.2.1, through simulations of the formation of the first stars in the Universe much work has been done to constrain the characteristic masses of the first stars. The mass ranges predicted by these works are summarised in Figure 1.5. While the key result of these studies is the characteristic mass of Pop III stars, i.e. the dominant mass in the population, this figure gives an insightful visual summary of how the predicted minimum and maximum masses of the first stars have changed over time. The variation in the predicted mass ranges also highlights how variable the nature of the Pop III IMF is from one study to another, which can be due to differences in the resolution of the simulation, the number of minihaloes followed during the simulation, or the types of feedback that are included. The first hydrodynamical simulations (e.g. Omukai & Palla 2001; Bromm et al. 2002; Abel et al. 2002; Omukai & Palla 2003; Yoshida et al. 2006; McKee & Tan 2008) predicted preferential formation of very massive first stars ($\geq 100\,\mathrm{M}_{\odot}$), many of which would explode as pair-instability SNe (PISNe). However, later simulations predicted significant fragmentation (Stacy et al. 2010; Clark et al. 2011b), the formation of binaries (Turk et al. 2009; Stacy et al. 2012), and a typical mass of about $40\,\mathrm{M}_{\odot}$ for the first stars (Hosokawa et al. 2011). These new findings for the characteristic masses of the first stars inferred that they would explode as core-collapse SNe (CCSNe) and not as PISNe, which was a significant shift in paradigm, most significantly because CCSNe leave behind a black hole or a neutron star, while PISNe leave no remnant. This has been consistent with observations, in that no clear signatures of chemical enrichment from PISNe of extremely metal-poor stars have been seen (Umeda & Nomoto 2002; Nomoto et al. 2006) with Karlsson et al. (2008) predicting a number fraction of primordial PISNe of less than 0.07, suggesting that Pop III stars with masses above $100\,\mathrm{M}_{\odot}$ may have been rare. There are a few candidates for PISNe at high redshift (Gal-Yam et al. 2009; Cooke et al. 2012), however they are not thought to arise from Pop III stars. Furthermore, their identification as PISNe is disputed (Dessart et al. 2013). The rarity of Pop III PISNe is in agreement with Bromm (2013) which suggests that fragmentation and the formation of multiple star systems move away from the idea of a predominantly very massive IMF as initially predicted in Bromm et al. (2002).

More recent simulations from Hirano et al. (2014, 2015) predict a wide initial mass distribution from tens to hundreds of solar masses. In fact, a redshift dependent IMF for Pop III stars is proposed in Hirano et al. (2015), where stars form on the order of hundreds of solar masses at redshifts $z \gtrsim 20$, while stars form on the order of tens of solar masses at lower redshifts due to relatively cool formation environments. This is illustrated in Figure 1.6 (Figure 17 from Hirano et al. 2015), where the predicted IMFs for Pop III stars are plotted for a range of different redshifts. Here they show two different classes of Pop III IMF, Pop III.1 and Pop III.2_{D}. These mass distributions differ because of the conditions under which they form. For redshifts $z \lesssim 15$, Hirano et al. (2015) found that half of the simulated star-forming clouds are exposed to far-ultraviolet (FUV) radiation which prevents cooling and thus prevents the formation of stars with initial masses $\lesssim 100\,\mathrm{M}_{\odot}$. The distributions formed under FUV radiation are thus known as Pop III.2_{D} stars, while Pop III.1 stars can form with initial masses on the order of tens of solar masses due to efficient H_2 and HD molecular cooling. Similarly, it was found in Stacy & Bromm (2014) that Pop III stars with initial masses from $<1\,\mathrm{M}_{\odot}$ to

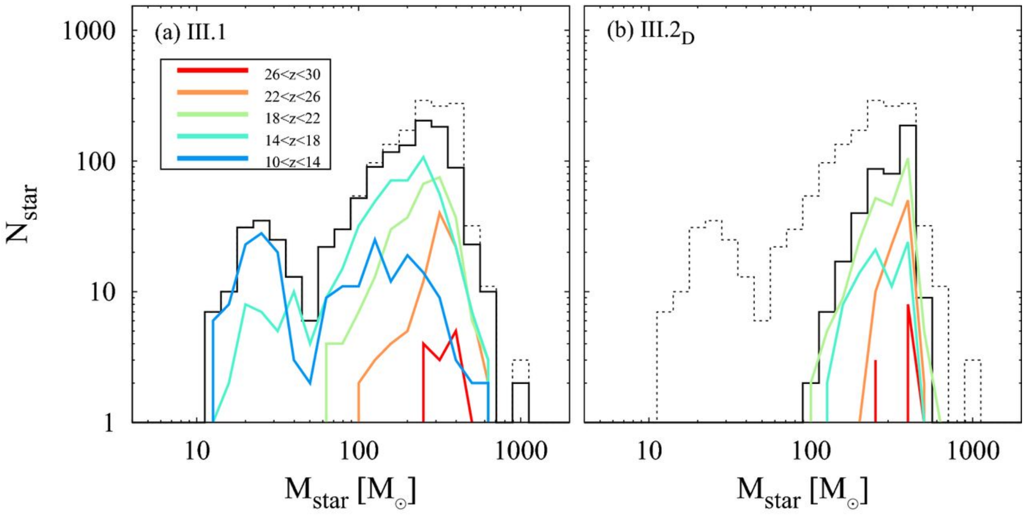

Figure 1.6: Resultant mass distributions of Pop III.1 (left) and Pop III.$2_{\rm D}$ (right) stars for different redshifts. The different colours represent different redshift ranges as shown in the legend. The black solid lines show the total distributions over all redshifts for each population whereas the dotted lines show the sum of them. Taken from Hirano et al. (2015), Figure 17.

5 $M_\odot$ could form at z=15, which illustrates how minihalo environments can vary greatly moving to lower redshifts. Although research to constrain the exact distribution of the Pop III IMF continues, there is general agreement on a top-heavy primordial IMF (Greif et al. 2011; Stacy & Bromm 2013; Susa et al. 2014; Hirano et al. 2014, 2015; Hosokawa et al. 2016; Stacy et al. 2016; Jeřábková et al. 2018; Wollenberg et al. 2020), and that the characteristic mass of the first stars is on the order of tens of solar masses. The dominance of massive stars in the first stellar populations has important implications for the history of the early Universe, and implies that high-redshift environments were dominated by stellar explosions and strong ionizing feedback. This further emphasises the importance of studying the stellar evolution of massive stars at zero metallicity, and understanding how massive stars may have impacted the early Universe.

1.2.3 Mass Loss

In Section 1.1.6, we discussed how mass loss is impacted by metallicity. Radiatively driven stellar winds rely on heavy elements at the surface for opacities necessary to accelerate and drive mass loss. The relation predicted by Vink et al. (2001), $\dot{M} \propto Z^{0.85} \nu_\infty^p$ (Section 1.1.6), inferred zero radiatively driven mass loss at $Z=0$. However, it remained unclear as to whether a radiative wind can develop during the evolution of Pop III stars as heavier elements are produced. This question was investigated in Krtička & Kubát (2006, 2009), by examining how the enrichment of the stellar surface with CNO elements could allow stellar winds to develop in zero-metallicity models. It was found that while Pop III stars do not have any wind driven purely by hydrogen and helium, CNO driven winds may exist in more luminous stars. However, for very hot stars, CNO elements are too ionized to drive a wind. In addition, the derived mass-loss rate for CNO driven winds is much less than that of a solar-metallicity stellar wind. This is expected since the dominant element in accelerating a radiative stellar wind is iron, of which there is negligible surface abundance in Pop III stars. That work was therefore consistent with the relation proposed by Vink et al. (2001), in that metal-free stars do not produce an efficient radiatively driven stellar wind.

Despite the absence of a radiatively driven wind, Pop III stars may still experience mass loss during their lifetime. Mass loss can be triggered by instabilities in the star, for example if the critical rotation limit is reached, or from the gravitational pull of a close companion in a binary system. As discussed in Section 1.1.4, mass loss due to rotation can produce decretion disks. These decretion disks produce emission lines which change the spectroscopic signature of the stars, classifying them as Oe/Be stars. It has been found that the frequency of Oe and Be stars increases at lower metallicities (Maeder et al. 1999; Martayan et al. 2007), which suggests that low-metallicity stars experience higher mass loss through rotation or binary effects than at higher metallicity. Star formation studies have suggested widespread multiplicity in the first stellar generations (Section 1.2.1), but it was proposed recently in Liu et al. (2021) that these would be mainly wide binaries which are less likely to experience interaction, so it is currently unclear how binary interaction will impact mass loss of the first stars. In lieu of binary interaction, rotation may still play a large role in producing Oe and Be stars if the critical rotation limit is reached.

Pop III stars could also experience mass loss if they evolve to regions of instability in the HR diagram and develop pulsations. One such instability is known as the Eddington limit. The Eddington limit refers to the limit above which stars are no longer stable against radiation pressure, and is set by the Eddington luminosity, L_{edd},

$$L_{\mathrm{edd}} = \frac{4\pi c G M}{\kappa_F} \tag{1.3}$$

where κ_F refers to the flux mean opacity, and M is the total stellar mass. The proximity of a star to this limit is typically defined by the Eddington parameter, Γ,

$$\Gamma = \frac{L}{L_{\mathrm{edd}}} = \frac{L\kappa_F}{4\pi c G M} \tag{1.4}$$

which is a dimensionless quantity given by the ratio of the stellar luminosity to the Eddington luminosity. Therefore, a star is said to have reached the Eddington limit at $\Gamma = 1$. Since zero-metallicity stars are expected to have much higher luminosities than stars of higher metallicities, it is plausible that they may approach the Eddington limit. As stars approach the Eddington limit of $\Gamma \sim 1$ they develop strong continuum-driven winds which are metallicity independent. This mass-loss process is theorised to cause LBVs (see Section 1.1.3), and could impact Pop III stars significantly if they become subject to these strong mass-loss rates. Mass loss at the Eddington limit has been studied in works such as Smith & Owocki (2006); van Marle et al. (2008); Vink et al. (2011) and Gräfener et al. (2011), which have shown that this limit can produce extreme mass-loss events observed as LBV eruptions. Smith & Owocki (2006) studied these continuum driven winds in the context of Pop III stars, explaining that this metallicity-independent mass loss could play a pivotal role in the evolution and final fate of the first stars in the Universe. Other metallicity-independent mass-loss processes that could significantly impact Pop III stellar evolution include, pulsation-driven outbursts if they reach the RSG phase (Yoon & Cantiello 2010; Fuller 2017; Leung & Fuller 2020), and pre-SN wave-driven outbursts in the very late burning stages such as O burning (Wu & Fuller 2021). These events are highly dependent on the stellar structure in the post MS phases, and could have significant consequences for the final fate of metal-free stars and their impact on their environments. As such, it is important that we have a good understanding of the evolution of the interior structure of the first stars in the Universe, and how sensitive they are to these episodic mass-loss processes.

1.2.4 Rotation

We have discussed rotation in Section 1.1.4, its general effects on stellar structure and evolution, and why it is important in stellar evolution modelling. Rotation is just as important for Pop III stars as it is for higher-metallicity stars. In fact, it may be even more important given that star formation studies of the first stars in the Universe have predicted high rotation rates among the first stellar populations (Stacy et al. 2011, 2013; Hirano & Bromm 2018; see Section 1.2.1). Rapid rotation of early stellar populations has also been predicted through observed abundances of second-generation metal-poor stars (e.g. Choplin et al. 2017, 2018), as we will later describe in Section 1.3.1. Furthermore, the absence of radiatively driven winds in zero-metallicity stars may leave them more susceptible to the effects of rotation, given that (aside from potential metallicity-independent mass-loss processes; Section 1.2.3) they have no mechanism for removing angular momentum. The stellar structure of Pop III stars is also distinct from higher-metallicity models (as we will discuss in Section 1.2.5), which will change the nature of rotational effects among the first stars.

For example, the transport of angular momentum is weaker in zero-metallicity stars compared to higher metallicities because of their more compact structure. The transport of angular momentum within these stars is driven by the meridional circulation, which arises from the impossibility for a rotating star to be in hydrostatic and radiative equilibrium at the same time (see Section 1.1.4). The temperatures at the pole and equator cannot remain equal, leading to meridional currents which facilitate the transport of angular momentum between the core and the envelope. The velocity of these currents, the meridional velocity $U(r)$, is inversely dependent on density: $U(r) \propto \frac{1}{\rho}$. The increased density of zero-metallicity stars therefore decreases their meridional velocity and weakens the transport of angular momentum through meridional circulation (Ekström et al. 2008). This is an important effect, because the transport of angular momentum determines how efficiently rotation impacts the structure of the star. If angular momentum becomes large close to the stellar surface, then the star may approach critical rotation and trigger mass loss. If there is mass loss, then angular momentum is removed from the star which lowers the rotational velocity. The frequency of this mechanical mass loss at the critical rotation limit will depend on the efficiency of these meridional currents, because as angular momentum is replenished near the surface, rotational velocity may increase once again. Due to their initially metal-free composition, Pop III stars may also be more sensitive to chemical transport than stars with higher metallicities, and chemical transport will increase with increased rotational mixing. Rotation is thus expected to play a significant role in the chemical enrichment of primordial stars and their enrichment of subsequent generations (e.g. Meynet et al. 2006). It is clear then, that the nature of rotational effects among the first stars in the Universe is hugely important, and will have significant consequences for our understanding of the evolution of Pop III stars.

1.2.5 Surface Properties

We discuss in Section 1.1.6 how surface properties are impacted as the metallicity of the initial composition decreases. We explain how recent work by Farrell et al. (2021a) has found that decreases to the central CNO abundance increase stellar compactness, and lead to higher surface temperatures and luminosities. In Pop III stars, which form without any carbon, nitrogen, or oxygen, this effect will be even more extreme. Interestingly their lack of CNO can continue to impact Pop III stars after the ZAMS, and subsequently zero-metallicity stars have some notable features during their MS evolution which distinguish them from even extremely metal-poor stars. Stars begin H-core burning through two processes, proton-proton chain (p-p chain) reactions, and the CNO cycle. We have discussed in Section 1.1.2 that H fusion in massive stars is dominated by the CNO cycle, but the first stars formed without C, N or O to act as catalysts for this reaction. Without the CNO cycle the energy generation rate is not high enough to support the large gravitational pressure of massive stars, and so the star contracts. To produce these elements, the stellar core needs to be hot enough ($T_{\text{cen}} = 10^8\,\text{K}$) for the triple-$\alpha$ process to occur. Through this process small amounts of He can be burned to form enough C, N and O for normal H-core burning to begin through both p-p chain reactions and the CNO cycle. If the central temperature of the star is not high enough, the star will contract until a temperature of $T_{\text{cen}} = 10^8\,\text{K}$ is reached and the CNO cycle can begin (Marigo et al. 2001; Ekström et al. 2008). This continued contraction leads to even higher effective temperatures on the MS and separates Pop III stars from even the most metal-poor stars in how they experience H-burning.

In Section 1.1.3, we explain how the transition between the end of the MS (TAMS) and the beginning of He burning in higher metallicity stars causes a large decrease in surface temperature as the inactive core contracts. This core contraction continues until the central temperature required for He burning is reached. However, we know that Pop III stars must already acquire this central temperature to trigger the CNO cycle on the MS. Therefore, zero-metallicity stars will experience a much smoother transition to He burning from the TAMS, without the need for this large core contraction. This significantly impacts the temperature evolution of Pop III stars on the HR diagram compared to stars of higher metallicity, since without this contracting phase they can remain in the blue ($T_{\text{eff}} \gtrsim 10^4\,\text{K}$) for He ignition. We also discuss in Section 1.1.6 that the increased compactness of low-metallicity stars creates a flatter temperature profile, and again this effect will be enhanced in metal-free stars. This can lead to strong H-burning regions in the envelopes of these stars in the post-MS phases which can further impact the surface properties of zero-metallicity stars. This illustrates the sensitivity of Pop III surface properties to their unique composition and evolution. The unique stellar structure of the first stars will impact their energy generation, stellar lifetimes, chemical enrichment, and rotational effects. Thus, they make for very interesting subjects in stellar evolution studies. There is still much we have to learn about how these surface properties vary with properties such as rotation, convection, mass loss, and magnetic fields. With continued improvement of stellar evolution modelling techniques we can expand our knowledge of the evolutionary features of the very first stars.

1.2.6 Previous Stellar Evolution Models

Several groups have investigated the evolution of the first stars with numerical stellar evolution codes. Marigo et al. (2001) studied zero-metallicity, non-rotating stellar evolution models with initial masses in the range $M_{\text{ini}} = 0.7 - 100\,\text{M}_{\odot}$, with subsequent work focusing on rotating models with $M_{\text{ini}} = 120 - 1000\,\text{M}_{\odot}$ (Marigo et al. 2003). In their first paper they focused on the evolution of zero-metallicity models at constant mass and described the triggering of the CNO cycle during the MS, the pollution of the stellar surface through dredge-up events, the upper mass limit for the achievement of super-Eddington luminosities, and the pulsational properties of zero-metallicity stars. Given the impact of evolutionary behaviour of zero-metallicity stars on the early Universe, they were particularly interested in how the lack of CNO group elements in these models changes their nuclear energy generation and interior structure. For this initial grid of $M_{\text{ini}} = 0.7 - 100\,\text{M}_{\odot}$ they evolved the models at constant mass and rotation, and included convective overshooting.

One of their main results is illustrated in Figure 1.7, relating to the mass ranges for which there was surface enrichment. This pollution of the surface is typically caused by dredge up events. The first dredge up occurs when a star experiences He ignition close to the Hayashi line, where stars are fully convective (Maeder 2009, Chapter 20), in the red giant region of the HR diagram. The star therefore has a deep convection zone which penetrates into layers where H burning had previously occurred. The surface ^{12}C/^{13}C and C/N ratios subsequently decrease as material from these inner regions is mixed outwards through convection. The second dredge up typically occurs in intermediate mass stars with $M_{\rm ini} = 4$–$8\,{\rm M}_\odot$ after He-core exhaustion. In the second dredge up He fusion comes to an end in the core and the convective envelope grows larger, its lower boundary then reaches the location of previous H-shell burning and mixes the products of the CNO cycle outwards. This results in an increase to the surface abundances of ^{4}He and ^{14}N, while the abundances of ^{12}C and ^{16}O decrease. The third dredge up occurs after a star enters the asymptotic giant branch (AGB) phase and a flash[¶] occurs along a He-burning shell. This dredge up causes He, C and s-process (described in Section 1.3.1) products to be brought to the surface.

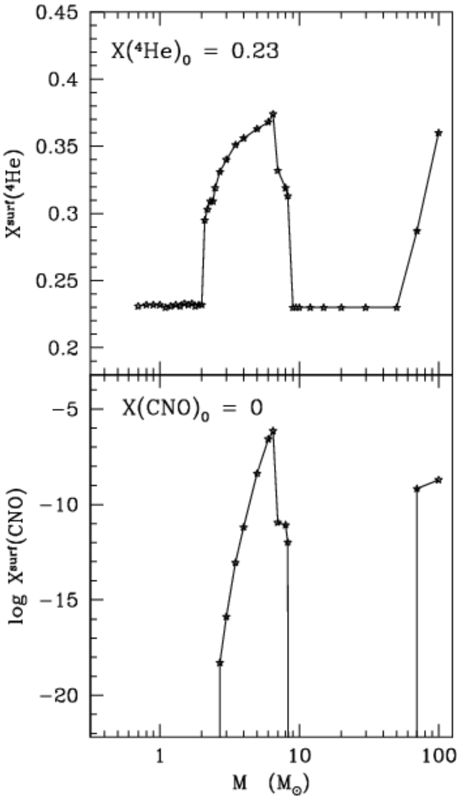

Figure 1.7: Surface abundances of ^{4}He and CNO elements as a function of stellar mass, from Marigo et al. (2001), Figure 14.

These dredge-up events are seen in many higher metallicity models, however, at zero metallicity the interior structure is significantly different. Marigo et al. (2001) found that for low mass models ($0.7\,{\rm M}_\odot \leq M_{\rm ini} \leq 1.1\,{\rm M}_\odot$) the first dredge up changes the surface chemical abundances by negligible amounts, while for higher mass models ($M_{\rm ini} \geq 1.2\,{\rm M}_\odot$) the first dredge up cannot occur since the onset of He burning occurs far from the Hayashi tracks. It was found however, that the second dredge up occurs for models with $2.1\,{\rm M}_\odot \leq M_{\rm ini} \leq 8.3\,{\rm M}_\odot$ allowing the surface enrichment seen in Figure 1.7 to take place. For higher mass models of $70\,{\rm M}_\odot \leq M_{\rm ini} \leq 100\,{\rm M}_\odot$ the second dredge up was again observed. These models were found to settle on their Hayashi tracks during the He-burning phase and remain there until C ignition, enhancing the surface abundance in both He and CNO group elements as seen in Figure 1.7. As one of the first

---

[¶] This flash is commonly referred to as the 'helium flash', and is a well known phenomenon that typically occurs at the onset of He burning in low-mass stars. For more on this see Chapter 33, Kippenhahn et al. (2012).

detailed explorations of the interior evolution of Pop III stars this was an important conclusion, since surface enrichment can impact stellar winds and mass loss and affect the final fates of these stars.

Having studied zero-metallicity models in the mass range $M_{\rm ini} = 0.7 - 100\,{\rm M}_\odot$, their later paper (Marigo et al. 2003) explored a higher initial mass regime and investigated the effects of rotation and mass loss on very massive primordial stars. At that time, the primordial IMF was theorised to peak in the very high mass domain at $M_{\rm ini} \geq 100\,{\rm M}_\odot$ (e.g. Bromm et al. 2002; see Section 1.2.2) so extending their grid to models in the mass regime $M_{\rm ini} = 100 - 1000\,{\rm M}_\odot$ was important to understand the nature of the first stellar populations. Particular attention was paid to whether these very massive stars could develop efficient mass loss through stellar winds and rigid rotation was included to see if this would enhance radiative mass-loss rates. The analytical recipe for rotationally driven mass loss as described in Maeder & Meynet (2000a) was included in that work, where the mass-loss rate from a rotating star, $\dot{M}(\upsilon_{\rm rot})$, can be described as a function of the purely radiative mass-loss rate, $\dot{M}_{rad}$, and the rotational correction factor, F_Ω.

$$\dot{M}(\upsilon_{\rm rot}) = F_\Omega \times \dot{M}_{Rad}(\upsilon_{\rm rot} = 0) \tag{1.5}$$

$$F_\Omega = \frac{(1-\Gamma)^{\frac{1}{\alpha}-1}}{[1-(T_\Omega+\Gamma)]^{\frac{1}{\alpha}-1}} \qquad T_\Omega = \frac{\Omega^2}{2\pi G\rho_m} \approx \frac{4}{9}\frac{\upsilon_{\rm rot}^2}{\upsilon_{\rm crit}^2} \tag{1.6}$$

where Γ is the Eddington parameter (eq. 1.4) and α is a parameter corresponding to the slope of the line strength distribution. T_Ω contains the effects of rotation, where Ω is the angular velocity, ρ_m is the internal mean density, and $\upsilon_{\rm crit}$ refers to the break-up velocity (eq. 1.2). The evolution of the mass-loss and rotational parameters are shown in Figure 1.8 for the $120\,{\rm M}_\odot$ model. That figure shows that the rotational correction factor, F_Ω, stays close to one during the MS phase so the mass-loss rate remains low. Eventually the model reaches both the critical Ω- and $\Omega\Gamma$- limits[‖], but this is maintained for only a short time. Similar results were found for the $500\,{\rm M}_\odot$ model where rotation had little effect on the already inefficient line-driven stellar wind. For higher mass models ($M_{\rm ini} = 750, 1000\,{\rm M}_\odot$) the radiation-driven mass loss was found to become efficient, allowing these models to remove angular momentum during the MS, and consequently made the effects of rotation even weaker for these extremely massive models. In summary, Marigo et al. (2003) found the radiation pressure in these stars to not be an efficient driving force of mass loss. It was discussed that rotation could trigger powerful winds at the critical point but the star would then spin down quickly afterwards.

While the work of Marigo et al. (2001) and Marigo et al. (2003) allowed for a much

---

[‖] The Ω-limit refers to the critical rotation limit, and the $\Omega\Gamma$-limit refers to the instability where both the critical rotation and Eddington limits are reached.

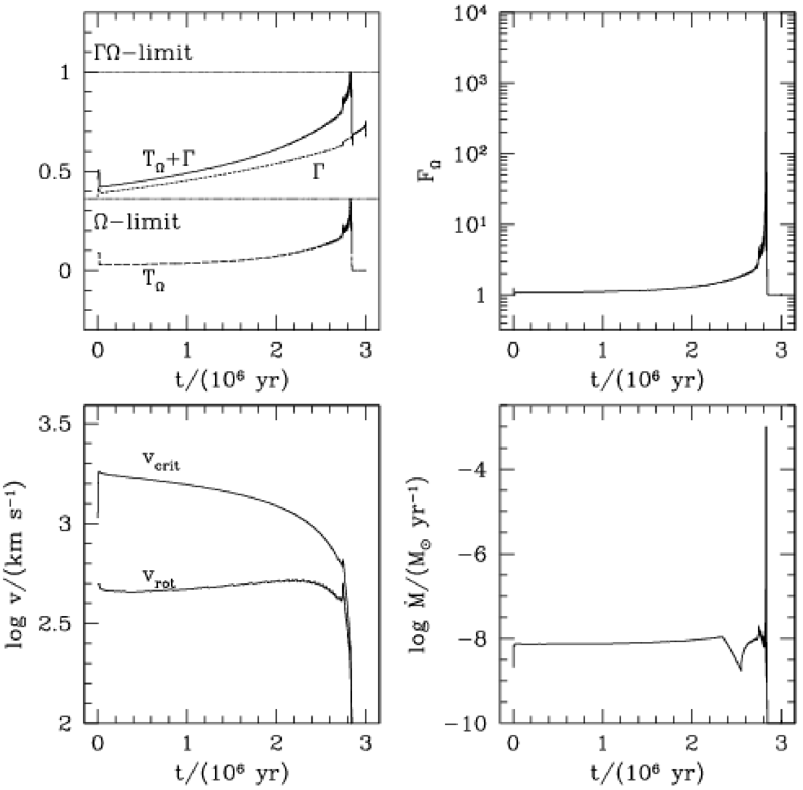

Figure 1.8: Evolution of the rotational parameters and mass-loss rates for the 120 $M_\odot$ model calculated with $V_{\rm rot,0} = 500\,{\rm km\,s^{-1}}$ from Marigo et al. (2003), Figure 6. *Top-left panel:* Relevant terms determining the rotational correction factor. The Ω- and ΩΓ-limits are indicated by horizontal lines showing the maximum values for T_Ω and $T_\Omega + \Gamma$, respectively. *Top-right panel:* Rotational correction factor. *Bottom-left panel:* Evolution of surface ($\upsilon_{\rm rot}$) and critical ($\upsilon_{\rm crit}$) rotational velocities. *Bottom-right panel:* Evolution of the mass-loss rate.

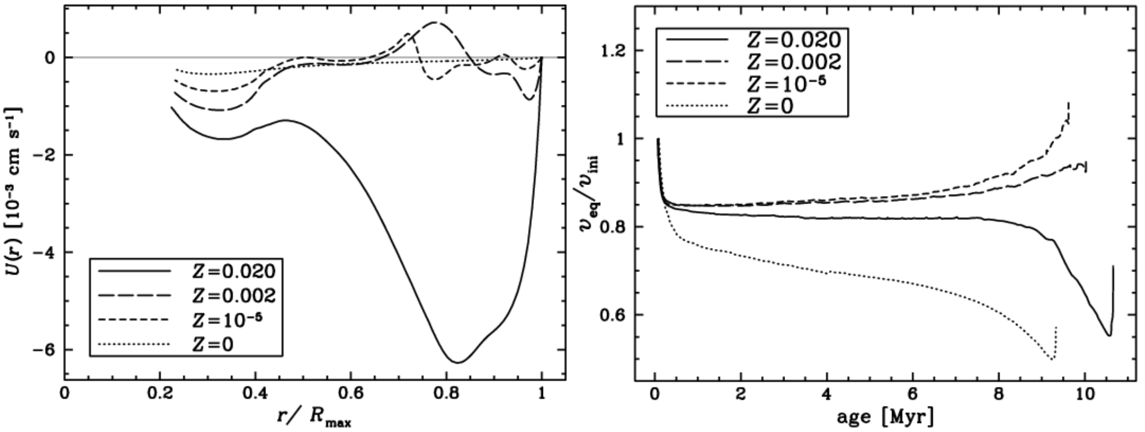

Figure 1.9: Models with $M_{\rm ini} = 20\,M_\odot$ at various metallicities with $\Omega_{ini}/\Omega_{crit} = 0.5$, from Ekström et al. (2008), Figure 3. *Left*: Internal profile of $U(r)$ for normalised stellar radii. All the models are at the same evolutionary stage, when the central H mass fraction is about 0.40. *Right*: Evolution of the equatorial velocity, normalised to the initial velocity.

improved understanding of the effect of rigid rotation on primordial stellar evolution, there was still a need to investigate the effects of differential rotation. This was addressed by Ekström et al. (2008) where primordial stars of initial masses $M_{\rm ini} = 9-200\,{\rm M}_\odot$ were investigated with emphasis on how differential rotation affects their evolution. That work was done using the Geneva stellar evolution code (GENEC) and included advection in both chemical species and angular momentum transport (discussed further in Chapter 2), allowing for a more accurate treatment of rotational mixing. It was found that, although still impactful, the effect of rotation on the first stars is smaller than for even extremely metal-poor stars. This was believed to result from continuous nuclear burning at the end of the MS, and the weak meridional circulation of Pop III stars. The stellar cores of these models are hotter and denser than those of higher metallicity so require very little structural readjustment at the end of the MS to ignite He burning (Section 1.2.5), resulting in continuous nuclear burning following H-core exhaustion. Since there is little change to the interior structure, it was found that rotational mixing had minimal effect on the evolution at the onset of He burning. It was also found that, when these stars do eventually cool down later in the evolution, their outer convective layer remains thin, hindering the efficiency of dredge-up events and the subsequent enhancement of surface abundances. Without surface enrichment the envelope remains transparent to radiation and mass loss is negligible.

One of the main findings of Ekström et al. (2008) relates to the second reason for these weak rotational effects, the weakness of meridional circulation at zero metallicity. As we explain in Section 1.2.4, that work showed that the increased density of Pop III stars reduces the meridional velocity and weakens angular momentum transport. Without an efficient mechanism to transport angular momentum it was found that these models reach critical rotation late in their evolution, and that little mass loss is needed to bring them to sub-critical rotation. For models with initial mass $M_{\rm ini} < 40\,{\rm M}_\odot$, there was found to be an inflation of the radius during the evolution which causes these models to spin down, again minimising rotational effects. The left panel of Figure 1.9 shows a comparison of the meridional velocities of higher metallicity models, all with initial mass $M_{\rm ini} = 20\,{\rm M}_\odot$. A negative value of $U(r)$ indicates the outward transport of angular momentum from the core to the envelope, while a positive value indicates transport inwards. It is therefore seen that, while models of metallicity Z=0.02 have strong meridional currents outwards, lower metallicity models have weaker meridional circulation, with even weaker meridional circulation for zero-metallicity models. The subsequent spin-down of this primordial model is evident from the right panel where v_{eq}/v_{ini} decreases to $\sim$0.5. This detailed examination of Pop III stellar evolution greatly improved the understanding of the interiors of the first stars in the Universe, and how differently they are impacted by rotation compared to stars at higher metallicities.

One property that was not explored in Marigo et al. (2001), Marigo et al. (2003) or Ekström et al. (2008) was the inclusion of magnetic fields and their effect on primordial

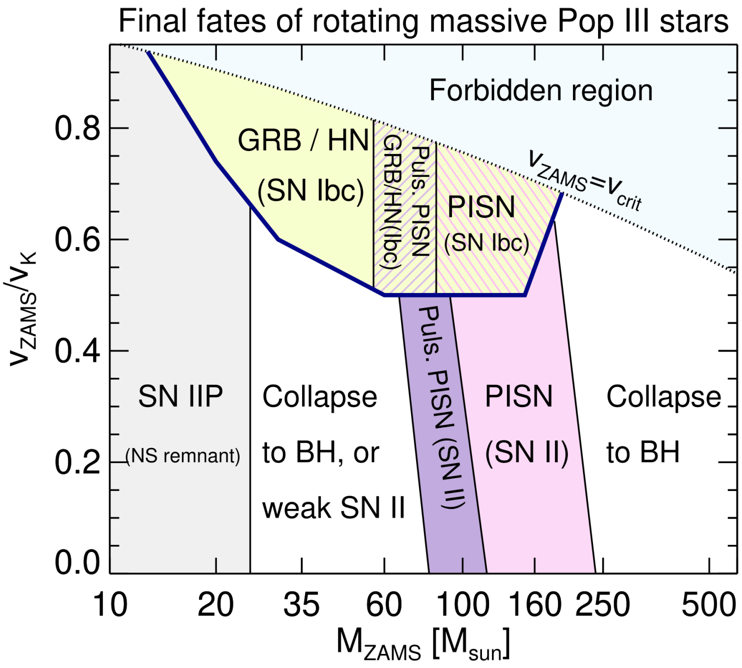

Figure 1.10: Final fates of Pop III stars from Yoon et al. (2012), Figure 12, based on the initial (ZAMS) mass and the initial velocity as a fraction of the Keplerian value of the equatorial rotational velocity. The dotted line indicates the limit above which the rotational velocity at the surface would exceed the critical velocity. The blue solid line separates the yellow region where CHE is achieved.

evolution. Magnetism can change many features in stellar evolution by providing strong core-envelope coupling. It can vary how angular momentum is transported, give rise to chemically homogeneous evolution (CHE), and increase mass loss, all of which can drastically affect the evolution. The implementation of magnetic fields as a possible driver for mass loss in primordial models is discussed in Ekström et al. (2008) where the impact of magnetism on their results is acknowledged. This was then explored in Yoon et al. (2012), which included magnetic fields in stellar evolution models of the first stars assuming a Spruit-Taylor dynamo, for an initial mass range $M_{\rm ini} = 10 - 1000\,{\rm M}_\odot$. This allowed for a different approach to the effects of rotation in these stars where CHE is achieved through magnetism. In these models chemical mixing is dominated by Eddington-Sweet circulations (also known as the meridional circulations; Section 1.1.4) and follow the Kippenhahn (1974) prescription where the circulation velocity is given as:

$$v_e = \left(\frac{\omega_r}{\omega_{K,r}}\right)^2 v_{e,K} \tag{1.7}$$

$$v_{e,K} := \frac{\nabla_{ad}}{\delta(\nabla_{ad} - \nabla)} \frac{L_r}{GM_r} \left(\frac{2(\epsilon_n + \epsilon_\nu)r^2}{L_r} - \frac{2r^2}{M_r} - \frac{3}{4\pi\rho r}\right) \tag{1.8}$$

Here ω_r is the angular velocity at a radius r, $\omega_{K,r}$ the local Keplerian value, ϵ_n the nuclear energy generation rate, and ϵ_ν is the energy loss rate due to neutrino emission. The adiabatic gradient is given by $\nabla_{ad} = \frac{P\delta}{\rho T C_P}$ (eq. 2.7) and $\nabla = \frac{dlnT}{dlnP}$ refers to the local temperature gradient of the medium, for more detail on stellar temperature gradients see Kippenhahn et al. (2012), Chapter 4.

The models in Yoon et al. (2012) included overshooting and rotation as well as magnetic torques and, unlike Marigo et al. (2001), Marigo et al. (2003) and Ekström et al. (2008), they varied the initial rotational velocity. This allowed them to predict the final fates of these stars in a parameter space spanned by initial mass, but also initial rotation. The predicted final fates from that work are shown in Figure 1.10. The solid blue line in the figure separates the parameter space for which CHE was achieved at initial masses $13\,\mathrm{M}_{\odot} \leq M_{\mathrm{ini}} \leq 190\,\mathrm{M}_{\odot}$ for models with higher rotational velocities. As discussed in that work, thermodynamic conditions in more massive stars are more favourable for chemical mixing, however, more massive stars can reach critical rotation at an earlier stage of their evolution, inducing rapid loss of angular momentum. Therefore, for a given rotational velocity, CHE is favoured in a higher mass star, until at a certain mass when mass loss due to critical rotation hinders chemical mixing. This is how the mass-range for CHE was constrained to $13\,\mathrm{M}_{\odot} \leq M_{\mathrm{ini}} \leq 190\,\mathrm{M}_{\odot}$. This result is important because CHE has a significant effect on the final fates of these stars, leading to more explosive phenomena such as gamma-ray bursts, hypernovae and Type Ib/c[**] PISNe. Yoon et al. (2012) also showed that slower rotators, which do not achieve CHE, end their lives either as Type-II SNe or by directly collapsing to a black hole.

More recently, Windhorst et al. (2018) produced a grid of Pop III models with the MESA stellar evolution code (Paxton et al. 2011, 2013, 2015) and investigated their detectability through cluster caustic transits. Cluster caustic transits refer to the gravitational lensing of bright objects, in this case massive Pop III stars. In that work they modelled Pop III stars with initial masses $1\,\mathrm{M}_{\odot} \leq M_{\mathrm{ini}} \leq 1000\,\mathrm{M}_{\odot}$ from the ZAMS to the end of the He-burning phase. From their surface properties, they determined mass-luminosity relations, and subsequently estimated the maximum possible contribution of Pop III stars and their stellar-mass BH accretion disks (see Section 1.3.3) to the observed near-IR sky surface brightness. The idea is that cluster caustic transits could amplify the signal from Pop III stars and their BH accretion disks, and potentially be observed by near-IR telescopes such as JWST, at redshifts of $z \simeq 7-17$. That work is an example of how stellar evolution models can place constraints on observations and help us to understand the statistics of high-redshift objects in the Universe. The more accurate and detailed our stellar evolution models are, the more we can understand about these future observations.

Another significant work on stellar evolution of zero-metallicity stars was Heger & Woosley (2002), where stellar evolution models of He cores were used to investigate the death of massive Pop III stars. Through studying a range of He cores of masses 60-140 $\mathrm{M}_{\odot}$, the nucleosynthetic yields were determined for stars expected to undergo pulsational pair instabilities (see Section 1.3.3). Among the key findings from that work

---

[**] Type I and Type II SNe are defined by their H-poor and H-rich content respectively. Type Ib SNe refer to stellar explosions where no signatures of H or Si II are observed, and Type Ic SNe refer to stellar explosions where no signatures of H, He I, or Si II are observed. For a review on SNe classification see Filippenko (1997).

were that nucleosynthesis in PISNe varies greatly for different He core masses, and that PISNe from Pop III stars are deficient in elements with an odd nuclear charge such as Na, Al, Mn, etc. This result is important for determining the chemical signature of the first stars and their impact on the metallicity of subsequent stellar populations. Detailed nucleosynthesis studies of zero-metallicity stars, such as Heger & Woosley (2002), are crucial for understanding observations of second-generation stars (see Section 1.3.1), and rely on the robustness of the evolution modelling to accurately predict nucleosynthetic yields. It is therefore imperative that such works are supported by updated stellar evolution modelling research.

All of these studies have greatly improved our understanding of the first stars in the Universe. However, there is still much to learn about Pop III stars and how much rotation impacts them. As numerical simulations and high-redshift observations continue to advance, our stellar evolution models must do the same. In the coming decade we expect to make huge strides in our understanding of primordial stars, and stellar evolution modelling must be at the forefront of this research if we are to understand the evolution of the first stars and how they impacted their environments.

1.3 Impact of the First Stars

Thus far, we have given an overview of massive star evolution and the unique aspects of stellar evolution at zero metallicity. Now we address the importance of the first stars in the Universe, and how they impacted their surroundings. The history of the Universe, and the role of the first stars in that history, is illustrated in Figure 1.11. This figure shows the formation of the first stars (see Section 1.2.1) and the subsequent generations of stars and galaxies which followed them. From Figure 1.11 we can observe how the nature of Pop III stars influenced the structure of the local Universe. They determined the chemical evolution of the Universe by providing the first heavy elements, they are thought to be largely responsible for the reionization of hydrogen, and they can help us to answer some of the key questions in physics of the early Universe, including the origin of quasars and dust. We outline these effects in the following sections, and discuss why understanding the nature of the first stars is a crucial topic in Astrophysics.

1.3.1 Chemical Enrichment

We will first discuss how the first stars impacted their environments through chemical enrichment. The first stars are hugely impactful in the chemical enrichment of the Universe because they were the very first sources of elements heavier than helium. Prior to the formation of the first stars there were only trace amounts of metals such as lithium and beryllium which had formed in the Big Bang (Sarkar 1996). Therefore, understanding the nucleosynthesis of the first stars and how they dispersed these newly formed heavy

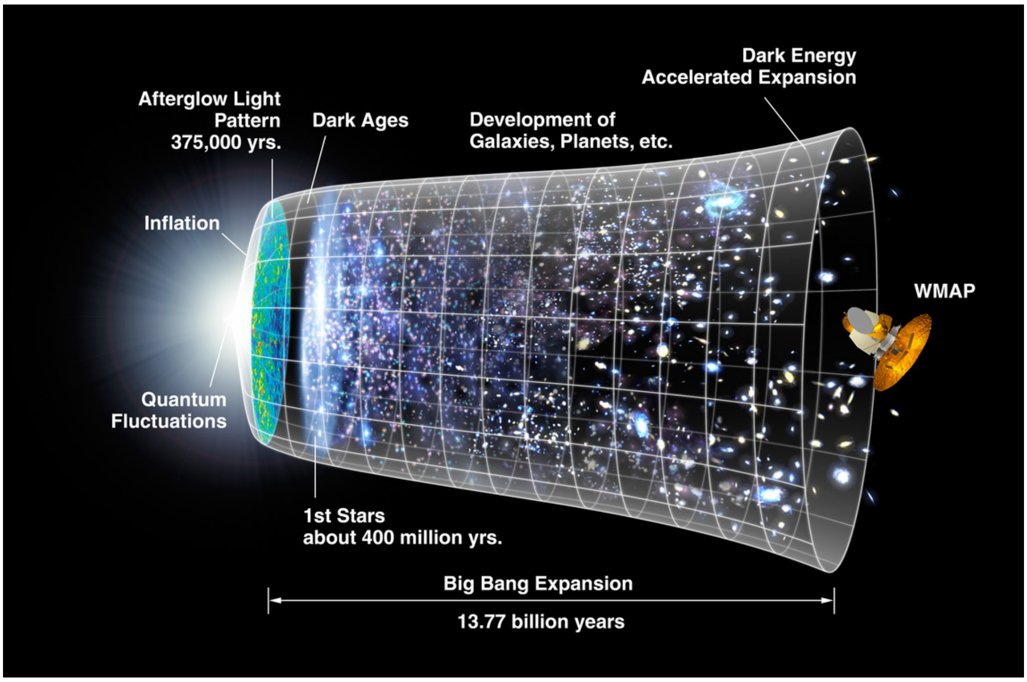

Figure 1.11: Evolution of the Universe, showing spacial expansion and time evolution from the Big Bang to modern day. Indicated are key eras in the history of the Universe, including the 'Dark Ages' and the formation of the first stars (Section 1.2.1). Credit: NASA / WMAP Science Team.

elements is vital in understanding the chemical evolution of the Universe. Many works have investigated how the first stars chemically enriched their surroundings through their SN explosions. Predictions of the chemical yields of primordial SNe were presented in Woosley & Weaver (1995); Umeda & Nomoto (2002); Chieffi & Limongi (2004); Nomoto et al. (2006); Tominaga et al. (2007); Heger & Woosley (2010); Joggerst et al. (2010); Limongi & Chieffi (2012); Takahashi et al. (2014) and Tominaga et al. (2014), and have provided insight into how populations of Pop III stars may have enriched the early Universe. There are not yet observations of Pop III SNe, but much work has been done to understand their contribution to chemical enrichment through observations of second generation (Pop II) stars, otherwise known as extremely metal-poor (EMP) stars. There have been numerous simulations which have modelled the chemical enrichment of EMP stars by Pop III SNe, such as Mackey et al. (2003); Kitayama & Yoshida (2005); Greif et al. (2007, 2010); Whalen et al. (2008); Kobayashi et al. (2011); Smith et al. (2015); Hartwig et al. (2019); Welsh et al. (2019, 2021) and Hicks et al. (2021). These works have tested a variety of SN channels, including PISNe and CCSNe, at different redshifts. Depending on the strength and yields of the events, they have predicted the number of Pop III stars required to pollute observed EMP stars, and the nature of the explosions that best fit their observed abundances. A recent discovery of an ultra metal-poor star in the Sculptor dwarf spheroidal galaxy, AS0039 (Skúladóttir et al. 2021), provides new opportunity for understanding chemical enrichment from Pop III stars. In that work it is suggested that the unique abundance pattern of AS0039 may result from enrichment from a Pop III SN with a $\sim 20\,\mathrm{M}_{\odot}$ progenitor, based on the Heger & Woosley (2010) predicted primordial SNe yields.

There is particular interest in a peculiar category of Pop II stars known as carbon-enhanced metal-poor (CEMP) stars (Beers & Christlieb 2005; Aoki et al. 2007), whose low iron ($[\mathrm{Fe/H}] \leq -1$) and high carbon ($[\mathrm{C/Fe}] > 0.7$) content is thought to arise from enrichment from Pop III sources. The subclasses of CEMP stars, as defined by Beers & Christlieb (2005), see their Table 2, are based on the abundances of other heavy elements, mainly barium and europium. These subclasses include, CEMP-r, which refers to elements produced by the rapid neutron capture process (r-process) such as europium; CEMP-s, referring to elements captured by the slow neutron capture process (s-process) such as barium; CEMP-r/s containing both r-process and s-process elements; and CEMP-no which do not have significant enhancement of r- and s-process elements. These CEMP-no stars are expected to be the best candidates for direct enrichment from Pop III stars, with studies such as Cooke & Madau (2014); Sharma et al. (2018); Hartwig & Yoshida (2019); Chiaki et al. (2020) and Jeon et al. (2021) showing that faint SNe from Pop III stars can reproduce the peculiar abundance patterns of CEMP-no stars.

CEMP stars can also help us to constrain the properties of the first stars. For example, Umeda & Nomoto (2003); Hartwig et al. (2015); de Bennassuti et al. (2017) and Ishigaki et al. (2018) have used CEMP and EMP stars to constrain the characteristic masses of Pop III stars, finding that matching the observed abundances of these Pop II stars infers a top-heavy IMF in agreement with cosmological simulations of star formation (Section 1.2.2). Following these works, Sarmento et al. (2019) investigated the IMF and the critical metallicity defining the boundary between Pop III and Pop II stars, and concluded that the Pop III IMF is dominated by stars in the mass range $M_{\mathrm{ini}} = 20 - 120\,\mathrm{M}_{\odot}$ that generate SN with carbon-enhanced spectra. CEMP stars have also been used to constrain the mixing processes and rotation of the first stars. Choplin et al. (2017) found that some CEMP-s stars may be enriched by the SNe of rapidly rotating Pop III stars, and Choplin et al. (2018) showed that s-process elements can be explained by high rotation rates of up to $\upsilon_{\mathrm{ini}} = 0.7\,\upsilon_{\mathrm{crit}}$ which supports predictions of rapid rotation at high redshifts (Stacy et al. 2011, 2013; Hirano & Bromm 2018; Section 1.2.4). In terms of mixing processes, Choplin et al. (2016) found that mixing of the helium and hydrogen layers in the first generation of stars could reproduce the abundance pattern of CEMP-no stars. Moreover, interactions between He-rich and H-rich layers in Pop III stars give rise to different reaction chains and affect final abundances, with interesting implications for CEMP-no stars, as has been found in Clarkson et al. (2018); Clarkson & Herwig (2020). As work continues in this field and observations of the early Universe grow, we can bridge the gap between the properties of the first stars in the Universe and the lowest-metallicity stars observed to date. This will help us to understand how the first stars enriched their environments, and will also improve our knowledge of stellar evolution of zero-metallicity stars.

1.3.2 Reionization

We will now discuss the present research on how the first stars impacted their environments through ionization, and why this is important for the epoch of reionization. As discussed in Section 1.2.1, and shown in Figure 1.11, at the beginning of the Universe, following the Big Bang, the Universe was fully ionized. The epoch known as the 'Dark Ages' followed, as hydrogen and helium recombined and neutral atoms formed. The formation of the first stars ended the so-called Dark Ages and brought light into the Universe. They also triggered the beginning of what is known as the reionization era. This era is split into two phases, the reionization of hydrogen, and the reionization of helium. It is generally accepted that the first stellar populations were a significant, and perhaps dominant, source for the reionization of hydrogen in the intergalactic medium (IGM; Haehnelt et al. 2001; Faucher-Giguère et al. 2008, 2009; Becker & Bolton 2013; Wise et al. 2014). Active galactic nuclei (AGNs; see Section 1.3.4) also contribute to reionization and are thought to be the drivers of the full reionization of helium in the IGM (Barkana & Loeb 2001; Faucher-Giguère et al. 2009; McQuinn 2016; Worseck et al. 2016). The relative contribution of AGN and stars to cosmic reionization is a topic at the forefront of Astrophysics research, with ongoing observational and theoretical efforts from different groups.

Hydrogen in the early Universe was reionized by ionizing photons, which are photons with enough energy to split hydrogen into electrons and photons. As the energy of the photon increases, or in other words as you move to radiative flux of shorter wavelengths, photons become capable of ionizing He I and He II as well. The energy of the radiative flux emitted by a star depends on the luminosity and the temperature. It is therefore expected that Pop III stars produce many ionizing photons since zero-metallicity stars are more luminous and hotter than stars at higher metallicities (Section 1.2.5). There have been several studies which have investigated ionizing photon production of stars at various metallicities. The ionizing photon production rates for higher metallicity stars have been studied in Topping & Shull (2015). In that work, ionizing photon production rates were determined for a range of metallicities from stellar evolution model grids of Ekström et al. (2012) and Georgy et al. (2013a), and compared to work from Schaerer (2003) on ionizing photon production at very low metallicities ($Z = 10^{-5} - 10^{-7}$). It was found that lower-metallicity models produce more ionizing photons because of their higher temperatures and luminosities. The impact of rotation was also examined, and it was found that rotation can increase He I ionizing photon production by $\sim 90\%$ for solar-metallicity (Z=0.014) models, and $22 - 35\%$ for SMC metallicity (Z=0.002) models.

For ionizing photon production of Pop III stars, predictions have been made in Tumlinson & Shull (2000); Schaerer (2002); Heger & Woosley (2010) and Yoon et al. (2012). Using the available evolutionary tracks of metal-free stars at that time (Castellani et al. 1983; El Eid et al. 1983; Chieffi & Tornambe 1984), Tumlinson & Shull (2000) used a fitting method to produce 'static stellar models' and, combined with atmosphere models, predicted the ionizing photon production of the first stars. That work provided a first look at how much more efficient Pop III stars are at producing ionizing photons than higher metallicity stars, but there was still much to be done in accurately modelling surface properties of the first stars. With new stellar evolution model grids of zero-metallicity stars, Schaerer (2002) combined stellar evolution and atmosphere models to predict ionization rates. That was an important step, because for the first time it allowed the study of the evolution of ionizing photon production rates over the lifetime of Pop III stars. Based on the Geneva stellar evolution models at that time, they found that redward evolution of Pop III stars decreased ionizing photon production by a factor of two over the stellar lifetime. This shows the significant impact that stellar evolution can have on ionizing photon production, and why it is important to have updated predictions with the most recent model grids available. A new stellar evolution grid of Pop III models was presented in Heger & Woosley (2010) for a fine grid of 120 non-rotating models in the mass range 10-100 $M_{\odot}$, from which the ionizing photon production per solar mass was determined. This provided further insight into how a population of zero-metallicity stars may have contributed to reionization. The effects of rotation on the ionizing photon production of Pop III stars was explored for the first time in Yoon et al. (2012). The models in that work also included internal magnetic fields and studied the impact of chemically homogeneous evolution on the first stars, as discussed in detail in Section 1.2.6. That work was a significant development in understanding how stellar properties impact ionizing photon production, and further demonstrates the importance of exploring how internal mixing impacts the ionizing photon production of the first stars. It should be noted that the contribution of the first stars to reionization not only depends on their ionizing photon production rates, but also on the escape fraction of ionizing photons to the IGM. As work continues to constrain the escape fraction of ionizing radiation in the early Universe (e.g. Whalen et al. 2004; Alvarez et al. 2006; Wise & Cen 2009; Benson et al. 2013; Wise et al. 2014) this limit must be considered in determining the contribution of Pop III stars to reionization.

1.3.3 Stellar Black Holes and Gravitational Sources

In recent years there have been huge developments in the area of gravitational wave research since the development of the Laser Interferometer Gravitational-Wave Observatory (LIGO) detectors (Abramovici et al. 1992; LIGO Scientific Collaboration et al. 2015), which for the first time in 2015, observed gravitational waves from a merger of two black holes, GW150914 (Abbott et al. 2016). In the years since there have been numerous detections of binary black hole (BBH) mergers and neutron star mergers. One of the most significant observations was that of the binary neutron star merger GW170817 (Abbott et al. 2017), where for the first time gravitational waves were observed alongside electromagnetic radiation from a merger event. This has created a surge in research related to Pop III progenitors of black holes. For example, Hartwig et al. (2016, 2018) investigated the merger rates of black holes at high redshifts ($z \geq 15$), and Uchida et al. (2019) computed the gravitational waves that would be emitted by the collapse of a $320\,\mathrm{M}_\odot$ Pop III star. These observations and theoretical studies can help us to constrain properties of the first stellar populations. By understanding the statistics of these extreme binary systems, we can learn more about the initial mass function and the final fates of Pop III stars.

Gravitational waves can be detected from black hole and neutron star mergers because of their extreme compactness. Their enormous densities create ripples in space-time as they accelerate in mergers, which we then observe as gravitational waves. Black holes (BHs) and neutron stars (NSs) are expected to form as remnants of massive stars, depending on their final fate. The basic channels for formation are the following, a star undergoes a CCSN and the remaining stellar core collapses to a NS; a star undergoes a CCSN and the core collapses to a BH; or the star fails to explode and the full stellar mass collapses to a BH. As discussed briefly in Section 1.1.1, whether a SN is successful or not depends on the final core mass and compactness, and the burning shells and density profile in the stellar envelope. Typically a less massive stellar core will produce a NS, and a more massive one will produce a BH. The upper limit for formation of stellar mass BHs is set by the so-called pair instability mass gap, which proposes that BHs with masses $\sim 55 - 130\,\mathrm{M}_\odot$ are not expected to form (e.g. Heger et al. 2003; Belczynski et al. 2016; Spera & Mapelli 2017; Woosley 2017). This mass gap is set by the pulsational pair-instability regime, where larger core masses become unstable in the final evolutionary stages. It is expected that for CO core masses of $30\,\mathrm{M}_\odot \lesssim M_{\mathrm{CO}} \lesssim 60\,\mathrm{M}_\odot$, the production of electron-positron pairs in the core during late nuclear burning phases (Fowler & Hoyle 1964) will result in pulsations followed by a collapse to a BH called a pulsational pair-instability SN (PPISN; Chatzopoulos & Wheeler 2012; Chen et al. 2014b; Woosley 2017; Leung et al. 2019). For higher CO core masses of $60\,\mathrm{M}_\odot \lesssim M_{\mathrm{CO}} \lesssim 120\,\mathrm{M}_\odot$ the creation of these electron-positron pairs results in complete disruption of the star in a PISN leaving no remnant (Fryer et al. 2001; Kasen et al. 2011), and for even higher M_{CO} the whole star collapses to a BH due to energy losses from photodisintegration (Heger et al. 2003). While the CO core mass limit for the pair-instability regime is quite robust, the maximum BH mass of $\sim 55\,\mathrm{M}_\odot$ before the mass gap is not well constrained. This is because it is expected that stars with CO core masses $\lesssim 28\,\mathrm{M}_\odot$ can collapse directly to a BH (Woosley 2017) in the event of a failed CCSN, which would then include their envelope mass. The total mass of this collapsing star differs due to evolutionary effects such as mass loss, rotation and metallicity, with lower metallicity or reduced mass loss producing larger BHs for the same CO core mass, and subsequently increasing this maximum BH mass limit before pair-instability. For example a possible explanation for the discovery of a BH of mass $68^{+13}_{-11}\,\mathrm{M}_{\odot}$ in the outskirts of the Milky Way (Liu et al. 2019) has been proposed in Groh et al. (2020) through reduced mass loss in the post-MS evolutionary stages.

The recent discovery of the black hole merger event GW190521 (Abbott et al. 2020a,b) has drawn much attention to this topic because of the masses of the BHs in the merger of $85^{+21}_{-14}\,\mathrm{M}_{\odot}$ and $66^{+17}_{-18}\,\mathrm{M}_{\odot}$, which fall within the pair-instability mass gap. The discovery of these large BHs has sparked more interest in Pop III stellar evolution, given that these stars with higher compactness and less mass loss can offer an explanation for the mass of this merger. Pop III stars have been discussed as progenitors for this event in Liu & Bromm (2020b); Safarzadeh & Haiman (2020); Farrell et al. (2021b), and Kinugawa et al. (2021), with Tanikawa et al. (2021b) also proposing that Pop III binary black holes may fall within the mass gap. These works show that the evolution and final fates of metal-free stars are fundamental in understanding the origin of these extreme merger events at high redshift. Furthermore, Umeda et al. (2020) and Tanikawa et al. (2021a) examine the impact of convective overshooting on the formation of Pop III BHs, showing the sensitivity of the BH mass to mixing processes during the evolution. With renewed interest in the study of primordial stars in relation to gravitational wave observations, it is imperative that we have updated and detailed theoretical models to support this new research.

1.3.4 Supermassive Stars and Black Holes

One of the great mysteries of the early Universe is the origin of supermassive black holes (SMBHs). In the previous section, we discussed the origin of stellar mass BHs, which result from the death of massive stars. Stellar mass BHs have masses on the order of a few solar masses to a few hundred solar masses, while SMBHs have much higher masses of $10^6\,\mathrm{M}_{\odot} \lesssim M_{\mathrm{BH}} \lesssim 10^{10}\,\mathrm{M}_{\odot}$ (Ferrarese & Ford 2005; Volonteri 2010). These SMBHs are of galactic scale, and sit in the centre of galaxies, where their enormous gravitational pull powers a large accretion disk of $\sim$ a few light days across. This accretion disk produces large amounts of non-thermal (temperature independent) radiation, with luminosities comparable to that of the galaxy. These central power sources of galaxies are known as active galactic nuclei (AGNs), and are crucial to understanding the origin of galaxies. Observations of these SMBHs with masses $\sim 10^9\,\mathrm{M}_{\odot}$ at redshifts $z \gtrsim 6$ (e.g. Fan et al. 2001, 2003, 2004, 2006; Mortlock et al. 2011; Wu et al. 2015; Bañados et al. 2018; Wang et al. 2021) have evoked fascination into how these objects of such extreme masses could have formed so early in the Universe. Despite these observations and the importance of SMBHs in the evolution of galaxies, their origin is still unknown. However, continued advancement of numerical simulations has allowed for many developments in this field in recent years.

The main candidates for the origin of these SMBHs at present is the collapse of supermassive stars (SMSs). It has been proposed that SMBHs could form from the so-called direct collapse model (Bromm & Loeb 2003), in which a massive seed BH forms through the gravitational collapse of a $\sim 10^5\,\mathrm{M}_\odot$ SMS. In order to have formed by the observed redshifts $z \gtrsim 6$, many studies propose the collapse of Pop III SMSs as the BH seeds for SMBHs. Some of the simulations which have studied this formation scenario, include Dijkstra et al. (2008); Latif et al. (2013); Regan & Downes (2018) and Regan et al. (2019), which show that the collapse of Pop III SMSs is a feasible explanation for the origin of quasars in the early Universe. The large masses of these SMSs may be achieved because of exposure to strong Lyman-Werner flux (11.1-13.6 eV) from a nearby Pop III halo, which destroys molecular hydrogen and prevents fragmentation, as was found in Regan et al. (2017).

Recent studies have provided new insights into the nature of Pop III supermassive stars and their role in the formation of the first quasars (Johnson et al. 2012, 2013; Hosokawa et al. 2013; Umeda et al. 2016; Woods et al. 2017; Haemmerlé et al. 2018). That work has shown that Pop III protostars can continue to accrete material at rates of $\geq 0.01\,\mathrm{M}_\odot\mathrm{yr}^{-1}$ towards masses of $\geq 10^5\,\mathrm{M}_\odot$ without an increase in ionizing feedback that would halt accretion, which favours the case for the formation of the first quasars through direct collapse. Further studies have continued to constrain the accretion rates of these Pop III SMSs (Haemmerlé et al. 2019; Haemmerlé 2021a,b; Haemmerlé et al. 2021), finding masses of $\gtrsim 10^6\,\mathrm{M}_\odot$ for these SMBH seeds depending on the rotation and density structure of the SMS. To date there have been no observations of these extreme objects, but their detectability with JWST has been investigated in Martins et al. (2020), showing that SMSs should be detectable if they are luminous and relatively cool. Additionally, for a narrow range of initial masses it had been found that SMSs may explode as general relativitistic supernovae (GRSNe). These are extremely luminous events which are theorised to occur if explosive nuclear burning unbinds the SMS following the collapse triggered by the general relativistic instability. It is generally accepted that SMSs will undergo a dynamical collapse due to general relativistic effects. However, in Chen et al. (2014a) it was found that Pop III stars with masses of 55'500 $\mathrm{M}_\odot$ may explode due to the large energy release from explosive He burning during the collapse after the onset of central He burning. Similarly, Montero et al. (2012) studied the relativistic collapse of SMSs and discovered that GRSNe may occur for stars up to $5 \times 10^5\,\mathrm{M}_\odot$ if explosive H burning through the CNO cycle can halt the collapse. They describe how the increased temperature and density from the collapse increases the nuclear energy generation rate by H burning which may liberate enough energy to produce a thermal bounce and disrupt the SMS. The detectability of such enormous explosive events by JWST and the Galaxy and Reionization EXplorer (G-REX) was studied recently in Moriya et al. (2021). They found that GRSNe would have long plateau phases that appear as persistent sources at high redshifts, but would be distinguishable from high-redshift galaxies. If future facilities can confirm what theoretical works have predicted and prove the existence of SMSs, then we may finally have our answer as to how the first quasars formed.

1.3.5 Origin of Dust

Another open question in understanding the early Universe is the origin of dust. Dust plays a critical role in star formation and regulating cooling processes in galaxies (e.g. Yamasawa et al. 2011). Since the first stars produced the first heavy elements in the Universe, they are important candidates for producing the first dust. However, this would require high mass-loss rates and significant chemical enrichment. Following observations from the Sloan Digital Sky Survey (SDSS) of $\sim 4\times10^8\,\mathrm{M}_\odot$ of dust in the high redshift ($z = 6.4$) quasar J1148+5251, Dwek & Cherchneff (2011) investigated two scenarios for the origin of this dust. Determining the origin of the dust observed in J1148+5251 presents an important challenge because the mass of dust observed is about 10 times larger than the mass of dust in the Milky Way (Sodroski et al. 1997). The two scenarios proposed to explain the origin of this large reservoir of dust in that work were, the galaxy is young (much younger than the age of the Universe) such that only SNe could have produced the dust, and the galaxy is old ($\geq 400\,\mathrm{Myr}$) such that AGB stars are the dominant source of dust. AGB stars refer to asymptotic giant branch stars, which are low and intermediate mass stars ($M_{\mathrm{ini}} \lesssim 8\,\mathrm{M}_\odot$), in the post He-burning phase, characterized by the presence of H and He shells above a carbon-oxygen core (see Kippenhahn et al. 2012, Chapter 34). Understanding whether AGB stars or SNe dominate dust formation in the early Universe therefore greatly impacts our knowledge of the nature of the Pop III and Pop II initial mass functions. Dwek & Cherchneff (2011) confirmed that AGB stars can produce the required amount of dust in J1148+5251, while SNe are less likely candidates. The production of dust by SNe scenario is less likely because it would require a $\sim 20\,\mathrm{M}_\odot$ SN to produce $\sim 1\,\mathrm{M}_\odot$ of dust, but theoretical and observational estimates have suggested that dust production by such events is only 0.1-0.15$\,\mathrm{M}_\odot$ (Cherchneff & Dwek 2010).

Another study was carried out in Valiante et al. (2011) to explain the large dust observation in J1148-5251, this time investigating the production of dust by Pop III and higher-metallicity stellar populations, and testing different characteristic masses, while also testing the AGB vs. SN scenarios similarly to Dwek & Cherchneff (2011). It was found from that work that Pop II/I stars[††] with characteristic masses of $5\,\mathrm{M}_\odot$ and a top-heavy IMF are best able to produce the dust observed at $z = 6.4$. That work showed the importance of understanding the nature of the IMF at high redshifts, but

---

[††] Pop I stars refer to the youngest generation of stars in the Universe, with metallicities in the range $0.1\,Z_\odot \leq Z \leq 3\,Z_\odot$.

also the importance of understanding the evolutionary properties of high-redshift stellar populations, such as stellar mass loss and chemical mixing which produces the dust, and UV feedback from SNe which can destroy the dust. Other works have investigated the formation of dust at redshifts of $\sim 6 \leq z \leq 8$ (Gall et al. 2011; Dwek et al. 2014; Dwek 2016; Michałowski 2015; Leśniewska & Michałowski 2019), with Gall et al. (2011), Michałowski (2015) and Leśniewska & Michałowski (2019) finding SNe to be more efficient producers of dust than AGB stars in the early Universe. How the large amounts of dust observed around quasars at high redshifts formed thus remains an open question. It is clear however, that the initial mass function and evolutionary behaviour of early stellar populations is central to solving this mystery.

1.4 Thesis Motivation and Structure

It is clear from the previous sections that the first stars are hugely important in understanding the evolution of the Universe. We have summarised the work that has been done so far to improve our understanding of Pop III stars and their impacts. The work presented in this thesis is motivated by the importance of the first stars in the Universe, and the aspects of the evolution which remain unclear, specifically the role of their rotation in their stellar evolution and its impact on observable signatures such as surface properties, chemical enrichment, and ionizing photon production.

Since the stellar evolution studies of zero-metallicity stars in Marigo et al. (2001, 2003); Ekström et al. (2008) and Yoon et al. (2012), a new series of papers was started to investigate stellar evolution with GENEC. These publicly-available grids include updated physical ingredients and are suitable for various metallicities. Described in Section 1.1.2, Ekström et al. (2012) investigated solar metallicity models. This was followed by grids at lower metallicities in Georgy et al. (2013a) and Groh et al. (2019), as we have discussed in Section 1.1.6. In this thesis, we present our new grid of Geneva stellar evolution models at $Z = 0$. We share our analysis and results from our detailed examination of these new models, including their rotational effects and nucleosynthesis. Not only do these new models provide insight into the evolution of zero-metallicity stars with the most up-to-date physics, but their consistent input physics with these higher metallicity grids will allow for important future investigations of metallicity effects in stellar evolution. This new model grid is publicly available and will be valuable for numerous future studies of the early Universe, including Pop III SNe and remnant studies, population synthesis, and chemical enrichment of metal-poor stars. Furthermore, this new grid will be highly useful for understanding future observations of primordial populations and explosive events.

It is an exciting time for research of the early Universe ahead of new observational facilities, and we must prepare for the groundbreaking detections that are expected in the coming decade. As we have discussed in Section 1.3.2, one of the main areas of interest in the early Universe is the level of contribution of the first stars to the reionization era. To understand the impact of primordial stars on reionization, we need to have updated predictions for ionizing photon production from Pop III stars, for a broad range of parameters. Our new Pop III model grid provides opportunity to study the impact of rotation and initial mass on ionizing photon production, and hence improve our knowledge of how much metal-free stars could have contributed to reionization. Since surface properties of these stars directly impact ionization, it is important to make updated predictions with the latest stellar evolution models. In light of this, we present our new predictions for ionizing photon production of primordial stellar populations based on our new grid of Geneva stellar evolution models at zero metallicity.

This thesis is structured as follows. In Chapter 2 we outline the methods of this work, including a detailed description of the physics of GENEC from which we produce our grid of Pop III models, and how we use these models to determine their ionizing photon production. The following Chapters 3 to 5 outline the results of this work. In Chapter 3 we present our Geneva stellar evolution model grid of Pop III stars in the mass range $1.7\,\mathrm{M}_\odot \leq M_\mathrm{ini} \leq 120\,\mathrm{M}_\odot$ with and without rotation. In Chapter 4 we discuss our analysis of the massive models in our Geneva grid ($9\,\mathrm{M}_\odot \leq M_\mathrm{ini} \leq 120\,\mathrm{M}_\odot$) and how their evolution is affected by rotation, specifically their surface properties, metal enrichment, and the critical rotation limit. In Chapter 5 we then present our predictions for the ionizing photon production rates of Pop III stars based on our models, and discuss how they are impacted by rotation, convective overshooting and the nature of the IMF. Finally, in Chapter 6 we summarise the principal results and implications of this work, and discuss ideas for future studies which could build on the results of this thesis and advance our knowledge of the first stars in the Universe.

Chapter 2

Methods

In this chapter we outline the methods of this work and describe the basic concepts of stellar evolution modelling of Pop III stars with rotation. We first provide background to stellar evolution modelling using the Geneva stellar evolution code, including the treatment of rotation, convection and mass loss. We detail how we adjusted the models to deal with the unique computational difficulties of Pop III stars. We also explain how we can use our zero-metallicity models to predict ionizing photon production rates, and model the ionizing photon production of primordial populations. This section will thus provide the necessary background for Chapters 3 to 5.

2.1 The Geneva Stellar Evolution Code: Overview

The stellar evolution models presented in this work are calculated using the GENeva stellar Evolution Code, GENEC (Eggenberger et al. 2008), a one-dimensional (1-D) code for computing the stellar evolution of single stars. This code takes inputs such as initial mass, metallicity, and rotational velocity and computes the evolution of the star from the ZAMS until an iron core is formed. At each computational step it calculates properties such as the bolometric luminosity, effective temperature and chemical abundances so that a detailed study can be done of the behaviour of the star throughout its lifetime, not only of the observable properties, but also the interior structure and chemical evolution.

In GENEC the star is divided into three main zones, the atmosphere, the envelope, and the interior, with a specific treatment for each one. In the atmosphere, gravity and opacity κ are kept constant while optical depth τ is calculated using $d\tau = -\kappa\rho dr$.

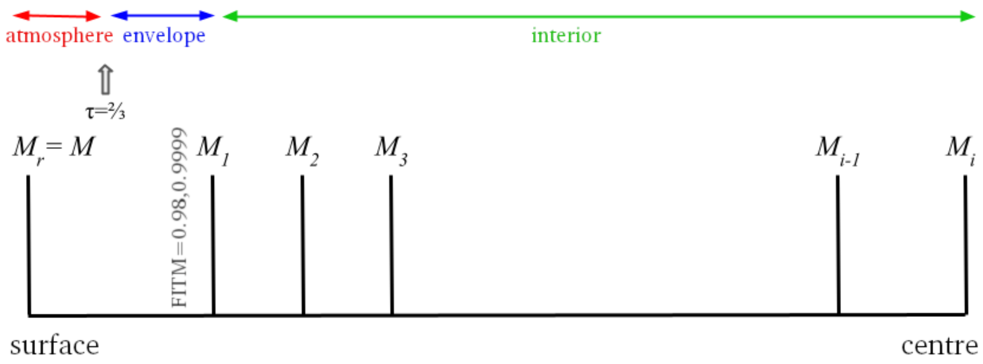

Figure 2.1: Divisions of mass shells in the code according to the Henyey method, as described in Maeder (2009). Figure is adapted by the author from earlier version by A. Maeder.

Beneath the atmosphere is the envelope*. Boundary conditions between the atmosphere and the envelope are defined at an optical depth of $\tau = \frac{2}{3}$. These include the luminosity L, the effective temperature $T_{\rm eff}$, the pressure P and the radius $R_\star$. For the envelope it is assumed that there is no energy generation from nuclear reactions, and that it rotates at a constant angular velocity equal to that of the first layer of the interior. It is also assumed to be partially ionized, thus convection is treated non-adiabatically as we will discuss in Section 2.4. The interior is then the main zone of the star where energy is produced by nuclear reactions and rotation is carefully accounted for. In the interior, the medium is assumed to be fully ionized with adiabatic convection. The boundary between the envelope and the stellar interior is defined by a parameter called FITM, also known as the ‘fitting mass’. This parameter defines the fraction of mass which is contained within the stellar interior and has a default value of FITM = 0.98 in non-rotating cases, and FITM = 0.9999 when rotation is included. This is to ensure that rotational effects such as the transport of angular momentum are accurately modelled in the outer layers of the star. The numerical method used is a relaxation method, first described in the context of stellar evolution by Henyey et al. (1964). According to this method, the spherical star is divided into mass shells from the surface to the centre, illustrated in Figure 2.1, where M_1 is at the boundary, defined by FITM, between the envelope and the stellar interior. Depending on the evolutionary stage of the star the number of these shells varies, for example at later stages the code requires more resolution as the interior structure becomes more complex.

A stellar evolution model produced using GENEC, begins with a range of input values such as initial composition, mass, and rotational velocity, and iteratively solves the four stellar structure equations from the surface to the centre of the star, such that the

---

[*] We note that this definition of the envelope may be confused with the more common usage of ‘the stellar envelope’ which refers to the interior region above the nuclear burning core and varies during the evolution with the size of the stellar core. Here we are referring to outer layers of the star where no nuclear reactions take place.

equations are satisfied at each shell.

The first equation of stellar structure describes the conservation of mass throughout the star, and is known as the mass continuity equation. To illustrate this mass conservation let us imagine that the star is static (i.e. $d/dt = 0$) and the total mass of the star is kept constant. If this is the case then the change in mass between stellar layers is $dm = 4\pi r^2 \rho dr$. Where $m = m(r,t)$ this becomes $dm = 4\pi r^2 \rho dr - 4\pi r^2 \rho \upsilon dt$ and so the mass continuity equation at each mass layer is

$$\frac{\partial r_P}{\partial M_P} = \frac{1}{4\pi {r_P}^2 \bar{\rho}} \tag{2.1}$$

Here r_P is defined as in Meynet & Maeder (1997) by $V_P = \frac{4\pi}{3} r_P^3$ where V_P is the volume surrounded by the isobar labelled by P. Thus M_P is the mass contained within the isobar and $\bar{\rho}$ is the mean density between two isobars. This is based on the Kippenhahn et al. (1970) method which accounts for rotational effects by solving the stellar structure equations on equipotentials where pressure P and density ρ are kept constant.

The second stellar structure equation describes hydrostatic equilibrium, illustrating the balance between gravitational forces and radiative pressure. Following the Henyey method (see Chapter 24, Maeder 2009) GENEC describes the stellar structure equations in Langrangian form, i.e. in mass and time coordinates, $\rho = \rho(m,t)$. Equating the inward gravitational force with the outward force due to radiation pressure (with respect to mass, $\partial P/\partial M_P$) the equation for hydrostatic equilibrium becomes

$$\frac{\partial P}{\partial M_P} = -\frac{G M_P}{4\pi {r_P}^4} f_P \tag{2.2}$$

where f_P is a factor to account for the effects of rotation, in which the centrifugal force impacts the effective gravitational force (see Section 1.1.4). This factor is defined as

$$f_P = \frac{4\pi {r_P}^4}{G M_P S_P} \frac{1}{\langle {g_{\text{eff}}}^{-1} \rangle} \tag{2.3}$$

where S_P is the total surface of the isobar, and $\langle g_{\text{eff}}^{-1} \rangle$ is the inverted effective gravitational acceleration, averaged over the whole surface S_P. Without rotation this parameter, f_P, would be equal to one, giving the classical case for hydrostatic equilibrium.

The third equation of stellar structure defines the conservation of energy within the star. In Meynet & Maeder (1997) they derived an expression for the conservation of energy following the isobar structure in eqs. 2.1 and 2.2 and taking into account the impact of rotation on stellar structure. From their assumptions they found the following equation,

$$\frac{\partial L_P}{\partial M_P} = \epsilon_{\text{nucl}} - \epsilon_{\nu} + \epsilon_{\text{grav}} \tag{2.4}$$

such that ϵ_{nucl} is the energy generated by nuclear reactions, ϵ_{ν} is the energy lost by neutrinos and ϵ_{grav} accounts for the contraction or expansion of the star. Contraction gives a positive value for ϵ_{grav} since this increases the internal energy of the star, and by contrast expansion gives a negative ϵ_{grav} value.

The final stellar structure equation (also derived in Meynet & Maeder 1997) describes energy transport. This equation is given by

$$\frac{\partial ln(T)}{\partial M_P} = -\frac{GM_P}{4\pi {r_P}^4} f_P \text{min}[\nabla_{\text{ad}}, \nabla_{\text{rad}} \frac{f_T}{f_P}] \tag{2.5}$$

$$\text{where} \qquad f_T = \left(\frac{4\pi {r_P}^2}{S_P}\right)^2 \frac{1}{\langle g_{\text{eff}} \rangle \langle {g_{\text{eff}}}^{-1} \rangle} \tag{2.6}$$

and f_P is the paramater defined in eq. 2.3. The rotational effects factors f_T and f_P are both shown here to depend on the effective gravity (g_{eff}) and the total surface of the isobar, S_P. Similarly to f_P, if the model is assumed to be non-rotating then f_T is equal to one. In eq. 2.5 for energy transport ∇_{ad} is the adiabatic temperature gradient and ∇_{rad} is the radiative temperature gradient, these are expressed as

$$\nabla_{\text{ad}} = \frac{P\delta}{\rho T C_P} \tag{2.7}$$

$$\nabla_{\text{rad}} = \frac{3}{16\pi acG} \frac{\kappa LP}{MT^4} \tag{2.8}$$

where C_P is the specific heat at constant pressure, and δ is a constant taken from the equation of state,

$$\frac{d\rho}{\rho} = \alpha \frac{dP}{P} + \varphi \frac{d\mu}{\mu} + \delta \frac{dT}{T} \tag{2.9}$$

where ρ is density, P is pressure, μ is mean molecular weight, T is temperature, and α and φ are other constants.

In summary, the four stellar structure equations describe the conservation of mass, hydrostatic equilibrium, conservation of energy, and energy transport in the star. These equations are the basis of the GENEC code and are used to determine the model's structural properties.

Summarised in Figure 2.2 is the chronological order of how GENEC models stellar evolution. Having solved the stellar structure equations from input parameters such as mass and metallicity, the model is said to have a composition $\text{X}_\text{i}(\text{t}_\text{n})$, and nuclear energy generation rate $\epsilon_i(\text{t}_\text{n})$, where i represents the mass layer (Figure 2.1) and n represents the current time step. Over the period, Δt, between time steps t_n and $\text{t}_{\text{n}+1}$ the nuclear reactions adjust chemical abundances, which subsequently modify values such as density ρ, opacity κ, the radiative gradient ∇_{rad}, and the adiabatic gradient ∇_{ad}. These new values are then inputted into the four equations of stellar structure, until a set of values are found to satisfy the equations through the relaxation method. This set of values

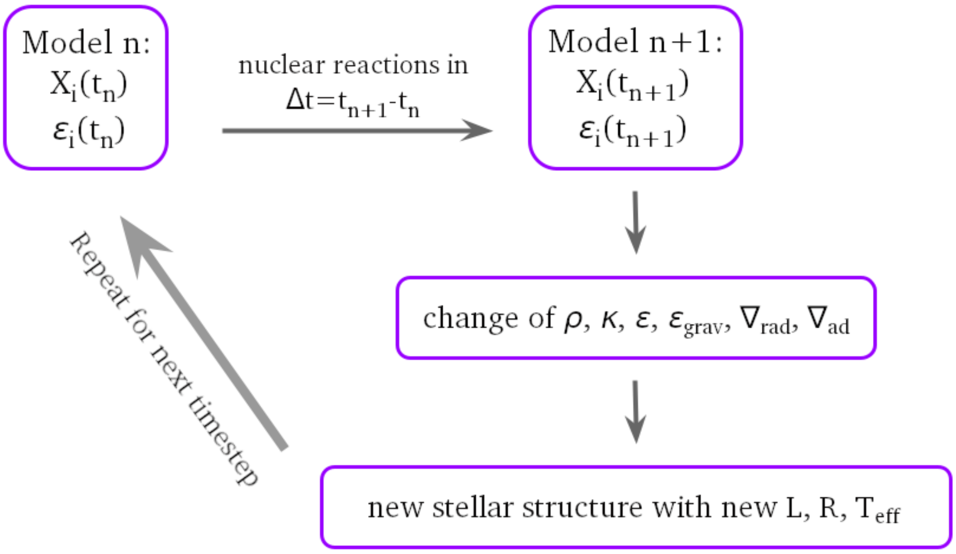

Figure 2.2: A summary of the steps in GENEC stellar evolution modelling, adapted by the author from Figure 24.1, Maeder (2009). Nuclear reactions update nuclear energy generation and chemical abundances at each time step, which in turn alter values such as density, ρ, and opacity, κ. This results in a model with new internal and surface properties, and the process repeats itself to study how the star evolves over time.

is then outputted and saved as the stellar structure at time step t_{n+1}. Repeating this process for each time step allows the model to advance along evolutionary plots such as the HR and Kippenhahn diagrams, and enables us to observe how these models evolve from their ZAMS to their final evolutionary stages.

2.2 Model Initialisation

Models produced using GENEC are initialised based on coarse model structures from previously computed simplified models. Based on the initial mass and composition selected for the model, the programme will interpolate between initial structures from this table of converged simplified models which includes values for the pressure, temperature, luminosity and radius at different mass layers. Alternatively, models can be initialised in GENEC using a polytrope to define the initial density structure of the pre-stellar seed. A polytrope follows the expression $P = K\rho^n$ where P and ρ are the pressure and density, and K and n are constants. For example, a polytropic index of $n = 0$ corresponds to a constant density profile from the centre to the surface of the protostar. From this point on the protostar contracts under its gravitational pressure which increases the central temperature of the star (initially set to $\sim 10^{4-5}$ K depending on the initial mass) until it reaches the temperature required for H-burning, $T_{\rm eff} \simeq 10^7$ K. During this stage the programme converges the model to find a ZAMS structure that is relevant for the initial mass and composition. Since we are interested in computing ZAMS models rather than pre-MS models, the default is that the model does not include deuterium burning. However, this can be included as is the case for the models presented in Haemmerlé et al. (2013) for example.

As described in Section 2.1, the equations which determine the stellar structure are solved for various mass layers in the star at different time steps to model the evolution. The initial number of mass layers depends on the initial mass of the model, where higher mass models have a higher number of mass layers. If we take the $9\,\mathrm{M}_{\odot}$ zero-metallicity model as an example, the initial number of mass layers is $\sim$200 while for the $120\,\mathrm{M}_{\odot}$ model the initial number is 450 layers. The mass zones are distributed throughout the stellar interior such that there are more mass layers near the stellar centre where the nuclear burning core develops. The initial number of mass layers remains largely unchanged by the ZAMS, but increases throughout the MS as more resolution is required in the stellar core to resolve the nuclear reactions sufficiently. In later stages such as He-core burning the number of mass layers further increases to aid the resolution in regard to chemical mixing. In addition, for rotating models the number of mass layers is increased to provide better resolution for angular momentum transport throughout the star, in rotating models the number of mass shells is typically $\sim$1000. GENEC is an adaptive mesh refinement code, which means that the number of mass layers can adapt based on the resolution required. For example, if there is a high temperature gradient between two layers the code will add a new layer between the two so as to provide higher resolution in that region.

The resolution of the time steps follows a similar behaviour by having larger time steps during the MS phase, and smaller time steps during later phases where more complex nucleosynthesis and chemical mixing takes place. The initial time step selected depends on the initial mass of the model with larger initial masses requiring smaller initial time steps. For example, the initial time step for a $9\,\mathrm{M}_{\odot}$ model is 1000 years but is 100 years for a $120\,\mathrm{M}_{\odot}$ model. Following the calculation of the equations at each mass layer the code then performs a convergence check. If successful, the programme increases the time step by a factor of 1.4 for the MS and 1.7 for later stages. However, if the convergence check fails the time step is halved and the calculations are repeated. This continues until a converged solution is found or the model crashes signalling that the current time step is too short. The time steps can also be manually altered which is preferable in cases which we expect may need further resolution, such as energy boosts to burning regions above the stellar core. In such cases we can restart the model from a point prior to the computationally difficult stage with manually reduced time steps.

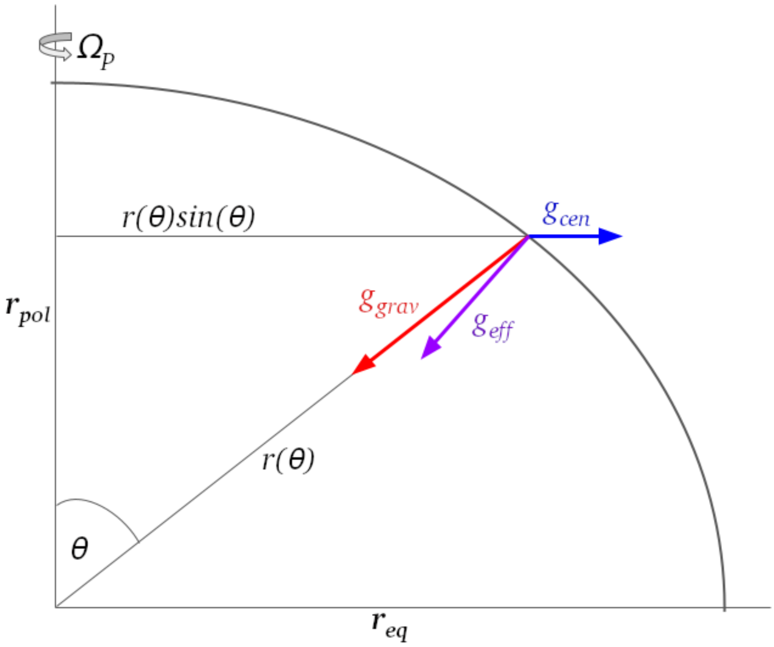

Figure 2.3: Schematic of how stellar structure is modified by rotation and visual representation of eq. 2.10. Adapted by the author from similar schematics by C. Georgy and A. Maeder.

2.3 Treatment of Rotation

In GENEC, rotation is treated within the frame of the Roche model, ie. the gravitational potential is approximated by GM_r/r where M_r is the mass inside the equipotential of radius r. The radius r that labels each equipotential is defined by $V_r = \frac{4\pi}{3}r^3$ where V_r is the volume (deformed by rotation) inside the equipotential considered. The classic Roche model describes the equilibrium of the rotating gas envelope in the gravitational field of the point mass, and is widely used in the investigation of a rotating star when there is a strong concentration of matter in the star's centre and the self-gravitation of the outer layers of the star can be considered negligible compared to the gravitational pull of the core. As described in Section 1.1.4, the centrifugal force of rotation modifies the effective gravity forcing the star to lose its spherical shape and become oblate. This is illustrated in Figure 2.3, where the acceleration of the centrifugal force, g_{cen}, acts against the gravitational acceleration, $g_{\rm grav}$, giving the effective gravitational acceleration, $g_{\rm eff}$. The shape of the rotating envelope depends on the degree of rotation, a non-rotating envelope has spherical form and becomes more oblate as the rotational velocity increases. This shape is given by values of radius r and colatitude θ which satisfy the equation

$$\frac{GM}{r(\theta)} + \frac{1}{2}\Omega_P^2 r(\theta)^2 sin^2\theta = \frac{GM}{r_{\rm pol}} \tag{2.10}$$

where $r(\theta)$ is the radius at colatitude θ, Ω_P is the angular velocity at a given isobar and $r_{\rm pol}$ is the polar radius. This equation essentially equates the potential energy at the colatitude θ and the potential energy at the stellar pole. The first term on the left-hand side is the gravitational potential at $r(\theta)$, and the second term is the potential from the centrifugal acceleration. If the star is non-rotating and $\Omega = 0$ then the star is spherical and the gravitational potential at $r(\theta)$ equals that at r_{pol}, otherwise the star becomes oblate (see Figure 2 of Maeder & Meynet 2012).

In this work differential rotation (see Section 1.1.4) is assumed and implemented following the Zahn (1992) prescription for shellular rotation, which states that the angular velocity Ω is constant on isobaric shells (Ω_P) and depends on the distance r to the stellar centre to first order. The expression for how angular velocity varies with r and θ according to this prescription is

$$\Omega(r,\theta) = \bar{\Omega}(r) + \Omega_2(r)P_2(cos\theta) \tag{2.11}$$

where $\Omega_2(r)P_2(cos\theta) \ll \bar{\Omega}(r)$. Here P_2 refers to the second Legendre polynomial, $P_2(x) = \frac{1}{2}(3x^2+1)$, and Ω_2 is the horizontal component of the angular velocity as derived in Equation 2.11b, Zahn (1992),

$$\Omega_2 = \frac{1}{5\upsilon_h}\bar{\Omega}(r)r[2V(r) - \alpha U(r)] \tag{2.12}$$

where υ_h is the velocity of the horizontal turbulence, $V(r)$ and $U(r)$ are the horizontal and vertical components of the meridional circulation velocity respectively, and $\alpha = \frac{1}{2}\frac{d\,ln(r^2\Omega)}{d\,ln(r)}$. The horizontal average $\bar{\Omega}(r)$ is given by

$$\bar{\Omega}(r) = \frac{\int_0^\pi \Omega\, sin^3\theta\, d\theta}{\int_0^\pi sin^3\theta\, d\theta} \tag{2.13}$$

There are some limitations to eq. 2.11. In particular, since isobars are not identical to spherical surfaces it only applies to low or moderate rotational velocities, and is non-conservative at high rotational velocities. Although the Kippenhahn et al. (1970) method is only applicable in conservative cases, Meynet & Maeder (1997) discuss how it can be applied to the shellular rotation case described here. In this case stellar shells are isobars, but they are not equipotentials and the star is thus baroclinic rather than barotropic.

The classical critical angular velocity (or the Ω-limit) is the limit at which the centrifugal force equates the gravitational force and thus the star becomes unstable. In the frame of the Roche model the Ω-limit is given by

$$\Omega_{\mathrm{crit}} = \left(\frac{2}{3}\right)^{\frac{3}{2}} \sqrt{\frac{GM}{R^3_{\mathrm{pol,crit}}}} \tag{2.14}$$

where M is the total mass of the star and $R_{\mathrm{pol,crit}}$ is the polar radius. Since $\upsilon^2_{\mathrm{crit}} = \Omega^2_{\mathrm{crit}}R^2_{eq,crit}$ the critical rotational velocity at the equator is thus

$$\upsilon_{\mathrm{crit}} = \sqrt{\frac{2}{3}\frac{GM}{R_{\mathrm{pol,crit}}}} \tag{2.15}$$

similary to eq. 1.2 but using $\frac{R_{\text{eq,crit}}}{R_{\text{pol,crit}}} = \frac{3}{2}$. There is a second critical rotational velocity to describe the ΩΓ-limit where the star reaches both the critical rotation limit and the Eddington limit (see Section 1.2.3). This second critical angular velocity for the ΩΓ-limit is derived as in Maeder & Meynet (2000a) which gives

$$\upsilon_{\text{crit,2}} = \frac{3}{2}\upsilon_{\text{crit}}\sqrt{\frac{1-\Gamma_{\text{edd}}}{V'(\omega)}\frac{R^2_{\text{eq,crit}}(\omega)}{R^2_{\text{pol,crit}}}} \tag{2.16}$$

$$\text{where} \qquad V^{'}(\omega) = \frac{V(\omega)}{\frac{4}{3}\pi R^3_{\text{pol,crit}}} \tag{2.17}$$

$$\text{and} \qquad \omega = \sqrt{\frac{\Omega^2 R^3_{\text{eq,crit}}}{GM}} \tag{2.18}$$

Here $V^{'}(\omega)$ is the dimensionless volume as a function of rotation ω, and υ_{crit} refers to the first critical velocity for the Ω-limit as defined in eq. 2.15.

The equations described here give an overview of how rotation is treated in the Geneva stellar evolution code. In the following subsections we will provide background as to the more detailed physical inputs of rotation in the code, including treatment of diffusion, meridional velocity, and angular momentum.

2.3.1 Diffusion Coefficients and Meridional Velocity

The shellular rotation model creates turbulent motions which lead to shear instabilities between layers of different velocities. We must therefore account for this strong horizontal turbulence in our 1-D modelling of differentially rotating stars. To do so a diffusion coefficient is introduced related to the viscosity caused by horizontal turbulence. This is derived from the Zahn (1992) prescription for horizontal turbulence and is defined as

$$D_h \approx \upsilon_h = \frac{1}{c_h} r|2V(r) - \alpha U(r)| \tag{2.19}$$

where c_h is a constant of the order of 1 (we take $c_h = 1$).

As previously discussed in Section 1.1.4, meridional circulation arises from the impossibility for a rotating star to be in hydrostatic and radiative equilibrium at the same time. Differential rotation results in a higher temperature at the pole than at the equator leading to meridional currents which facilitate the transport of angular momentum between the core and the envelope. These meridional currents are illustrated in Figure 2.4 for a solar-metallicity $20\,\text{M}_\odot$ model with $\upsilon_{\text{ini}} = 300\,\text{km}\,\text{s}^{-1}$ at the beginning of the MS phase. This figure demonstrates the macroscopic nature of meridional currents and their effectiveness as a global transport of chemical elements and angular momentum. The central sphere represents the nuclear burning core and meridional currents are shown by the two inner and two outer tori around this core. As explained by the caption, if focusing on the upper right quadrant of the sphere, matter turns counterclockwise in the outer torus and clockwise in the inner torus. To understand the 3-D motions of the meridional currents its velocity is split into vertical, $U(r)$, and horizontal, $V(r)$, components.

The amplitude of the vertical component of the meridional velocity is defined in the code as

$$U(r) = \frac{P}{\rho g C_P T} \frac{1}{[\nabla_{\rm ad} - \nabla_{\rm rad} + (\varphi/\delta)\nabla_\mu]} \left(\frac{L}{M_*}[E_\Omega + E_\mu] + \frac{C_P}{\delta}\frac{\partial \Theta}{\partial t} \right) \tag{2.20}$$

where $M_* = M(1 - \frac{\Omega^2}{2\pi g \rho_m})$ is the modified stellar mass by the Gratton-Öpik term $\frac{\Omega^2}{2\pi g \rho_m}$ which encapsulates the effects of mass loss on the meridional circulation; and $\Theta = \tilde{\rho}/\bar{\rho}$ is the ratio of the variation of the density to the average density on an equipotential. Both φ and δ are constants taken from the equation of state (eq. 2.9), and E_Ω and E_μ are expressions used to separate the terms that depend on the Ω- and μ-distributions respectively, these are defined in Maeder & Zahn (1998). This vertical component of the meridional velocity can be understood from Figure 2.4 as follows. In the smaller tori just beyond the stellar core, the fluid elements go upwards on the inner side of the torus and descend toward the equator on the outer side of the torus i.e. $U(r)$ is positive. Due to the density dependence of the Gratton-Öpik term, the direction of circulation is modified in the outer tori where the density is lower, and $U(r)$ becomes negative. This effect is lessened at lower metallicity due to the increased density of low-metallicity stars (see Section 1.1.6).

To combine the effects of horizontal diffusion and meridional circulation an effective diffusion coefficient, $D_{\rm eff}$, is defined in the code as

$$D_{\rm eff} = \frac{1}{30}\frac{rU(r)^2}{D_h} \tag{2.21}$$

Another effect of differential rotation which is considered in the code is shear turbulence, an instability induced at the interface of layers with different rotational velocities. According to the Richardson criterion (see Maeder 1995), a layer can remain stable as long as the excess kinetic energy from differential rotation does not overcome the buoyancy force. Shear is what arises when thermal dissipation reduces this buoyancy force. The default prescription for the coefficient of shear diffusion ($D_{\rm shear}$) in GENEC is that of Maeder (1997), and is given by

$$D_{\rm shear} = \frac{K}{\frac{\varphi}{\delta}\nabla_\mu + (\nabla_{\rm ad} - \nabla_{\rm rad})} \frac{H_P}{g\delta} \left[f_{\rm energy} \left(\frac{9\pi}{32}\Omega \frac{d\,ln\Omega}{d\,ln\,r} \right)^2 - (\nabla_{\rm int} - \nabla) \right] \tag{2.22}$$

where $K = \frac{4acT^3}{3\kappa\rho^2 C_P}$ is the thermal diffusivity, $f_{\rm energy}$ is the fraction of the excess energy in

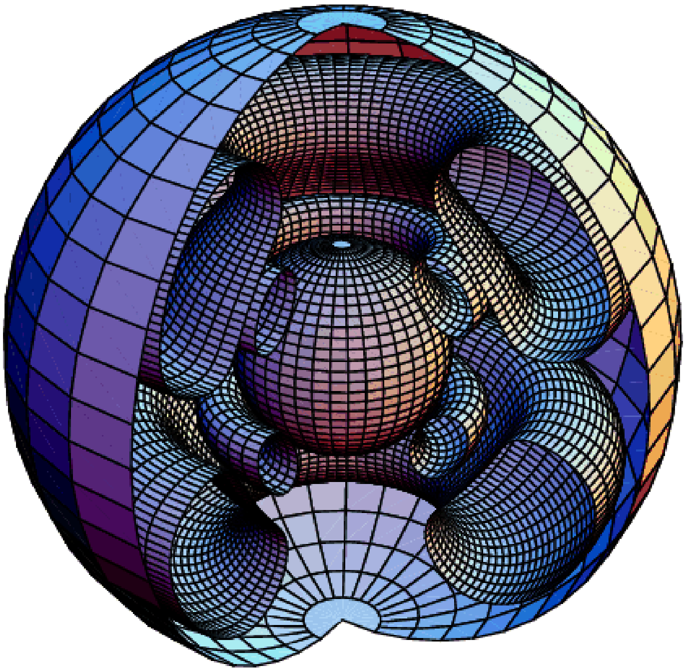

Figure 2.4: Schematic structure with stream lines of meridional circulation in a solar-metallicity $20\,\mathrm{M}_\odot$ model of $5.2\,R_\odot$ with $\upsilon_{\mathrm{ini}} = 300\,\mathrm{km\,s^{-1}}$, at the beginning of the MS phase, from Meynet & Maeder (2002). The structure is presented as a function of M_r. In the upper hemisphere on the right section, matter is turning counterclockwise along the outer stream line and clockwise along the inner one. The inner sphere is the convective core which has a radius of $1.7\,R_\odot$.

the shear that contributes to mixing (taken as 1), and $\nabla_{\mathrm{int}} - \nabla$ is the difference between the internal non-adiabatic temperature gradient and the local temperature gradient of the medium, however this value is negligible in most cases as we will discuss in Section 2.4.

2.3.2 Transport of Angular Momentum

The transport of angular momentum involves both global transport and local turbulence, it therefore requires both advection and diffusion. In many stellar models advection is treated as a diffusive process, however, this is inaccurate as advection is a transport which results from the coherent displacement of relatively large volume elements, such as streams or currents. Diffusion is by contrast a transport that involves chaotic motions. In diffusive processes arising from hydrodynamical instabilities, only the quantities with a gradient are transported. Convection acts as a diffusive process for example, mixing elements with short timescales, while other diffusive processes typically have much longer timescales. GENEC treats advection separately from diffusive processes, since, unlike diffusion, advection is a global transport. The transport of angular momentum inside a star is then implemented in GENEC following the prescription described in Maeder & Zahn (1998), which is updated from the Zahn 1992 prescription, where both advection and diffusion are accounted for. The transport in the radial direction obeys the equation,

$$\rho \frac{d}{dt}(r^2 \bar{\Omega})_{M_r} = \frac{1}{5r^2}\frac{\partial}{\partial r}(\rho r^4 \bar{\Omega} U(r)) + \frac{1}{r^2}\frac{\partial}{\partial r}\left(\rho D r^4 \frac{\partial \bar{\Omega}}{\partial r}\right) \tag{2.23}$$

This expression uses the Langrangian formulation where r is linked to M_r through $dM_r = 4\pi\rho r^2 dr$. The first term on the right hand side is the divergence of the advected flux and the second term is that of the diffused flux. The coefficient D is the total diffusion coefficient in the vertical direction, taking into account the various instabilities that transport angular momentum such as convection and shears, and $\bar{\Omega}$ is the horizontal average of the angular velocity as defined in eq. 2.13.

2.3.3 Angular Momentum Conservation

Angular momentum conservation is of vital importance in stellar evolution modelling since the final angular momentum content of a star is a key determining property of its final fate. In GENEC the conservation of angular momentum ($\Omega r^2 =$ constant) is checked throughout the evolution of the model. A physical source of variation for the total angular momentum content would be, for example, the removal of angular momentum through mass loss of a rotating star. However, there can also be numerical variations due to inaccuracies in the resolution of the advection-diffusion equation for angular momentum transport, and the structure of the code itself. In GENEC models, the envelope is defined as the region above a given mass coordinate in which the luminosity is considered a constant, and where partial ionisation is accounted for (see Section 2.1). This envelope effectively floats above the stellar interior, and so its angular momentum content is imposed by the behaviour of the interior. The final angular momentum content obtained after the computation of the structure therefore differs from the expected one, which is calculated based on the amount of angular momentum lost through mass loss from stellar winds. However, GENEC employs a correction amount, $\Delta\mathcal{L}_{\mathrm{corr}}$, which accounts for these numerical variations.

2.3.4 Transport of Chemical Species

The treatment of chemical transport in the code is based on the findings of Chaboyer & Zahn (1992), where it is shown that the horizontal turbulence competes efficiently with the advective term of the meridional circulation. Consequently, horizontal turbulent diffusion must be taken into account when calculating the transport of chemical species and angular momentum within radiative zones. The change in abundance for a given chemical X_i in the shell is therefore calculated using the expression,

$$\rho \frac{dX_i}{dt} = \frac{1}{r^2} \frac{\partial}{\partial r} \left(\rho r^2 [D + D_{\mathrm{eff}}] \frac{\partial X_i}{\partial r} \right) + \left(\frac{dX_i}{dt} \right)_{\mathrm{nucl}} \tag{2.24}$$

The first term on the right hand side accounts for the transport of chemical species by both meridional circulation and horizontal turbulence, computed as a diffusive process. Here D refers to the diffusion coefficient due to convection and shear transport mechanisms, while D_{eff} refers to the effective diffusion coefficient due to meridional circulation and horizontal turbulence (eq. 2.21). The final term accounts for the change in abundance produced by nuclear reactions. In GENEC diffusive processes are assumed to arise from rotational instabilities (e.g. shear turbulence, meridional circulation), therefore in models without rotation eq. 2.24 becomes

$$\rho\frac{dX_i}{dt} = \left(\frac{dX_i}{dt}\right)_{\rm nucl} \tag{2.25}$$

However, chemicals can still be transported in non-rotating models through convective mixing. In convective regions mixing is so strong that the region becomes chemically homogenous. Convection is thus a very effective mechanism for chemical transport. In the next section we will discuss how convection is treated in the code, and provide background into how the theory of convective mixing has been adapted for 1-D stellar evolution modelling.

2.4 Treatment of Convection

The majority of energy transport in stars occurs through two mechanisms, radiative transfer, and turbulent motions known as convection. Convective transport of energy is essentially an exchange of heat between hotter and cooler layers through the exchange of convective 'bubbles' or mass elements. Convection develops in regions where there is an excess of heat with respect to what radiation can transfer, a limit which is commonly described by the Ledoux and Schwarzschild criteria (see Chapter 6, Kippenhahn et al. 2012). We will first discuss the Ledoux criterion, and how it describes the conditions necessary for stability in a radiative region of a star. The Ledoux criterion states that a region remains stable against convection if

$$\nabla_{\rm rad} < \nabla_{\rm ad} + \frac{\varphi}{\delta}\nabla_{\mu} \tag{2.26}$$

where ∇_{μ} is the mean molecular weight gradient, φ and δ are constants from the equation of state (eq. 2.9), and $\nabla_{\rm rad}$ and $\nabla_{\rm ad}$ are the radiative and adiabatic temperature gradients as defined in eqs. 2.7 and 2.8. When this criterion is not satisfied the region will become convective. If there is a homogeneous chemical composition, then $\nabla_{\mu} = 0$. This is the assumption of the Schwarzschild criterion which states that a region remains stable against convection if

$$\nabla_{\rm rad} < \nabla_{\rm ad} \tag{2.27}$$

From the Schwarzschild criterion the dynamical limit, $r_{\Delta T}$, is defined where the adiabatic temperature gradient, $\nabla_{\rm ad}$, is approximately equal to the radiative temperature gradient, $\nabla_{\rm rad}$. This dynamical limit then defines the boundary of convective regions. At the dynamical limit the acceleration of the convective cells is zero, however convective motions still continue above this limit until their velocity is zero. The point where their velocity becomes zero is called the kinematical limit r_v. It follows therefore that the difference between the dynamical and kinematical limits will give the distance of convective overshooting, d_{ov}, which is the distance that the fluid elements will travel above the surface of the convective region. This distance d_{ov} is thus defined as,

$$d_{\mathrm{ov}} = |r_{\nu} - r_{\Delta T}| \tag{2.28}$$

Understanding this convective overshooting distance is fundamental to understanding the mixing of stellar interiors. Convective overshooting plays a significant role in determining the size of the convective core in massive stars, in that higher convective overshooting can mix material inwards and increase the fuel available for the nuclear burning core. Since the size of the convective core determines the stellar structure and the nature of the final fate of the star (e.g. Sections 1.1.3 and 1.3.3), constraining the parameters which define convective overshooting is crucial in stellar evolution modelling.

The most common method of modelling convective overshooting in 1-D stellar evolution codes is through 'mixing-length theory' (Böhm-Vitense 1958). Mixing-length theory (MLT) expresses the parameters of the non-local phenomena of convection in terms of local quantities. This is an oversimplification since overshooting is a non-local process which depends on the properties of the adjacent convective layers. However, it avoids computational difficulties and can mimic convective energy transport effectively. The basic assumption of MLT is that fluid elements can be represented by average cells, which move outwards in the star over a vertical distance l called the mixing length. These fluid elements can be thought of as 'bubbles' which, after travelling this distance l deliver their energy excess to the surrounding medium through heat dissipation. This mechanism is illustrated in Figure 2.5. From the figure we can visualise how one of these fluid elements, or 'convective bubbles', moves from the hotter inner region to the cooler outer region and transports energy through its excess heat. The mixing-length l across which the fluid element travels is defined in terms of the pressure scale height, H_P, as $l = \alpha_{\mathrm{MLT}} H_P$, where α_{MLT} is a free parameter which determines the mixing-length (see Maeder & Meynet 1989). This is how convective overshooting above the stellar core is defined in GENEC. In terms of d_{ov}, α_{MLT} becomes

$$\alpha_{\mathrm{ov}} = \frac{d_{\mathrm{ov}}}{H_P} \tag{2.29}$$

where α_{ov} is the free parameter employed by GENEC to determine the level of convective overshooting above the core. This overshooting parameter α_{ov} is a stepwise approximation and should not be confused with the exponential overshooting parameter f_{ov} (Herwig et al. 1997) which is used in the MESA stellar evolution code (Paxton et al. 2011, 2013, 2015) to model convective overshooting as a diffusive process.

If d_{ov} exceeds the radius of the convective core, R_{cc}, then the total extension of the stellar core is given instead by $R_{\mathrm{cc}}(1 + \alpha_{\mathrm{ov}})$. While α_{ov} is a free parameter in the code, the outer convective zones above the stellar core are treated instead by a

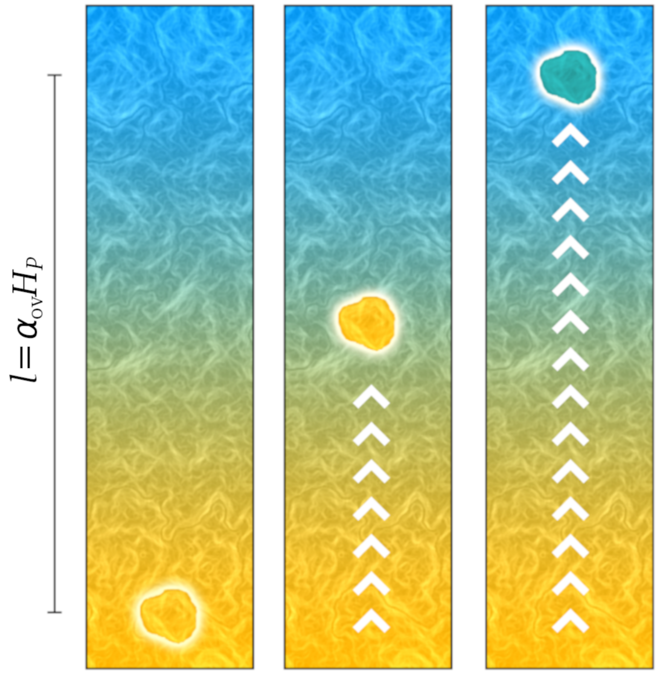

Figure 2.5: Schematic of mixing length theory (MLT) in fluid mechanics where a bubble rises by a distance $l = \alpha_{\rm ov} H_P$ and transfers energy through heat dissipation.
Source: Wikimedia commons.

fixed, solar-calibrated value. For stars of initial masses $M_{\rm ini} > 1.25\,{\rm M}_\odot$ this value is $\alpha_{\rm MLT} = 1.6$ (Schaller et al. 1992). For the most luminous models, the effects of increased turbulence need to be included in the treatment of convection in the envelope. This is done according to Maeder (1987) using a mixing-length taken on the density scale instead of the pressure scale,

$$\alpha_{\rm MLT} = \frac{l}{H_\rho} = \frac{l(\alpha - \delta\nabla)}{H_P} = 1 \tag{2.30}$$

where H_ρ is the density scale height and ∇ is the local temperature gradient of the medium (eq. 2.22). The use of H_ρ rather than H_P here prevents the occurrence of an unphysical density inversion in the envelope with increased turbulence (Stothers & Chin 1973). The disadvantage of this treatment is that the redwards extension of evolutionary tracks in the HR diagram is reduced by 0.1-0.2 dex in $T_{\rm eff}$ (Maeder & Meynet 1987). For this reason, the use of H_ρ is restricted to models with initial masses $M_{\rm ini} \geq 40\,{\rm M}_\odot$, which are not expected to extend to low effective temperatures.

As mentioned in Section 2.1, in GENEC the interior treatment of convection is adiabatic while the outer layers are partially ionized and thus convection must be treated non-adiabatically. Due to the extremely hot temperatures of stellar interiors of the order of millions of degrees K, the average temperature excess of convective fluid elements is very low compared to the thermal energy content of the star. Therefore, the adiabatic treatment of convection is a reasonable assumption. However, in the outer layers where the temperatures are lower, adiabatic convection is no longer valid. In general, non-adiabatic treatment of convection is required where H and He are not fully ionized, as is the case for the outer layers in GENEC models. To adjust the mixing-length theory for non-adiabatic convection, the temperature excess ΔT is defined in terms of the pressure scale height H_P and mixing length l as

$$\frac{\Delta T}{T} \simeq \frac{1}{H_P}(\nabla - \nabla_{\text{int}})\frac{l}{2} \tag{2.31}$$

where ∇_{int} is the temperature gradient of the fluid element known as the interior gradient, and ∇ is the temperature gradient of the external medium, similarly to eq. 2.22. Using this value for temperature excess ΔT we can now evaluate the convective energy flux,

$$F_{\text{conv}} = \rho \upsilon C_P \Delta T \tag{2.32}$$

where υ is the convective velocity. This value, F_{conv} is then added to the radiative flux to contribute to the total flow of energy inside the star.

The treatment of convection for 1-D stellar evolution modelling described in this section has been found to reasonably reproduce observations and the large-scale properties of stars. However, theoretical works such as Meakin & Arnett (2007) have found that while MLT gives a good description of the velocity scale and temperature gradients for shell convection, there are other important effects that it does not capture. Specifically Meakin & Arnett (2007) found through their 3-D simulations that the MLT assumption of zero net up/down kinetic energy flux is inaccurate. Therefore, further work is required to constrain the nature of convective mixing for 1-D models. Recently, 3-D stellar evolution simulations have again been used to investigate convective mixing in the evolution of massive stars, and find ways to improve our assumptions for convection in 1-D stellar evolution models. In Cristini et al. (2017, 2019), turbulent convective mixing is simulated using the 3-D Implicit Large Eddy Simulation paradigm (ILES; Margolin et al. 2006) which is a methodology for modelling complex, high Reynolds' number[†] flows. Turbulence, energy transport and mass entrainment can not be self-consistently modelled in 1-D stellar evolution codes, so these 3-D simulations can be used to improve our assumptions for energy and mass transport through convective mixing in 1-D simulations. Convective mixing of the C-burning shell in a 15 $\mathrm{M}_\odot$ solar-metallicity model was investigated in Cristini et al. (2017), and the Kippenhahn diagram for that model is shown in Figure 1.2. In that work they found that mass entrainment could be represented by its dependence on the luminosity, which drives convection, and the bulk Richardson number (Ri_{B}), which defines the stiffness of the convective boundary (see Appendix A of Cristini et al. 2017). This conclusion was further tested and explored in Cristini et al. (2019) where it was also found that entrainment is inversely dependent on the bulk Richardson number. That work is an example of how 3-D simulations of

---

[†] Reynolds' number is a dimensionless parameter defined as the ratio of the inertial forces to the viscous forces in a fluid. More turbulent flows (eddies) have higher Reynolds' numbers.

specific periods of stellar evolution can inform our 1-D modelling of the full evolution from ZAMS to pre-SN.

The Cristini et al. (2017, 2019) Ri_{B}-dependence of mass entrainment is implemented into 1-D stellar evolution models in Scott et al. (2021). In that work it was found that Ri_{B} decreases monotonically with increasing mass. Due to the decrease in Ri_{B}, entrainment and mixing increase with mass. This finding also impacts how we fit the convective overshooting parameter with 1-D stellar evolution models, given that higher entrainment widens the MS in a similar fashion to convective overshooting (Castro et al. 2014; Martinet et al. 2021). It is important that we continue this effort to improve the physics of convection in stellar evolution models. For instance, Kaiser et al. (2020) found that varying the input parameters of convection can lead to uncertainties in the final core masses and total masses of up to 70%. Therefore, a combination of increasing understanding of convective mixing through 3-D simulations (see also Arnett et al. 2018, 2019) and fitting model behaviour with observations (Castro et al. 2014; Martinet et al. 2021) is required to ensure that the treatment of convection in 1-D stellar evolution modelling is physically robust.

2.5 Treatment of Mass Loss

As has been discussed in Chapter 1, mass loss is a hugely influential property in the evolution of massive stars. The implementation of mass loss in stellar evolution codes subsequently has a huge impact on the behaviour of our models. Mass-loss prescriptions must therefore be carefully selected based on extensive research by both theorists and observers. In this section we will outline the treatment of mass loss in the Geneva stellar evolution code, and give background to the relevant properties of mass loss for this work.

2.5.1 Radiative Mass Loss

The main mass-loss mechanism discussed in stellar evolution of massive stars is that of radiative mass loss. This is because massive stars typically have strong radiative mass loss through continuous stellar winds, and thus shed large proportions of their initial mass throughout their lifetimes. The fundamental properties of the stellar wind are the mass-loss rate itself $\dot{M}$, and the terminal velocity of the wind υ_∞, which are related to each other through the equation of mass continuity $\dot{M} = 4\pi r^2 \rho(r)\upsilon(r)$ (see eq. 2.1). The velocity $\upsilon(r)$ is then approximated as

$$\upsilon(r) = \upsilon_\infty \left(1 - \frac{R_\star}{r}\right)^\beta \tag{2.33}$$

based on the β-law as outlined in Lamers & Cassinelli (1999), where $R_\star$ is the stellar radius. From this relation the stellar wind velocity $\upsilon(r)$ can be fully parameterized by the exponent β, which can be constrained based on spectroscopic and hydrodynamical studies (e.g. Groenewegen & Lamers 1989; Crowther et al. 2006; Muijres et al. 2012; Bouret et al. 2013). Through such studies mass-loss rate prescriptions can be developed for stellar evolution modelling, which predict how the mass-loss rate will vary as a function of properties such as luminosity, surface temperature and initial metallicity.

The Geneva stellar evolution code has 11 options for mass-loss rate prescriptions throughout the evolution of the star. These include radiative mass-loss prescriptions de Jager et al. (1988) and Vink et al. (2001), as well as WR mass-loss prescriptions such as Nugis & Lamers (2000) and Gräfener & Hamann (2008), and RSG mass-loss prescriptions such as van Loon et al. (2005). Details on how these mass-loss prescriptions are selected for the current Geneva grids can be found in Ekström et al. (2012); Georgy et al. (2013a); Groh et al. (2019).

The most widely used mass-loss prescription for hot massive stars is that of Vink et al. (2001) (and its revisions e.g. Vink & Sander 2021) which defines $\dot{M}$ in terms of υ_∞ and the initial metallicity Z. As described in Section 1.1.6, this prescription gives a global dependence of mass loss on initial metallicity, which is

$$\dot{M} \propto Z^{0.85} \upsilon_\infty^{p} \tag{2.34}$$

with $p = -1.23$ for $T_{\rm eff} \gtrsim 25000\,$K, and $p = -1.60$ for $T_{\rm eff} \lesssim 25000\,$K. This formula infers a negligible radiative wind for Pop III stars and, as is discussed in Section 1.2.3, the research by Krtička & Kubát (2006, 2009) substantiates this in finding inefficient line-driven winds for metal-free stars.

As outlined in Ekström et al. (2012), GENEC also includes a correction to the radiative mass-loss rate for rotation. This correction is the analytical recipe for rotationally driven mass loss (Maeder & Meynet 2000a), which is given in eqs. 1.5 and 1.6 in Section 1.2.6.

2.5.2 Mechanical Mass Loss

Due to the metallicity dependence of radiative mass loss, mechanical mass loss is of particular importance in our models. Since radiative winds of primordial stars are not efficient drivers of mass loss they struggle to remove angular momentum. This means that particularly for more massive models, they are likely to spin up during their evolution and may reach critical velocity. Upon reaching critical velocity the outer layers of the star become gravitationally unbound (e.g. Krtička et al. 2011, see Section 1.1.4) so it is expected that some mass would be removed until the star spins down below the critical velocity. For numerical reasons it is very difficult to compute the evolution when the star is rotating at critical velocity. To combat this, an implementation was developed for the code (see Georgy et al. 2013b) to calculate the amount of mass that should be removed in order to bring the model back below the critical limit. This is based on the amount of angular momentum that must be lost for subcritical rotation, $\Delta\mathcal{L}_{\rm mec}$, given by:

$$\Delta\mathcal{L}_{\mathrm{mec}} = \Delta M_{\mathrm{mec}} R_{\mathrm{eq}}^2 \Omega_1 \tag{2.35}$$

where R_{eq} is the equatorial radius of the star, Ω_1 is the angular velocity of the first layer of the interior (layer closest to the surface, see Figure 2.1), and ΔM_{mec} is the amount of mass lost during each time step to the disk. The value ΔM_{mec} is thus the decrease in mass required to evolve away from critical rotation. From calculating the change in angular momentum in the star, $\mathcal{L}_{\mathrm{tot}}^{\mathrm{fin}} = \mathcal{L}_{\mathrm{tot}}^{\mathrm{ini}} - \Delta\mathcal{L}_{\mathrm{rad}} - \Delta\mathcal{L}_{\mathrm{mec}}$, this value can be expressed as

$$\Delta M_{\mathrm{mec}} = \frac{\mathcal{L}_{\mathrm{tot}}^{\mathrm{ini}}\left(1 - \frac{\Omega_1^{\mathrm{lim}}}{\Omega_1}\right) + \mathcal{L}_{\mathrm{env}}^{\mathrm{ini}} \frac{\Omega_1^{\mathrm{lim}}}{\Omega_1} \frac{\Delta M_{\mathrm{rad}}}{M_{\mathrm{env}}} - \Delta\mathcal{L}_{\mathrm{rad}}}{R_{\mathrm{eq}}^2 \Omega_1 - \mathcal{L}_{\mathrm{env}}^{\mathrm{ini}} \frac{\Omega_1^{\mathrm{lim}}}{\Omega_1 M_{\mathrm{env}}}} \tag{2.36}$$

where Ω_1^{lim} is the critical angular velocity in the first layer of the interior, ΔM_{rad} is the amount of mass lost through the stellar wind, and M_{env} is the mass in the envelope ($M_{\mathrm{tot}} - M_1$, see Figure 2.1). Using this value, ΔM_{mec}, a mechanical mass-loss rate can be calculated which the code implements when the star reaches critical velocity. If this mechanical mass-loss implementation allows the model to evolve away from the critical limit, the mass-loss rate then switches back to the radiative one.

2.6 Physical Ingredients of the Models

In this section we will discuss the physical inputs and selected initial parameters of the Pop III model grid presented in this work. For this, we use the latest version of GENEC, Origin 2016. Some of the key updates in this version to the previous Origin 2013 are improvements to the angular momentum correction $\mathcal{L}_{\mathrm{corr}}$, and improvements to boundary conditions of the differential equations to be more consistent with other assumptions in the code. These updates have thus improved the accuracy of the rotational treatment in the code.

In this work we have computed zero-metallicity models in the mass range $1.7\,\mathrm{M}_\odot \leq M_{\mathrm{ini}} \leq 120\,\mathrm{M}_\odot$, with a primordial initial composition of $X = 0.7516$ (75.16% hydrogen), $Y = 0.2484$ (24.84% helium), and $Z = 0$ (no heavier elements). The physical ingredients of the models presented in this work are consistent with those of the current Geneva model grids of higher metallicities (Ekström et al. 2012; Georgy et al. 2013a; Groh et al. 2019). This will enable future studies on the impact of initial metallicity on stellar evolution.

The opacities are generated using the OPAL tool (based on Iglesias & Rogers 1996), and are complemented at low temperatures by opacities from Ferguson et al. (2005). The opacity tables used for the models in this work are that of Asplund et al. (2005). The nuclear reaction rates are taken mainly from the NACRE database (Angulo et al.

1999), although some have been redetermined more recently and updated as outlined in Ekström et al. (2012). For example, the rate of the $^{14}N(p,\gamma)^{15}O$ fusion cycle, which controls energy production in the CNO cycle, is taken from Mukhamedzhanov et al. (2003) and is about half of the rate given by NACRE for temperatures below 10^8 K. We also note that the Ne, Na, Mg and Al fusion cycles are not included in H burning in this work. The isotopes included represent the minimum network of isotopes required to ensure the correct energy generation in the model. Therefore the isotopes in GENEC are mainly light elements and not all s-process (see Section 1.3.1) elements are included.

Also described in Ekström et al. (2012) is the nature of the equation of state for models of different initial masses. For models in this work, the equation of state is that of a mixture of perfect gas and radiation, and accounts for partial ionisation in the outermost layers (Schaller et al. 1992) and for the partial degeneracy in the interior in the advanced stages. As outlined in Schaller et al. (1992), partial recombination for H, He, C, O, Ne and Mg is treated in the equation of state, which is done by iteratively solving the Saha equation (see Maeder 2009, Chapter 7) as described in Cox & Giuli (1968). The equation of state is the same throughout the stellar interior, unless the core becomes degenerate at which point the equation of state is updated accordingly within the degenerate region.

Convective zones are determined using the Schwarzschild criterion, and for the MS and the He-burning phases the convective core is extended with an overshoot parameter $\alpha_{\rm ov} = 0.1$ (see Section 2.4). This value for convective overshooting is selected for consistency with the earlier grid papers Ekström et al. (2012); Georgy et al. (2013a); Groh et al. (2019). As described in Ekström et al. (2012), the value $\alpha_{\rm ov} = 0.1$ was selected to fit the empirical width of the MS obtained for solar-metallicity stars in the mass range $M_{\rm ini} = 1.7 - 2.5\,{\rm M}_\odot$. However, we note that in recent research it has been predicted that the overshooting parameter could be higher for massive stars, with $\alpha_{\rm ov} = 0.3 - 0.5$ more closely matching observations of massive MS stars (Castro et al. 2014; Schootemeijer et al. 2019; Higgins & Vink 2019; Martinet et al. 2021).

We compute non-rotating and rotating models, the latter with an initial rotational velocity of $\upsilon_{\rm ini} = 0.4\,\upsilon_{\rm crit}$. This rotational velocity is consistent with the Geneva model grids and based on the peak velocity distribution of young solar-metallicity B-type stars in Huang et al. (2010b). As discussed in Section 1.2.4, recent work indicates that extremely low metallicity stars may have rotated as fast as $\upsilon_{\rm ini} = 0.7\upsilon_{\rm crit}$ in order to reproduce the abundance pattern of some CEMP stars enriched in s-process elements (Choplin et al. 2017; Choplin & Hirschi 2020). Simulations of Pop III star formation (Stacy et al. 2011, 2013) also indicate that these early stars would have formed with significant rotation. Since fast rotating models are challenging to compute due to convergence problems, we defer to future work an extension of our grid to models with higher initial surface rotation. However, we have also produced models at the slower rotational velocity of $\upsilon_{\rm ini} = 0.2\,\upsilon_{\rm crit}$ for certain initial masses. This allows us to investigate the impact of a change of the initial rotation on the results, rather than relying on rotating models at a single velocity versus non-rotators.

We note that we do not consider the effects of magnetic fields in this work, and so our models are differentially rotating. The treatment of rotation follows that of the previous Geneva model grids, having been developed in a series of papers by the Geneva group (Maeder 1997; Meynet & Maeder 1997; Maeder & Zahn 1998; Maeder & Meynet 2000a), as outlined in Section 2.3.

Our models predict that Pop III stars in the mass range 9-120 $\mathrm{M}_\odot$ are hot stars throughout their lifetimes. As has been discussed, theoretical works suggest decreasing mass loss with metallicity (Vink et al. 2001), with zero or negligible mass loss at $Z = 0$ (Krtička & Kubát 2006, 2009). Therefore, our models have no mass loss except when approaching critical rotation. To investigate this we computed non-rotating models using the prescription from Vink et al. (2001) and corresponding models with their mass loss set to zero. It was indeed found that radiative mass loss had a negligible impact on the evolution, even for our most massive model, $M_{\mathrm{ini}} = 120\,\mathrm{M}_\odot$. Upon reaching critical velocity the code implements mechanical mass loss as outlined in Section 2.5.2. In order to effectively evolve our models away from critical velocity we have implemented further mass loss at this stage as will be discussed in Section 2.7.

2.7 Modifications for Population III Stars

Due to the zero-metallicity composition of Pop III stars there are some computational difficulties that arise when modelling their stellar evolution. In this section we discuss modifications to our models in order to solve these computational issues.

2.7.1 Mass Loss

It is numerically difficult to compute stellar evolution models when the star is rotating at critical velocity. As desribed in Section 2.5.2, GENEC employs a mechanical mass-loss prescription to handle mass loss at the critical rotation limit (Georgy et al. 2013b). When using this implementation, the estimated value for ΔM_{mec} brings the model just below the critical limit. However, unlike models at higher metallicities, further mass loss through radiative winds is inefficient in Pop III stars. Therefore, our zero-metallicity models remain close to the critical limit which causes numerical problems. To successfully evolve the models, instead of using mechanical mass loss we assume an averaged mass loss rate of $\dot{M} = 10^{-5}\,\mathrm{M}_\odot\mathrm{yr}^{-1}$ upon reaching the critical limit. For computational convenience, the mass loss rate is kept at that value until the star is sufficiently far from the critical limit. Physically, this could correspond to another process such as pulsational mass loss (see Section 1.2.3 for discussion on pulsational mass loss). We note that this mass loss leads to a difference in the angular momentum profile depending on which mass-loss regime is imposed. This difference arises because rather than having angular momentum loss calculated as $\Delta\mathcal{L}_{\mathrm{mec}}$ (eq. 2.35), as is the case for the mechanical mass-loss implementation (Georgy et al. 2013b), we instead calculate angular momentum loss as $\Delta\mathcal{L}_{\mathrm{rad}}$. This value of $\Delta\mathcal{L}_{\mathrm{rad}}$ is computed in GENEC through the angular momentum loss rate for stellar winds,

$$\dot{\mathcal{L}} = \frac{2}{3}\dot{M}\Omega_1 R_{\mathrm{mean}}^2 \quad \text{with} \quad R_{\mathrm{mean}} = \sqrt{\frac{L}{4\pi\sigma\langle T_{\mathrm{eff}}\rangle^4}} \tag{2.37}$$

where σ is the Stefan-Boltzmann constant. In nature, the difference in these regimes means that GENEC's implementation assumes that material and angular momentum are lost at the equator which would lead to an equatorial decretion disk, while our mass loss regime assumes for simplicity a spherical distribution of angular momentum loss which would form circumstellar material. Having tested both regimes we have found that our averaged mass-loss rate does not affect the overall evolution along the MS and thus is a reasonable approximation. However, we encourage further hydrodynamical studies to explore the behavior of Pop III stars near critical rotation.

2.7.2 Chemical Gradients

Another example of computational difficulty in Pop III models relates to their large compositional gradients. Since these models begin their evolution devoid of metals, when they begin forming elements such as carbon and oxygen this creates strong compositional gradients between the exterior regions and the region where the element has just formed. As this material is mixed outwards towards regions of lower resolution closer to the surface, these sharp gradients make it difficult for the code to find converging solutions between neighbouring layers with and without heavier elements. Calculating the relative abundance of chemical species can also lead to numerical errors, since a metal-free composition can lead to division by a chemical species of which the abundance is zero. Another problem which arises for Pop III models is the dominant energy generation of the H-burning shell, which can also cause computational issues due to the lower resolution of regions above the nuclear burning core. Therefore, particularly in post MS phases where there is nuclear burning above the core and increased chemical enrichment, Pop III models can be very difficult to compute.

There are convergence parameters (GKORM, ALPH) that can be adjusted in the code to increase the accepted deviation in solutions to the stellar structure equations from one time step to the next. However, to ensure that our models are physical these convergence parameters must be kept low for the majority of the evolution, so adjusting them to avoid numerical difficulty only works for brief periods. We subsequently tested increasing the resolution of our models in the layers above the stellar core. This can be done by changing the 'DG' convergence parameters which have options to change the relative variations accepted in pressure P, luminosity L, and chemical abundances of ^{4}He, ^{12}C and ^{16}O, from one layer to the next. Increasing these DG parameters essentially adds layers (increases resolution) in zones where these properties vary by large amounts. Since we are interested in increasing resolution around burning regions and chemically enriched layers we increased the resolution based on the chemical abundances, i.e. increasing DGY, DGC and DGO.

In some cases, increased resolution has the opposite of the desired effect, and makes it harder for the code to converge since there are more layers to compute. To combat this we took another approach by smoothing the chemical gradient between layers. This can be done using a locally weighted smoothing technique in GENEC, which can be used to smooth the mean molecular weight μ, angular velocity Ω or vertical component of the meridional circulation (eq. 2.20) U profiles. To ensure that this smoothing did not lose the physics of the models we tested its impact on the 15 M$_\odot$ rotating model, and found that it successfully smoothed small regions of the μ profile without any macroscopic alterations.

Significant computational difficulty was encountered for the rotating models in our grid towards the end of the He-burning phase. Again, this results from the large chemical gradients in the outer layers of the stellar interior, where nuclear burning products have been transported through rotational mixing. In the code, there are some modifications to enable modelling the evolution of Pop III stars, which are triggered by setting the physics parameter Pop III=1. For example, the nuclear reactions are modified to allow the star to undergo He burning at the early MS to produce the necessary CNO elements (see Section 1.2.5), and the threshold for trace elements is lowered (from 10^{-9} to 10^{-75}) to assist with CNO ignition and chemical mixing. These modifications serve an important purpose for the main burning phases of the star's life. However in late He burning, as the stellar interior becomes more polluted by metals, they are no longer necessary for massive models, and in fact can make computations more difficult. Therefore, one solution for our models was to switch off this Pop III setting and allow the code to compute the rest of the evolution as it would for low-metallicity stars. In some cases, for the very end stages of He burning we also turned off diffusion in the more massive rotating models. We do not expect this to have a significant effect on our results as in this work we focus mainly on the evolution of these stars throughout the MS and He-burning phases.

2.8 Ionizing Photon Production

Having computed our models we decided to use our data on the evolution of their surface properties to predict their ionizing photon production rates. In Section 1.3.2 the importance of the first stars in understanding the epoch of reionization is discussed. To understand how the first stars contributed to the reionization of the Universe we must

Figure 2.6: Schematic of solid angle used to calculate radiative flux, shown in spherical coordinates i.e. $d\Omega = sin\theta\, d\theta\, d\phi$. Courtesy of I. Boian.

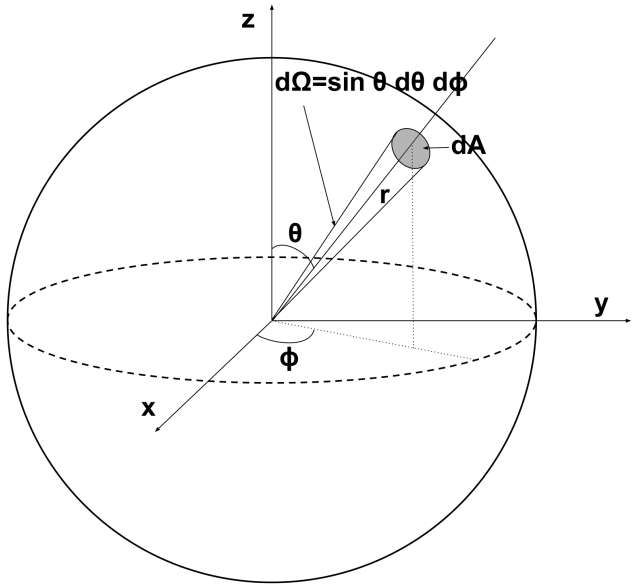

first have detailed predictions for their ionizing photon production. In this section we discuss how we compute the ionizing photon production of our models, and how we use this to predict the number of ionizing photons produced by populations of zero-metallicity stars.

2.8.1 Radiative Flux

To calculate the number of ionizing photons produced by the models during their lifetimes, we must first calculate the radiative flux produced at each time step. In the interest of saving computational time we fit a blackbody spectrum to obtain the radiative flux rather than computing radiative transfer models at each time step. For this we take the value of $T_{\rm eff}$ at each time step for each model and input it to the Planck function for a range of UV wavelengths, λ, to obtain the blackbody radiation, B_λ.

$$B_\lambda = \frac{2hc^2/\lambda^5}{e^{hc/\lambda k T_{\rm eff}} - 1} \tag{2.38}$$

From this we can now determine the radiative flux, F_λ, by integrating over the solid angle, dΩ.

$$F_\lambda\, d\lambda = \int B_\lambda\, d\lambda \cos\theta\, d\Omega = \int_{\phi=0}^{2\pi}\int_{\theta=0}^{\pi} B_\lambda\, d\lambda \cos\theta \sin\theta\, d\theta\, d\phi \tag{2.39}$$

The geometry of the solid angle dΩ is illustrated in Figure 2.6, which shows how dΩ can be expressed in terms of the polar coordinates θ and ϕ. Evaluating this integral and taking the emergent radiative flux leaves us with F_λ=πB_λ, which can then be used to calculate the ionizing photon production rates.

2.8.2 Ionizing Photon Production Rates

In Section 1.3.2 we defined ionizing photons as photons with enough energy to split hydrogen into electrons and photons. We also discussed how at higher energies photons are capable of ionizing He I and He II. In this work we are interested in predicting the number of photons produced by Pop III stars which are capable of ionizing H, He I and He II. The production rates of these ionizing photons are calculated by integrating across the radiative flux energetic enough to ionize these chemical species. Therefore, we determine the ionizing photon production rates by integrating below the threshold wavelengths for photons capable of ionizing H, He I and He II. These wavelengths are 912 Å, 504 Å, and 228 Å for H, He I, and He II respectively. The full calculation for calculating the ionizing photon production rates, Q_{i}, in photons s^{-1} (Tumlinson & Shull 2000; Schaerer 2002) is

$$Q_{\mathrm{i}} = \frac{4\pi}{hc} R_{\star}^{2} \int_{0}^{\lambda_i} \lambda \, F_{\lambda} \, d\lambda \tag{2.40}$$

where $R_{\star}$ is the stellar radius. The integration of the radiative flux is illustrated in Figure 2.7, for four of our models on the ZAMS. These include the non-rotating $20\,\mathrm{M}_{\odot}$, $40\,\mathrm{M}_{\odot}$, $60\,\mathrm{M}_{\odot}$, and $120\,\mathrm{M}_{\odot}$ models. The radiative flux plotted for each model is therefore calculated from the effective temperature, T_{eff}, of each model on the ZAMS (see eqs. 2.38 and 2.39), while the surface luminosity on the ZAMS, with T_{eff}, determines the stellar radius in eq. 2.40. Shown in Figure 2.7 are the threshold wavelengths, λ_{H}, λ_{HeI} and λ_{HeII}, for ionizing H, He I, and He II. Therefore, the green shaded regions give the integrated radiative flux required to calculate the number of He II ionizing photons, the blue and green shaded regions give the He I ionizing photons, and the grey, blue and green shaded regions give the H ionizing photons.

It is clear from the figure that more massive models produce more ionizing photons due to their higher luminosities and temperatures. In general, increasing the luminosity increases the amplitude of the spectrum while increasing temperature shifts the spectrum to shorter wavelengths (higher energies). We can see from Figure 2.7 that the calculation of H ionizing photons is strongly affected by the change in amplitude of the spectrum, while He II ionizing photons are more impacted by the peak of the spectrum moving to shorter wavelengths. It is expected then that He II ionizing photons will be less impacted by changes in luminosity and more impacted by changes in surface temperature. We discuss this further in Chapter 5.

We have shown how the ionizing photon production rates at each time step in the evolution can be calculated using eq. 2.40. In order to determine the total ionizing photons produced by the models we then integrate Q_i across the stellar lifetime. This gives us the total ionizing photons produced, N_i,

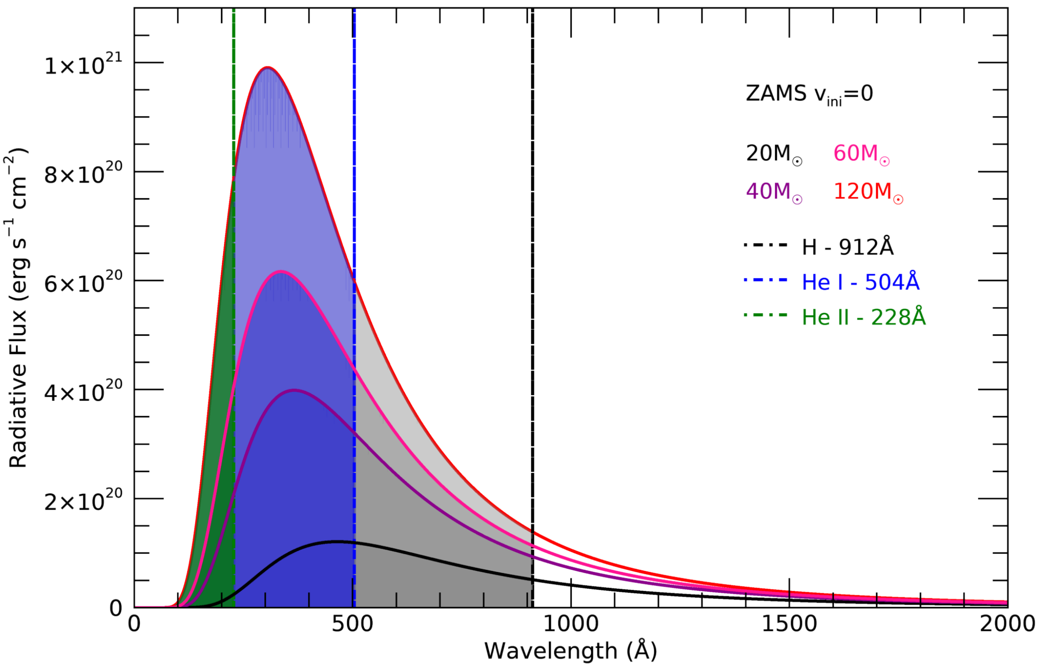

Figure 2.7: Calculating the ionizing photon production rates $Q_\mathrm{H}, Q_\mathrm{HeI}, Q_\mathrm{HeII}$, from the radiative flux of the non-rotating 20 $\mathrm{M}_\odot$, 40 $\mathrm{M}_\odot$, 60 $\mathrm{M}_\odot$ and 120 $\mathrm{M}_\odot$ models on the ZAMS, as indicated by the legend. Black, blue and green dashed lines represent the threshold wavelengths for H, He I, and He II respectively. The shaded regions represent the integrated flux, see eq. 2.40.

$$N_\mathrm{i} = \int_0^\tau Q_\mathrm{i}\, dt \tag{2.41}$$

where τ is the stellar lifetime. Through changing the integration limit τ this equation can also be used to determine the number of ionizing photons produced up to a given point in the evolution.

2.8.3 Modelling the Initial Mass Function

In the previous section we discussed how we calculate the ionizing photon production of individual stars from our Pop III model grid. In this section and Section 2.8.4 we now discuss how we determine the ionizing photon production of populations of these stars.

To calculate the ionizing photon production of a stellar population, we first need to know how many stars of different initial masses there are in the population. This allows us to use our predictions for the ionizing photon production of individual Pop III stars, and scale their contribution to the population accordingly.

To determine the number of stars formed at various initial masses in a population, we use the initial mass function (IMF; Section 1.2.2) of the form

$$\xi(M) = \xi_0 M^{-\alpha} \tag{2.42}$$

where α is the slope of the IMF, and ξ_0 is a factor that depends on the total mass of the population. Through varying the slope, α, of the IMF we can produce different populations where different initial masses will dominate ionizing photon production. The slope values we consider in this work vary from $\alpha = -1$ to $\alpha = 2.35$ to cover a range of potential IMFs from top-heavy ($\alpha < 0$ Greif et al. 2011; $\alpha < 2$ Bromm 2012) to the Salpeter IMF ($\alpha = 2.35$; Salpeter 1955). Within the slope range $-1 \leq \alpha \leq 2.35$ we include the IMF slope $\alpha = 0.17$, which is found in Stacy & Bromm (2013) (discussed in Section 1.2.2), to represent the IMF for a Pop III stellar population.

For consistent comparisons of populations with different IMF slopes in our investigation of the ionizing photon production of zero-metallicity stellar populations, we keep the total stellar mass of the population constant. To do this we first find an initial IMF, $\xi(M)$, using an arbitrary value for ξ_0. We then determine the total mass of this test IMF with the integral

$$\mathrm{M}_{\mathrm{tot}} = \int_{M_{\mathrm{min}}}^{M_{\mathrm{max}}} M_{\mathrm{ini}} \xi(M)\, dM \tag{2.43}$$

where M_{min} and M_{max} are the minimum and maximum masses of the population. From this value for the total mass of the test IMF population we can determine a mass factor, f_{mass}, which is the fraction of the desired total mass to the current total mass. By multiplying this factor by the IMF, $\xi(M)$, we thus normalise the total stellar mass of each population of varying IMF slope. For most of this work we take a total mass of the population of $\mathrm{M}_{\mathrm{tot}} = 10^6\,\mathrm{M}_\odot$. This value is increased to $10^8\,\mathrm{M}_\odot$ when testing the effect of varying the minimum and maximum masses of the population.

2.8.4 Ionization from Stellar Populations

To determine the total number of ionizing photons produced by a stellar population, N_{pop}, we then use the following equation,

$$N_{\mathrm{pop}} = \int_{M_{\mathrm{min}}}^{M_{\mathrm{max}}} \int_0^t Q_{\mathrm{i}} \xi(M)\, dt\, dM \tag{2.44}$$

For most of this work we assume a minimum mass (M_{min}) of $9\,\mathrm{M}_\odot$, and a maximum mass (M_{max}) of $120\,\mathrm{M}_\odot$. We also test the effect of decreasing M_{min} on the ionizing photons produced using our intermediate mass models of $M_{\mathrm{ini}} = 1.7$-$7\,\mathrm{M}_\odot$. Similarly, we test the effect of increasing M_{max} by using newly computed zero-metallicity models of initial masses $M_{\mathrm{ini}} = 180, 250, 300, 500\,\mathrm{M}_\odot$ (Martinet et al., 2021 in prep.). These very massive star models are non-rotating, and unlike our Pop III grid models use opacity tables of Grevesse & Noels (1993) rather than Asplund et al. (2005), and use the Ledoux criterion for convective boundaries with convective overshooting of $\alpha_{\mathrm{ov}} = 0.2$. We note that these massive stars have very large convective cores and thus the differences in the implementation of the physics with respect to the models in this work are not very relevant here. The very massive star models are also run only to the end MS, so we assume that the total photons produced by the end of the MS account for 90% of the total photons produced by the end of the evolution. This assumption gives an upper estimate to the ionizing photons produced given that models tend to have lower effective temperatures in post MS phases.

The time interval for integration in eq. 2.44, t, refers to the age of the population. Since stellar lifetime increases with decreasing initial mass M_{ini}, t must be at least the lifetime of the smallest initial mass model in order for all of the stars in the population to have produced their total ionizing photons. Therefore, if considering a population without rotation where $M_{\text{min}} = 9\,\text{M}_{\odot}$, the time interval must be $t = 20\,\text{Myr}$, the lifetime of the non-rotating $9\,\text{M}_{\odot}$ model, for the population to have produced its total ionizing photons after a single starburst, i.e. $N_{\text{pop}} = \int_{M_{\text{min}}}^{M_{\text{max}}} N_{\text{i}}\,\xi(M)\,dM$. However, we can also vary the value of t to study the evolution of the ionizing photons produced by the population.

Chapter 3

A New Grid of Geneva Stellar Evolution Models with Rotation for Population III stars

In the following three chapters we present the results of our work on the effects of rotation on zero-metallicity stars. In this chapter we present our Geneva stellar evolution grid of Pop III stars from $1.7\,M_\odot$ to $120\,M_\odot$, with and without rotation. The physical ingredients of the models are described in Section 2.6, and background to how they are produced using GENEC has been detailed extensively throughout Chapter 2. This model grid has been published in Murphy et al. (2021a), and electronic tables of the models are publicly available*. These electronic tables are presented in a format which is consistent with the higher-metallicity grids (Ekström et al. 2012; Georgy et al. 2013a; Groh et al. 2019) and are split into 400 selected data points corresponding to significant stages in the evolution to facilitate interpolation of the tracks. For further details of the format of the tables see Ekström et al. (2012).

Later, in Chapter 4, we present the results of our analysis of the massive stars within our grid from $9\,M_\odot$ to $120\,M_\odot$, including the effects of rotation on stellar structure and metal enrichment. Before we discuss those findings, this chapter describes our full grid of Pop III stars. We summarise the evolution of surface properties, and values such as initial mass and rotational velocity at key evolutionary phases.

---

*See https://obswww.unige.ch/Research/evol/tables_grids2011/

3.1 Models without Rotation

The stellar evolution tracks for non-rotating models are shown in Figure 3.1. As expected, the effective temperature, $T_{\rm eff}$, and luminosities at the ZAMS increase with increasing mass. Considering models in the mass range $9\,{\rm M}_{\odot} \leq M_{\rm ini} \leq 120\,{\rm M}_{\odot}$ first, models with $M_{\rm ini} \geq 30\,{\rm M}_{\odot}$ show a qualitative evolution during the MS that resembles that of higher metallicity models (Ekström et al. 2012; Georgy et al. 2013a; Groh et al. 2019). In these models, the surface properties of the star during H burning steadily evolve to higher luminosities and cooler surface temperatures as the stellar envelope expands. As can be observed from Figure 3.1, at the end of H burning stars with $M_{\rm ini} \geq 30\,{\rm M}_{\odot}$ will have cooled to approximately $log(T_{\rm eff}/{\rm K}) = 4.7$.

Similarly to previous works (e.g. Ekström et al. 2008), models with $M_{\rm ini} = 9 - 20\,{\rm M}_{\odot}$ spend a significant fraction of their MS lifetime burning H with only p-p chain reactions, since their central temperature is not yet high enough for producing C and O through the triple-α reaction (see Section 1.2.5). The star keeps contracting until this central temperature is reached and the CNO cycle begins. This contracting phase is visible in the HR diagram as the evolution towards higher $T_{\rm eff}$ from the ZAMS (Figure 3.1). The fraction of the MS that a model spends in the contracting phase decreases with increasing initial mass. This is because models of higher initial mass have higher central temperatures and therefore produce CNO elements earlier in their evolution than less massive models. For the same reason, models with $M_{\rm ini} \geq 30\,{\rm M}_{\odot}$ do not experience this contracting phase since they have cores that are hot enough to produce the C, N, O catalysts immediately. It can also be noted from Figure 3.1 that Pop III stars have smoother transitions between burning phases than higher-metallicity stars (Ekström et al. 2008; Marigo et al. 2001). This is evident in Figure 3.1 from the near overlap of end H-burning and start He-burning phases for models with initial masses $M_{\rm ini} = 9 - 120\,{\rm M}_{\odot}$.

Also included in Figure 3.1 are the intermediate mass models in the mass range $1.7\,{\rm M}_{\odot} \leq M_{\rm ini} \leq 7\,{\rm M}_{\odot}$. The non-rotating intermediate mass models spend even longer than the massive models in the contracting phase where only the p-p chain reactions contribute to the nuclear energy production. In fact they spend the majority of the MS contracting. However, this contracting phase is less defined for lower initial masses as the CNO-cycle becomes less important for maintaining hydrostatic equilibrium. Stars of low initial mass have lower gravitational pressure than massive stars, therefore p-p chain reactions are a sufficient source of energy generation for core H burning, and are thus less affected by a lack of CNO elements. There is also a distinctive loop feature at the beginning of the He-burning phase which is prominent in these models. This feature occurs for models with initial masses $M_{\rm ini} \leq 20\,{\rm M}_{\odot}$ as will be discussed in Section 4.1. We also note that none of the intermediate mass non-rotators become red giants before the end of the core He-burning phase. While the key focus of this work is the effect of rotation on massive Pop III models, these intermediate mass models ($M_{\rm ini} = 1.7 - 7\,{\rm M}_{\odot}$)

complement our grid and will be very useful for future work, for example in population synthesis.

3.2 Models with Rotation

The stellar evolution tracks for both non-rotating and rotating models are shown in Figure 3.2. The intermediate mass models are greatly impacted by rotation. They become much more luminous, with the $1.7\,\mathrm{M}_\odot$ model increasing in luminosity by ~ 1 dex and reaching the same luminosity as the rotating $3\,\mathrm{M}_\odot$ model. Rotating models also evolve to much lower T_{eff} than non-rotating ones, favouring red giant formation. This presents interesting possibilities for their evolution, especially if they are part of a binary system as a large radius would favour interaction with a companion.

Probably the most significant result from Figure 3.2 for massive stars is the variability in the behaviour of rotating models during He burning. Unlike non-rotators, which show a trend of larger decrease of T_{eff} with increasing mass, rotating models seem to experience a variety of evolutionary behaviour on the HR diagram with changing initial mass. This challenges us to question what drives the evolution along the HR diagram, or more specifically, what evolutionary behaviour during He burning dominates the evolution of surface properties. We will discuss this in the following chapter, Chapter 4, where we present the results of our analysis of the model grid.

3.3 Summary of Model Grid

In Table 3.1 we present a summary of our models at the ZAMS, the end of the MS (TAMS), and the end of the He-burning phase. We show key evolutionary properties such as the rotational velocity at the equator, υ_{eq}, the surface He abundance, Y_{surf}, as well as the MS and He-burning lifetimes, τ_{H} and τ_{He}. From the table we can already see the impacts of rotation on stellar lifetime and surface enrichment. Models with rotation have longer MS and He-burning lifetimes, and have higher He surface abundances due to rotational mixing.

We also see from Table 3.1 that the evolution of the rotational velocity varies significantly at different initial masses. This implies that the effects of rotation on zero-metallicity stars and their stellar structure is complex, which is consistent with the rotational effects on surface properties illustrated in Figure 3.2. Therefore, to understand how rotation affects the evolution of these stars we need to have a detailed understanding of the evolution of their interior structure, with and without rotation. This is the main aim of our analysis of the stellar evolution grid, the results of which are presented in the following chapter.

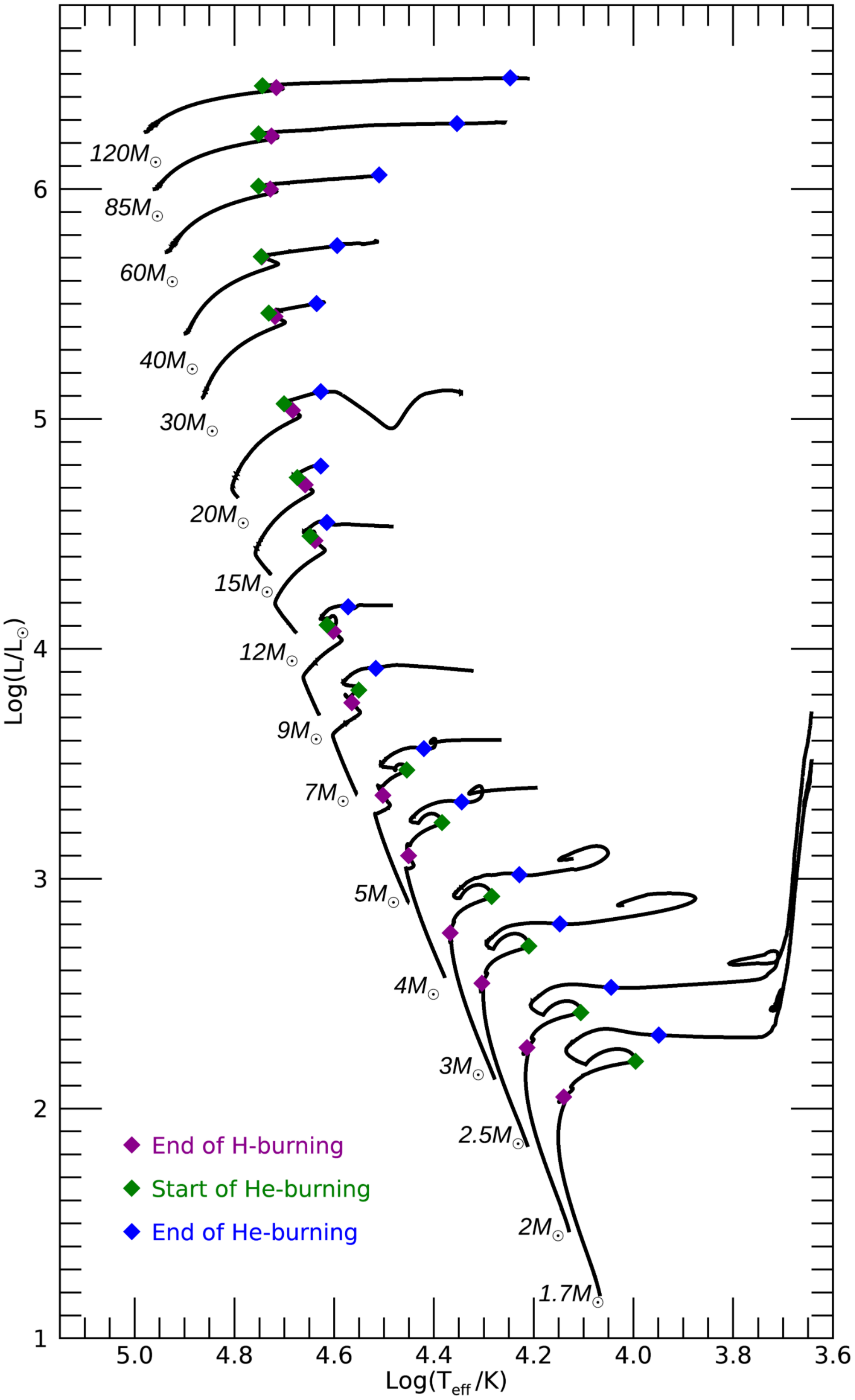

Figure 3.1: Evolutionary tracks of non-rotating models in the mass range $1.7\,M_\odot \leq M_{ini} \leq 120\,M_\odot$. Key evolutionary stages are given in the legend.

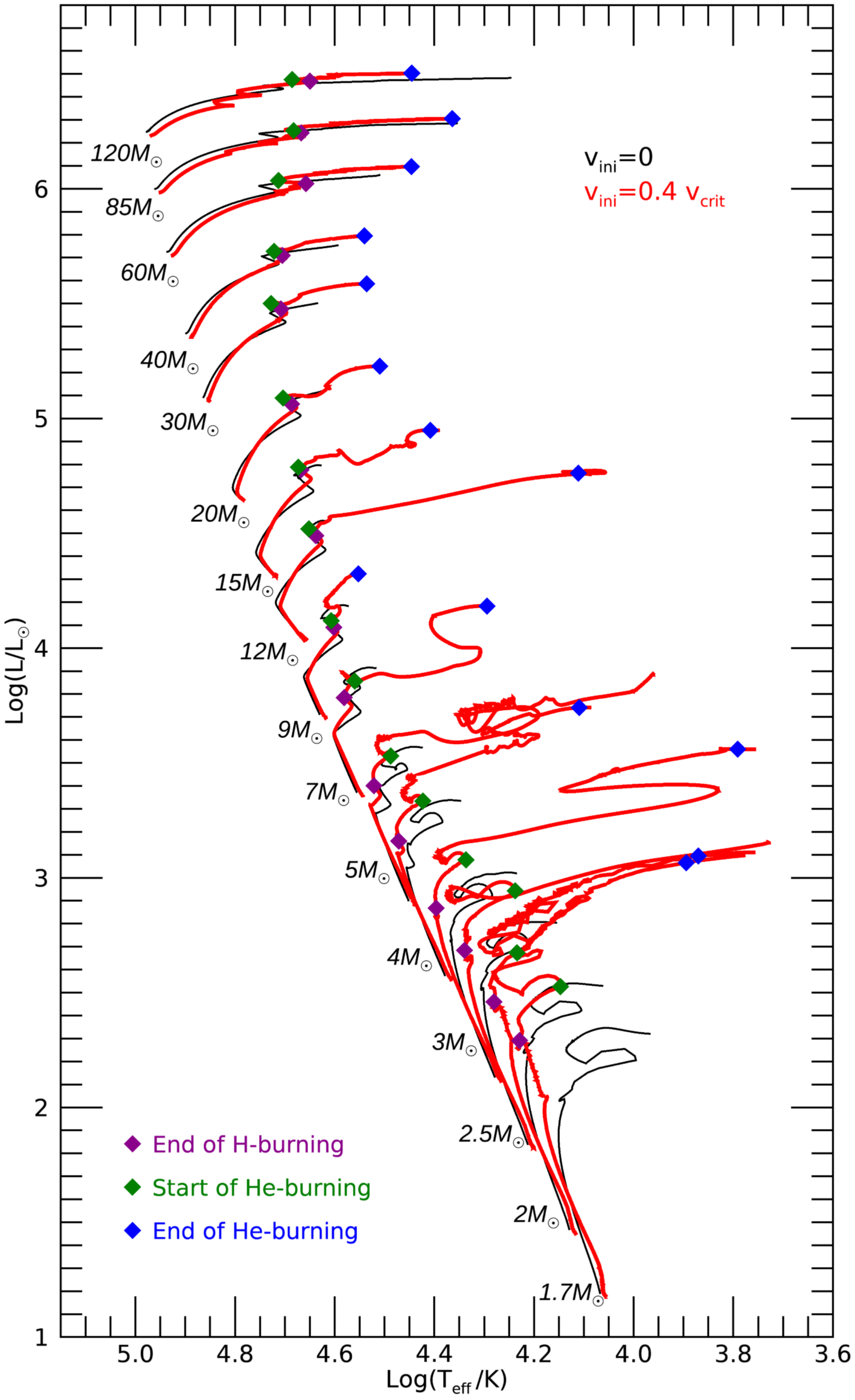

Figure 3.2: Similar to Figure 3.1 but including comparison between evolutionary tracks of non-rotating models (black) and rotating models with initial rotational velocity $\upsilon_{\rm ini} = 0.4\upsilon_{\rm crit}$ (red).

Table 3.1: Geneva Pop III grid summary. MS and He-burning lifetimes are given by τ_{H} and τ_{He} respectively. For each phase we quote υ_{eq} (velocity at the equator) and Y_{surf} (He mass fraction at the surface). Models whose τ_{He} is marked with an asterisk have not completed He burning and the values given are those at the final timestep. For the rotating 2.5 $\mathrm{M}_{\odot}$ model the final timestep is at Y_{c}=0.36 (central He mass fraction), for the rotating 5 $\mathrm{M}_{\odot}$ model the final timestep is at Y_{c}=0.45, and the value of τ_{He} refers to the time since the start of He burning in these cases.

ZAMS			End MS					End He burning				
M_{ini} ($\mathrm{M}_{\odot}$)	$\upsilon_{\mathrm{ini}}/\upsilon_{\mathrm{crit}}$	υ_{eq} (km/s)	τ_{H} (yrs)	M ($\mathrm{M}_{\odot}$)	υ_{eq} (km/s)	$\upsilon_{\mathrm{eq}}/\upsilon_{\mathrm{crit}}$	Y_{surf}	τ_{He} (yrs)	M ($\mathrm{M}_{\odot}$)	υ_{eq} (km/s)	$\upsilon_{\mathrm{eq}}/\upsilon_{\mathrm{crit}}$	Y_{surf}
1.7	0	0	1.0593e+09	1.7	0	0	0.2484	5.6226e+07	1.7	0	0	0.2484
2	0	0	6.2404e+08	2	0	0	0.2484	3.6087e+07	2	0	0	0.2484
2.5	0	0	3.1229e+08	2.5	0	0	0.2484	1.9922e+07	2.5	0	0	0.2484
3	0	0	1.8624e+08	3	0	0	0.2484	1.3277e+07	3	0	0	0.2484
4	0	0	8.8953e+07	4	0	0	0.2484	7.7600e+06	4	0	0	0.2484
5	0	0	5.3419e+07	5	0	0	0.2484	5.8460e+06	5	0	0	0.2484
7	0	0	2.6935e+07	7	0	0	0.2484	3.4315e+06	7	0	0	0.2484
9	0	0	1.7710e+07	9	0	0	0.2484	1.9080e+06	9	0	0	0.2484
12	0	0	1.7857e+07	12	0	0	0.2484	1.0795e+06	12	0	0	0.2484
15	0	0	1.2986e+07	15	0	0	0.2484	7.9322e+05	15	0	0	0.2484
20	0	0	9.5096e+06	20	0	0	0.2484	5.7343e+05	20	0	0	0.2484
30	0	0	6.1268e+06	30	0	0	0.2484	4.1925e+05	30	0	0	0.2484
40	0	0	4.7717e+06	40	0	0	0.2484	3.5607e+05	40	0	0	0.2484
60	0	0	3.6682e+06	60	0	0	0.2484	3.0269e+05	60	0	0	0.2484
85	0	0	3.0759e+06	85	0	0	0.2484	2.7141e+05	85	0	0	0.2484
120	0	0	2.7362e+06	120	0	0	0.2484	2.5342e+05	120	0	0	0.2484
1.7	0.4	187	1.3767e+09	1.7	305	0.78	0.3391	3.3354e+07	1.7	11.9	0.16	0.3556
2	0.4	199	8.0525e+08	2	340	0.79	0.3327	2.3438e+07	2	12	0.15	0.3398
2.5	0.4	221	3.9862e+08	2.5	402	0.82	0.3192	2.5540e+07*	2.5	8.1	0.10	0.3228
3	0.4	236	2.3540e+08	3	396	0.73	0.3090	1.6905e+07	3	21	0.27	0.3239
4	0.4	267	1.0906e+08	4	351	0.57	0.3014	9.6393e+06	4	58.4	0.34	0.3148
5	0.4	291	6.3927e+07	5	322	0.48	0.2967	9.9270e+06*	5	0.3	0.00	0.3009
7	0.4	330	3.1744e+07	7	287	0.40	0.2937	6.7908e+06	7	76.2	0.27	0.3137
9	0.4	372	2.0910e+07	9	274	0.38	0.2858	2.4597e+06	9	60.3	0.11	0.2861
12	0.4	371	1.9722e+07	12	292	0.41	0.2866	2.4166e+06	12	31.6	0.19	0.3122
15	0.4	427	1.4970e+07	15	289	0.40	0.2811	1.2313e+06	15	67.5	0.19	0.2878
20	0.4	526	1.0712e+07	20	309	0.41	0.2765	9.7126e+05	20	192	0.44	0.2767
30	0.4	527	6.9983e+06	30	359	0.47	0.2769	4.9810e+05	30	297	0.62	0.2783
40	0.4	562	5.3330e+06	40	445	0.57	0.2677	4.2979e+05	40	340	0.51	0.2688
60	0.4	613	4.0619e+06	59.8	657	0.87	0.2648	3.6082e+05	59.7	302	0.75	0.2689
85	0.4	659	3.2966e+06	84.1	551	0.70	0.2654	3.0919e+05	84	269	0.73	0.2689
120	0.4	708	2.8885e+06	116.5	473	0.64	0.3026	2.5413e+05	116.5	274	0.59	0.3114

Chapter 4

The Effects of Rotation on the Evolution of Population III Stars: Surface Properties, Critical Rotation and Metal Enrichment

In this chapter we discuss the analysis of our Geneva stellar evolution grid of Pop III stars, which is presented in Chapter 3. This analysis covers models with initial masses in the range $9\,\mathrm{M}_\odot \leq M_{\mathrm{ini}} \leq 120\,\mathrm{M}_\odot$, with and without rotation. We investigate the evolution of their surface properties and interior structure, and study how their chemical enrichment occurs. By investigating these properties in detail for rotating and non-rotating models we learn how rotation impacts the evolution of zero-metallicity stars. The work presented here has been published in Murphy et al. (2021a).

4.1 Evolution on the HR Diagram

Similarly to Figure 3.1, the stellar evolution tracks for non-rotating models in the mass range $9\,\mathrm{M}_\odot \leq M_{\mathrm{ini}} \leq 120\,\mathrm{M}_\odot$ are shown in Figure 4.1. Unlike Figure 3.1, here we present only the massive models so that their features can be more clearly seen to aid the reader throughout the text. As described in Chapter 3, models with $M_{\mathrm{ini}} \geq 30\,\mathrm{M}_\odot$ show a qualitative evolution during the MS that resembles that of higher metallicity

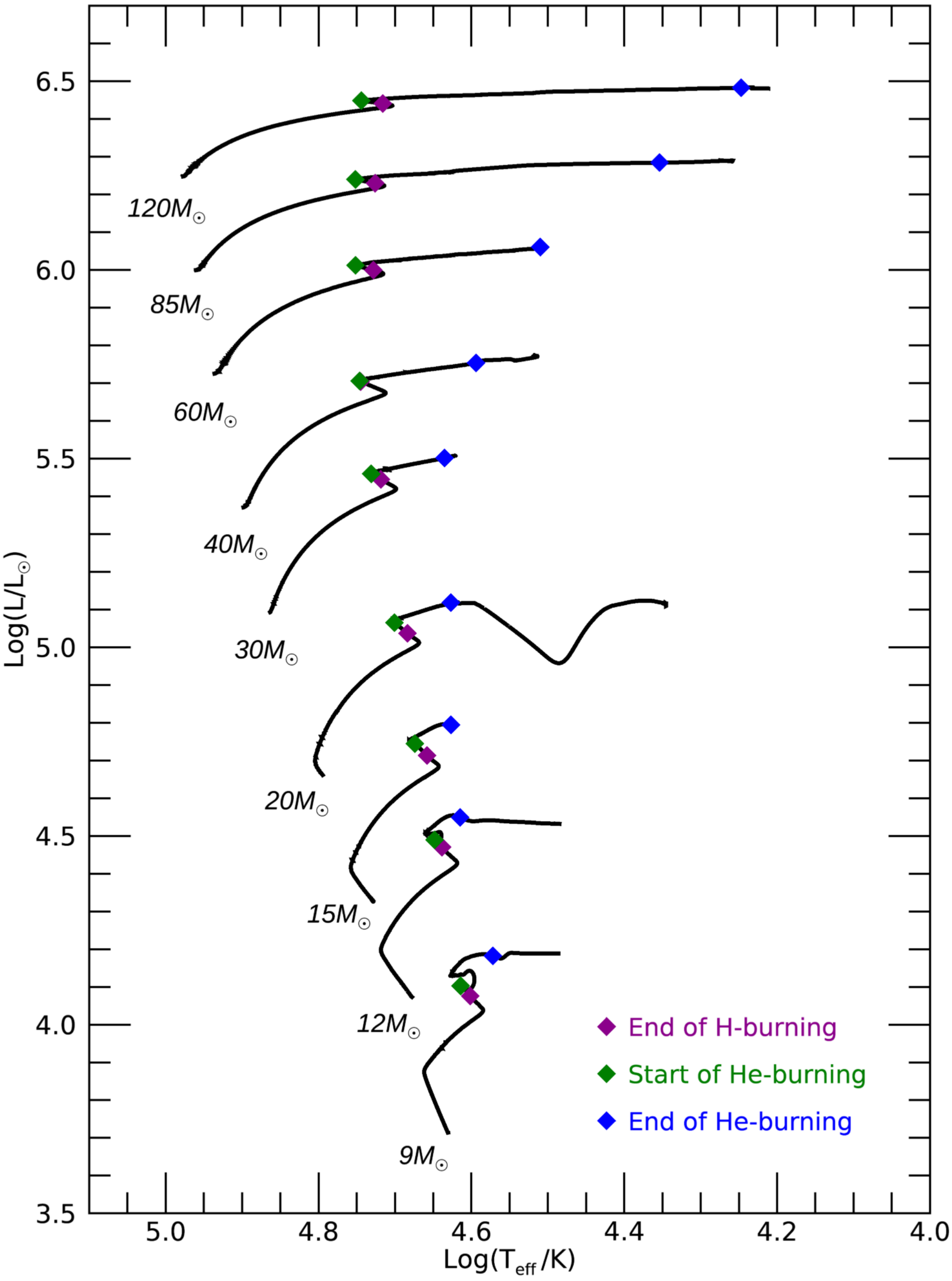

Figure 4.1: Evolutionary tracks of non-rotating models in the mass range $9\,M_\odot \leq M_{ini} \leq 120\,M_\odot$. Key evolutionary stages are given in the legend. This figure is a zoom-in of Figure 3.1, placed here to allow the reader to more easily follow the surface evolution of our massive models as described in the text.

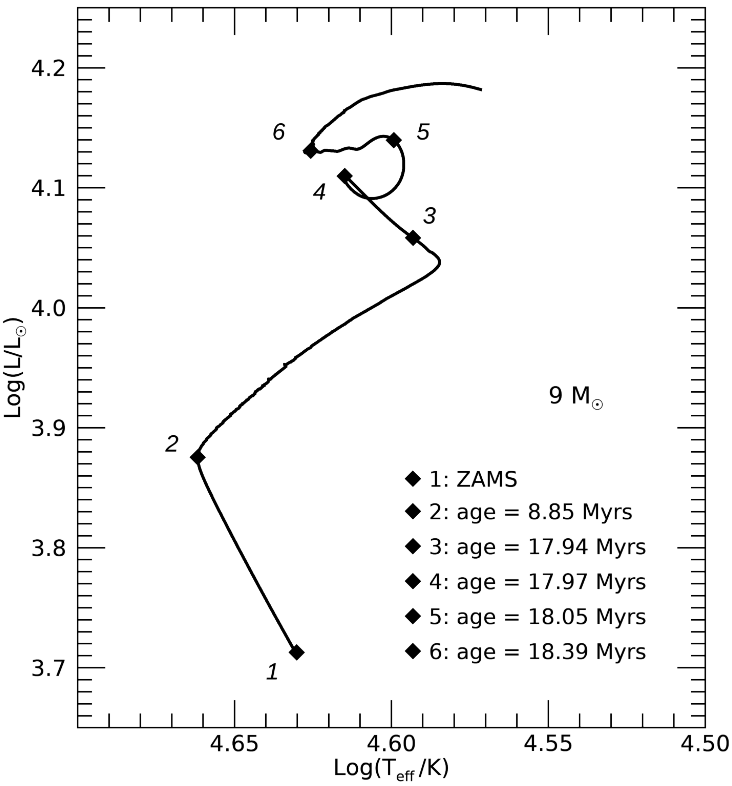

Figure 4.2: Evolution of the non-rotating $9\,\mathrm{M}_\odot$ model. Selected key stages of the evolution are indicated. Stages 1 and 2 illustrate the contracting phase during H-burning where stage 1 marks the ZAMS and stage 2 marks where the CNO cycle becomes dominant, ie. $\epsilon_{\rm CNO} > \epsilon_{\rm pp}$. Stages 3-6 are used to understand the evolution from the late MS through to early He-burning, they correspond to the interior structure profiles in Figures A.1, A.3 and A.4.

models (Ekström et al. 2012; Georgy et al. 2013a; Groh et al. 2019), and models with $M_{\rm ini} \leq 20\,\mathrm{M}_\odot$ experience a contracting phase at the start of the MS due to their lack of CNO elements. The star contracts until the CNO cycle begins, corresponding to the evolution towards higher $T_{\rm eff}$ from the ZAMS (Figure 4.1 and stages 1-2 in Figure 4.2). For models of higher initial masses $M_{\rm ini} \geq 30\,\mathrm{M}_\odot$, their core is hot enough to produce CNO elements immediately and so they do not experience this contracting phase. Also described in Chapter 3, is that Pop III stars have smoother transitions between burning phases than higher-metallicity stars which is evident from the near overlap of end H-burning and start He-burning phases for models with initial masses $M_{\rm ini} = 9 - 120\,\mathrm{M}_\odot$ (Figure 4.1).

Non-rotating models in the range 9-20$\,\mathrm{M}_\odot$ show a distinctive feature at the start of He burning (loop next to the green point in Figure 4.1, more clearly seen in Figure 4.2) that are relevant since they reflect changes to the abundance profile and core size, which affects the subsequent evolution during He burning, and in particular the final $T_{\rm eff}$. We use the non-rotating $9\,\mathrm{M}_\odot$ model to illustrate the change in surface properties that gives rise to this distinctive feature (stages 4-6 in Figure 4.2). This model shows a sharp decrease in $T_{\rm eff}$ immediately after He ignition (stages 4-5), followed by an increase in $T_{\rm eff}$ (stages 5-6). When H is depleted in the core the continuing contraction of the star (stages 3-4) ignites the H shell leading to a boost in luminosity at the surface. He-core burning then begins and there is a further boost to the luminosity (stages 4-5). Our models show that just prior to He-core ignition when the H-burning shell dominates, the now inactive core is strongly contracting while the envelope expands due to the energy boost from this H shell (stages 4-5). This puts the star out of thermal equilibrium. When He-core burning begins the star regains thermal equilibrium (stages 5-6). The combined effects of the H-burning shell, He-core contraction, He-core ignition, and the timescale to regain thermal equilibrium cause the complex $T_{\rm eff}$ evolution at the transition from H to He burning. We discuss this in further detail in Appendix A.

Once the star is in thermal equilibrium it evolves towards lower $T_{\rm eff}$ during He-core burning (Figure 4.1). A clear trend with initial mass can be seen for the end He burning position of non-rotating models on the HR diagram. For less massive models there is little change in $T_{\rm eff}$ during the He-burning phase, however, as initial mass increases it can be seen that there is a larger decrease in $T_{\rm eff}$ during this evolutionary phase. This trend is also observed at higher metallicities (e.g. Ekström et al. 2012), and may be caused by the high luminosities of more massive stars which can drive envelope expansion (e.g. Gräfener et al. 2012, discussed further in Section 5.5.4).

Another striking feature that can be observed in Figure 4.1 is the large luminosity dip after He burning in the $20\,{\rm M}_\odot$ model. This is caused by sudden changes in energy generation, as we will discuss in Sections 4.2.2 and 4.4.2, referred to as the CNO boost. We note also that the models have not all been evolved to the same final evolutionary stage due to computational difficulties (see Section 2.7.2) reaching the pre-SN stages. The final evolutionary stages reached by massive models in the grid are given in Table 4.1.

4.2 Effects of Rotation

Having discussed key features of Pop III evolution without rotation, we will now look at how rotation affects the evolution of these models.

4.2.1 HR Diagram

The stellar evolution tracks for both non-rotating and rotating models in the mass range $9\,{\rm M}_\odot \leq M_{\rm ini} \leq 120\,{\rm M}_\odot$ are shown in Figure 4.3. Again this is similar to Figure 3.2 but shows only the massive models so that we can observe their evolutionary tracks more clearly. Looking at Figure 4.3 we see that rotating models begin H burning with a lower luminosity than non-rotating models. This is because models with rotation begin their evolution with smaller cores, which is evident from Figure 4.4 (red dashed lines). Due to the centrifugal force in differentially rotating models, the effective gravity of their cores is lower (see Section 1.1.4). This leads to a steeper temperature gradient near the stellar centre, and since the convective core size is determined by the temperature profile of the model, their initial core size is lower than models without rotation. There is a general trend for the MS where rotating models become more luminous than non-rotating models, despite starting with lower luminosities as described above. This growth

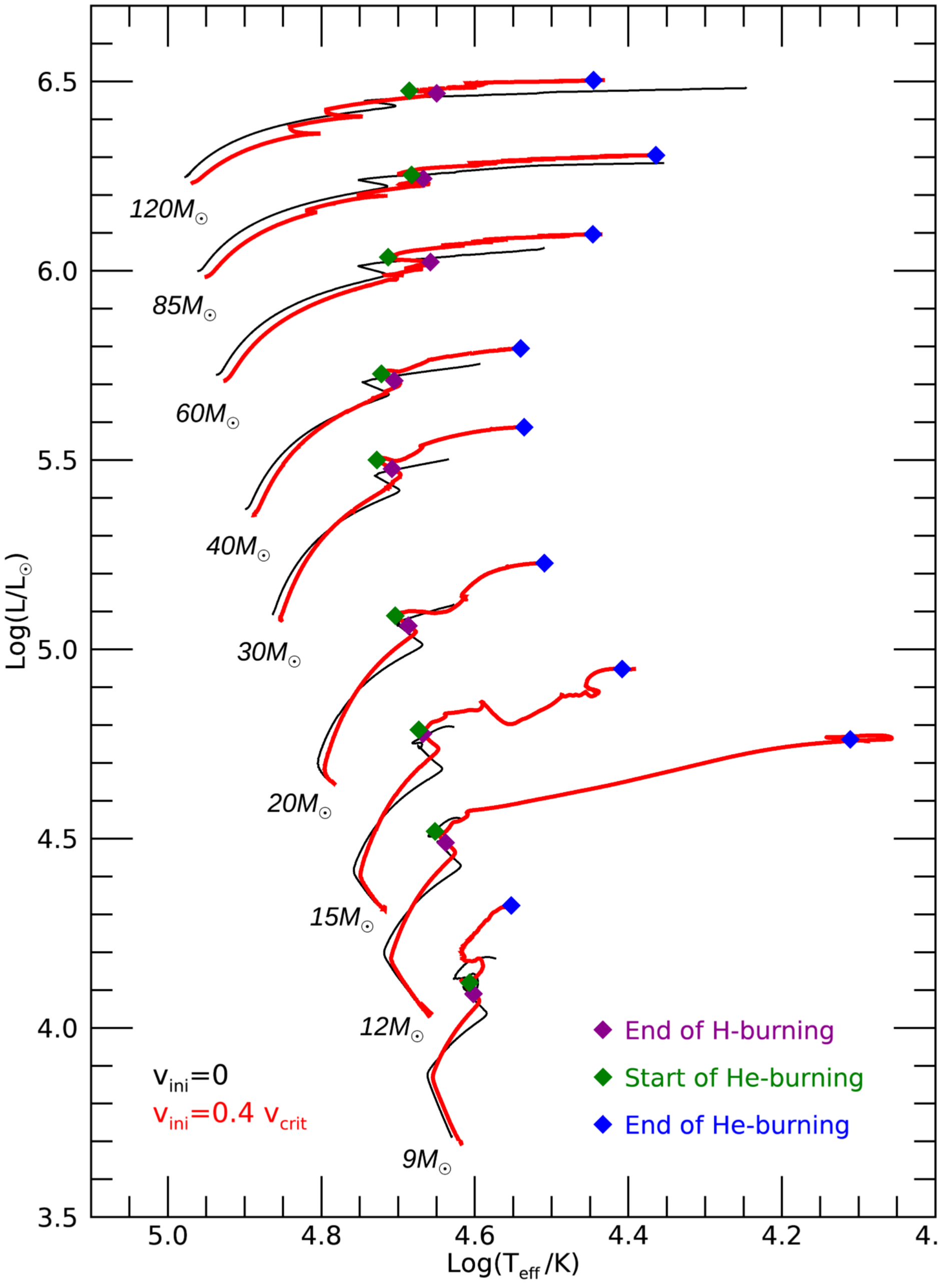

Figure 4.3: Similar to Figure 4.1 but including comparison between evolutionary tracks of non-rotating models (black) and rotating models with $\upsilon_{\rm ini} = 0.4\,\upsilon_{\rm crit}$ (red).

Figure 4.4: Effect of rotation on the stellar core mass fraction on the MS, for rotating models with $\upsilon_{\rm ini} = 0.4\,\upsilon_{\rm crit}$. The central H mass fraction is used here as a proxy for time spent on the MS. Also indicated in the plot are the initial masses of the models, $9\,{\rm M}_\odot \leq M_{\rm ini} \leq 120\,{\rm M}_\odot$.

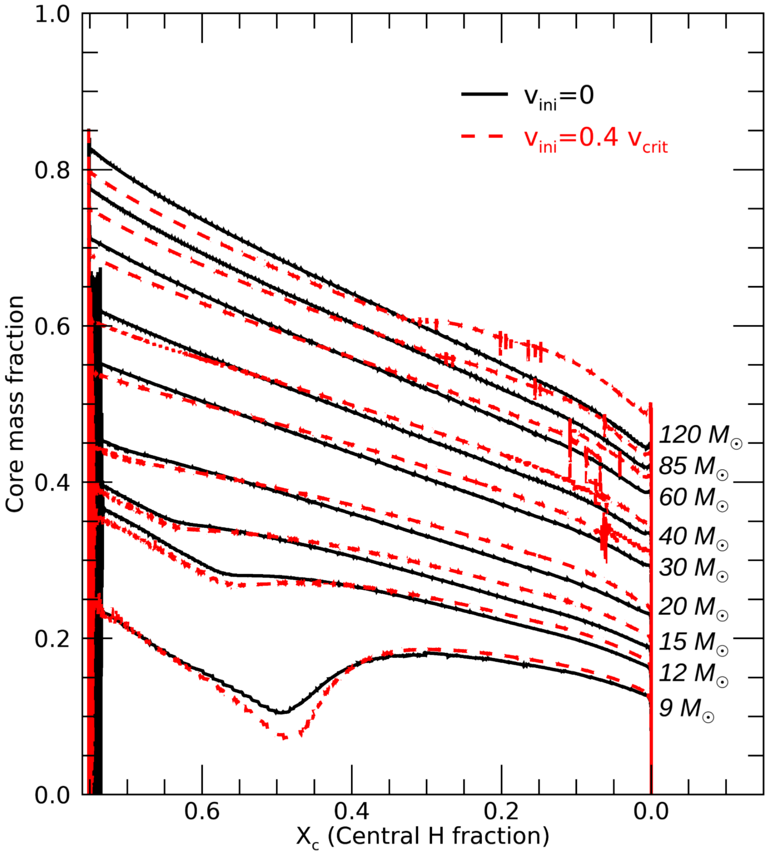

in luminosity is attributed to rotational mixing bringing additional H into the nuclear burning core and increasing its mass. This is seen in Figure 4.4 where the cores of rotating models do not decrease at the same rate as those of non-rotators. This effect is more pronounced for more massive models since rotational mixing is more efficient at higher masses. Furthermore, as we will discuss in Section 4.3, the most massive models of initial masses $85\,{\rm M}_\odot$ and $120\,{\rm M}_\odot$ reach critical rotation and experience mass loss before the end of the MS. This decreases their total mass and subsequently increases their core mass fraction. An additional effect is that rotation extends the MS lifetime (see Table 3.1), which follows from the rotational mixing of extra H into the core.

The MS evolution is otherwise similar to non-rotating models, with the exception of the jagged MS evolution for very massive models of $85\,{\rm M}_\odot$ and $120\,{\rm M}_\odot$, which is another consequence of evolution near critical rotation (Section 4.3). The $60\,{\rm M}_\odot$ model experiences increased mass loss due to critical rotation between the MS and the He-burning phase which leads to an increase in surface temperature, while the $85\,{\rm M}_\odot$ model experiences mass loss shortly before the end of the MS, and the $120\,{\rm M}_\odot$ model has experienced mass loss while on the MS. As a result, for some of the more massive models, there is some change to the surface properties between the end of the MS and the beginning of He burning. The $60\,{\rm M}_\odot$ model is a good example of this where there is an evolution towards higher $T_{\rm eff}$ before He ignition.

The He-burning phase brings even more variation when rotation is considered. There is no obvious trend, with some models becoming significantly more luminous like the 9 $\mathrm{M}_\odot$ and 20 $\mathrm{M}_\odot$ cases, while others evolve to lower T_{eff}, the most obvious example of this among massive models being the 12 $\mathrm{M}_\odot$ model. This indicates that the evolution becomes much more complex when we consider rotation, and there is much to investigate as we examine the interior structure and energy generation of these models. As a result of rotation, the less massive models have lower T_{eff} at the end of He-core burning with respect to non-rotating models, while more massive models (85 $\mathrm{M}_\odot$ and 120 $\mathrm{M}_\odot$) end their He-burning phase with higher T_{eff}, likely due to their mass loss at the critical rotation limit, see Section 4.3.

Following what was discussed in Chapter 3, a striking result from Figure 4.3 is the variability in the behaviour of rotating models during He burning. Through investigating the interior structure of our models we have found that the evolution of luminosity and effective temperature during He burning is determined by a balance of the relative strength of the He core and the H-burning shell. The dominant effects are that a larger core increases luminosity, and a stronger H shell decreases effective temperature. However, convection in the shell affects the structure of the star and subsequently the effective temperature. Additionally, approaching critical rotation simultaneously decreases surface temperature as the effective gravity of the outer layers decrease. In the following section we will discuss these findings and how they have been determined by studying how rotation impacts the internal structure of Pop III stars.

4.2.2 Internal Structure

We will focus on the 12 $\mathrm{M}_\odot$ and 15 $\mathrm{M}_\odot$ models first to visualise the complex effects of rotation on internal structure. These models are a good example of the diversity in post-MS surface evolution, with the 12 $\mathrm{M}_\odot$ model experiencing a significant decrease in surface temperature reaching a T_{eff} of almost 10^4 K (Figure 4.3) before the end of He-burning, while the 15 $\mathrm{M}_\odot$ shows more variance in luminosity but has a higher T_{eff} of roughly $10^{4.4}$ K ($\sim$ 25120 K) at the end of He burning. By looking at the interior structure of our rotating models it is clear that the nature of the H shell plays a dominant role in determining the model's structure and behaviour during the He-burning phase.

We show in Figures 4.5 and 4.6 the interior structure of the 12 $\mathrm{M}_\odot$ and 15 $\mathrm{M}_\odot$ rotating models with $\upsilon_{\mathrm{ini}} = 0.4\,\upsilon_{\mathrm{crit}}$ at three key points of He-burning evolution. Energy generation profiles are given in Figure 4.5 to show the relative contributions of the He-burning core and the H-burning shell to the total energy generation of the star. Abundance profiles are given in Figure 4.6 to show how the chemical abundances vary with changes to energy generation. We use the central He fraction (Y_{c}) as a reference point for evolutionary stage, where Y_{c}=1 would indicate the start, and Y_{c}=0 the end, of He burning. At Y_{c}=0.75 it can be seen that these models have a very similar structure

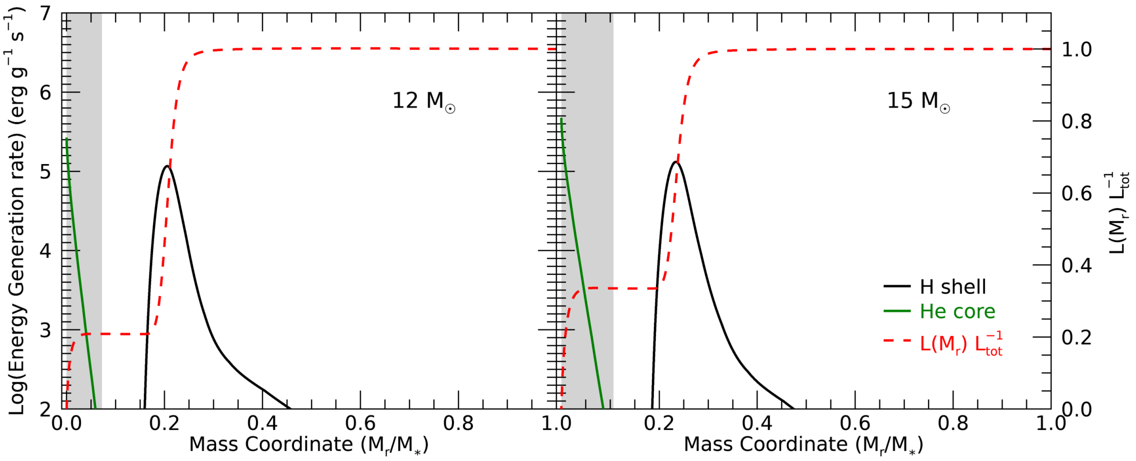

(a) Energy Generation: Y_c=0.75

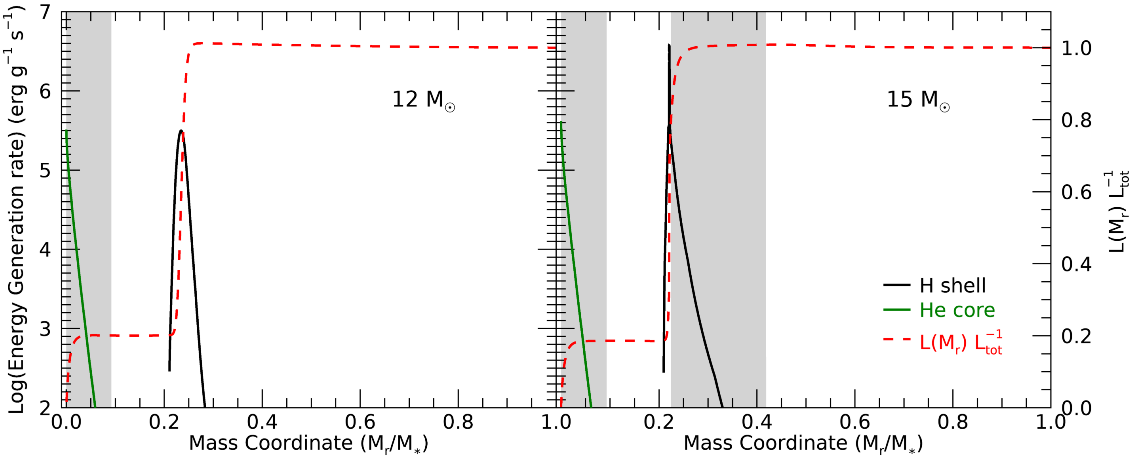

(b) Energy Generation: Y_c=0.5

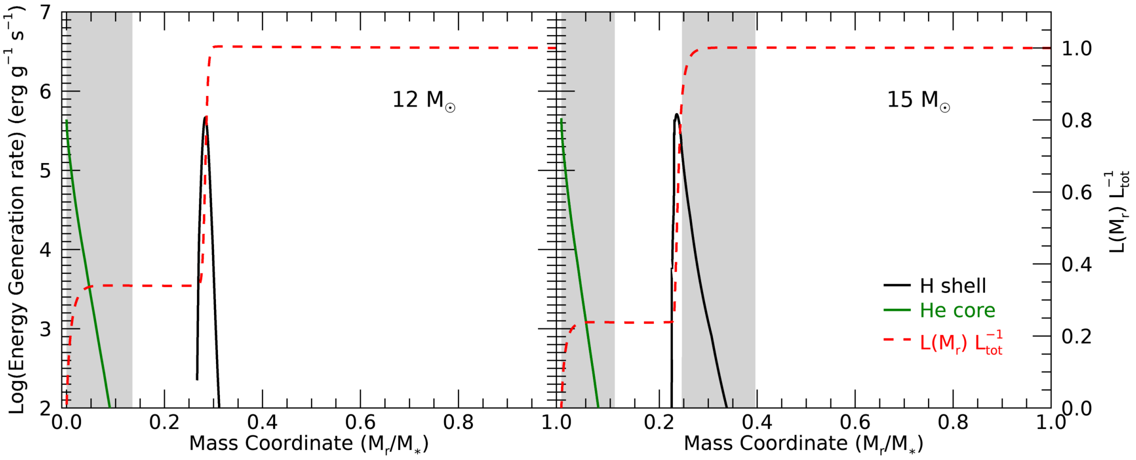

(c) Energy Generation: Y_c=0.25

Figure 4.5: Energy generation rates of the 12 M$_\odot$ and 15 M$_\odot$ rotating models at three separate points of He burning indicated by their central He fraction, Y_c. Green (black) solid lines indicate energy generation from He (H) burning. The fraction of luminosity contribution is given by the red dashed lines with values shown in the y-axis on the right-hand-side, for example in the 12 M$_\odot$ case the energy from the core contributes to 20% of the total luminosity at $Y_c = 0.75$. Convective regions are indicated by the grey shaded areas.

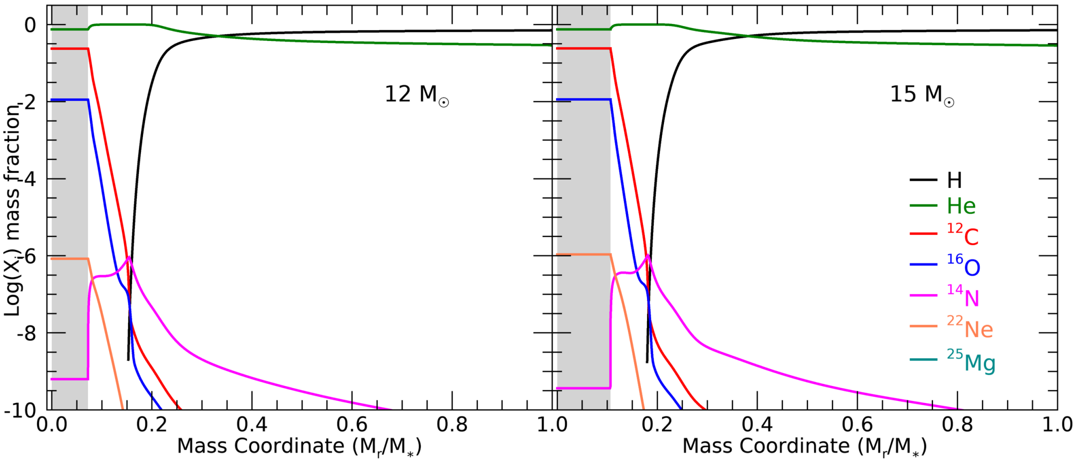

(a) Abundance profile: Y_c=0.75

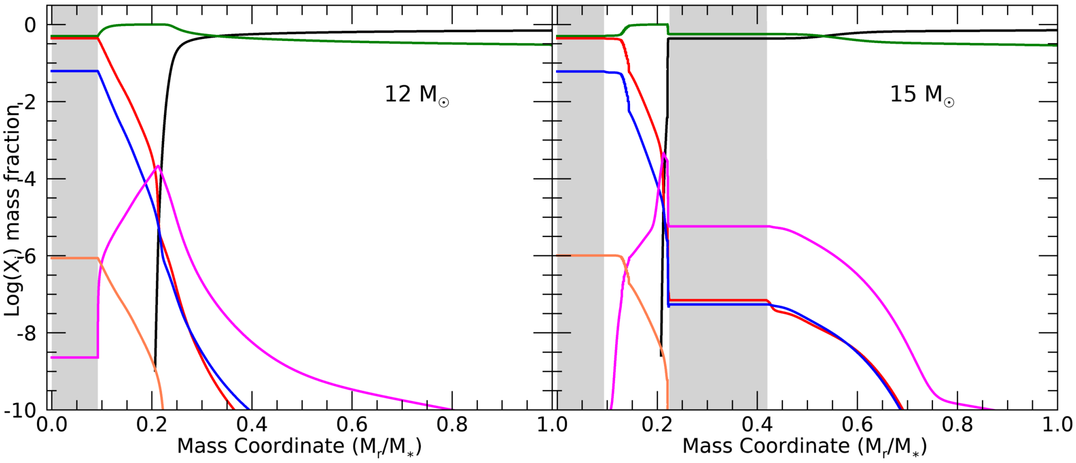

(b) Abundance profile: Y_c=0.5

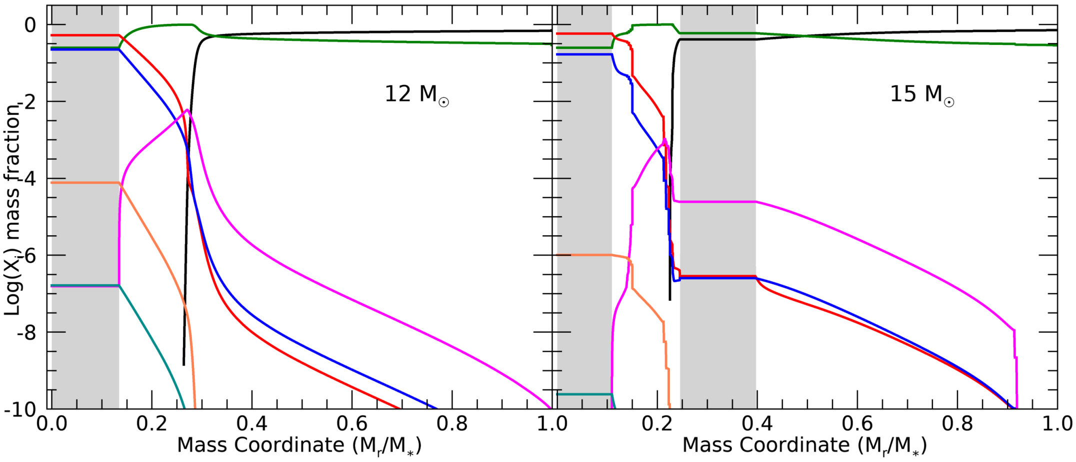

(c) Abundance profile: Y_c=0.25

Figure 4.6: Abundance profiles of the 12 M$_\odot$ and 15 M$_\odot$ rotating models at three separate points of He burning indicated by their central He fraction, Y_c. Abundance profiles show chemical abundances throughout the star from centre to surface where species are indicated by the legend (right panel of Figure 4.6a). Convective regions are indicated by the grey shaded areas.

both in abundance and in nature of the H shell (Figures 4.5a and 4.6a). The only significant difference between them is the size of the He-burning core where the 15 $M_\odot$ model's core is a larger fraction of the total mass. This is an important difference because more He-burning products are then transported to the H shell through rotational mixing. Indeed this mixing of He-burning products, such as ^{12}C and ^{16}O, towards the H shell can be seen in the abundance profile (Figure 4.6a).

Given that these are zero-metallicity models, the H shell relies on p-p chain reactions for nuclear burning until ^{12}C and ^{16}O reach these regions through rotational mixing. The introduction of these heavier elements triggers the CNO cycle, which significantly boosts energy generation in the H shell (Ekström et al. 2008). The 15 $M_\odot$ model is evidence of this where the mixing of ^{12}C and ^{16}O towards the H shell results in a strong CNO boost at Y_c=0.52. Figures 4.5b and 4.6b illustrate the consequences of this CNO boost shortly after its occurrence. While the temperature dependence of p-p chain reactions is roughly $\epsilon_{pp} \propto T^4$, the CNO cycle has a much higher temperature dependence of $\epsilon_{CNO} \propto T^{20}$. Therefore, the CNO cycle steepens the temperature gradient at the boundaries of the H shell which triggers convection. The CNO boost is named as such because of the effect that it has on energy generation, if we compare the 15 $M_\odot$ model in Figures 4.5a and 4.5b we can see this effect through the increased luminosity contribution of the H shell at Y_c=0.5. Earlier in the He-burning phase the H shell of the 15 $M_\odot$ model contributed to approximately 70% of the total luminosity (right panel Figure 4.5a), while after the CNO boost its contribution is more than 80% (right panel Figure 4.5b). This boost in energy of the shell causes the He-burning core to retract, an effect which is also seen in Ekström et al. (2008). This explains the decrease in luminosity observed in Figure 4.3, where a dip in $log(L/L_\odot)$ is seen at approximately $log(T_{\rm eff}/K)$=4.6. Now that the H shell is convective (right panels Figures 4.5b and 4.6b) it can maintain strong H-burning in this region by replenishing its fuel through convective mixing (right panels Figures 4.5c and 4.6c).

In contrast to the 15 $M_\odot$ model, the 12 $M_\odot$ model does not experience a strong CNO boost (left panels of Figures 4.5b and 4.6b), indicating that insufficient He-burning products reached the H shell for the CNO cycle to dominate H-burning. This is because the 12 $M_\odot$ model has a smaller He-burning core (Figures 4.5a and 4.6a) than the 15 $M_\odot$ model. The H-burning shell in the 12 $M_\odot$ model therefore remains dominated by p-p chain reactions and radiative. As this model evolves, the He core continues to grow while the H shell moves outwards (left panels of Figures 4.5c and 4.6c). This outward evolution of the H shell makes sense, because as it produces helium and depletes hydrogen in one layer of the star, it must move closer to the surface to source layers richer in hydrogen and continue burning. The evolution of the temperature profile may also play a role in how the H shell moves outwards as regions closer to the stellar surface become hot enough for H burning.

It can be seen from the energy generation profiles for this 12 $M_\odot$ model, that the

H shell is a significant source of luminosity for the star. It contributes to about 80% of the total luminosity at Y_c=0.75 (left panel of Figure 4.5a), and 65% at Y_c=0.25 (left panel of Figure 4.5c). Consequently, the changes to the H shell strongly impact the structure of the star, and are related to an increase in the stellar radius as the H shell evolves outwards. This explains the large decrease in $T_{\rm eff}$ that we observe in Figure 4.3 for the 12 $M_\odot$ model. The H shell dominates the total energy contribution and, therefore, the stellar structure, forcing the star to adopt a larger radius in order to maintain hydrostatic equilibrium. This behaviour is evident from our models given that the radius begins increasing at Y_c=0.6, just as the H shell begins moving outwards through the stellar envelope. We note here that determining the dominant factors for the evolution in the HR diagram is complex. According to Farrell et al. (2020), there are four main factors that drive the evolution to lower effective temperatures during central He burning. These are, an increase in He abundance in the H-burning shell; an increase in the core mass ratio in the regime of $M_{\rm core}/M_{\rm total} > 0.6$; an increase in the CNO abundance in the H-burning shell; and a decrease in the central He abundance (Y_c) during the latter half of core He burning (Section 1.1.3).

The 15 $M_\odot$ model on the other hand maintains the current structure of the star due to the convective mixing of the H-burning shell. This prevents the radius from increasing at the same rate as the 12 $M_\odot$ model, which explains why the 15 $M_\odot$ model does not reach values of $T_{\rm eff}$ as low as that of the 12 $M_\odot$ model.

Comparing the H profile of the 12 $M_\odot$ model and the 15 $M_\odot$ model in the abundance profile at Y_c=0.25 (Figure 4.6c) shows that the lower mass model has a higher H abundance in the envelope. Given that the opacity of these models is dominated by electron scattering the higher H abundance infers a higher opacity, so it makes sense that the 12 $M_\odot$ model reaches the redder part of the HR diagram in Figure 4.3. However, this does not drive the increasing radius. The energy provided by the outwards moving H shell to regions closer to the stellar surface drives the stellar expansion. The nature of the H shell is, therefore, responsible for the strong variation in evolution along the HR diagram during He burning, as this work confirms. Through investigating these two models we have also shown how sensitive this H-burning shell is to products of He burning that diffuse out from the core through rotational mixing.

Now that we better understand the complexities of how rotation affects stellar structure in these models, let us compare the behaviour of the 12 $M_\odot$ and 15 $M_\odot$ models to those of lower and higher initial mass. In the 9 $M_\odot$ model, the H shell is not significantly stronger than the He core and so we do not see a large decrease in $T_{\rm eff}$ (Figure 4.3). We do observe a considerable increase in luminosity however, which is indicative of the growing He core aided by rotational mixing.

The 20 $M_\odot$, 30 $M_\odot$, and 40 $M_\odot$ rotating models behave similarly to each other in the HR diagram. They each experience a substantial decrease in $T_{\rm eff}$ and a boost to their luminosity during He burning. This increase in luminosity results from the growth

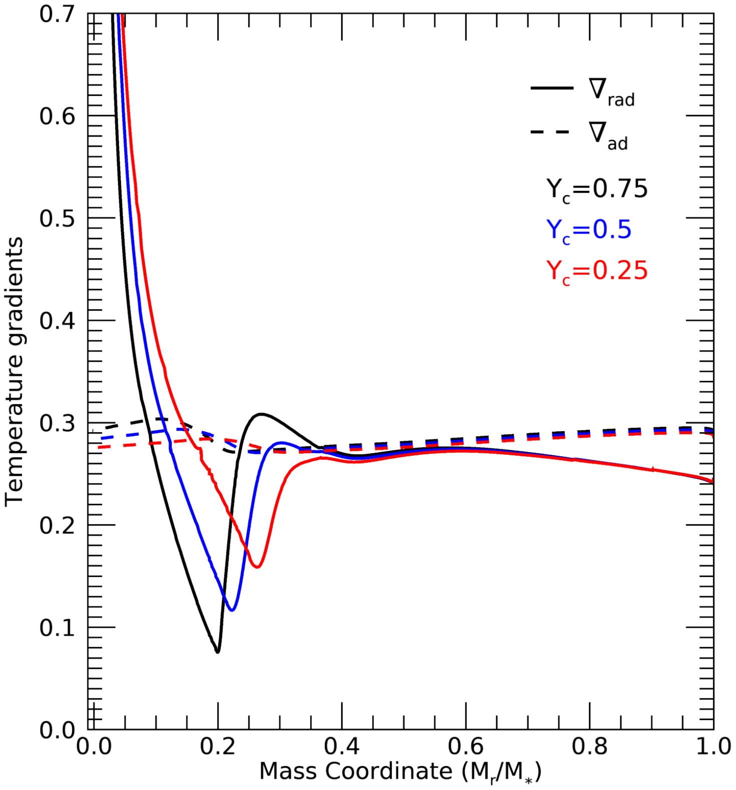

Figure 4.7: Evolution of the radiative and adiabatic gradients through He burning for the 20 $M_\odot$ model rotating at an initial velocity $\upsilon_{\rm ini} = 0.4\,\upsilon_{\rm crit}$. Central He fraction ($Y_c$) is indicated by the legend. Convection regions appear where $\nabla_{\rm rad} > \nabla_{\rm ad}$.

of the He core, which also triggers a reduction in the size of the convective H shell. In the 20 $M_\odot$ model, the H shell actually becomes radiative again. The growth of the He-burning core affects the temperature profile of the star which in turn changes the radiative temperature gradient ($\nabla_{\rm rad}$). This is shown in Figure 4.7 where $\nabla_{\rm rad}$ and the adiabatic temperature gradient ($\nabla_{\rm ad}$) are plotted for three stages of the He-burning phase ($Y_c = 0.75, 0.5, 0.25$.) The figure shows that as the core grows in size it flattens the radiative gradient profile. Since we only have convection where $\nabla_{\rm rad} > \nabla_{\rm ad}$, the convective region reduces in size until the H shell becomes radiative. Models from Farrell et al. (2020) support this conclusion in showing that for higher core mass ratios, the value of $\nabla_{\rm rad}$ is lower which tends to disfavour convection. Similarly to the 12 $M_\odot$ model, the now radiative H shell moves further towards the stellar surface driving expansion and ends up in a redder part of the HR diagram (Figure 4.3) than its non-rotating counterpart.

In summary, we find that the evolution of surface properties during He burning is moderated by a balance of the relative strength of the He core and the H-burning shell, and how this impacts the temperature profile. In some cases the H shell affects the size and strength of the He core, for instance when the CNO boost causes the core to retract. In other cases, the He core affects the size and strength of the H shell, for instance when the growth of the He core flattens the temperature profile and removes convection from the H shell. These effects are particularly important for fast rotating models where rotational mixing leads to increased energy production and changes to the chemical profile, affecting metal enrichment.

4.2.3 Final Fates and Proximity to Pair Instability

Models from this grid have been used to investigate the possibility of forming primordial black holes within the so-called pair instability mass gap (see Section 1.3.3). This is discussed in Farrell et al. (2021b) as a possible explanation for the black hole masses detected in the recent GW190521 merger event (Abbott et al. 2020b,a). Our zero metallicity models are promising candidates for the black hole mass required given their negligible mass loss and compact structure. Some models, e.g. the non-rotating 85 $M_{\odot}$ model, achieve lower CO core masses through CNO boosts (discussed in Section 4.2.2), which may help them avoid the pair instability regime. Other works have also suggested Pop III stars as potential progenitors for the GW190521 merger (Kinugawa et al. 2021; Liu & Bromm 2020b; Safarzadeh & Haiman 2020; Tanikawa et al. 2021b). Umeda et al. (2020) found that even if the CO core mass reaches the pulsational pair instability limit, these stars could remain mostly intact if their binding energy is high enough.

Since Pop III stars are more compact than higher metallicity stars, this is further evidence that they may raise the lower limit of the pair instability mass gap. This is in contrast to Chatzopoulos & Wheeler (2012) which suggested that rotational mixing would increase the core size of Pop III stars leading them to encounter the pair instability at lower initial masses than higher metallicity stars. The CO core (M_{CO}) and He core (M_{He}) masses for our models are given in Table 4.1. We find that rotational mixing does not lead to a general increase in core sizes at late evolutionary stages, and in fact most models show lower CO core mass with rotation. Rotational mixing does increase the core size during the MS, however, this is not necessarily true for the post-MS stages. This is largely because from He burning onwards rotational mixing strengthens the H-burning shell which tends to suppress the growth of the He core. The differences in behaviour of our models compared to earlier work could be due to the different assumptions about convection and rotational mixing. The Chatzopoulos & Wheeler (2012) models are run using MESA which includes different rotational effects to those outlined in Chapter 2 which impact rotational mixing and chemical transport. These differences may explain how rotation in our models strengthens the H shell and subsequently hinders He core growth unlike the models in Chatzopoulos & Wheeler (2012). Given their impacts on the final core mass of Pop III stars, further work is warranted on a detailed exploration of the physics of mixing in Pop III stars.

4.3 Critical Rotation and Mass Loss

Given the lack of radiative mass loss in Pop III models, there is no mechanism for removing angular momentum from the surface of these stars (Section 1.2.3). Although meridional currents are weak in zero-metallicity stars due to their higher density (Ekström et al. 2008, Section 1.2.4), angular momentum is still transported outwards from

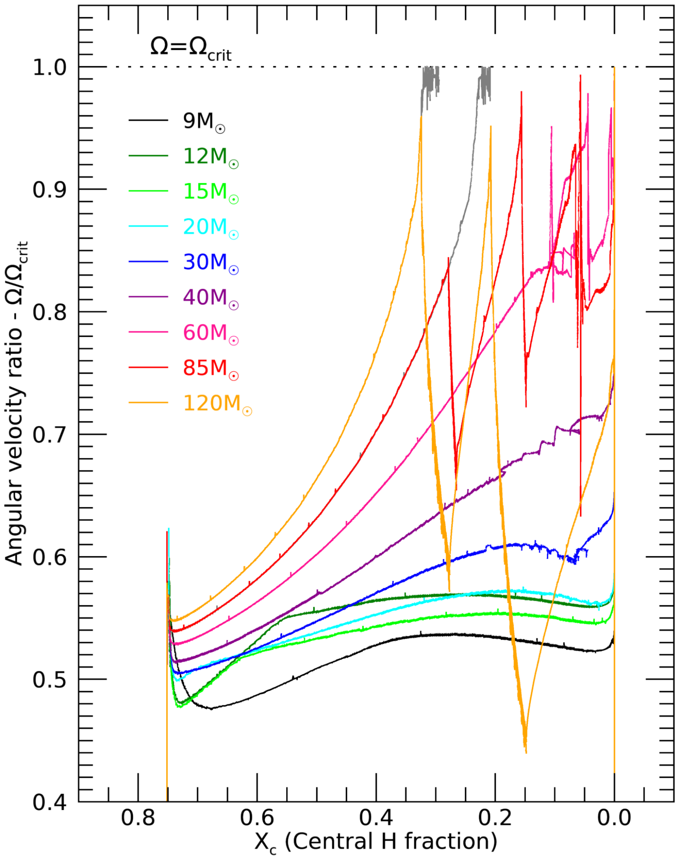

Figure 4.8: Evolution of the angular velocity ratio, $\Omega/\Omega_{\text{crit}}$, during the MS for models with $\upsilon_{\text{ini}} = 0.4\,\upsilon_{\text{crit}}$, initial masses are indicated in the legend. The dotted line indicates where models have reached critical velocity, the grey lines show the 85 M$_\odot$ and 120 M$_\odot$ models reaching critical rotation when we rely on the mechanical mass-loss implementation in the code. Their corresponding coloured lines show where our averaged mass-loss rate is added.

the core, and without mass loss this angular momentum builds at the surface. As a consequence, several of our models spin up during the MS. This can be seen in Figure 4.8, where the evolution of the angular velocity on the MS is plotted. The angular velocity is plotted as a fraction of critical, that is, the velocity at which the outer layers of the star become unbound. The dotted horizontal line indicates this point clearly, and allows us to observe how our models evolve towards this limit during H burning. As can be seen from the figure, models with $M_{\text{ini}} > 20\,\text{M}_\odot$ spin up on the MS with more massive ($M_{\text{ini}} \geq 60\,\text{M}_\odot$) models reaching critical. The grey lines show the 85 M$_\odot$ and 120 M$_\odot$ models reaching critical rotation when we rely on the mechanical mass-loss implementation in the code (see Section 2.5.2). The red and orange lines correspond to the 85 M$_\odot$ and 120 M$_\odot$ models where our averaged mass-loss rate (see Section 2.7.1) was switched on when the star approaches critical rotation. To explain this difference in mass-loss treatment we will look specifically at the 120 M$_\odot$ example.

When a model reaches critical velocity the outer layers of the star become unbound and it can be expected that the star will lose a significant amount of mass at this point, enough to lose sufficient angular momentum to fall below critical velocity again. This is the case for the 120 M$_\odot$ model with $\upsilon_{\text{ini}} = 0.4\,\upsilon_{\text{crit}}$ which reaches critical velocity mid-way through the MS. Its evolution along the HR diagram is shown in Figure 4.9. The red line shows the evolution of the star with only the mechanical mass-loss implementation,

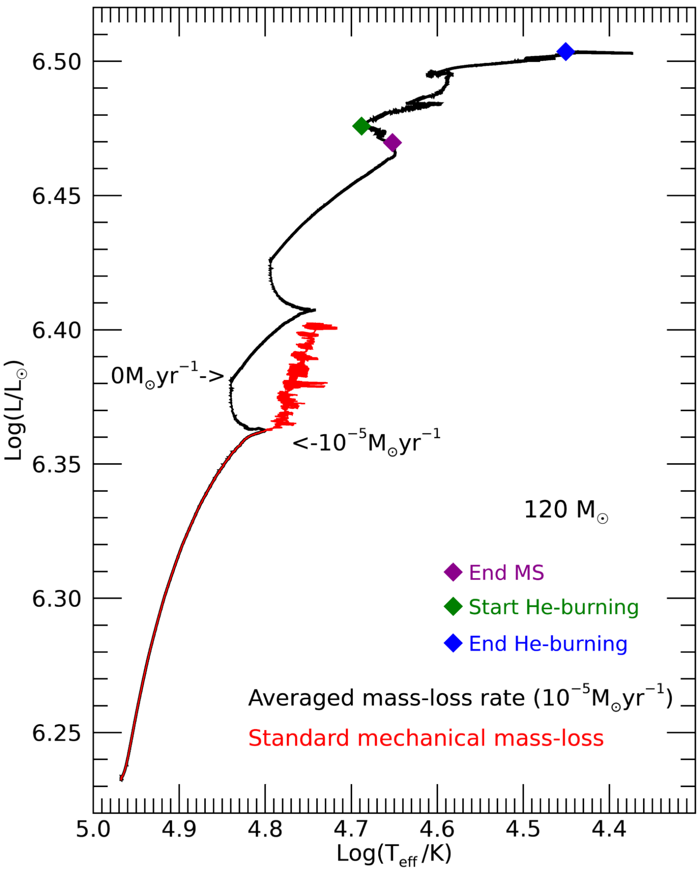

Figure 4.9: Evolution of the 120 M$_\odot$ model until the end of He burning as indicated in the legend. The black evolutionary track corresponds to the model where a mass-loss rate of $10^{-5}\,M_\odot yr^{-1}$ is switched on as the model approaches critical velocity (see arrows). The red evolutionary track corresponds to our model with the GENEC mechanical mass-loss implementation (see Section 2.5.2).

described in Section 2.5.2, to simulate mass loss at critical rotation, and corresponding to the grey line in Figure 4.8. With this mechanical mass-loss prescription the model remains at critical rotation, giving rise to the unstable region in Figure 4.9 at luminosities $6.36 \leq log(L/L_\odot) \leq 6.4$, and the evolution along the $\Omega = \Omega_{\rm crit}$ line in Figure 4.8. To resolve this instability we impose an averaged mass-loss rate of $10^{-5}\,M_\odot yr^{-1}$ just before the model reaches critical velocity, as described in Section 2.7.1. This treatment is shown by the black line in the HR diagram (Figure 4.9) and the orange line in Figure 4.8.

As the star spins up, its outer layers expand lowering the surface temperature and evolving the star to the right of the HR diagram. Upon reaching critical, our higher mass-loss rate was employed to allow the model to shed the unbound mass from the outer envelope (see arrow in Figure 4.9). This increases the surface temperature as deeper layers of the envelope are revealed. Once enough mass is lost to bring the rotational velocity below critical, the surface temperature stabilises and the increased mass-loss rate raises the luminosity. The mass-loss rate was then switched off again (see arrow in Figure 4.9) so as to allow the model to resume its MS evolution. However, as is evident from Figures 4.8 and 4.9, such a mass-loss event can reoccur if the model can spin up to critical again. This shows that angular momentum transport is efficient enough to replenish the angular momentum lost at the surface. As a result, this behaviour may occur multiple times before H-core depletion, depending on the initial mass and rotation of the star. During the first period of mass loss we see the velocity decrease as angular momentum is lost through the sharp dip in Figure 4.8 at $0.32 \geq X_c \geq 0.28$. We then see how quickly the model spins up again when mass loss is returned to zero at $\Omega/\Omega_{\rm crit}$=0.59. This illustrates how difficult it is for these massive Pop III models to evolve away from critical. The total mass lost by the 120 $M_\odot$ model is 3.5 $M_\odot$ (see Table 3.1), having spent ∼8% of its MS lifetime losing mass.

We use a similar mass-loss treatment for the 60 and 85 $M_\odot$ models before they reach critical rotation (pink and red lines in Figure 4.8, respectively.). These models experience shorter periods of mass loss since they evolve away from critical more easily. The 85 $M_\odot$ model loses roughly 1 $M_\odot$ during these mass-loss events, while 0.3 $M_\odot$ is lost by the 60 $M_\odot$ model (Table 3.1). The mass loss of the 60 $M_\odot$, 85 $M_\odot$ and 120 $M_\odot$ models also explains the increase in the core mass fraction in Figure 4.4 towards the end of the MS, when these models reach critical. During this time, the total mass of the star decreases, which leads to an increase in the core mass fraction. This behaviour may have significant impacts for the final fates of these models given the effect of mass loss during the MS on the core mass. Of course, the amount of mass lost by these models is a direct consequence of the assumed value of $\dot{M}$ in our models, and further study is needed to investigate the behaviour of mass loss in fast-rotating Pop III stars.

4.4 Metal Enrichment and Yields

One of the most important aspects of Pop III evolution is their metal enrichment. As outlined in Section 1.3.1, enrichment of Pop III stars has been investigated through studying EMP stars which are believed to be direct descendents of zero-metallicity stars and therefore can constrain their metal enrichment. Here we focus on the evolution of Pop III stars and how their enrichment is affected by initial mass and rotation. By connecting this with work being done on the second generation of stars we can get a better picture of how the first stars would have evolved and produced the first heavy elements in the Universe.

Table 4.1 shows the final amounts of ^{14}N, ^{12}C, and ^{16}O produced, noting that the evolutionary stage reached varies for each model. These chemical yields are calculated for mass coordinates above the gravitational remnant mass, which represents the estimated mass of the remaining core following a SN explosion. It is computed based on the CO core mass (Maeder 1992). The mass of the CO and He cores, shown in Table 4.1, are determined using the method by Heger et al. (2000), where the mass coordinate where H falls below 10^{-3} defines the He core, and similarly where He falls below 10^{-3} defines the CO core. For models where central He is not yet depleted enough for this definition ($M_{\rm ini} = 30\,M_\odot$ with $\upsilon_{\rm ini} = 0$ and $M_{\rm ini} \geq 40\,M_\odot$ with $\upsilon_{\rm ini} = 0.4\,\upsilon_{\rm crit}$) we instead take the mass coordinate where 75% of He has been burned. We note that CO core mass is highly dependent on the treatment of convection (e.g. Kaiser et al. 2020), which as we discuss in Section 2.6, is possibly underestimated here for consistency with the higher metallicity model grids (Ekström et al. 2012; Georgy et al. 2013a; Groh et al. 2019). As shown in Table 4.1, our models are all at various stages of post-MS evolution so this must be accounted for in establishing trends in metal enrichment. While the amount of ^{12}C and ^{16}O produced changes through late burning phases (C burning and O burning) the amount of ^{14}N produced remains largely constant, unless it is consumed by a He-burning region as we will discuss. It is therefore an ideal candidate for our study of metal enrichment. Shown in Figure 4.10 is the ^{14}N produced by non-rotating and fast-rotating ($\upsilon_{\text{ini}} = 0.4\,\upsilon_{\text{crit}}$) models. It is important to note that the ^{14}N abundance plotted here is that of the final model, which corresponds to a different evolutionary phase reached for each simulation. This ^{14}N abundance is the total mass of ^{14}N above the gravitational remnant mass at the final evolutionary stage for each model. Even without all of the models reaching the pre-SN stages, we would have still expected to see more ^{14}N produced with rotation. However, we find that rotating models do not always have higher metal enrichment. Some non-rotating models actually show more enrichment than their corresponding rotating model of the same initial mass, such as the $20\,\mathrm{M}_{\odot}$ model. The high ^{14}N enrichment in non-rotating models of 20-30$\,\mathrm{M}_{\odot}$ has also been found in Chieffi & Limongi (2004) and Ekström et al. (2008). It is therefore not as straightforward as more rotational mixing allows more enrichment. A strong CNO boost and subsequent ^{14}N enrichment can arise from multiple evolutionary behaviours. Let us first examine how enrichment of rotating models varies with initial mass.

4.4.1 Rotating Models

For the less massive models, $M_{\text{ini}} = 9, 12, 15\,\mathrm{M}_{\odot}$, we do see a trend with rotation in Figure 4.10, where rotating models show significantly more enrichment. To investigate this behaviour, we show in Figure 4.11 the evolution of the ^{14}N abundance during He burning, when we expect most of ^{14}N production to occur. Again the ^{14}N abundance is the total mass of ^{14}N above the gravitational remnant at each stage in the evolution, represented here by the central He fraction.

We see that ^{14}N abundance remains low for the $9\,\mathrm{M}_{\odot}$ model throughout He burning, and the high ^{14}N content seen in Figure 4.10 actually results from an interaction between the H and He shells following He burning. This highlights the importance of understanding how metal enrichment in these stars occurs, since significant ^{14}N production occurs whenever He burning products interact with a H-burning region, not just during the core He-burning phase. Similarly we note that the ^{14}N abundance of the $15\,\mathrm{M}_{\odot}$ model is approximately 1 dex lower at the end of He burning than its final value in Figure 4.10, again due to an increase in ^{14}N through a H-He interaction in the final evolutionary stages.

Figure 4.10: Total mass of ^{14}N above the gravitational remnant mass at the final stage in the evolution for each model, see Table 4.1, with initial mass in units of solar mass. Models with (without) rotation are shown in red (black) as indicated by the legend.

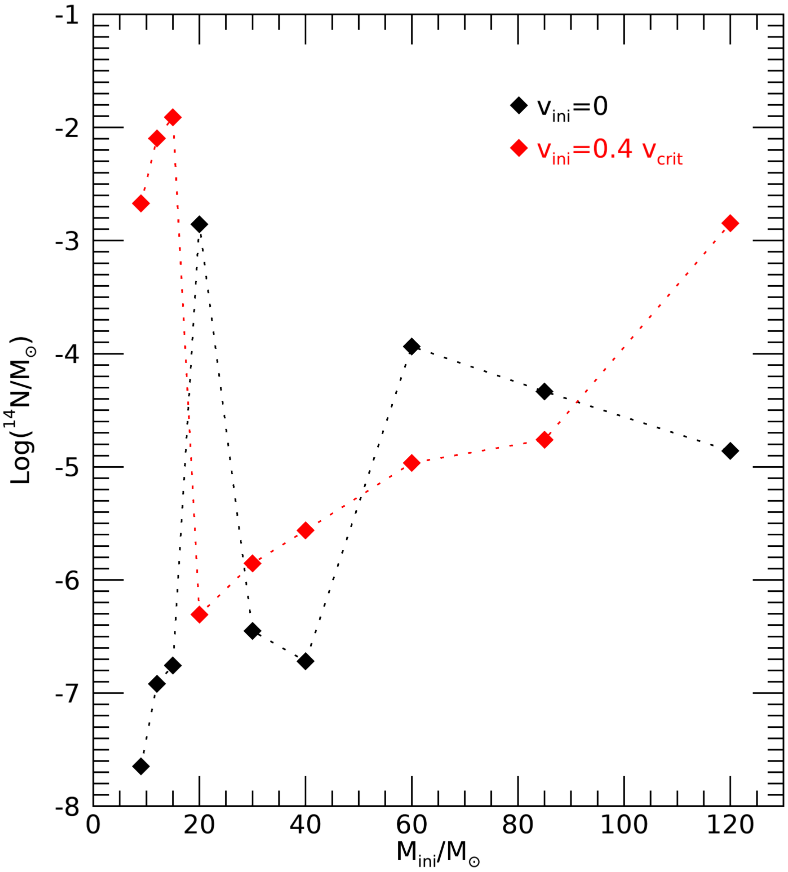

Figure 4.11: Evolution of ^{14}N abundance during He burning for models with initial velocity $\upsilon_{\rm ini}$=0.4$\upsilon_{\rm crit}$ and initial masses indicated by the legend. Colours are the same as Figure 4.8.

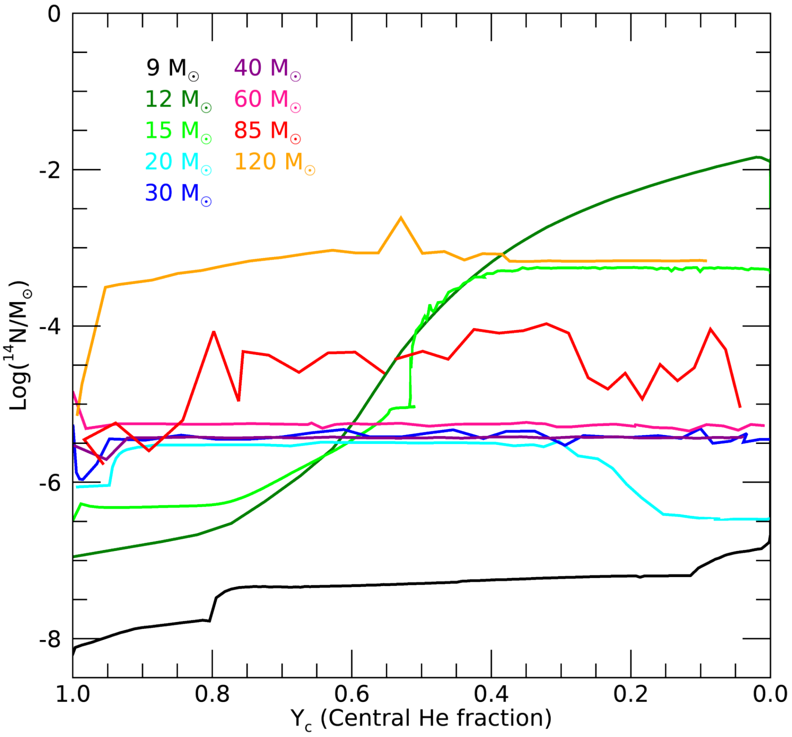

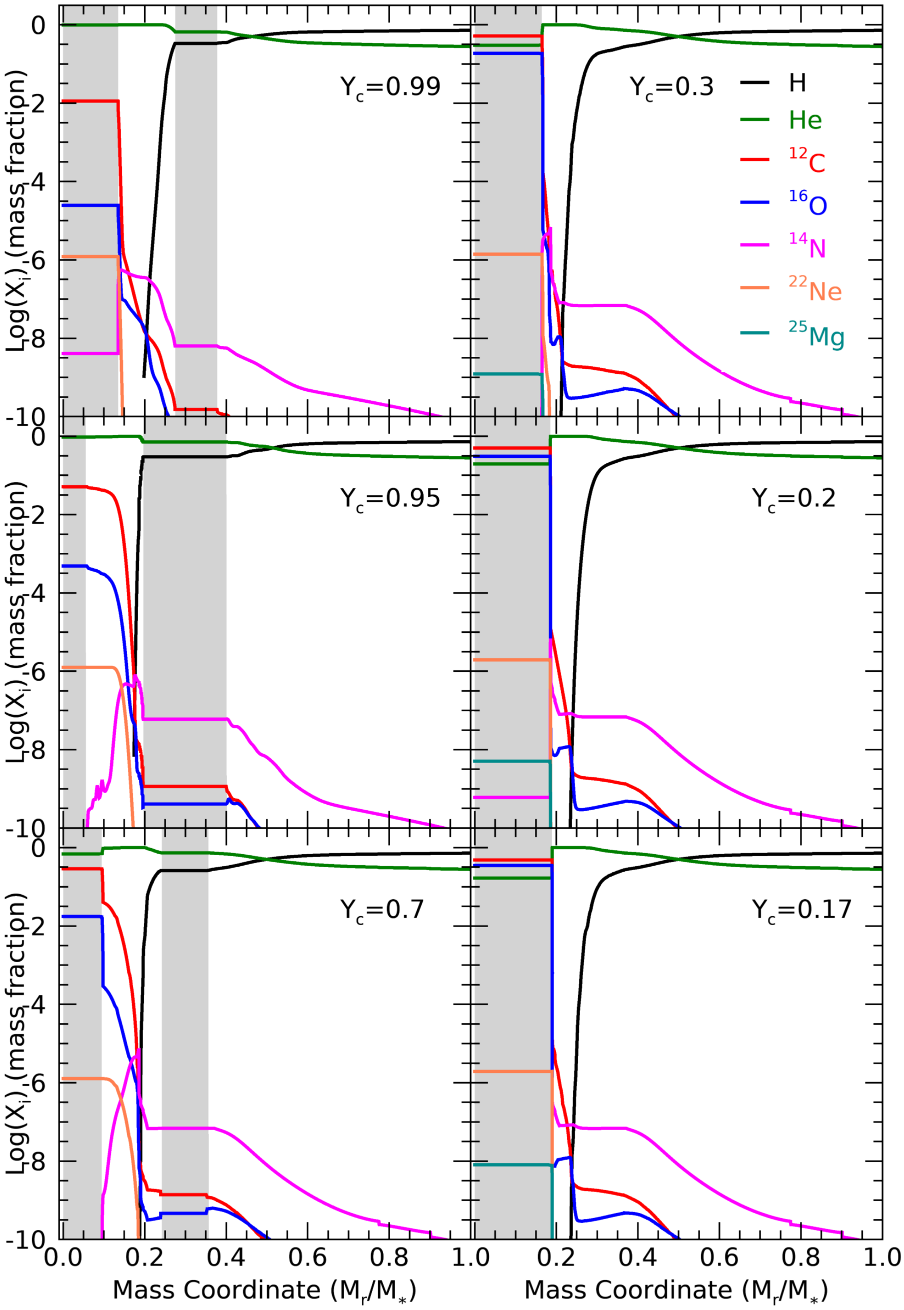

Figure 4.12: Evolution of the abundance profile for the 20 $M_\odot$ model rotating with initial velocity $\upsilon_{\rm ini}$=0.4$\upsilon_{\rm crit}$. Abundance profiles are shown for six points during He burning where the central He mass fraction is 99%, 95%, 70%, 30%, 20% and 17%. Species are indicated by the legend.

Figure 4.13: Same as Figure 4.11 but for non-rotating models.

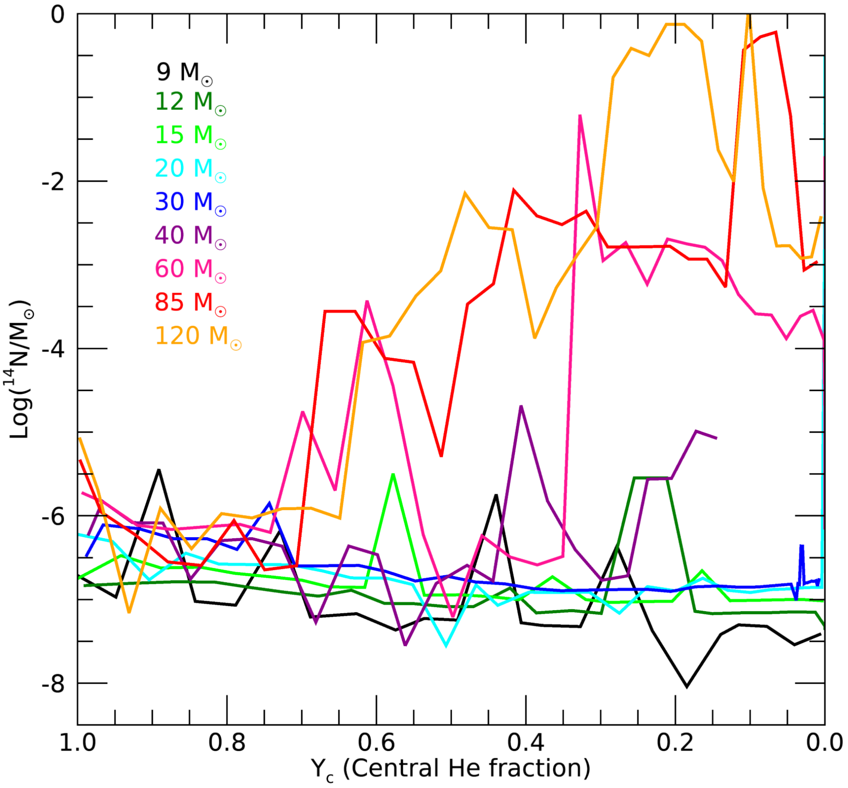

We find that the 12 M$_\odot$ and 15 M$_\odot$ models experience significantly higher ^{14}N production during He burning than other models (Figure 4.11). To understand this we can refer back to the energy generation and abundance profiles in Figures 4.5 and 4.6 where we examined the interior structure of these models at various points of He burning. There we see that the conditions of these models are ideal for maximising ^{14}N production. Rotational mixing gradually brings CO outwards from the core during He burning (Figures 4.6a to 4.6c), delivering it to the H-burning shell which is the dominant source of luminosity for the star (Figures 4.5a to 4.5c). Coming back to Figure 4.11, we see that the production of ^{14}N is more gradual for the 12 M$_\odot$ model. This is because the H shell receives less CO and the CNO cycle is not strong enough to trigger convection. The radiative nature of the shell does not affect the growing He core, as is the case for the 15 M$_\odot$ model (see Section 4.2.2), thus allowing for continuous ^{14}N enrichment.

We observe a sudden drop in ^{14}N yield for the 20 M$_\odot$ model, followed by a steady increase for higher masses (Figure 4.10). Our question then becomes, what changes between the 15 M$_\odot$ and 20 M$_\odot$ models to hinder enrichment? Through examining the interior structure of the 20 M$_\odot$ rotator we observe that it experiences its CNO boost at the beginning of He burning. This causes the core to recede, which hinders the C and O that can be produced and delivered to this region where ^{14}N enrichment occurs.

The effect of this early CNO boost on the stellar structure of the 20 M$_\odot$ model is shown in the three left panels of Figure 4.12. Here we have plotted the abundance profile of the 20 M$_\odot$ rotator at three different stages of He burning, before the CNO boost ($Y_{\mathrm{c}} = 0.99$), shortly after the boost ($Y_{\mathrm{c}} = 0.95$), and one to show the structure later on in He burning ($Y_{\mathrm{c}} = 0.7$). Between $Y_{\mathrm{c}} = 0.99$ and $Y_{\mathrm{c}} = 0.95$ we note the large increase in size of the convective H shell and the resulting retraction of the core. Following the CNO boost, as the star regains equilibrium, the core begins to grow again aided by rotational mixing. As the core grows the H shell moves outwards (see Section 4.2.2) and so the CO produced in the He core never reaches the H shell. In other words, rotational mixing of material from the core is slower than the moving H shell. This is particularly evident from the bottom-left panel ($Y_{\mathrm{c}} = 0.7$) in Figure 4.12, where the base of the H shell is now at a mass coordinate of $\sim 0.25\,M_{\star}$ while rotationally mixed CO extends only to $\sim 0.2\,M_{\star}$. Essentially the early triggering of the CNO boost limits the amount of CO that reaches a H-burning region, and in turn limits ^{14}N enrichment.

The growing He core can have another effect however, if the He-burning core expands into a region where ^{14}N has formed it converts this ^{14}N into ^{22}Ne. This is what happens towards the end of He burning for the $20\,\mathrm{M}_{\odot}$ rotator and explains the dip in ^{14}N for $Y_{\mathrm{c}} \leq 0.3$ in Figure 4.11. This effect is shown in the right panels of Figure 4.12. At $Y_{\mathrm{c}} = 0.3$ (top-right panel Figure 4.12) we note the peak in ^{14}N just outside the He core. By $Y_{\mathrm{c}} = 0.2$ (middle-right panel Figure 4.12) the growing core has engulfed this ^{14}N rich region leading to an increase in ^{22}Ne in the core. Finally, by $Y_{\mathrm{c}} = 0.17$ (bottom-right panel Figure 4.12) the ^{14}N transported to the core has been converted into ^{22}Ne and subsequently into ^{25}Mg through the s-process (see Section 1.3.1).

For models with 30-60 $\mathrm{M}_{\odot}$ in Figure 4.11 we see a largely constant ^{14}N abundance through He burning, owing to the early CNO boost as is the case with the $20\,\mathrm{M}_{\odot}$ model, but without ^{14}N being swallowed up by the core. In fact, for models $\geq 30\,\mathrm{M}_{\odot}$ the CNO boost actually occurs before He ignition. The most massive rotating models in our grid, $85\,\mathrm{M}_{\odot}$ and $120\,\mathrm{M}_{\odot}$, see more significant ^{14}N production during He burning, mainly because they have larger He cores and produce more CO for enrichment.

4.4.2 Non-Rotating Models

Our non-rotating models do not show a clear trend of increasing ^{14}N enrichment as a function of M_{ini} (Figure 4.10), and instead display non-monotonic behaviour. The key effects that influence this variety in ^{14}N enrichment are, H-He shell interactions at late phases, and interaction of the He core with ^{14}N which converts it to ^{22}Ne. To investigate this, we look at the time evolution of ^{14}N abundance through He burning for our non-rotating models in Figure 4.13. We see that all non-rotating models with initial masses $M_{\mathrm{ini}} < 60\,\mathrm{M}_{\odot}$ have little ^{14}N enrichment during He burning. Without the aid of rotational mixing there is less CO available to the H shell to produce ^{14}N. However, as initial mass increases, the relative core size also increases, making it easier for CO to reach the H shell, and we see greater enrichment for the $60\,\mathrm{M}_{\odot}$, $85\,\mathrm{M}_{\odot}$ and $120\,\mathrm{M}_{\odot}$ models in Figure 4.13.

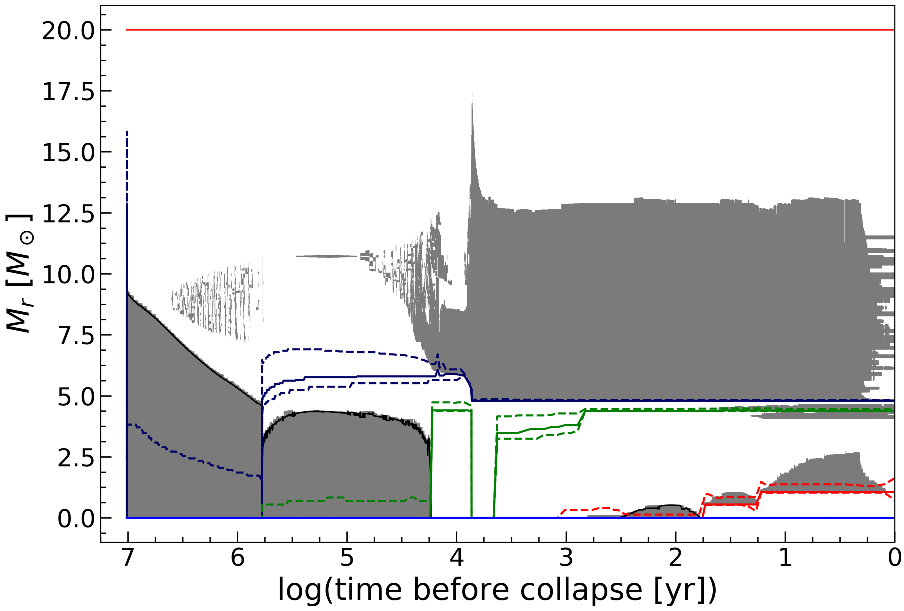

Figure 4.14: Kippenhahn diagram of the non-rotating $M_{\rm ini} = 20\,{\rm M}_\odot$ model, showing the evolution of the stellar structure in terms of the mass coordinate as a function of time to core collapse. The red line at the top indicates the total mass of the star. The grey-shaded areas correspond to convective regions. The solid (dashed) lines correspond to the peak (10%) of the energy generation rate for H burning (blue), He burning (green), and C burning (red).

The largest ^{14}N production seen for non-rotating models in Figure 4.10 is that of the $20\,{\rm M}_\odot$ non-rotator, which experiences a large CNO boost when the H shell moves inwards following He burning. This model is therefore an example of how H-He shell interactions complicate any trends we may predict for ^{14}N enrichment. This large CNO boost can be seen in Figure 4.14 where the convective region in the envelope suddenly increases reaching a mass coordinate of $\sim 17.5\,{\rm M}_\odot$. The contraction of the star in this late phase brings the H shell inwards where He burning had previously taken place, and the CO rich region allows for sudden and strong ^{14}N production.

What is also important to note about Figure 4.10, which can be seen in Figure 4.13, is that for non-rotating models where ^{14}N production occurs close to the He core boundary the ^{14}N abundance is highly variable. We see this behaviour for the $60\,{\rm M}_\odot$, $85\,{\rm M}_\odot$, and $120\,{\rm M}_\odot$ models. The proximity of the He core to ^{14}N rich regions means it can easily mix ^{14}N inwards to form ^{22}Ne, which in Figure 4.13 appears as a rather jagged evolution of ^{14}N abundance. In some cases the growing He core actually interacts directly with the H shell as happens with the $60\,{\rm M}_\odot$ non-rotator (Figure 4.15a), giving rise to a sudden increase in ^{14}N as the H shell receives a large boost in He-burning products. Interestingly, the $85\,{\rm M}_\odot$ non-rotator does experience a CNO boost giving rise to a convective H shell and reducing the convective He core (Figure 4.15b). Conversely, the H shell in the $120\,{\rm M}_\odot$ non-rotator remains radiative throughout He burning (Figure 4.15c), allowing

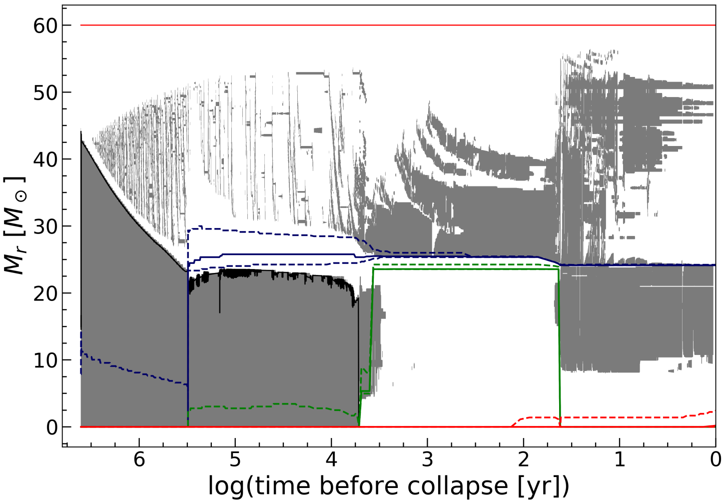

(a) $M_{\rm ini} = 60\,\mathrm{M}_\odot$

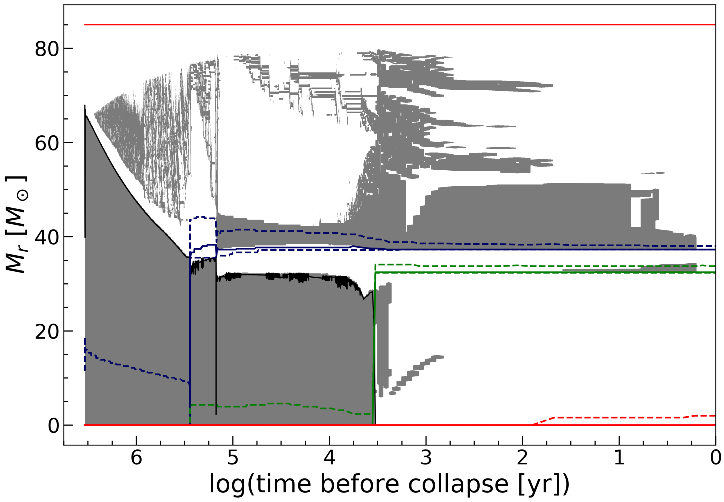

(b) $M_{\rm ini} = 85\,\mathrm{M}_\odot$

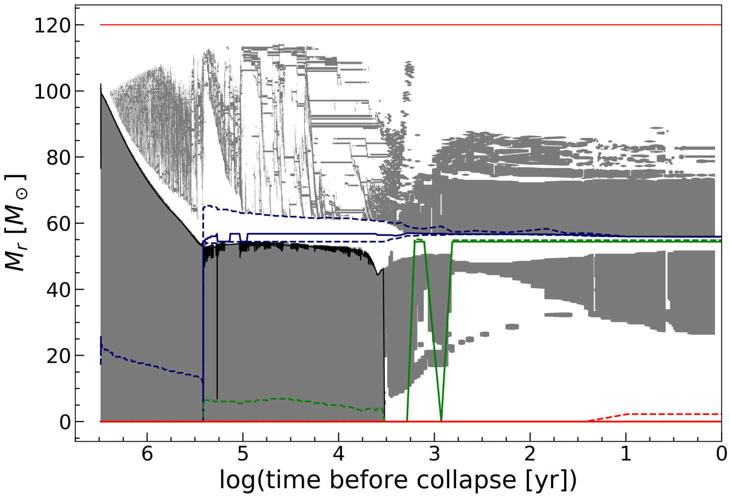

(c) $M_{\rm ini} = 120\,\mathrm{M}_\odot$

Figure 4.15: Similar to Figure 4.14, but for more massive non-rotating models with $M_{\rm ini} = 60$, 85, $120\,\mathrm{M}_\odot$.

for a progressive increase in N abundance.

4.4.3 Summary

In summary, we find that the final ^{14}N abundance is highly variable due to the diverse evolutionary routes to enrichment. We do find that rotational mixing helps to mix C and O out from the core to the H-burning shell, and subsequently aids ^{14}N enrichment. However, rotational mixing can give rise to earlier CNO boosts which in fact hinders overall ^{14}N enrichment. Early CNO boosts cause a strong retraction of the core creating significant distance between the He core and the H shell. When the core begins to grow the H shell simultaneously moves outwards, meaning that CO mixed outwards from the core struggles to reach the H shell. This effectively limits ^{14}N production to whatever was achieved during this early CNO boost. It seems that the $12\,\mathrm{M}_\odot$ and $15\,\mathrm{M}_\odot$ models have the ideal conditions of enough rotational mixing to deliver sufficient CO to the H shell, without triggering the CNO boost too early. We also expect that increasing rotation or overshooting would shift the trends seen in Figure 4.10 to lower masses. For example, if we used a higher rotational velocity we would expect the dip between the $15\,\mathrm{M}_\odot$ and $20\,\mathrm{M}_\odot$ rotators in Figure 4.10 to be seen earlier, perhaps between the $12\,\mathrm{M}_\odot$ and $15\,\mathrm{M}_\odot$ rotators. This is because we expect that extra mixing would give rise to an earlier CNO boost, which is what hinders enrichment in this case. Table 4.2 provides a summary of the nature of the CNO boosts for each of our models, the timing of the CNO boost, whether it triggers a convective H shell during the core He-burning phase, in addition to the ^{14}N yields from Table 4.1.

Additionally, there are multiple channels for CO elements interacting with H-burning regions that are not limited to this outward mixing during He burning. Many of these channels are discussed in Clarkson & Herwig (2020) as H-He interactions, and consist of events such as the inward moving H shell following He burning seen for the $15\,\mathrm{M}_\odot$ rotator and the $20\,\mathrm{M}_\odot$ non-rotator. It is clear from the discrepancy between the final abundance in Figures 4.11 and 4.13 and the values in Figure 4.10, that these interactions in late burning stages can give rise to significant enrichment. Given that not all of our models evolve past the end of He burning, further work is needed to assess the frequency of these H-He shell interactions among our models. The nature of these H-He interactions affects the production of i-process elements (Clarkson et al. 2018; Clarkson & Herwig 2020), and has important implications for the most metal-poor stars observed and their constraints on the first stars, so these interactions in late phases of the evolution are certainly worth further attention. However, a detailed investigation of these nuclear processes and comparison with higher metallicity models is beyond the scope of this work.

Table 4.1: Summary of the final properties of our model grid. We show the initial mass, rotational velocity as a fraction of critical velocity, evolutionary stage reached by the end of the model run, as well as the He-core and CO-core masses, and the total mass of ^{14}N , ^{12}C, and ^{16}O above the gravitational remnant mass (see Section 4.4) at the evolutionary stage given in the third column.

Initial Mass ($M_\odot$)	$\upsilon_{\rm ini}/\upsilon_{\rm crit}$	evolutionary stage	$M_{\rm He}$ ($M_\odot$)	$M_{\rm CO}$ ($M_\odot$)	$^{14}N_{\rm prod}$ ($M_\odot$)	$^{12}C_{\rm prod}$ ($M_\odot$)	$^{16}O_{\rm prod}$ ($M_\odot$)
9	0	degenerate before C-ignition	1.857	1.039	2.25×10^{-8}	9.51×10^{-2}	2.07×10^{-2}
12	0	End He burning	2.700	1.819	1.21×10^{-7}	0.6096	0.6547
15	0	End He burning	4.194	2.551	1.75×10^{-7}	0.8802	0.1.3822
20	0	Ne burning	4.801	4.386	1.39×10^{-3}	0.6441	1.6452
30	0	He burning, Y_c=0.007	11.813	8.586	3.54×10^{-7}	3.2524	8.8982
40	0	Ne burning	14.996	13.202	1.91×10^{-7}	2.1055	7.8767
60	0	C burning	24.135	24.046	1.16×10^{-4}	3.043	15.697
85	0	C burning	52.225	32.389	4.63×10^{-5}	9.8349	47.1081
120	0	End He burning	73.277	54.406	1.38×10^{-5}	4.8774	40.9261
9	0.4	degenerate before C-ignition	2.328	1.336	2.13×10^{-3}	0.2326	0.2793
12	0.4	Ne burning	3.952	2.355	8×10^{-3}	0.3127	0.9704
15	0.4	C burning	2.852	2.266	0.0123	0.4366	0.6262
20	0.4	C burning	7.198	4.297	4.94×10^{-7}	1.2338	4.1089
30	0.4	End He burning	9.82	6.703	1.4×10^{-6}	0.8876	3.6803
40	0.4	He burning, Y_c=0.04	20.354	10.307	2.74×10^{-6}	2.3408	4.878
60	0.4	He burning, Y_c=0.002	35.122	20.936	1.08×10^{-5}	5.6166	27.2175
85	0.4	He burning, Y_c=0.027	52.364	31.286	1.73×10^{-5}	10.9537	41.6622
120	0.4	He burning, Y_c=0.092	73.938	56.399	1.42×10^{-3}	28.3493	65.812

Table 4.2: Summary of the nature of the CNO boost and the H shell for each model. The third column gives central He fraction at the beginning of the CNO boost when ^{14}N abundance is increased in the H shell. The fourth column states whether convection is triggered in the H shell during the core He-burning phase. We note that models where convective H shells develop after core He burning are not marked here, and models which develop small temporary convective zones are not marked as having a convective shell. This typically occurs for massive non-rotators (see Heger et al. 2000 and Hirschi et al. 2004). ^{14}N yields given (N_{prod}) are the same values from Table 4.1.

Initial Mass ($M_\odot$)	$\upsilon_{ini}/\upsilon_{crit}$	Stage of CNO boost ($\simeq$)	Convective H shell (He burning)	N_{prod} ($M_\odot$)
9	0	N/A		2.25×10^{-8}
12	0	N/A		1.21×10^{-7}
15	0	N/A		1.75×10^{-7}
20	0	post He burning		1.39×10^{-3}
30	0	N/A		3.54×10^{-7}
40	0	N/A		1.91×10^{-7}
60	0	Y_c=0.75		1.16×10^{-4}
85	0	Y_c=0.7	✓	4.63×10^{-5}
120	0	Y_c=0.6		1.38×10^{-5}
9	0.4	Y_c=0.8		2.13×10^{-3}
12	0.4	Y_c=0.7		8×10^{-3}
15	0.4	Y_c=0.5	✓	0.0123
20	0.4	Y_c=0.9	✓	4.94×10^{-7}
30	0.4	Y_c=0.95	✓	1.4×10^{-6}
40	0.4	pre He burning, Y_c=1	✓	2.74×10^{-6}
60	0.4	pre He burning, Y_c=1	✓	1.08×10^{-5}
85	0.4	pre He burning, Y_c=1	✓	1.73×10^{-5}
120	0.4	pre He burning, Y_c=1	✓	1.42×10^{-3}

4.5 Varying Initial Velocity

In this section we compare our models rotating at an initial velocity $\upsilon_{\rm ini} = 0.4\,\upsilon_{\rm crit}$ with the slower rotators that we have modelled of initial rotational velocity $\upsilon_{\rm ini} = 0.2\,\upsilon_{\rm crit}$. As discussed in Section 2.6, this allows us to infer trends in evolutionary behaviour with rotation. From Figure 4.16 we can see that varying the rotational velocity does lead to changes in the HR evolution of these models. There appears to be a general trend where slower rotators evolve similarly to models of lower initial mass with higher rotation. For example, the $20\,{\rm M}_\odot$ model with $\upsilon_{\rm ini}{=}0.2\,\upsilon_{\rm crit}$ evolves similarly to the $15\,{\rm M}_\odot$ $\upsilon_{\rm ini}{=}0.4\,\upsilon_{\rm crit}$ model during He burning. That is to say that it experiences a similar CNO boost where the strong triggering of convection in the H shell leads to a retraction of the He core and subsequent decrease in luminosity, see Section 4.2.2. This is evident in Figure 4.16 from the sharp decrease in luminosity of the $20\,{\rm M}_\odot$ $\upsilon_{\rm ini}{=}0.2\,\upsilon_{\rm crit}$ model, which resembles the beginning of the luminosity dip experienced by the $15\,{\rm M}_\odot$ fast rotating model. Essentially, with less rotational mixing at this lower rotational velocity, less CO is delivered to the H shell so convection is triggered in the H shell for higher initial masses than would be the case at higher rotation. The $12\,{\rm M}_\odot$ and $15\,{\rm M}_\odot$ models with $\upsilon_{\rm ini}{=}0.2\,\upsilon_{\rm crit}$ both maintain radiative H shells throughout He burning and therefore see significant expansion and decrease to lower effective temperatures. The $12\,{\rm M}_\odot$ fast rotator ($\upsilon_{\rm ini}{=}0.4\,\upsilon_{\rm crit}$) sees greater expansion than the slower rotator because the H shell is stronger while still remaining radiative and migrating outwards (Section 4.2.2).

The $9\,{\rm M}_\odot$ model shows particularly interesting behaviour as rotational velocity increases. The differences in energy generation for the three $9\,{\rm M}_\odot$ models at different rotational velocities are shown in Figure 4.17 at different stages of He burning. For the $\upsilon_{\rm ini}{=}0.2\,\upsilon_{\rm crit}$ model the effect of rotation is as we see for the $12\,{\rm M}_\odot$ and $15\,{\rm M}_\odot$ models where rotational mixing strengthens the H shell. However, as we move to higher rotation again, $\upsilon_{\rm ini} = 0.4\,\upsilon_{\rm crit}$, the H shell is in fact weaker. We do note that the He core is larger for this higher rotational velocity. Indeed it is clear through the contribution to the total luminosity that the faster rotator is more dependent on the He core than the slower rotator. This explains the behaviour that we see on the HR diagram in Figure 4.16. The slow rotator evolves to low effective temperatures due to the dominant H shell, while the fast rotator remains at higher effective temperature. This emphasises the conclusion from Section 4.2, that the relative core and shell strength dominate the evolution of the surface properties. Rotation plays a vital role in this balance of core and shell strength, it provides additional fuel through rotational mixing into the core, but it also boosts the H shell through delivery of heavy elements from the core which can result in core retraction. It seems then that there are two competing effects, rotational mixing either increases He core size, or it leads to a stronger dominant H shell which suppresses the core. In the $12\,{\rm M}_\odot$ case the H shell wins out, while rotational mixing favours growth of the core for the $9\,{\rm M}_\odot$ model.

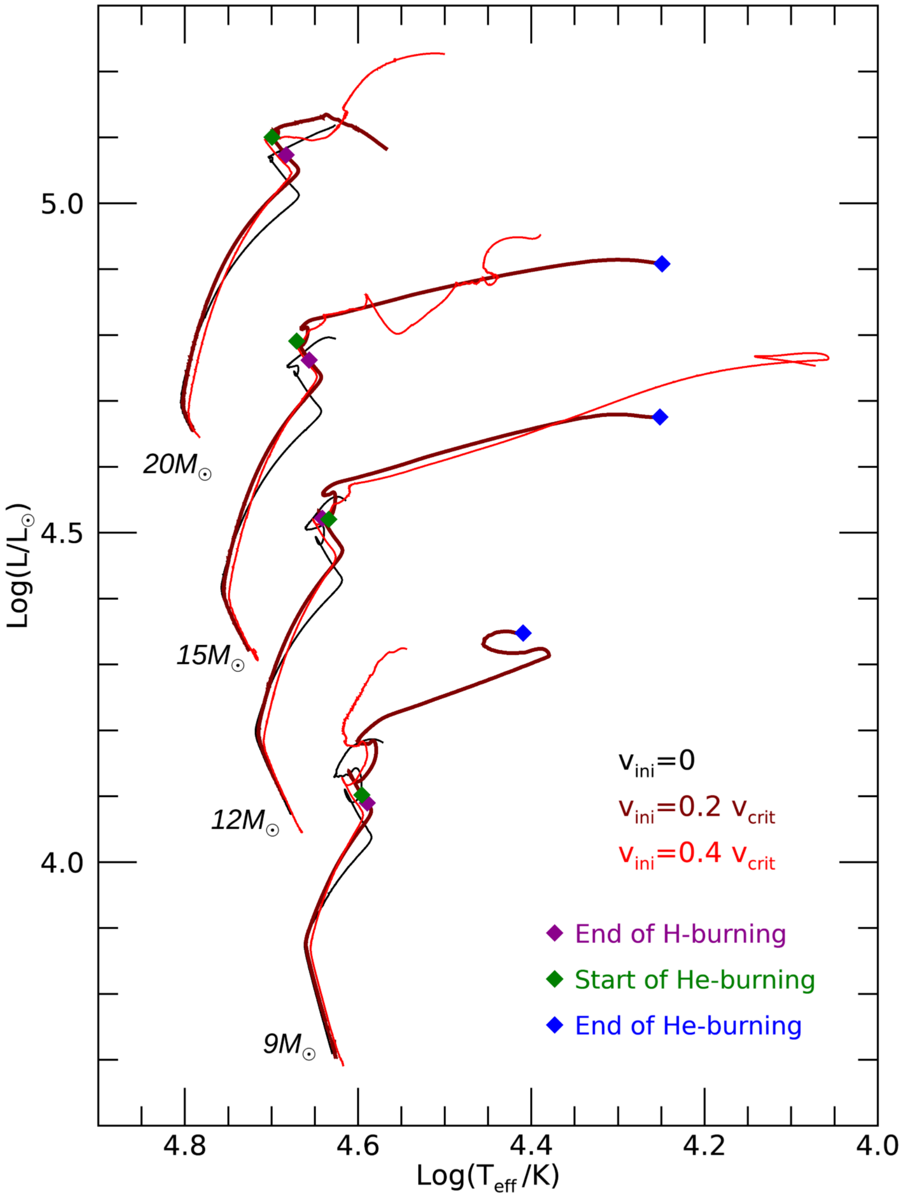

Figure 4.16: Evolution along the HR diagram for models with initial masses $M_{\rm ini} = 9-20\,{\rm M}_\odot$ with three rotational velocities. Non-rotating models are shown in black, rotating models with initial rotational velocity $\upsilon_{\rm ini} = 0.2\,\upsilon_{\rm crit}$ are shown in maroon, and rotating models with $\upsilon_{\rm ini} = 0.4\,\upsilon_{\rm crit}$ are shown in red. Models are evolved to the end of He burning, with the exception of the $20\,{\rm M}_\odot$ model with $\upsilon_{\rm ini} = 0.2\,\upsilon_{\rm crit}$ which was evolved until $Y_c = 0.31$. Evolutionary phases for models with $\upsilon_{\rm ini} = 0.2\,\upsilon_{\rm crit}$ are indicated by the legend.

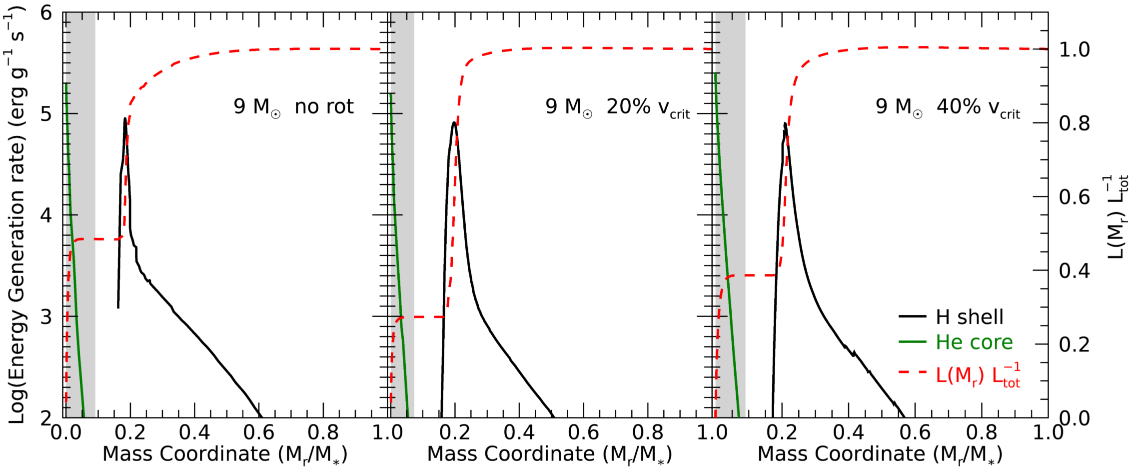

(a) Energy Generation at Y_c=0.5

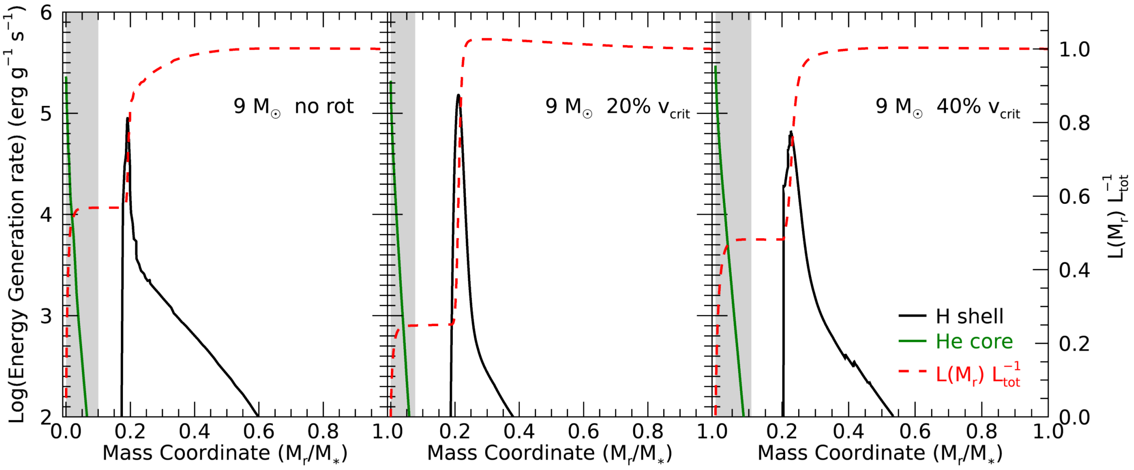

(b) Energy Generation at Y_c=0.25

Figure 4.17: Similar to Figures 4.5a to 4.5c, but for $9\,M_\odot$ models of rotational velocities $\upsilon_{\rm ini} = 0, 0.2, 0.4\,\upsilon_{\rm crit}$ at two stages during He burning indicated by their values of Y_c.

4.6 Conclusions

Pop III models are unique in their evolution in a number of ways that impact their observable features and rotational effects. Their zero-metallicity nature means that they are unable to burn hydrogen through the CNO cycle initially and without this crucial energy supply they experience a contraction phase during the early MS. The lack of CNO elements is not only an issue for the central regions of the star but also leads to sharp μ-gradients and energy increases (due to triggering of the CNO cycle) in the stellar envelope as He-burning products are transported outwards. Therefore rotational mixing has a unique impact in these stars. We have carried out a detailed investigation of the interior structure of these models throughout their evolution and how this has driven the evolution of the surface properties. This has given us a new understanding and perspective on the role of rotation for Pop III stars. The following are our main conclusions from this chapter.

- Rotation has a significant impact on the observable signatures of Pop III stars through two main effects. Firstly, rotational mixing brings additional fuel into the nuclear burning core which increases luminosity as well as stellar lifetimes. Secondly, rotational mixing brings He-burning products from the core to the H-burning shell during later evolutionary phases. This changes the temperature profile, and can lead to significant expansion in some models depending on the relative core size. The relative core size is crucial here, because the contribution of the shell and the core to the total energy produced tells us about the structure of the star and what dominates with regard to the evolution of the surface properties.

- Despite weaker meridional currents for Pop III stars, angular momentum can build up at the surface for fast rotating massive models because of their negligible mass loss through radiative winds. This spin up brings models $M_{\rm ini} \geq 60\,{\rm M}_\odot$ with $\upsilon_{\rm ini} = 0.4\,\upsilon_{\rm crit}$ to critical rotation on the MS which leads to increased mass loss with as much as $3.5\,{\rm M}_\odot$ of material lost for our most massive model of $M_{\rm ini} = 120\,{\rm M}_\odot$. Further work is needed to determine the nature of this mass loss.

- Rotational mixing strongly affects metal enrichment, but does not always increase metal production as we see at higher metallicities. Rotation leads to an earlier CNO boost to the H shell during He burning, which may hinder metal enrichment. This is true for precise mass and initial velocity domains, and only for the core He-burning phase. In these cases the triggering of convection by the CNO boost in the H shell causes a retraction of the He-burning core. As the core grows the H shell moves outwards and does so more quickly than He-burning products can be rotationally mixed out from the core, therefore hindering the interaction of these products with the H-burning shell, which is required for metal enrichment. The H-He shell interactions after core He burning play a crucial role in metal production, and there rotation may boost enrichment. This highlights the complexity in the metal enrichment processes of these models. A detailed understanding of the interior structure is therefore required to accurately predict metal yields.

- Through comparing our models with slower rotators at $\upsilon_{\rm ini} = 0.2\,\upsilon_{\rm crit}$, we have shown that a general trend exists where higher rotation in a model of a certain initial mass leads to similar evolutionary behaviour of a more massive model with lower initial rotation. There is a trade off between increasing initial mass and rotational velocity in order to see the same evolution of model structure. For example, the $M_{\rm ini} = 20\,{\rm M}_\odot$ model with $\upsilon_{\rm ini} = 0.2\,\upsilon_{\rm crit}$ sees a strong CNO boost with significant change to total luminosity, similarly to the $M_{\rm ini} = 15\,{\rm M}_\odot$ model with $\upsilon_{\rm ini} = 0.4\,\upsilon_{\rm crit}$ model which also sees this behaviour, indicated by the luminosity dip on the HR diagram.

Chapter 5

Ionizing Photon Production of Population III Stars: Effects of Rotation, Convection and Initial Mass Function

In this chapter we present our predictions for the ionizing photon production rates of Pop III stars based on our stellar evolution model grid presented in Chapters 3 and 4. In Section 2.8 we describe how we calculate the ionizing photon production rates of our models, including our blackbody approximation in Section 2.8.1. We also detail how we estimate the ionizing photon production of zero-metallicity populations in Section 2.8.3 and Section 2.8.4. Given the importance of the first stars in understanding the reionization of the Universe (Section 1.3.2), the predictions presented here will provide valuable data for future hydrodymanical simulations of the early Universe and the epoch of reionization. The work discussed in this chapter has been published in Murphy et al. (2021b).

5.1 Analytical Fits

We first present our analytical fits of the total ionizing photons produced by non-rotating models in the full mass range $1.7\,\mathrm{M}_\odot \leq M_{\mathrm{ini}} \leq 500\,\mathrm{M}_\odot$. This includes the non-rotating intermediate and high mass models from our Geneva stellar evolution grid presented in Chapter 3, and also includes the very massive models described in Sec-

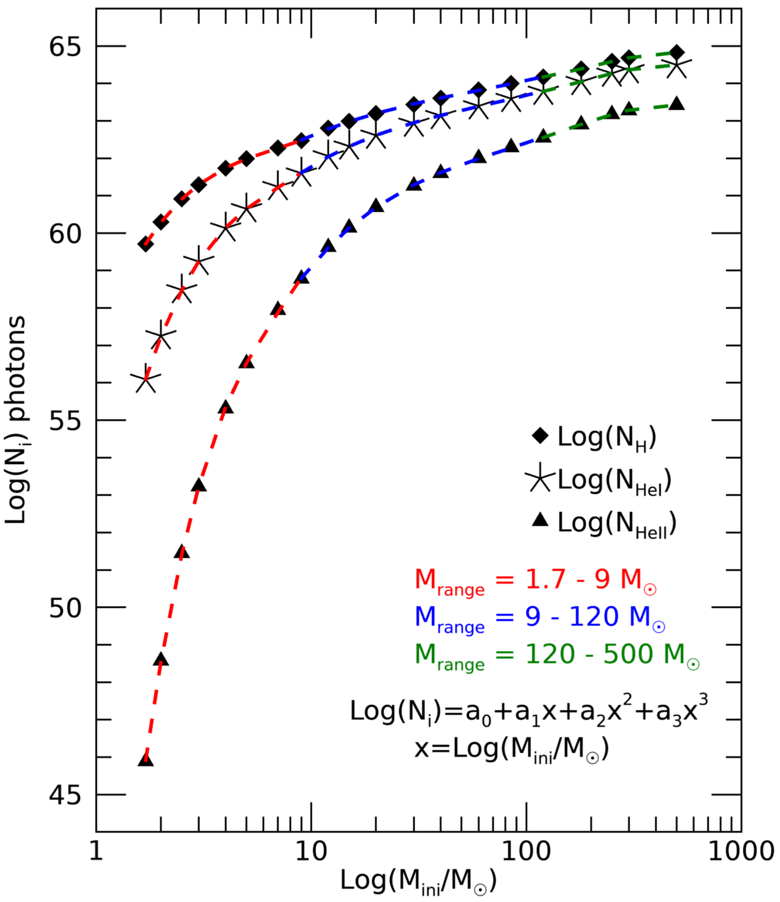

Figure 5.1: Total ionizing photons produced, $\log(N_{\rm i})$, by individual non-rotating models in the mass range $1.7\,\mathrm{M}_\odot \leq M_{\rm ini} \leq 500\,\mathrm{M}_\odot$. The different symbols correspond to photons capable of ionizing H (diamonds), He I (asterisks), and He II (triangles). Also indicated are the mass ranges corresponding to the different fits, and the equation of the cubic polynomial fit. The coefficients of each of the six fits are presented in Table 5.1.

tion 2.8.4 ($M_{\rm ini} = 180, 250, 300, 500\,\mathrm{M}_\odot$, Martinet et al., 2021 in prep.). These fits will be useful for future studies and allow for convenient calculation of primordial ionizing photon production in hydrodynamical simulations. In Figure 5.1 we plot the total ionizing photons produced, $\log(N_{\rm H})$, $\log(N_{\rm HeI})$ and $\log(N_{\rm HeII})$ (see eq. 2.41), versus the initial mass, $\log(M_{\rm ini}/\mathrm{M}_\odot)$, along with their least-squares polynomial fits for the mass ranges $1.7-9\,\mathrm{M}_\odot$, $9-120\,\mathrm{M}_\odot$, and $120-500\,\mathrm{M}_\odot$. These fits are described by $\log(N_{\rm i}) = a_0 + a_1 x + a_2 x^2 + a_3 x^3$, where $x = \log(M_{\rm ini}/\mathrm{M}_\odot)$, and the coefficients for each fit are presented in Table 5.1. We note that unlike Schaerer (2002) these values are based on a blackbody approximation (Section 2.8.1). For zero-metallicity stars the main effect of not using stellar atmospheres will be seen in the emission of He II (and to a lesser degree He I) ionizing photons. H ionizing photons are not expected to be significantly impacted since H is fully ionized in the atmospheres of our models. We investigate the impact of this blackbody approximation in Section 5.5.2. In the following sections we study how rotation and convection impact the ionizing photon production. These analytical fits, in conjunction with our predictions for variations with evolutionary parameters, can be used to inform future studies on Pop III ionizing radiation.

Table 5.1: Coefficients of least-squares polynomial fits of total ionizing photons produced, $\log(N_\mathrm{i})$, by non-rotating models in the full mass range $1.7\,\mathrm{M}_\odot \leq M_\mathrm{ini} \leq 500\,\mathrm{M}_\odot$, of the form $\log(N_\mathrm{i}) = a_0 + a_1x + a_2x^2 + a_3x^3$, where $x = \log(M_\mathrm{ini}/\mathrm{M}_\odot)$. The mass range is divided into three ranges to cover the intermediate mass models 1.7-9 $\mathrm{M}_\odot$ (Murphy et al. 2021a), the massive models 9-120 $\mathrm{M}_\odot$ (Murphy et al. 2021a), and the very massive models 120-500 $\mathrm{M}_\odot$ (Martinet et al., 2021 in prep.). These fits are illustrated in Figure 5.1.

Quantity	M_ini	a_0	a_1	a_2	a_3
$\log(N_\mathrm{H})$	1.7-9 $\mathrm{M}_\odot$	56.97	15.26	-16.02	6.36
$\log(N_\mathrm{H})$	9-120 $\mathrm{M}_\odot$	57.81	7.89	-3.82	0.72
$\log(N_\mathrm{H})$	120-500 $\mathrm{M}_\odot$	96.12	-44.18	19.84	-2.88
$\log(N_\mathrm{HeI})$	1.7-9 $\mathrm{M}_\odot$	50.76	29.54	-30.19	11.68
$\log(N_\mathrm{HeI})$	9-120 $\mathrm{M}_\odot$	54.53	12.11	-5.95	1.09
$\log(N_\mathrm{HeI})$	120-500 $\mathrm{M}_\odot$	92.51	-41.09	18.96	-2.81
$\log(N_\mathrm{HeII})$	1.7-9 $\mathrm{M}_\odot$	33.55	68.19	-69.13	26.64
$\log(N_\mathrm{HeII})$	9-120 $\mathrm{M}_\odot$	44.96	23.64	-11.52	2.03
$\log(N_\mathrm{HeII})$	120-500 $\mathrm{M}_\odot$	86.11	-36.27	17.61	-2.70

5.2 Effects of Rotation

In this section we will discuss how the ionizing photon production of Pop III stars varies with rotation based on the initial rotational velocity of our grid presented in Chapter 3, $\upsilon_\mathrm{ini} = 0.4\,\upsilon_\mathrm{crit}$. We will first investigate how rotation impacts the ionizing photon production rate, Q_i (eq. 2.40), throughout the evolution, and will then study how rotation subsequently impacts the total ionizing photons produced by individual Pop III stars.

5.2.1 Impact on Ionizing Photon Production Rate

The evolution of the ionizing photon production rate, Q_i, is shown in Figure 5.2 for photons capable of ionizing H, He I and He II. Higher initial mass models can be distinguished by their shorter stellar lifetimes. We see that the higher the initial mass the larger the ionizing photon production rate. This is not surprising given that more massive models are typically hotter and more luminous than models of lower initial mass. Figure 5.2 shows that there are two competing effects in determining how many ionizing photons will be produced by a model during its lifetime, the ionizing photon production rate, which depends on the surface properties; and the stellar lifetime, which limits the time available for producing ionizing photons. Models including rotation are indicated by dashed lines and are noticeable for their longer lifetimes compared to non-rotating models (solid lines). We would expect that this will then increase the total number of ionizing photons produced by rotators, but this is not clear given that the ionizing photon production rate varies due to differences in surface properties with rotation.

To further illustrate how the ionizing photon production rate varies with different

Figure 5.2: Evolution of the ionizing photon production rate (Q_i) for models in the mass range $9\,\mathrm{M}_\odot \leq M_\mathrm{ini} \leq 120\,\mathrm{M}_\odot$. Three ionizing photons species are shown, H (upper panel), He I (middle panel), He II (lower panel). Solid lines show non-rotating models, dashed lines show rotating models, and colours indicate different initial masses as shown in legend.

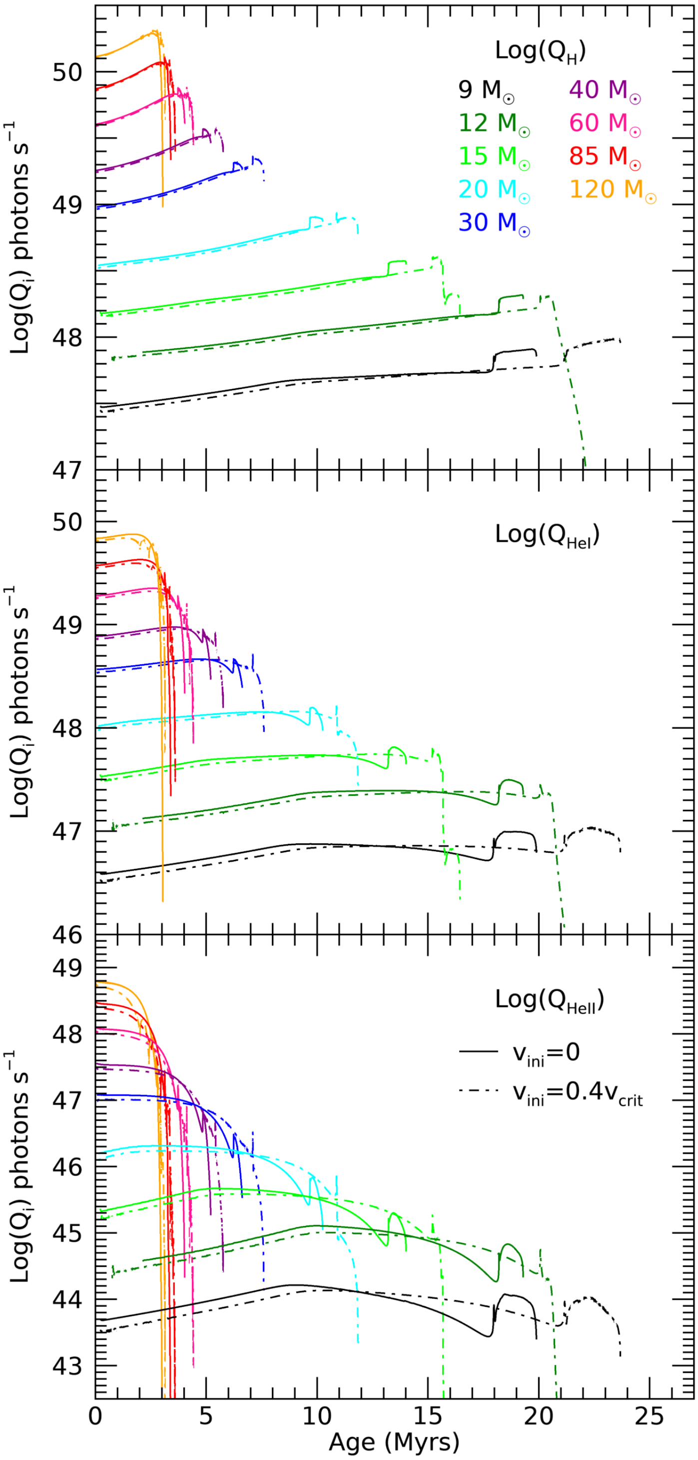

initial masses we plot the production rate of H ionizing photons, $\log(Q_{\mathrm{H}})$, over the evolutionary tracks of the models in Figure 5.3. The values of $\log(Q_{\mathrm{H}})$ are taken at equal intervals of age, so this also has the advantage of visualising the time evolution across the HR diagram, and where each model spends the majority of its time producing ionizing photons. Since these stars spend approximately 90% of their lifetimes on the MS, it is not surprising that they produce the majority of their ionizing photons there. From this figure we can see how the H ionizing photon production rate varies in different regions of luminosity and effective temperature, and visualise why models of higher initial mass have higher ionizing photon production rates. We can also observe how rotational effects on the surface properties result in changes to the ionizing photon production rate. For example, the $12\,\mathrm{M}_{\odot}$ model with rotation experiences a decrease in surface temperature (T_{eff}) at late evolutionary stages which results in a large decrease in Q_{H}.

To better understand how the ionizing photon production rate, Q_{i}, varies with rotation we calculate the ratio of Q_{i} for models with rotation to those without, $\frac{Q_{\mathrm{rot}}}{Q_{\mathrm{norot}}}$, for each of the three ionizing photon species, H, He I, and He II. In order to compare their time evolutions properly, this is done for the normalised age of each model. These ratios are shown in Figure 5.4 for each initial mass in the range $9\,\mathrm{M}_{\odot} \leq M_{\mathrm{ini}} \leq 120\,\mathrm{M}_{\odot}$. It can be seen that rotation impacts the production rate of each species differently. In the case of H ionizing photons (upper panel Figure 5.4), while rotating models start their lives producing less H ionizing photons, the ratio of Q_{rot} to Q_{norot} increases steadily through most of the lifetime, although there is some divergence in late stages for the more massive models. Focusing now on He I ionizing photons (middle panel Figure 5.4) we see an earlier divergence in the trend for varying initial masses. From about half-way through the lives of the models, less massive models see an increase of Q_{rot} to Q_{norot} while more massive models see a decrease in this ratio. We also note that, with the exception of the late stages of models with $M_{\mathrm{ini}} = 9 - 20\,\mathrm{M}_{\odot}$, more He I ionizing photons are produced by non-rotating models. Finally we look at the effect of rotation on the production of He II ionizing photons (lower panel Figure 5.4). The changes in behaviour moving from H to He I ionizing photons seem amplified here. That is to say that the ratio of Q_{rot} to Q_{norot} has decreased even further, with more massive rotating models producing as little as half the He II ionizing photons as their non-rotating counterparts for a significant fraction of the lifetime. These evolving trends for different photon species call into question how these ionizing photon production rates depend on the surface properties.

To understand the trends seen in Figure 5.4 and what leads to differences from species to species, we look at the impact of rotation on surface properties throughout the normalised lifetimes. This is shown in Figure 5.5, again using ratios to disentangle where rotating models are hotter or more luminous than non-rotating models, and vice versa. We see separate trends here for these two surface properties. On the one hand, the effective temperature of rotating models tends to decrease over the evolution relative

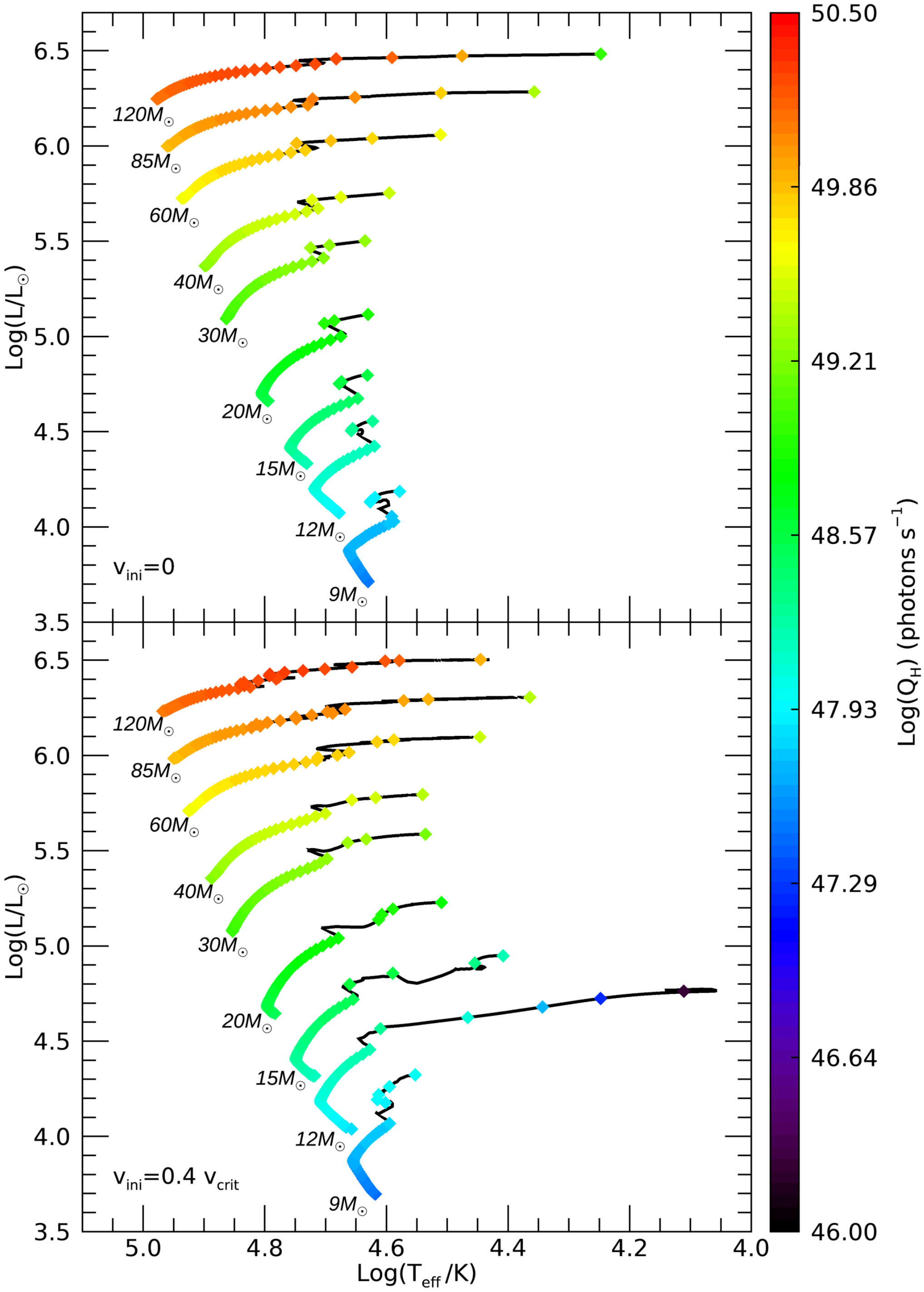

Figure 5.3: *Upper:* Evolutionary tracks of non-rotating models from Chapters 3 and 4 in the mass range $9\,M_\odot \leq M_{\rm ini} \leq 120\,M_\odot$. Overplotted are the values for the H ionizing photon production rate, $\log(Q_{\rm H})$, as indicated by the colour bar on the right-hand side. *Lower:* Same as upper panel but for models rotating with initial velocity $\upsilon_{\rm ini} = 0.4\,\upsilon_{\rm crit}$.

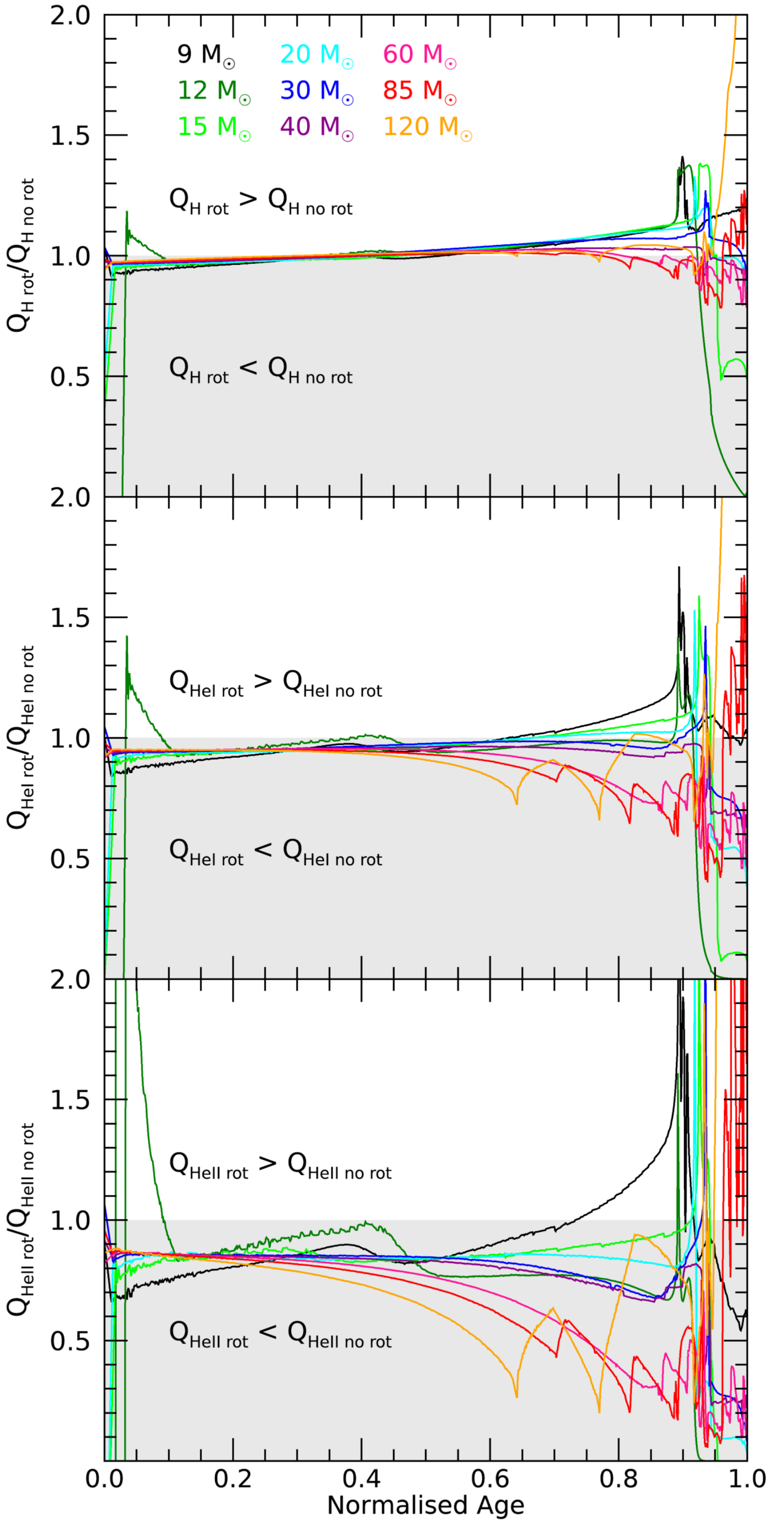

Figure 5.4: *Upper:* Evolution of the ratio of the H ionizing photon production rate, Q_{H} (eq. 2.40), by models with rotation to models without rotation. Colours represent different initial masses, M_{ini}. The white region indicates where Q_{H} is higher with rotation, conversely the grey region indicates where non-rotating models have higher Q_{H}. *Middle:* Same as upper panel but for He I ionizing photons. *Lower:* Same as upper panel but for He II ionizing photons.

to non-rotating models, a trend which is more strongly seen as initial mass increases. This decrease in T_{eff} for more massive models, M_{ini}=60, 85, 120 $M_{\odot}$, corresponds to their approach towards critical rotation (see Figure 4.8). On the other hand, the luminosity of rotating models tends to increase over the evolution relative to non-rotating models, and in contrast to the trend for temperature this is more strongly seen for less massive models. This explains two things from Figure 5.4. Firstly, it explains the dichotomy of trends with initial mass at late stages where the impact of rotation appears to diverge, and secondly, it illustrates which of the surface properties dominates the production rate of each ionizing photon species. We can now observe that H ionizing photons are dominated by the luminosity of the model since the trends seen in the upper panel of Figure 5.4 most closely resemble the trends seen in the lower panel of Figure 5.5. Similarly we deduce that He II ionizing photons are dominated by effective temperature, while the dependencies of He I ionizing photons on the surface properties lie somewhere in between. This is a reflection of how each species of photon is determined in the first place, and the sensitivity of the stellar radiative flux to the effective temperature in different wavelength domains. As discussed in Sections 2.8.1 and 2.8.2, we use a blackbody approximation to obtain the radiative flux and subsequently integrate below the different threshold wavelengths to determine the ionizing photon production rate for each species. In Figure 2.7 we illustrated this calculation for the three different ionizing photon species. From that figure it is evident that the lower the wavelength, the larger the effect of changing the effective temperature on the number of photons at that wavelength. This phenomenon would be similar had we used detailed atmospheres.

5.2.2 Impact on Total Ionizing Photons Produced

As has been identified in Section 5.2.1, while Q_{i} increases with initial mass, more massive models also have shorter lifetimes, and therefore the outcome for total ionizing photons produced by a star of a given initial mass, N_{i} (eq. 2.41), depends on the combination of these two effects. In Figure 5.6 we present the results for total ionizing photons produced by each initial mass model, with and without rotation. These values are also presented in Table 5.2. From this figure it is clear that the total number of ionizing photons produced increases with increasing initial mass, despite the decrease in stellar lifetimes. This is true for all three species of ionizing photons. The trend with initial mass is apparent from the upper panel of this figure, however, the trend with rotation is more difficult to observe. To clarify this we present in the lower panel of Figure 5.6 the ratio of total ionizing photons produced by rotating and non-rotating models of a given initial mass. The complexity of the trends in this figure reflects the complexities of the impact of rotation on the surface properties. The effect of rotation is not the same for each initial mass, and each species is affected differently by rotation, following what we

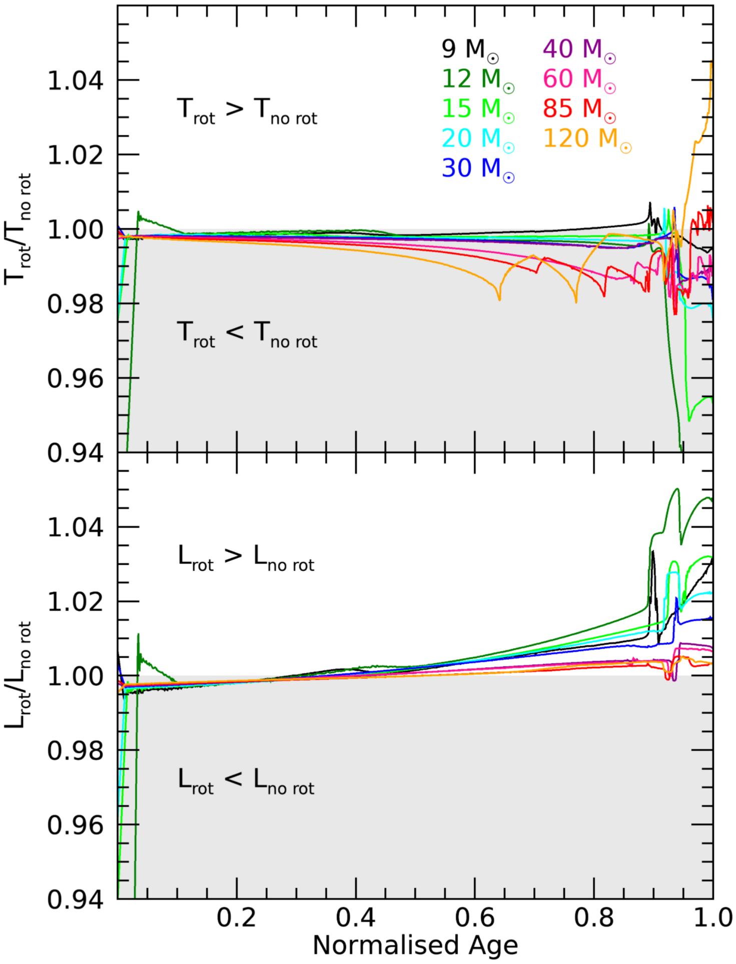

Figure 5.5: *Upper:* Evolution of the ratio of $T_{\rm eff}$ of models with rotation to models without rotation. Colours represent different initial masses, $M_{\rm ini}$. The white region indicates where $T_{\rm eff}$ is higher with rotation, conversely the grey region indicates where non-rotating models have higher $T_{\rm eff}$. *Lower:* Same as upper panel but for luminosity.

have discussed in Section 5.2.1. For each ionizing photon species we see a decrease in the ratio $N_{\rm rot}/N_{\rm norot}$ as we move to higher initial masses. For the $9\,{\rm M}_\odot$ model, we see that rotation increases the total ionizing photons produced for all three species, with the rotating model producing ∼25% more H ionizing photons than the non-rotating $9\,{\rm M}_\odot$ model. For all other initial masses rotating models produce less He II ionizing photons than non-rotating models, with the $120\,{\rm M}_\odot$ rotating model producing ∼25% less He II ionizing photons than the non-rotating model. This result is important, because it tells us that not only will the total ionizing photons produced change for differing initial masses, but the rotational effects vary also. We have discussed the impact of rotation on surface properties and stellar evolution of the first stars in Chapter 4. While rotational effects are complex and differ significantly with initial mass, the dominant effects are increasing luminosity, due to larger convective cores, and decreasing surface temperature, due to changes to stellar structure. The outcome of these two competing effects varies with initial mass. We saw this in Figure 5.5, where decreasing surface temperature with rotation was more prominent for higher initial masses, and increasing luminosity with rotation was more prominent for lower initial masses. From Section 5.2.1 we found that H ionizing photons are dominated by luminosity effects, and He II ionizing photons are

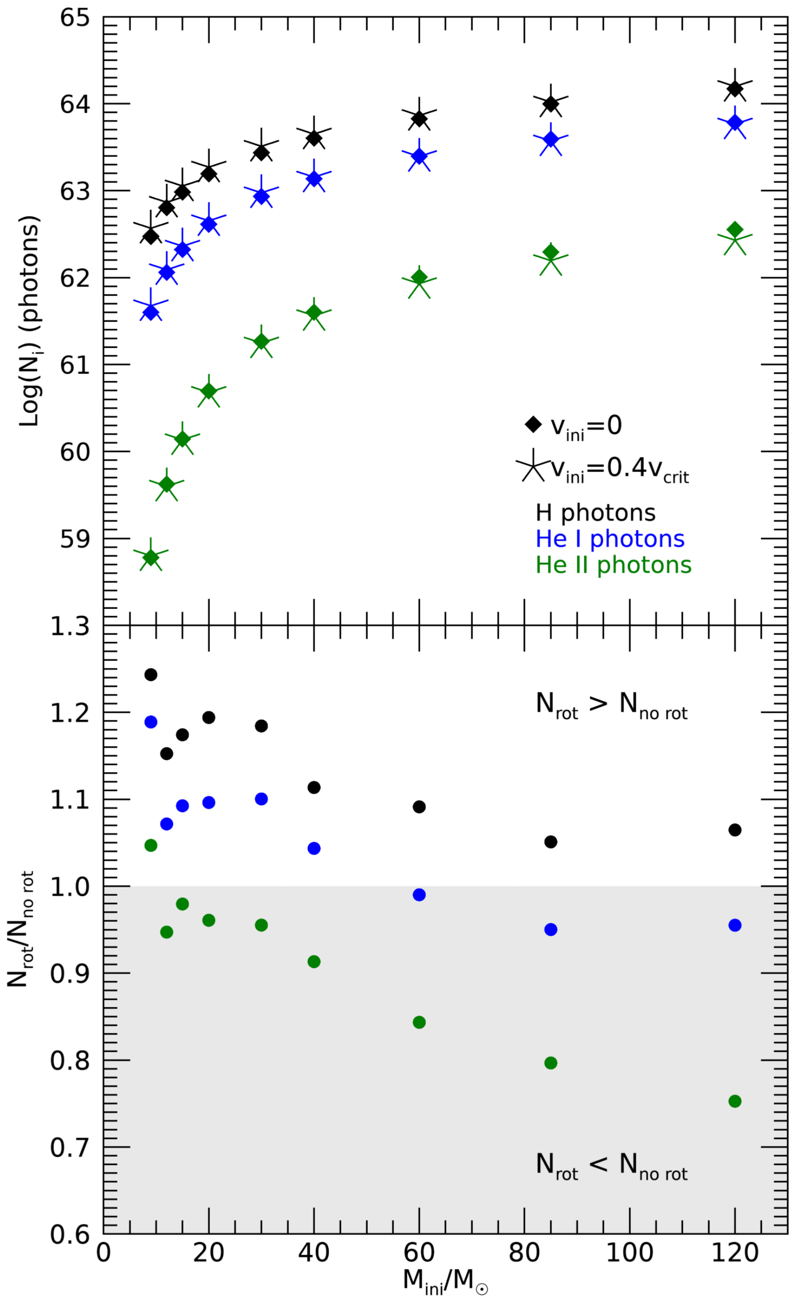

Figure 5.6: *Upper:* Total ionizing photons produced from the ZAMS to end He burning as a function of M_{ini}. Models with (without) rotation are indicated by an asterisk (diamond) symbol. Colours show the different ionizing photon species. *Lower:* Ratio of total ionizing photons produced by models with rotation to models without rotation as a function of M_{ini}. Similarly to Figure 5.4, the grey region shows where rotating models produced less ionizing photons from the ZAMS to the end of He burning, and the white region shows where more ionizing photons were produced by rotators.

dominated by surface temperature effects. This is why in the lower panel of Figure 5.6 we see a stronger change to H ionizing photons with rotation at lower initial masses, and a stronger change to He II ionizing photons at higher initial masses. The mass dependency of rotational effects is thus evident in the ionizing photon species most impacted. This effect should be considered in studying the impact of the initial mass function on ionizing photons produced.

5.3 Convective Overshooting

Having investigated the effects of rotation on ionizing photon production, we now turn our attention to convective mixing. In this section we will discuss how increased convective overshooting impacts the total ionizing photons produced by Pop III stars.

5.3.1 Impact on Total Ionizing Photons Produced

Similarly to rotation, convective overshooting above the core increases interior mixing and impacts stellar evolution significantly. As described in Section 2.6, our model grid takes a value of $\alpha_{\rm ov} = 0.1$ for the overshooting parameter for consistency with previous Geneva stellar evolution grids (Ekström et al. 2012; Georgy et al. 2013a; Groh et al. 2019). However, in recent research it has been predicted that the overshooting parameter could be higher for massive stars, with $\alpha_{\rm ov} = 0.3 - 0.5$ more closely matching observations of massive MS stars (Castro et al. 2014; Schootemeijer et al. 2019; Higgins & Vink 2019; Martinet et al. 2021). We therefore want to investigate the impact that increased convective overshooting will have on ionizing photon production. To do this we take additional Geneva stellar evolution models of Pop III stars with consistent physical ingredients to our non-rotating grid (Section 2.6), barring the overshooting parameter which in this new set of models is $\alpha_{\rm ov} = 0.3$. By comparing these models we can discern the effect that increased convective overshooting has on the surface properties, and subsequently the ionizing photon production.

The results of this investigation are presented in Figure 5.7, with values given in Table 5.2. We show the total ionizing photons produced by each model in the upper panel, while the lower panel shows the ratio of photons produced by the models with higher overshooting, to those with the lower overshooting parameter in our original model grid. We find that for all ionizing photon species, at all initial masses considered here, that increased convective overshooting increases the total ionizing photons produced. This increase varies for different initial masses, but generally speaking we find an increase of approximately 20% to ionizing photons produced. This result is a reflection of the increased luminosity and surface temperature of the models with higher convective overshooting, but mainly results from the increased lifetime of models with higher overshooting. This is evident from the variations in the percentage increase of ionizing photons for different initial masses. The most notable increase in ionizing photons produced is that of the $15\,{\rm M}_{\odot}$ model, which experiences the largest increase in MS lifetime with higher overshooting for this initial mass range. Similarly to what we discussed regarding Figure 5.6, the impact on different ionizing photon species tells us the dominant effect on surface properties for different initial masses. Changes to surface temperature impact He II ionizing photons more strongly, while changes to luminosity predominantly impact H ionizing photons. Despite these variations for different stellar masses, higher

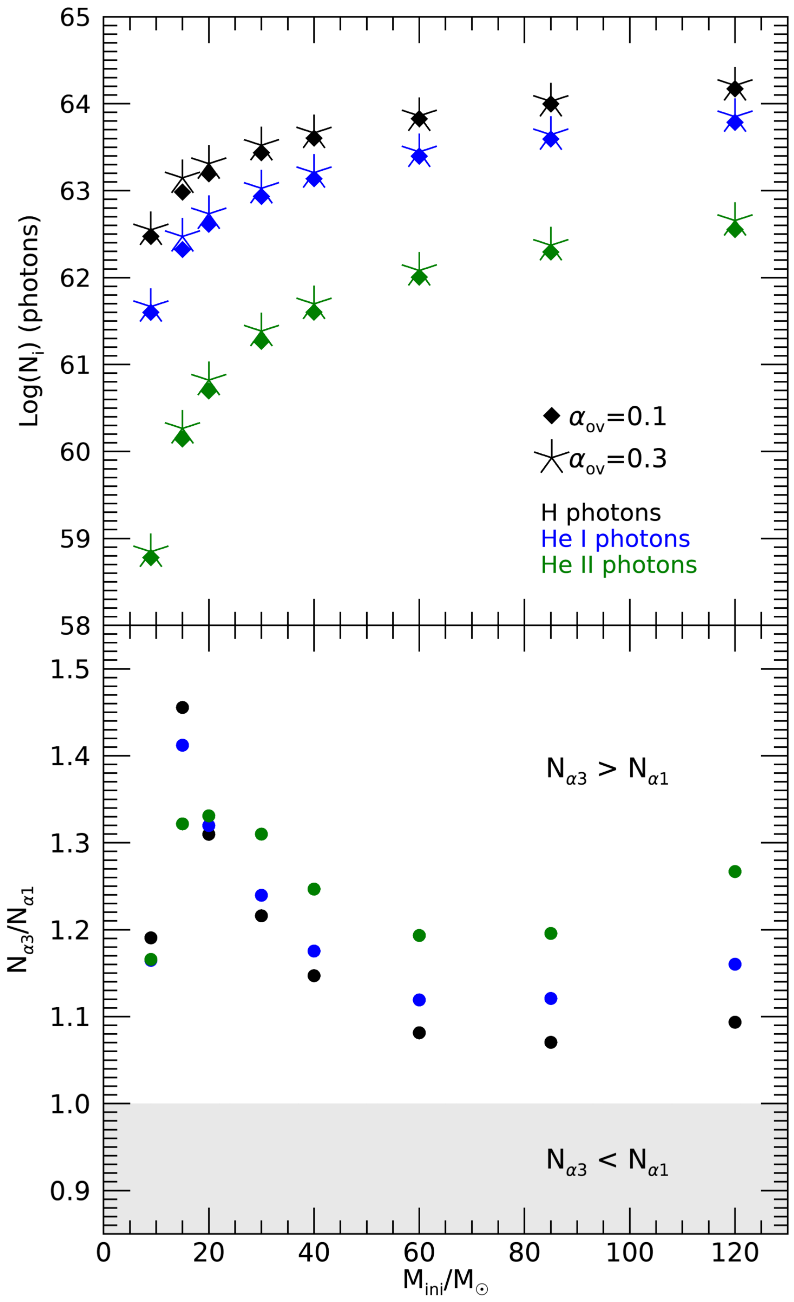

Figure 5.7: *Upper:* Total ionizing photons produced by models with convective overshooting parameter $\alpha_{ov} = 0.1$ (diamond symbols) and $\alpha_{ov} = 0.3$ (asterisk symbols). *Lower:* Ratio of total ionizing photons produced by models with $\alpha_{ov} = 0.3$ to models with $\alpha_{ov} = 0.1$.

overshooting increases ionizing photon production for all initial masses considered here, which suggests that we can scale the contribution of Pop III stars to ionization with the overshooting parameter considered.

5.4 Initial Mass Function

Now that we understand ionizing photon production for individual stars at zero metallicity, we focus now on the ionizing photon production of populations of these stars. In this section we will study how varying the nature of the initial mass function (IMF) impacts ionizing photon production of zero-metallicity populations. We investigate the impact of varying the slope of the IMF for different star formation assumptions, and later test the impact of the minimum and maximum masses of the population.

5.4.1 Impact on Ionizing Photons Produced by Stellar Populations

For this investigation we produce IMFs of the form $\xi(M) \propto M^{-\alpha}$ (Section 2.8.3) and vary the slope, α, with a fixed total stellar mass for the population of $\mathrm{M_{tot}} = 10^6\,\mathrm{M_\odot}$. Figure 5.8 shows the total ionizing photons produced by stars of different initial masses weighted by the different IMFs, i.e. $\log(N_\mathrm{i}\xi(M))$. The stars considered here are non-rotating with a convective overshooting parameter of $\alpha_\mathrm{ov} = 0.1$. For each IMF, the total ionizing photons produced at each initial mass vary depending on the number of stars produced at that initial mass. Furthermore, the total ionizing photons produced as depicted here represents the number produced following the lifetime of each model, such that each star has enough time to produce their total number of ionizing photons, N_i (see Section 2.8.2). From this figure we find which initial mass model dominates the ionizing photon production for different IMFs. For the steepest IMF, the Salpeter IMF (α=2.35), less massive models dominate ionizing photon production, then as you move to lower values of α the more massive models become more important for ionization. This trend holds for each ionizing photon species, however, the more energetic He ionizing photons are dominated by higher initial masses than H ionizing photons. For the Salpeter IMF (α=2.35), the $12\,\mathrm{M_\odot}$ stars contribute most to H ionizing photon production, the $15\,\mathrm{M_\odot}$ stars contribute most to He I ionizing photon production, and the production of He II ionizing photons is dominated by $40\,\mathrm{M_\odot}$ stars. However, for the Stacy & Bromm (2013) (SB13, α=0.17) IMF, the $120\,\mathrm{M_\odot}$ model dominates H, He I, and He II ionizing photon production.

The impacts of rotation and convection for varying IMF slopes are summarised in Figure 5.9. Similarly to Figures 5.6 and 5.7, the total ionizing photons produced for different initial conditions are shown in the upper panel, and ratios of these points are shown in the lower panel. Unlike Figures 5.6 and 5.7, which showed ionizing photons produced by individual stars of different initial masses (N_i), this plot shows the total ionizing photons produced by stellar populations of different IMF slopes (N_pop, eq. 2.44). We assume here a population stellar mass of $\mathrm{M_{tot}} = 10^6\,\mathrm{M_\odot}$, and that all stars in the population have produced their total ionizing photons for their full lifetimes, having formed from a single starburst. This figure depicts the importance of the choice of IMF in determining a population's contribution to reionization. As the IMF slope increases, the number of massive stars in the population decreases. Since these more massive stars produce the most ionizing photons, we see a trend of decreasing ionizing photon production with increasing IMF slope. We see this clearly for He II ionizing photons, however, for H ionizing photons the decrease with increasing IMF slope is much less

Figure 5.8: *Upper:* Total H ionizing photons produced by non-rotating stars of different initial masses weighted by initial mass functions of the form $\xi(M) \propto M^{-\alpha}$. The total mass of stars in each population is $10^6\,\mathrm{M}_\odot$. Ionizing photons produced at each initial mass vary based on the number of stars produced at that mass by the given IMF. IMF slope values are indicated by the legend. *Middle:* same as upper panel but for He I ionizing photons. *Lower:* same as upper panel but for He II ionizing photons.

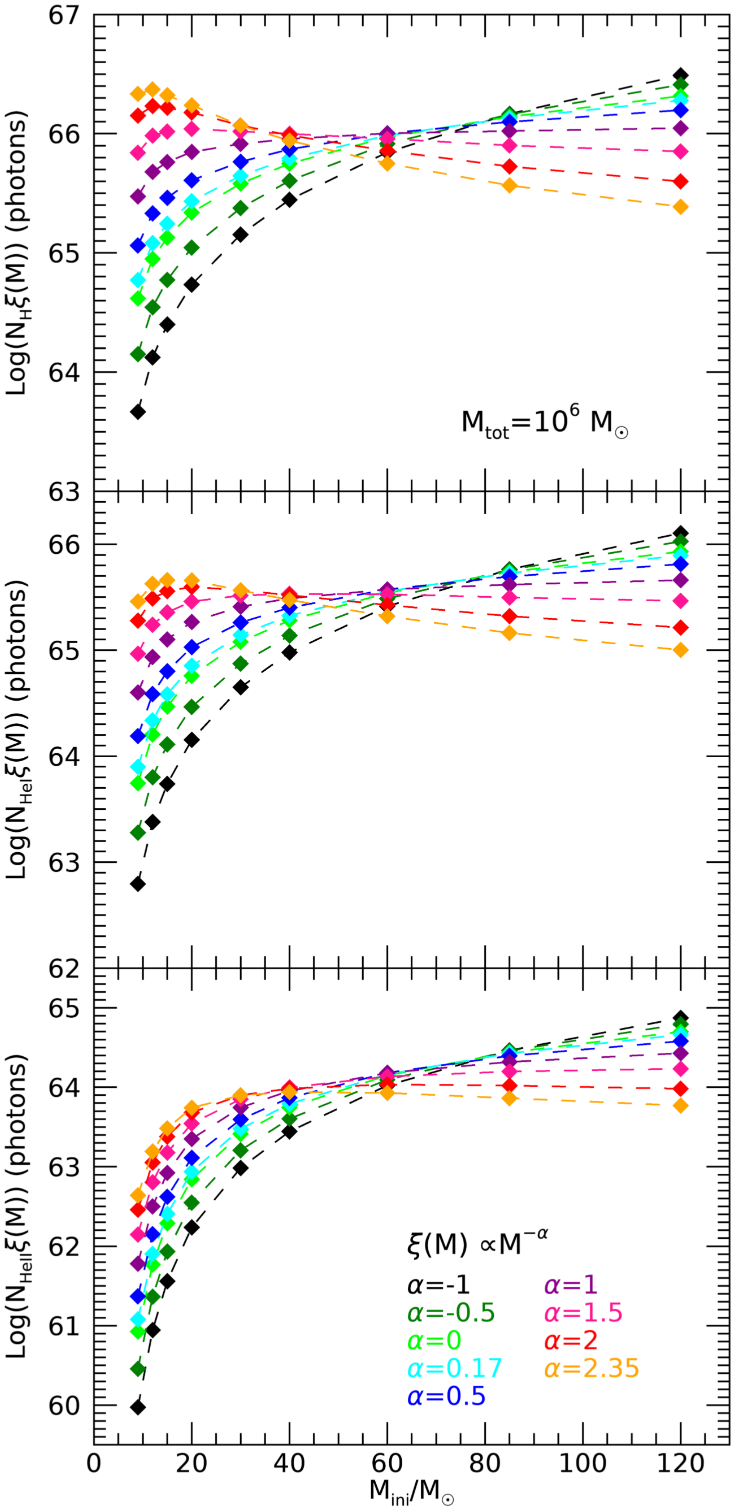

significant, and may be less than effects due to convection or rotation depending on the IMF slopes being compared. This infers that the H ionizing photon production per solar mass of stars of different initial masses ($N_{\mathrm{H}}/M_{\mathrm{ini}}$) is more similar than that of He II ionizing photon production per solar mass ($N_{\mathrm{HeII}}/M_{\mathrm{ini}}$).

The lower panel of Figure 5.9 shows how effects due to rotation and convection vary with IMF slope. Since the IMF slope determines the dominant initial mass in the population, the rotational effects seen here are a reflection of the trends seen in the lower panel of Figure 5.6, and equivalently the effects of convection seen here are a reflection of the trends seen in Figure 5.7. Lower IMF slopes follow the trend for more massive models, for example a stronger decrease in He II ionizing photons produced by rotating stars. By contrast, as IMF slope increases we start to observe the trend for less massive models, which is a stronger increase in H ionizing photons produced by stars with rotation, and stars with higher overshooting. The differences between effects due to rotation and convection in this figure serve as a reminder that rotational effects are more complex than changes in convective core size alone. This reinforces the importance of accurately modelling rotational effects in stellar evolution models, to fully understand the impact that rotation has on stellar structure.

The main conclusion from Figure 5.9 is the relative importance of rotation, convective overshooting, and slope of the initial mass function, in determining the total ionizing photons produced by a population of zero-metallicity stars of a given fixed total mass. Taking the non-rotating $\alpha_{\mathrm{ov}}=0.1$ SB13 population as a reference, the value for total H ionizing photons produced per stellar mass of the population ($N_{\mathrm{pop}}/\mathrm{M}_{\mathrm{tot}}$) is 1.13×10^{62} photons $\mathrm{M}_{\odot}^{-1}$ (see Table 5.4). This value increases by 7.7% when rotation of $\upsilon_{\mathrm{ini}}=0.4\,\upsilon_{\mathrm{crit}}$ is included, by 9.9% with higher overshooting of $\alpha_{\mathrm{ov}}=0.3$, and decreases by 26% when we assume a Salpeter IMF slope. Therefore, if comparing between the SB13 and Salpeter IMF slopes, then the choice of IMF slope is relatively more impactful than the effect of rotation or convective overshooting for the values considered here.

5.4.2 Evolution of Ionizing Photon Production

Now we investigate the time evolution of the ionizing photons produced by a population of Pop III stars. The results of this are shown for IMF slopes $-1\leq\alpha\leq2.35$ in Figure 5.10, for non-rotating stars with convective overshooting $\alpha_{\mathrm{ov}}=0.1$. At each time, t, from 1-20 Myr after formation, the total ionizing photons produced (N_{pop}) are shown, where the time considered is the time since the starburst when the population with total stellar mass $\mathrm{M}_{\mathrm{tot}}=10^{6}\,\mathrm{M}_{\odot}$ formed. The mass range here is $9\,\mathrm{M}_{\odot}\leq M_{\mathrm{ini}}\leq120\,\mathrm{M}_{\odot}$, thus at 20 Myr the population has produced its total ionizing photons. Therefore, the rightmost point in each panel of Figure 5.10 represents the total ionizing photons produced by the population, over the full lifetimes of each star within the population. In the case of the SB13 IMF ($\alpha=0.17$) we note that the total H ionizing photons produced by the population changes little after 4 Myr, having produced 93% of its H ionizing photons by this time. This is because a population with IMF slope $\alpha = 0.17$ is dominated by massive stars with lifetimes of only a few million years. On the other hand, we see a more gradual evolution in total H ionizing photons produced by the Salpeter IMF ($\alpha = 2.35$) population, with 60% of H ionizing photons produced in the first 4 Myr, and 94% of H ionizing photons produced by 10 Myr. It is clear from Figure 5.10 that the lower the IMF slope α, the faster the ionizing photon production, which is expected given that more massive models have shorter lifetimes. This demonstrates that the chosen IMF of the population could have an important impact on the reionization timescale, with more top-heavy IMFs potentially resulting in an earlier end to the reionization epoch.

We now provide estimates for ionizing photon production in the case of continuous star formation. To find the number of ionizing photons produced we need to know the mass of stars formed. To address this we present the number of ionizing photons formed per solar mass of the population, $N_{\mathrm{i}}/\mathrm{M}_{\mathrm{tot}}$ weighted by $\xi(M)$, in Figure 5.11, for a population based on the SB13 IMF. By doing so, to know the number of ionizing photons produced by a Pop III population by time t since initial star formation, you would only need to multiply by the mass of stars formed by that time. We are essentially representing continuous star formation by dividing the total ionizing photons produced by a population by the population's total mass, which, under the assumption of continuous and constant star formation, allows one to determine the number of ionizing photons produced at any time t by the mass of stars formed at that time. This is a basic estimate and we encourage further studies to investigate the evolution of the ionizing photon production of Pop III stars. All three ionizing photon species are included in Figure 5.11, for populations with and without rotation, and with higher overshooting. These values are also quoted in Table 5.3. This data is valuable for understanding the contribution of Pop III stars of different initial masses, weighted by the IMF, to reionization. We also present the total number of ionizing photons produced per solar mass by populations with different IMFs in Figure 5.12. This is the same trend as is seen in the upper panel of Figure 5.9, but now can be scaled based on the stellar mass of the population. These values are presented in Table 5.4. We note that the escape fraction is expected to vary with population mass (Kitayama et al. 2004; Wise et al. 2014), so this needs be considered in scaling these values and determining the contribution to reionization of a given Pop III population, the escape fraction is discussed further in Section 5.5.6.

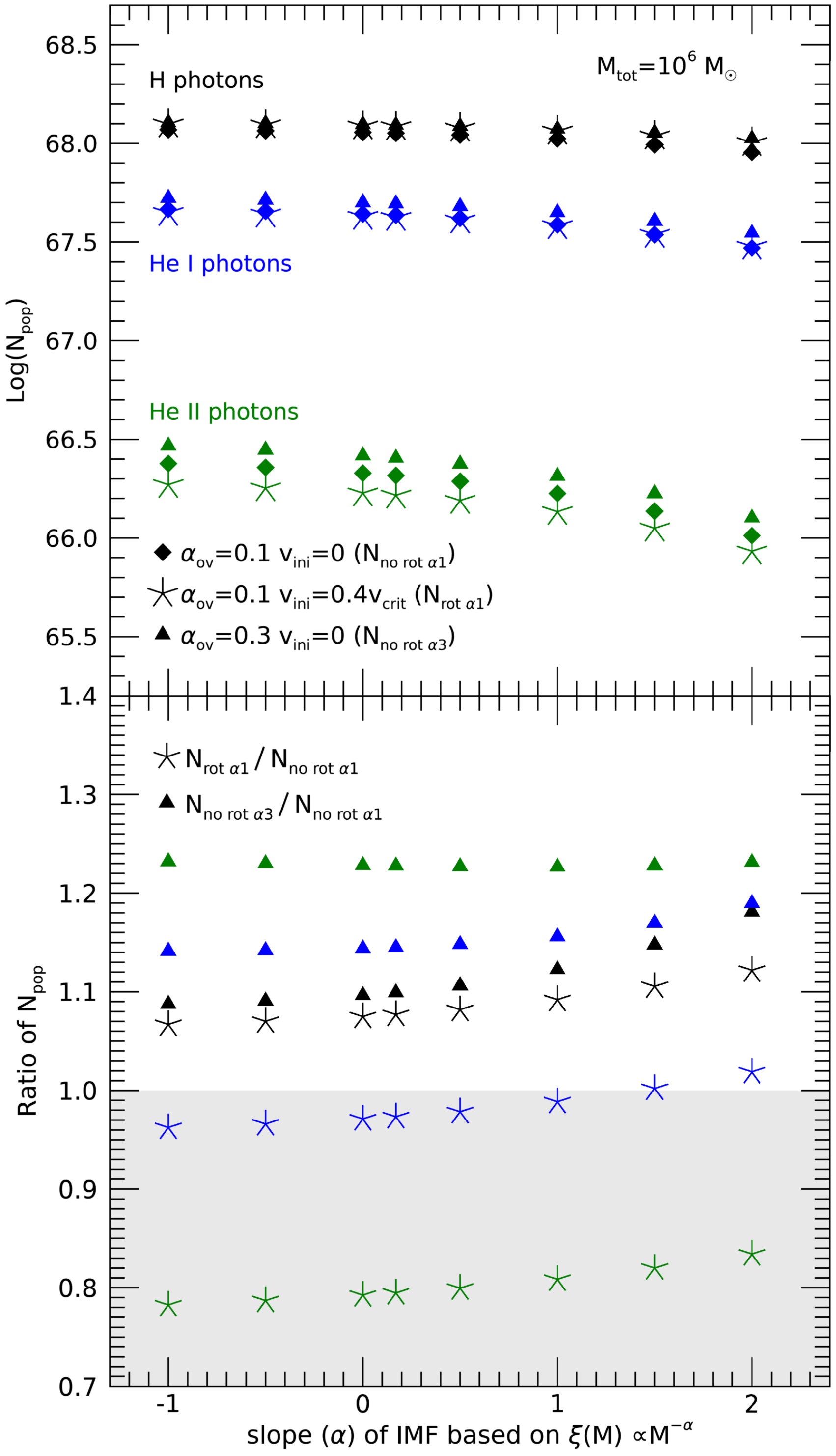

Figure 5.9: *Upper:* Total ionizing photons produced by populations of varying IMF slope α. Three model sets are shown. The non-rotating models with overshooting parameter $\alpha_{ov}=0.1$ (diamond symbols), the rotating models with $\alpha_{ov}=0.1$ (asterisk symbols), and finally the non-rotating models with higher overshooting $\alpha_{ov}=0.3$ (triangle symbols). Colours show the different ionizing photon species. The total mass of stars in each population is $10^6\,M_\odot$. *Lower:* Asterisk symbols show the ratio of total ionizing photons produced by models with rotation to models without rotation for each IMF slope, while triangle symbols show the ratio of total ionizing photons produced by models with higher overshooting to models with lower overshooting.

Figure 5.10: Temporal variation of N_{pop} (eq. 2.44) for different IMF slopes, α, indicated by different colours as shown in the legend. The three panels show H (upper), He I (middle), and He II (lower) ionizing photons. The time, t, considered is the time since the starburst when the non-rotating population with total stellar mass $\mathrm{M_{tot}} = 10^6\,\mathrm{M_\odot}$ formed. The mass range here is $9\,\mathrm{M_\odot} \leq M_{\mathrm{ini}} \leq 120\,\mathrm{M_\odot}$, thus at 20 Myr the population has produced its total ionizing photons.

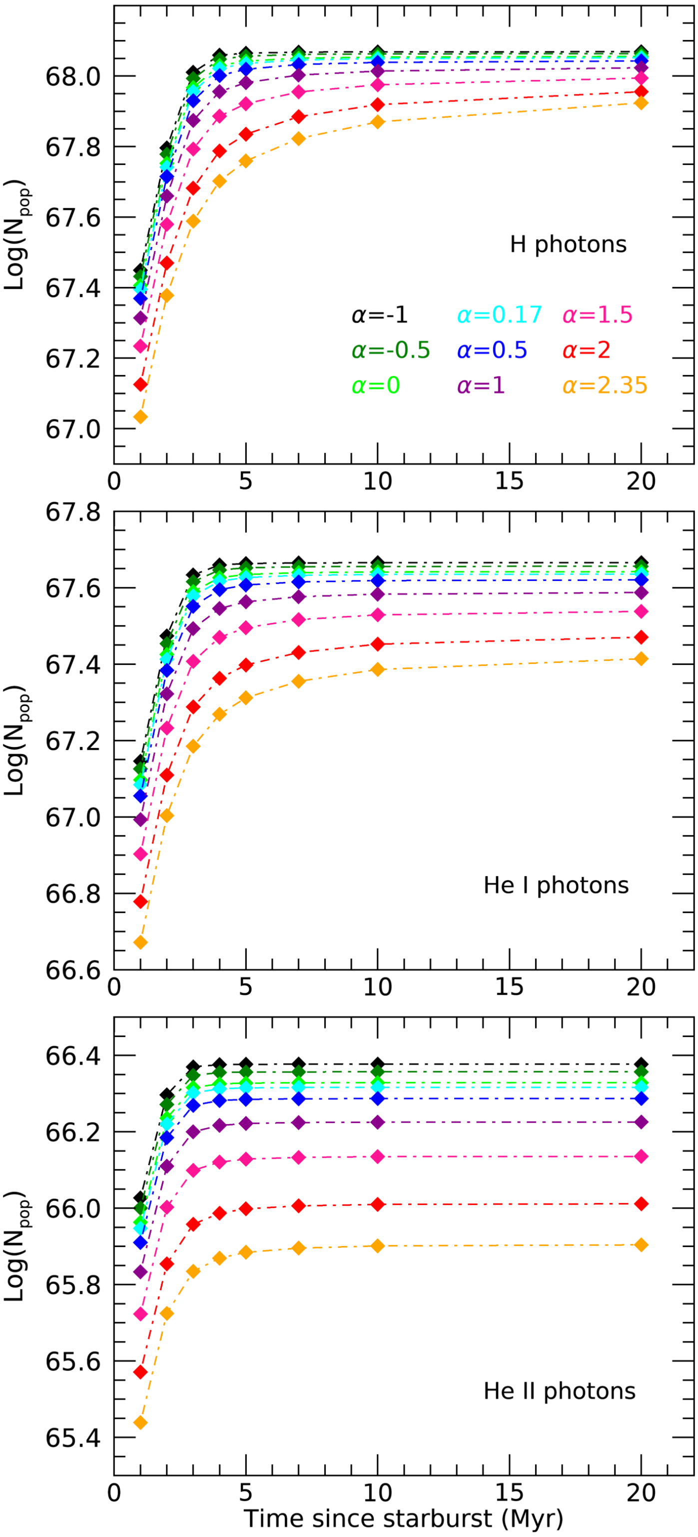

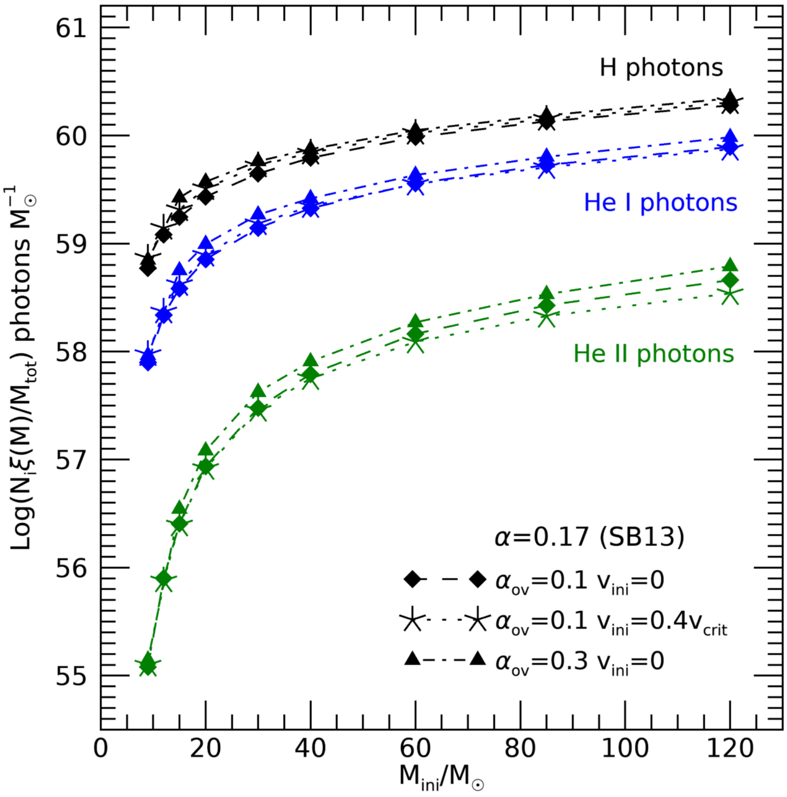

Figure 5.11: Total number of ionizing photons produced per solar mass of the population, by stars of different initial masses, based on a population of IMF slope $\alpha = 0.17$, i.e. $\log(N_i\,\xi(M)/M_{tot})$. Black, blue and green symbols indicate ionizing photon species H, He I and He II respectively, as shown in legend. Different symbols and line styles show initial parameters corresponding to rotation and convective overshooting. The values shown here are also presented in Table 5.3.

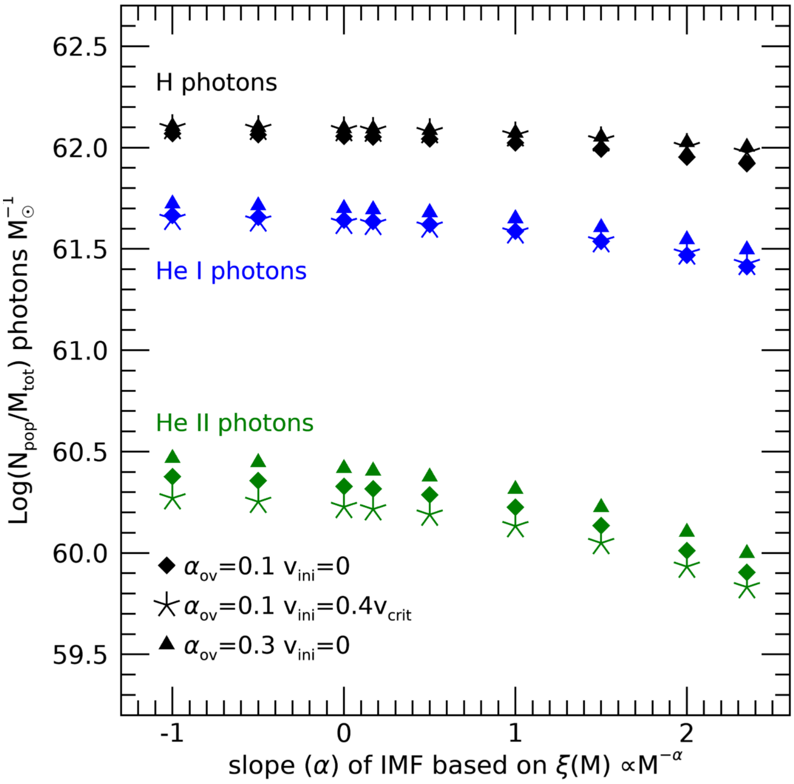

Figure 5.12: Total number of ionizing photons produced per solar mass of the population, by populations of various IMF slopes. Similarly to Figure 5.11, colours indicate different ionizing photon species, and symbols indicate different initial parameters corresponding to rotation and convective overshooting. The values shown here are also presented in Table 5.4.

Table 5.2: Total number of ionizing photons produced by individual stars over their lifetime ($N_{\rm i}$), for different initial masses. Headings indicate ionizing photon species H, He I and He II, and initial conditions where the top section gives non-rotating vs. rotating models, and the bottom section gives lower vs. higher overshooting models. These values are graphically presented in the upper panels of Figures 5.6 and 5.7.

$M_{\rm ini}$ ($\mathrm{M}_\odot$)	$\mathrm{N_H}$ (no rot)	$\mathrm{N_H}$ (rot)	$\mathrm{N_{HeI}}$ (no rot)	$\mathrm{N_{HeI}}$ (rot)	$\mathrm{N_{HeII}}$ (no rot)	$\mathrm{N_{HeII}}$ (rot)
9	2.9697e+62	3.6921e+62	3.9789e+61	4.7302e+61	6.0183e+58	6.3006e+58
12	6.3686e+62	7.3393e+62	1.1477e+62	1.2298e+62	4.2085e+59	3.9861e+59
15	9.6272e+62	1.1304e+63	2.1015e+62	2.2958e+62	1.3917e+60	1.3631e+60
20	1.5595e+63	1.8620e+63	4.1023e+62	4.4970e+62	4.9688e+60	4.7739e+60
30	2.7315e+63	3.2348e+63	8.5739e+62	9.4340e+62	1.8505e+61	1.7676e+61
40	4.0139e+63	4.4694e+63	1.3697e+63	1.4293e+63	3.9957e+61	3.6487e+61
60	6.6986e+63	7.3097e+63	2.4910e+63	2.4663e+63	1.0103e+62	8.5209e+61
85	9.9302e+63	1.0436e+64	3.9221e+63	3.7264e+63	1.9661e+62	1.5662e+62
120	1.4816e+64	1.5774e+64	6.1039e+63	5.8296e+63	3.5737e+62	2.6896e+62

$M_{\rm ini}$ ($\mathrm{M}_\odot$)	$\mathrm{N_H}$ ($\alpha_{\rm ov}$=0.1)	$\mathrm{N_H}$ ($\alpha_{\rm ov}$=0.3)	$\mathrm{N_{HeI}}$ ($\alpha_{\rm ov}$=0.1)	$\mathrm{N_{HeI}}$ ($\alpha_{\rm ov}$=0.3)	$\mathrm{N_{HeII}}$ ($\alpha_{\rm ov}$=0.1)	$\mathrm{N_{HeII}}$ ($\alpha_{\rm ov}$=0.3)
9	2.9697e+62	3.5357e+62	3.9789e+61	4.6342e+61	6.0183e+58	7.0159e+58
15	9.6272e+62	1.4013e+63	2.1015e+62	2.9675e+62	1.3917e+60	1.8393e+60
20	1.5595e+63	2.0425e+63	4.1023e+62	5.4138e+62	4.9688e+60	6.6130e+60
30	2.7315e+63	3.3212e+63	8.5739e+62	1.0628e+63	1.8505e+61	2.4239e+61
40	4.0139e+63	4.6039e+63	1.3697e+63	1.6100e+63	3.9957e+61	4.9812e+61
60	6.6986e+63	7.2436e+63	2.4910e+63	2.7878e+63	1.0103e+62	1.2056e+62
85	9.9302e+63	1.0629e+64	3.9221e+63	4.3961e+63	1.9661e+62	2.3507e+62
120	1.4816e+64	1.6202e+64	6.1039e+63	7.0818e+63	3.5737e+62	4.5272e+62

Table 5.3: Total number of ionizing photons produced per solar mass of the population, by stars of different initial masses, based on a population of IMF slope $\alpha = 0.17$ ($N_i \xi(M)/\mathrm{M_{tot}}$). Headings indicate ionizing photon species H, He I and He II, and initial conditions where the top section gives non-rotating vs. rotating models, and the bottom section gives lower vs. higher overshooting models. These values are graphically presented in Figure 5.11.

M_{ini} ($\mathrm{M_\odot}$)	$\mathrm{N_H}$ $\mathrm{M_\odot^{-1}}$ (no rot)	$\mathrm{N_H}$ $\mathrm{M_\odot^{-1}}$ (rot)	$\mathrm{N_{HeI}}$ $\mathrm{M_\odot^{-1}}$ (no rot)	$\mathrm{N_{HeI}}$ $\mathrm{M_\odot^{-1}}$ (rot)	$\mathrm{N_{HeII}}$ $\mathrm{M_\odot^{-1}}$ (no rot)	$\mathrm{N_{HeII}}$ $\mathrm{M_\odot^{-1}}$ (rot)
9	5.9137e+58	7.3522e+58	7.9233e+57	9.4194e+57	1.1984e+55	1.2546e+55
12	1.2077e+59	1.3917e+59	2.1763e+58	2.3320e+58	7.9805e+55	7.5586e+55
15	1.7576e+59	2.0637e+59	3.8366e+58	4.1913e+58	2.5408e+56	2.4886e+56
20	2.7112e+59	3.2371e+59	7.1321e+58	7.8183e+58	8.6384e+56	8.2996e+56
30	4.4325e+59	5.2492e+59	1.3913e+59	1.5309e+59	3.0029e+57	2.8684e+57
40	6.2027e+59	6.9066e+59	2.1166e+59	2.2086e+59	6.1746e+57	5.6384e+57
60	9.6618e+59	1.0543e+60	3.5929e+59	3.5573e+59	1.4572e+58	1.2290e+58
85	1.3499e+60	1.4187e+60	5.3319e+59	5.0658e+59	2.6728e+58	2.1292e+58
120	1.8995e+60	2.0223e+60	7.8254e+59	7.4738e+59	4.5816e+58	3.4482e+58

M_{ini} ($\mathrm{M_\odot}$)	$\mathrm{N_H}$ $\mathrm{M_\odot^{-1}}$ ($\alpha_{\mathrm{ov}}=0.1$)	$\mathrm{N_H}$ $\mathrm{M_\odot^{-1}}$ ($\alpha_{\mathrm{ov}}=0.3$)	$\mathrm{N_{HeI}}$ $\mathrm{M_\odot^{-1}}$ ($\alpha_{\mathrm{ov}}=0.1$)	$\mathrm{N_{HeI}}$ $\mathrm{M_\odot^{-1}}$ ($\alpha_{\mathrm{ov}}=0.3$)	$\mathrm{N_{HeII}}$ $\mathrm{M_\odot^{-1}}$ ($\alpha_{\mathrm{ov}}=0.1$)	$\mathrm{N_{HeII}}$ $\mathrm{M_\odot^{-1}}$ ($\alpha_{\mathrm{ov}}=0.3$)
9	5.9137e+58	7.0406e+58	7.9233e+57	9.2282e+57	1.1984e+55	1.3971e+55
15	1.7576e+59	2.6572e+59	3.8366e+58	5.6272e+58	2.5408e+56	3.4878e+56
20	2.7112e+59	3.7289e+59	7.1321e+58	9.8840e+58	8.6384e+56	1.2073e+57
30	4.4325e+59	5.7741e+59	1.3913e+59	1.8477e+59	3.0029e+57	4.2141e+57
40	6.2027e+59	7.4710e+59	2.1166e+59	2.6126e+59	6.1746e+57	8.0832e+57
60	9.6618e+59	1.1193e+60	3.5929e+59	4.3080e+59	1.4572e+58	1.8630e+58
85	1.3499e+60	1.5331e+60	5.3319e+59	6.3408e+59	2.6728e+58	3.3906e+58
120	1.8995e+60	2.2025e+60	7.8254e+59	9.6272e+59	4.5816e+58	6.1545e+58

Table 5.4: Total number of ionizing photons produced per solar mass of the population, by populations of various IMF slopes ($N_{\mathrm{pop}}/\mathrm{M}_{\mathrm{tot}}$). Headings indicate ionizing photon species H, He I and He II, and initial conditions where the top section gives non-rotating vs. rotating models, and the bottom section gives lower vs. higher overshooting models. These values are graphically presented in Figure 5.12.

IMF slope (α)	$\mathrm{N_H}$ $\mathrm{M}_\odot^{-1}$ (no rot)	$\mathrm{N_H}$ $\mathrm{M}_\odot^{-1}$ (rot)	$\mathrm{N_{HeI}}$ $\mathrm{M}_\odot^{-1}$ (no rot)	$\mathrm{N_{HeI}}$ $\mathrm{M}_\odot^{-1}$ (rot)	$\mathrm{N_{HeII}}$ $\mathrm{M}_\odot^{-1}$ (no rot)	$\mathrm{N_{HeII}}$ $\mathrm{M}_\odot^{-1}$ (rot)
-1.00	1.1718e+62	1.2502e+62	4.6294e+61	4.4556e+61	2.3815e+60	1.8638e+60
-0.50	1.1575e+62	1.2386e+62	4.5298e+61	4.3759e+61	2.2745e+60	1.7900e+60
0.00	1.1360e+62	1.2211e+62	4.3854e+61	4.2588e+61	2.1306e+60	1.6886e+60
0.17	1.1264e+62	1.2131e+62	4.3221e+61	4.2068e+61	2.0709e+60	1.6458e+60
0.50	1.1033e+62	1.1937e+62	4.1727e+61	4.0826e+61	1.9363e+60	1.5482e+60
1.00	1.0541e+62	1.1510e+62	3.8649e+61	3.8206e+61	1.6805e+60	1.3588e+60
1.50	9.8479e+61	1.0887e+62	3.4484e+61	3.4555e+61	1.3669e+60	1.1207e+60
2.00	8.9836e+61	1.0078e+62	2.9491e+61	3.0045e+61	1.0273e+60	8.5692e+59
2.35	8.3354e+61	9.4503e+61	2.5874e+61	2.6696e+61	8.0269e+59	6.7897e+59
IMF slope (α)	$\mathrm{N_H}$ $\mathrm{M}_\odot^{-1}$ ($\alpha_{\mathrm{ov}}=0.1$)	$\mathrm{N_H}$ $\mathrm{M}_\odot^{-1}$ ($\alpha_{\mathrm{ov}}=0.3$)	$\mathrm{N_{HeI}}$ $\mathrm{M}_\odot^{-1}$ ($\alpha_{\mathrm{ov}}=0.1$)	$\mathrm{N_{HeI}}$ $\mathrm{M}_\odot^{-1}$ ($\alpha_{\mathrm{ov}}=0.3$)	$\mathrm{N_{HeII}}$ $\mathrm{M}_\odot^{-1}$ ($\alpha_{\mathrm{ov}}=0.1$)	$\mathrm{N_{HeII}}$ $\mathrm{M}_\odot^{-1}$ ($\alpha_{\mathrm{ov}}=0.3$)
-1.00	1.1718e+62	1.2745e+62	4.6294e+61	5.2839e+61	2.3815e+60	2.9342e+60
-0.50	1.1575e+62	1.2625e+62	4.5298e+61	5.1727e+61	2.2745e+60	2.7978e+60
0.00	1.1360e+62	1.2456e+62	4.3854e+61	5.0164e+61	2.1306e+60	2.6171e+60
0.17	1.1264e+62	1.2381e+62	4.3221e+61	4.9490e+61	2.0709e+60	2.5427e+60
0.50	1.1033e+62	1.2205e+62	4.1727e+61	4.7916e+61	1.9363e+60	2.3762e+60
1.00	1.0541e+62	1.1831e+62	3.8649e+61	4.4709e+61	1.6805e+60	2.0623e+60
1.50	9.8479e+61	1.1297e+62	3.4484e+61	4.0389e+61	1.3669e+60	1.6801e+60
2.00	8.9836e+61	1.0605e+62	2.9491e+61	3.5192e+61	1.0273e+60	1.2682e+60
2.35	8.3354e+61	1.0064e+62	2.5874e+61	3.1397e+61	8.0269e+59	9.9623e+59

5.4.3 Impact of Minimum Mass

Up to now we have assumed a minimum mass of the population of $M_{\rm min} = 9\,{\rm M_\odot}$. We will now investigate how the ionizing photon production of the population is impacted by decreasing $M_{\rm min}$. To compare how changing $M_{\rm min}$ impacts the total ionizing photons produced by the population, we reevaluate the number of stars at each initial mass in a population of ${\rm M_{tot}} = 10^8\,{\rm M_\odot}$. The results of this investigation are presented in Figure 5.13. It is clear from the plot that the impact of varying $M_{\rm min}$ is highly dependent on the IMF slope. For IMF slopes of $\alpha \leq 0.5$ the ionizing photon production of the population remains largely unchanged as the minimum mass decreases. However, for IMF slopes ≥ 1 we begin to see a significant decrease to the total ionizing photons produced. For example, we find a reduction of $\sim 50\%$ to H ionizing photons produced by a population with a Salpeter IMF when $M_{\rm min}$ is decreased from $9\,{\rm M_\odot}$ to $1.7\,{\rm M_\odot}$. This result is unsurprising given that steeper IMFs significantly increase the fraction of low-mass stars for a population of fixed total mass. Decreasing the minimum mass in these steeper IMF populations thus reduces the number of ionizing photons produced because lower-mass models are cooler and less luminous (see Figures 3.1 and 3.2), therefore, they have much lower ionizing photon production rates.

Since the Pop III IMF is expected to be top-heavy (Greif et al. 2011; Stacy & Bromm 2013; Susa et al. 2014; Hirano et al. 2014, 2015; Hosokawa et al. 2016; Stacy et al. 2016; Jeřábková et al. 2018; Wollenberg et al. 2020), a variation of minimum mass in the range $1.7 - 9\,{\rm M_\odot}$ may have little effect on the ionizing photon production of the population. However, it is important to keep this effect in mind as research on the primordial IMF continues. We also note that changing the minimum mass of the population may have a significant impact on the timescale of reionization. As we discussed in Section 5.4.2 more top-heavy IMF populations produce their ionizing photons faster than populations with a Salpeter IMF slope since more massive models have shorter lifetimes. Reducing the minimum mass of the population would delay the production of ionizing photons by a Salpeter IMF population even further, since the lifetimes of these low-mass stars can be significantly longer. A $1.7\,{\rm M_\odot}$ Pop III star has a lifetime of $\sim$ a billion years, compared to the 20 Myr lifetime of a $9\,{\rm M_\odot}$ star. Furthermore, the escape fraction is expected to change rapidly as a function of redshift (e.g. Haardt & Madau 2012), so not only will decreasing the minimum mass increase the timescale for ionizing photon production, but the escape fraction may be very different, which will impact the number of ionizing photons that reach the IGM.

5.4.4 Impact of Maximum Mass

We now turn our attention to the upper mass limit of the population, and investigate how the ionizing photon production of the population is impacted by increasing the maximum mass, $M_{\rm max}$, using our original minimum mass value of $M_{\rm min} = 9\,{\rm M_\odot}$. We

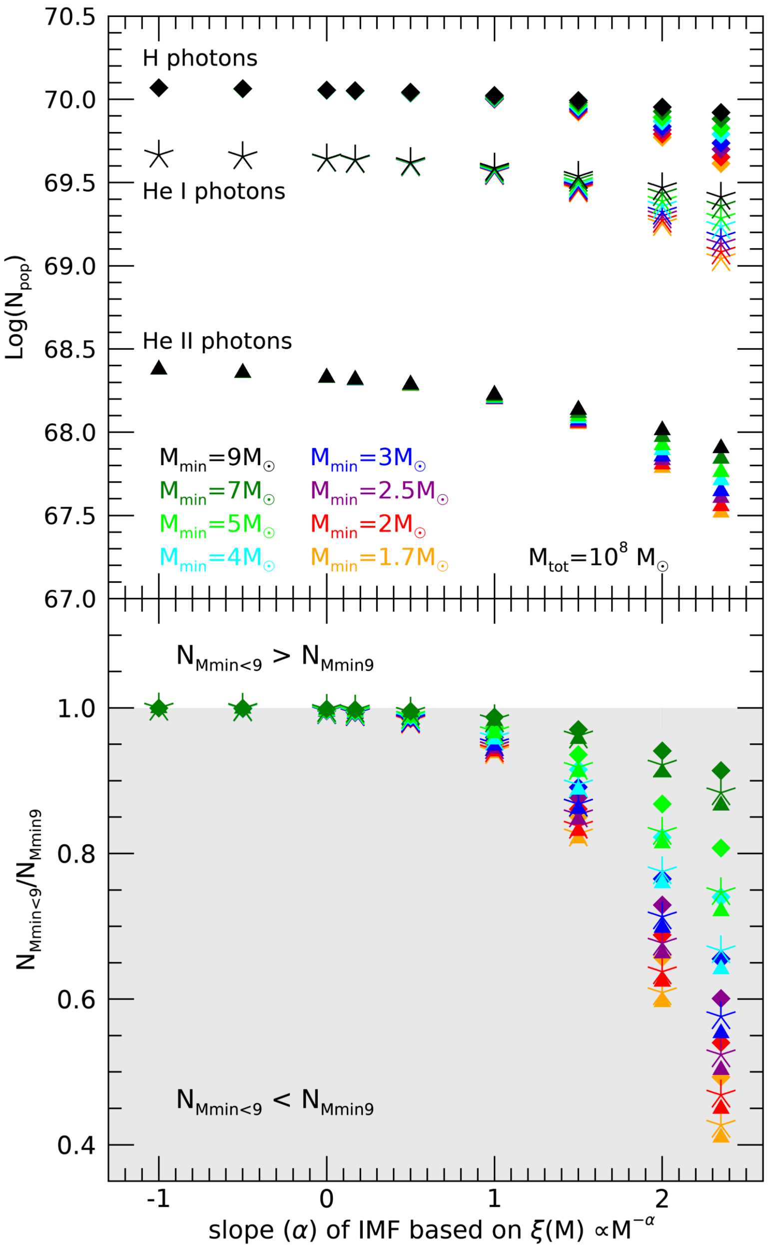

Figure 5.13: Impact of varying the minimum mass of the population, M_{min}, on the ionizing photons produced by populations of different IMF slopes, α, based on the relation $\xi(M) \propto M^{-\alpha}$. All stars are non-rotating with convective overshooting of $\alpha_{\text{ov}} = 0.1$, and the total mass of the population is $\mathrm{M_{tot}} = 10^8\,\mathrm{M_\odot}$ as indicated in the figure. Colours indicate the minimum mass of the population, and H, He I and He II ionizing photons are indicated by different symbols. *Upper:* Total ionizing photons produced. *Lower:* Ratio of ionizing photons produced by populations of lower minimum mass to our fiducial population with $M_{\text{min}} = 9\,\mathrm{M_\odot}$, for H, He I and He II ionizing photons.

use the recently computed zero-metallicity very massive star models from Martinet et al. (2021 in prep.), with initial masses $M_{\text{ini}} = 180, 250, 300, 500\,\mathrm{M_\odot}$ (see Section 2.8.4). Similarly to Section 5.4.3, we vary M_{max} and reevaluate the number of stars in the population, keeping the total stellar mass constant with $\mathrm{M_{tot}} = 10^8\,\mathrm{M_\odot}$. Figure 5.14 shows how varying the maximum mass affects the total ionizing photons produced by a zero-metallicity population. It can be clearly seen from Figure 5.14 that increasing the maximum mass from $120\,\mathrm{M_\odot}$ increases the total ionizing photons produced by the population for all IMF slopes shown here. We know from Section 5.2.2 that total ionizing photons produced, N_{i}, increases with increasing initial mass, and the same is true for masses $> 120\,\mathrm{M_\odot}$. However, from Figure 5.14 we see an interesting change in trend for the $M_{\rm max} = 500\,\rm M_{\odot}$ case.

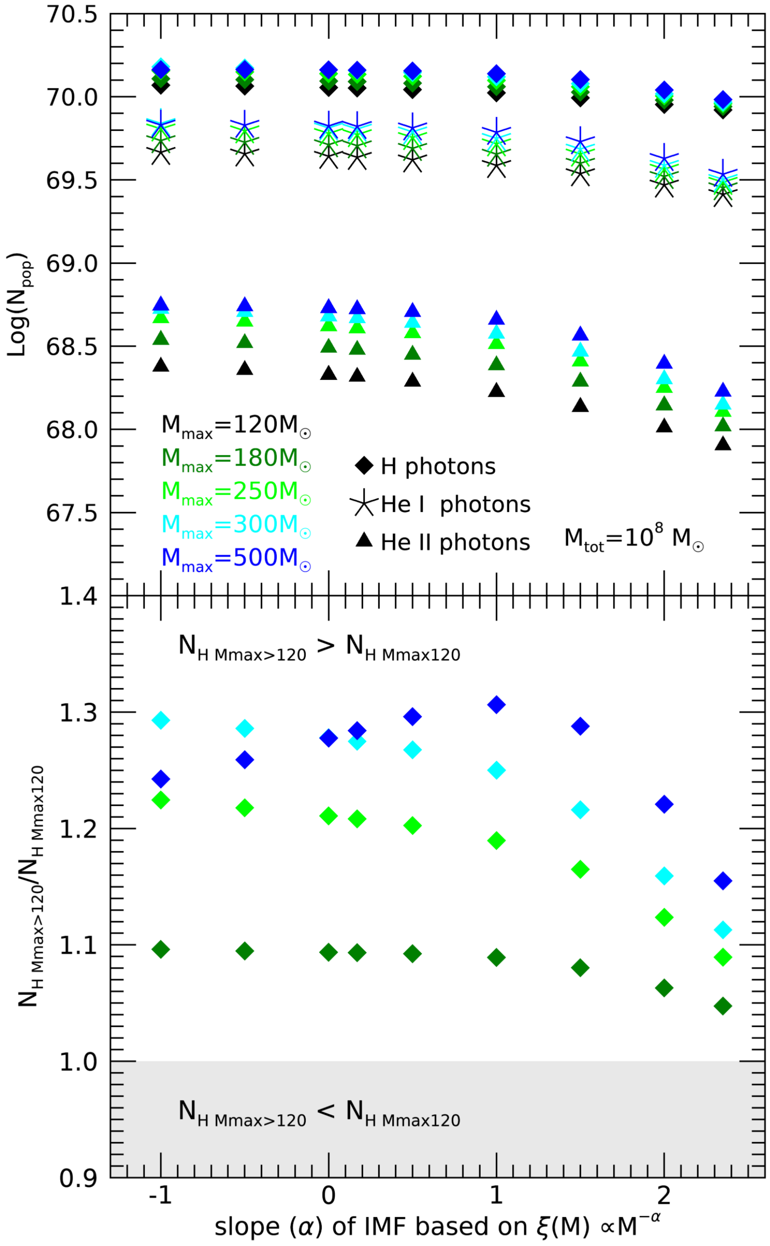

Figure 5.14: Impact of varying the maximum mass of the population, $M_{\rm max}$, on the ionizing photons produced by populations of different IMF slopes, α, based on the relation $\xi(M) \propto M^{-\alpha}$. All stars are non-rotating with convective overshooting of $\alpha_{\rm ov} = 0.1$, and the total mass of the population is $\rm M_{tot} = 10^8\,M_{\odot}$ as indicated in the figure. Colours indicate the maximum mass of the population, and H, He I and He II ionizing photons are indicated by different symbols. *Upper:* Total ionizing photons produced. *Lower:* Ratio of H ionizing photons produced by populations of higher maximum mass to our fiducial population with $M_{\rm max} = 120\,\rm M_{\odot}$.

Looking at the lower panel it can be observed that when increasing $M_{\rm max}$ to $500\,\rm M_{\odot}$, the maximum increase in emission of H ionizing photons occurs at an IMF slope of $\alpha = 1$. For $\alpha \leq 0$ the increase to H ionizing photon produced is in fact higher for $M_{\rm max} = 300\,\rm M_{\odot}$ than $M_{\rm max} = 500\,\rm M_{\odot}$. We have found that this occurs because, despite the $500\,\rm M_{\odot}$ model producing more ionizing photons than the $300\,\rm M_{\odot}$ model, it produces less ionizing photons per solar mass than the $300\,\rm M_{\odot}$. This can be observed from Figure 5.15, where we plot the total ionizing photons produced by individual stars divided by their initial mass ($N_{\rm i}/M_{\rm ini}$). From this figure we see that the total H ionizing photons produced per initial mass increases rapidly moving from intermediate mass models ($1.7\,\rm M_{\odot} \leq M_{\rm ini} \leq 9\,\rm M_{\odot}$)

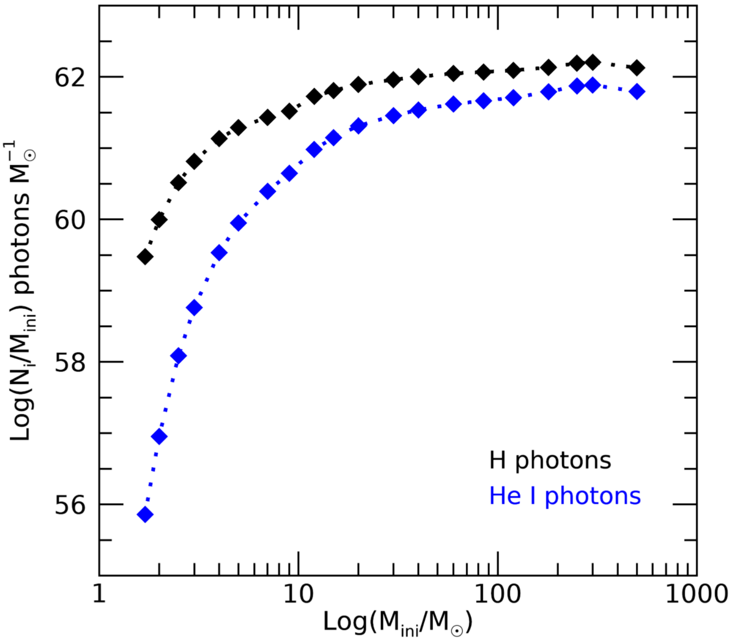

Figure 5.15: Total ionizing photons (N_i) produced by models in the mass range $1.7\,\mathrm{M}_\odot \leq M_\mathrm{ini} \leq 500\,\mathrm{M}_\odot$, divided by their initial mass (M_ini), for H ionizing photons in black, and He I ionizing photons in blue.

to massive models $M_\mathrm{ini} \geq 9\,\mathrm{M}_\odot$, showing that massive models will play a dominant role in ionizing photon production. The values for $\log(N_\mathrm{i}/M_\mathrm{ini})$ then peak at $300\,\mathrm{M}_\odot$ and decrease moving to $500\,\mathrm{M}_\odot$. This means for instance that two $250\,\mathrm{M}_\odot$ stars would produce more ionizing photons than one $500\,\mathrm{M}_\odot$ star. Since the stellar mass of the population is kept constant, when $500\,\mathrm{M}_\odot$ models are included the total ionizing photons produced decrease compared to the population with $M_\mathrm{max} = 300\,\mathrm{M}_\odot$, or $M_\mathrm{max} = 250\,\mathrm{M}_\odot$.

This decrease in $\log(N_\mathrm{i}/M_\mathrm{ini})$ for $500\,\mathrm{M}_\odot$ models occurs due to an inflation of their envelope due to their high Eddington factors (e.g. Sanyal et al. 2017). This inflation causes their temperature to decrease, thus impacting their ionizing photon production. It is clear that the ionizing photons produced per solar mass is crucial in understanding how stars of different initial mass will contribute to the ionizing photon production of the population. We will further discuss the impact of envelope inflation in Section 5.5.4. We also note from Figure 5.15 that He I ionizing photons vary more than H ionizing photons per solar mass. This explains the trend seen in the upper panel of Figure 5.9 where the more energetic He ionizing photons are more impacted by the change of IMF slope than H ionizing photons. As mentioned in Section 5.4.1 that trend infers that $N_\mathrm{H}/M_\mathrm{ini}$ is more similar for different initial masses than $N_\mathrm{HeI}/M_\mathrm{ini}$ or $N_\mathrm{HeII}/M_\mathrm{ini}$, which is now evident from Figure 5.15.

From Figure 5.14 we find that varying the maximum mass of the population can increase the total H ionizing photons produced by up to $\sim$30% for $M_\mathrm{max} = 500\,\mathrm{M}_\odot$ compared to $M_\mathrm{max} = 120\,\mathrm{M}_\odot$. We have found that for a SB13 IMF ($\alpha = 0.17$) the total H ionizing photons produced increases by 28.4% when M_max is increased from $120\,\mathrm{M}_\odot$ to $500\,\mathrm{M}_\odot$, while for a Salpeter IMF ($\alpha = 2.35$) this increase is 15.5%. Given that the minimum and maximum initial masses of Pop III stars are still debated in cosmological simulations (see Table 1 of Stacy et al. 2016, and Figure 1.5), this significant shift in total ionizing photons produced as maximum mass varies should be considered in future studies of how the first stars contributed to reionization.

We note here that we have considered a constant IMF slope across the full mass range of the population. Hydrodynamical simulations of Pop III star formation predict a more complex distribution however (e.g. Figure 1.6, Figure 17 of Hirano et al. 2015), with a non-monotonic IMF. While a top-heavy IMF is predicted, the characteristic mass is not yet certain and the nature of the IMF above this characteristic mass is yet to be constrained. Therefore, while the maximum mass of the population is expected to be $>120\,\mathrm{M}_\odot$ the IMF slope may change for very massive stars, and thus we advise the reader to carefully consider the nature of the IMF slope in different mass ranges, as well as the minimum and maximum masses in predicting Pop III ionizing photon production for a given IMF.

5.5 Discussion

In this section we discuss other factors which may impact the ionizing photon production of Pop III stars and their contribution to the reionization of the Universe. We also compare our findings to previous ionizing photon predictions from Schaerer (2002) and Yoon et al. (2012).

5.5.1 Impact of Mixing Processes: SNAPSHOT Models

The luminosity, effective temperature and ionizing photon production rate are ultimately set by the internal abundance profile. To test the effects of the uncertainties in the internal hydrogen abundance profile on the production of ionizing photons produced in our models, we compute several SNAPSHOT stellar structure models using the method described in (Farrell et al. 2020) with the MESA stellar evolution code (Paxton et al. 2011, 2013, 2015). The SNAPSHOT models allow us to test the effect of arbitrary internal abundance profiles on the luminosity and effective temperature without relying on results based on specific prescriptions for mixing. While the abundance profiles are artificial and generated by hand, they mimic the effects produced by physical processes such as rotation, convection, semi-convection and other mixing processes that may have effects but are not accounted for in these models. We find that slight variations in the internal hydrogen abundance profile can affect the rate of ionizing photons by up to 20% during the middle of the MS and by 30% at the end of the MS. Figure 5.16 shows the internal hydrogen abundance profile for four $20\,\mathrm{M}_\odot$ SNAPSHOT stellar models at the middle of the MS, as well as their location in the HR diagram. Quoted in the figure are the fractions, for models T, U, V, of ionizing photons produced relative to model W, for H, He I, and He II respectively. This gives an idea of the extent to which moderate adjustments to the abundance profile may impact surface properties, and subsequently the number of ionizing photons produced. We conclude that variations of the sort shown in Figure 5.16 can have a moderate effect on the overall result for ionizing photon production.

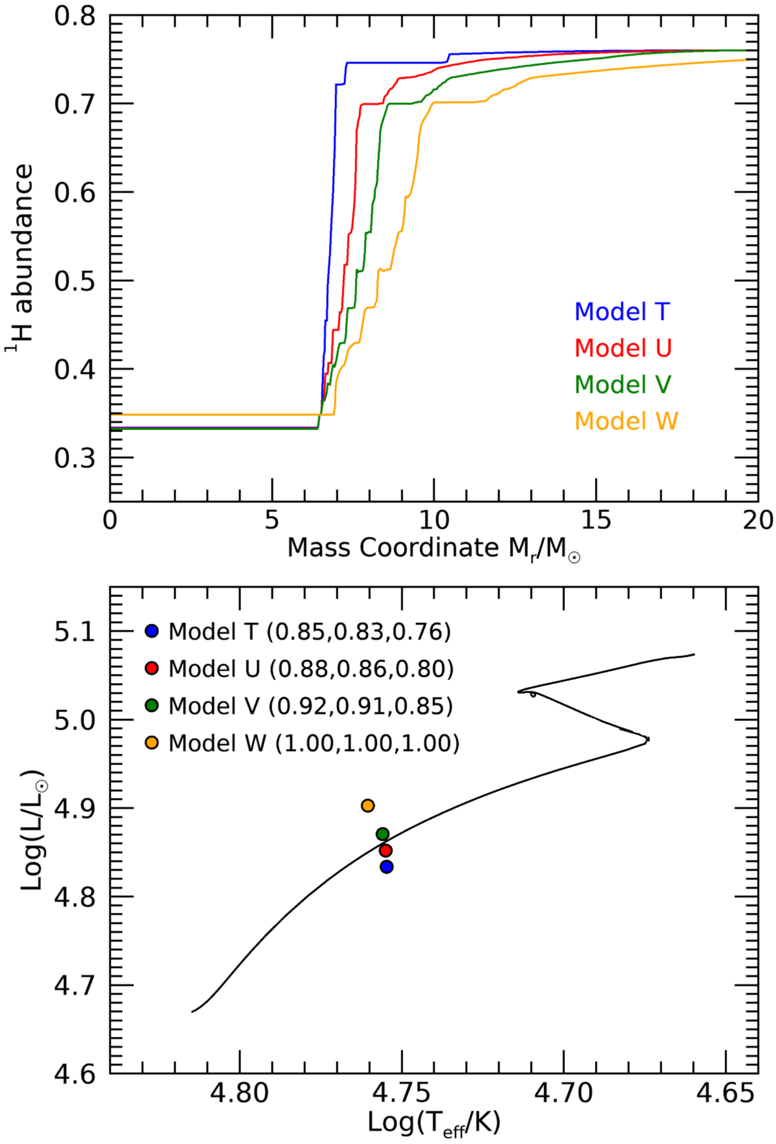

Figure 5.16: *Upper:* Internal hydrogen abundance profiles of four 20 $M_\odot$ SNAPSHOT stellar models at the middle of the MS phase. *Lower:* Location in the HR diagram of the models from the upper panel. For reference, we also plot the evolutionary track of a non-rotating 20 $M_\odot$ computed with MESA. For each SNAPSHOT model T, U, V, we quote the fraction of ionizing photons produced relative to model W in order of H, He I, He II respectively.

5.5.2 Impact of Detailed Stellar Atmosphere Modelling

To determine how much our results are impacted by using a blackbody rather than modelling the atmosphere we can compare to Schaerer (2002) (S02). Since the stellar evolution models used are not the same we choose three cases to compare our findings with the S02 values. Case 1 is the values of Q_{H}, Q_{HeI}, Q_{HeII} taken directly from Table 3 of S02, which are calculated from a modelled atmosphere. These values are the ionizing photon production rates at the ZAMS for each stellar evolution model. We select the values for initial masses in the range $9\,\mathrm{M}_\odot \leq M_{\mathrm{ini}} \leq 120\,\mathrm{M}_\odot$, of which four masses overlap with the initial masses included in this work, these are $M_{\mathrm{ini}} = 9, 15, 60, 120\,\mathrm{M}_\odot$. Case 2 takes the L and T_{eff} values from the same table in S02, but uses our method (see Section 2.8) to calculate Q_{H}, Q_{HeI} and Q_{HeII} through a blackbody fit, thus tests the impact of not modelling the atmosphere. Case 3 is then the ZAMS Q_{i} values from this work for our non-rotating models. The comparison of these three cases is shown in the upper panel of Figure 5.17, while ratios of case 2 to case 1, and case 3 to case 1 are shown in the lower panel. For each case we linearly interpolate the values so that we can compare all three cases for the full mass range $9\,\mathrm{M}_\odot \leq M_{\mathrm{ini}} \leq 120\,\mathrm{M}_\odot$.

It is clear from the figure that the most significant impact of not modelling the atmosphere is the overestimation of He II ionizing photons at low initial masses. In particular, if we look at the lower panel of Figure 5.17, we see that He II ionizing photons are overestimated for initial masses $M_{\mathrm{ini}} < 40\,\mathrm{M}_\odot$ when we use a blackbody fit. Referring back to the lower panel of Figure 5.8, we see that for all IMFs with slopes $\alpha \leq 2.35$ He II ionizing photon production is dominated by models of initial masses $M_{\mathrm{ini}} \geq 40\,\mathrm{M}_\odot$. In this mass range we have found that our blackbody fit reproduces the ionizing photon production rates with errors of less than 0.5 dex (see lower panel Figure 5.17). This is not necessarily the case for larger IMF slopes of > 2.35 where we expect that He II ionizing photon production is dominated by initial masses of $< 40\,\mathrm{M}_\odot$, however, simulations predict that there were more massive stars in the early universe (Turk et al. 2009; Clark et al. 2011b; Greif et al. 2012; Stacy & Bromm 2013; Hirano et al. 2014, 2015) and it is generally accepted that the Pop III IMF will have a lower slope than the Salpeter IMF.

The numbers of H and He I ionizing photons are well reproduced with a blackbody approximation within $\lesssim 0.2$ dex. Therefore, our comparison to the ionizing photon values presented in Schaerer (2002) has shown that our method of using a blackbody fit to determine ionizing photon production, rather than modelling the atmosphere, is a reasonable approximation. It is important to note here that this is for ZAMS values, therefore, we may see more absorption of ionizing photons at later times if surface metallicity increases, however this is not expected for our models.

5.5.3 Impact of Internal Magnetic Fields

It is also useful to compare to Yoon et al. (2012) (Y12) to study how differences in stellar evolution modelling will impact ionizing photon production. Internal magnetic fields were included in the Y12 Pop III stellar models, assuming a Taylor-Spruit dynamo (Spruit 2002). This allowed for a different approach to the effects of rotation in these stars, where chemically homogeneous evolution (CHE) is more easily achieved (see discussion in Groh et al. 2019). The evolution of stellar surface properties is strongly impacted by CHE, in particular CHE leads to much higher surface temperatures. Therefore, we expect

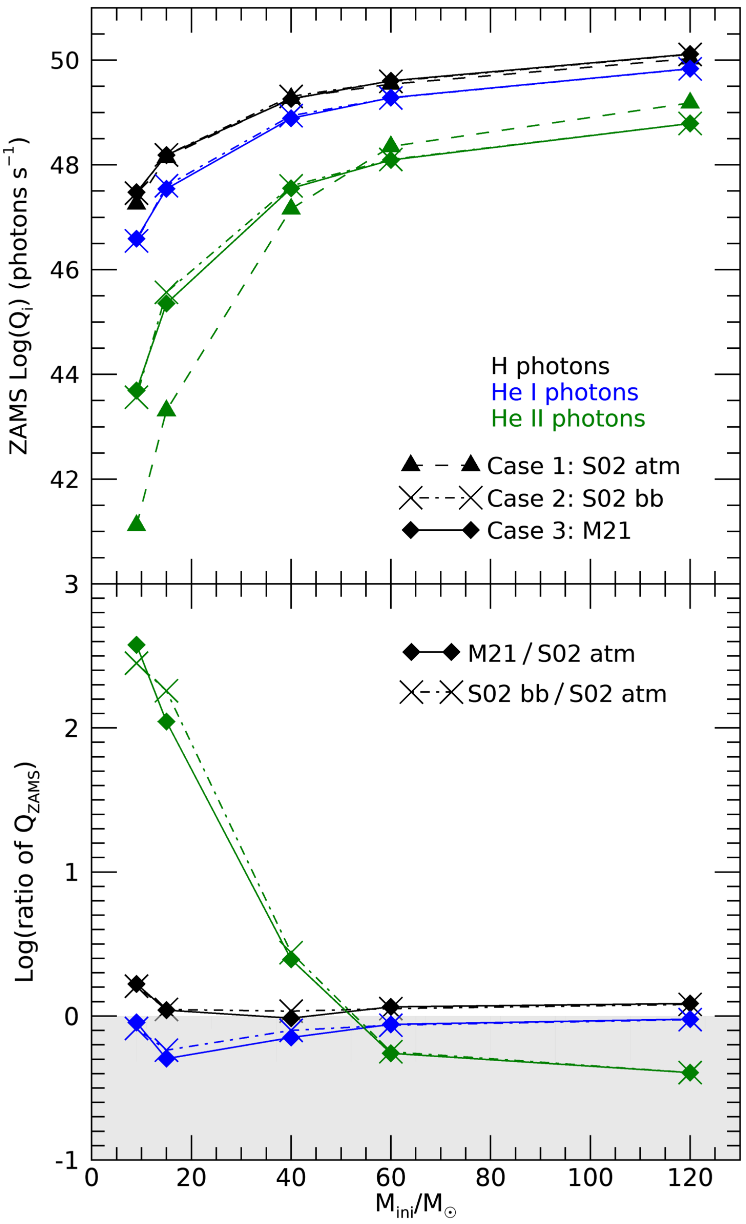

Figure 5.17: *Upper:* Comparison to Schaerer (2002) (S02) ionizing photon production rates (Q_i) for non-rotating ZAMS models. Triangle symbols and dashed lines indicate the values from Table 3 in S02. Cross symbols and dashed dotted lines indicate values using L and $T_{\rm eff}$ values from S02 but computed using our blackbody method described in Chapter 2. Diamond symbols and solid lines indicate ionizing photon production rates from non-rotating models in this work on the ZAMS. *Lower:* Ratio of Q_i from this work to S02 values (diamonds and solid lines), and ratio of Q_i from S02 calculated using blackbody to S02 values (crosses and dashed dotted lines). Results are logarithmically scaled. Colours indicate ionizing photon species as shown in the upper panel.

that the inclusion of magnetic fields and subsequent CHE will increase ionizing photon production. To test this we have selected four models from Y12 rotating models, for the same initial mass, with similar initial rotational velocities to our models of $\upsilon_{\rm ini}=0.4\upsilon_{\rm crit}$. These include m15vk04 ($\upsilon_{\rm ini}=0.43\upsilon_{\rm crit}$), m20vk04 ($\upsilon_{\rm ini}=0.44\upsilon_{\rm crit}$), m30vk04 ($\upsilon_{\rm ini}=0.47\upsilon_{\rm crit}$), and m60vk03 ($\upsilon_{\rm ini}=0.39\upsilon_{\rm crit}$), of initial masses $M_{\rm ini}=15, 20, 30, 60\,{\rm M}_\odot$, and we direct the reader to their paper for further details on initial parameters. We compare the total ionizing photons produced by these models (see Y12 Table 3) to the total ionizing photons produced by our rotating and non-rotating models of the same initial masses. The results of this comparison are presented in Figure 5.18. As expected we see that the ionizing photon output is higher for rotating Y12 models, with the exception of the $15\,{\rm M}_\odot$ case where CHE is not achieved. From the lower panel of Figure 5.18, we see that He II ionizing photons are the species most impacted by CHE. This is because He II ionizing photon production is dominated by surface temperature effects (Section 5.2.1). The average increase to He II ionizing photons produced with CHE (for $M_{\rm ini} = 20, 30, 60\,{\rm M}_\odot$) is 1.02 dex, while for He I ionizing photons the average increase is 0.46 dex, and for H ionizing photons the average increase is 0.27 dex. These results tell us that for our massive rotators ($M_{\rm ini} \geq 20\,{\rm M}_\odot$), we can expect to see an increase in ionizing photon production if magnetic fields are included. Looking at the lower panel of Figure 5.18, we also see a small increase (< 0.1 dex) in He II ionizing photons when we compare our non-rotating models to the Y12 non-rotators. This is due to higher surface temperatures in our models. As with this work, Yoon et al. (2012) assumed blackbody radiation. An important consequence of CHE is the increase to surface metallicity, so the increase in ionizing photon production with the inclusion of magnetic fields may vary with radiative transfer modelling of the atmosphere. Therefore, further work with modelling of the atmosphere is required to accurately determine the impact of magnetic fields on the production of ionizing photons by Pop III stars.

5.5.4 Impact of Envelope Inflation

Hot massive stars have envelopes in which the transport of energy occurs mainly through radiation. Gräfener et al. (2012) discussed the possibility of formation of inflated stellar envelopes when stars have high Eddington parameters, $\gtrsim 0.3$ (see also Ishii et al. 1999; Petrovic et al. 2006 for further discussion on envelope inflation), which is likely for very massive stars due to their high luminosities. In these works the inflation of the envelope is mainly triggered by the presence of a sudden increase in opacity due to Fe (the so-called Fe bump). Sanyal et al. (2017) presented numerical stellar evolution models for a range of metallicities, showing that the nature of the inflated envelopes is sensitive to the Fe content. They also showed that for Pop III models, the presence of inflated envelopes during the MS should occur for $M_{\rm ini} \gtrsim 150\,{\rm M}_\odot$. If these stars do experience inflation of their envelopes, their surface temperature will subsequently decrease, which in turn will decrease their ionizing photon production rates.

Based on these previous studies, we do not expect Pop III stars to experience substantial envelope inflation during the MS for $M_{\rm ini} \lesssim 150\,{\rm M}_\odot$, which is consistent with our model grid (Murphy et al. 2021a). Inflation may be important for the very massive star models, and based on the 1-D energy transport prescriptions available we estimate a decrease of around $\sim 20\%$ for the number of hydrogen ionizing photons coming from individual stars above $150\,{\rm M}_\odot$. This is a rough estimate, obtained by comparing the number of photons produced per ${\rm M}_\odot$ for the $300\,{\rm M}_\odot$ model to the $500\,{\rm M}_\odot$ model. As we discussed in Section 5.4.4, the impact will be lower than 20% for a population of fixed mass and reasonable IMF, since the majority of the stars will have $M_{\rm ini} < 150\,{\rm M}_\odot$.

It is worth noting that ultimately the structure and radial extension of radiatively-

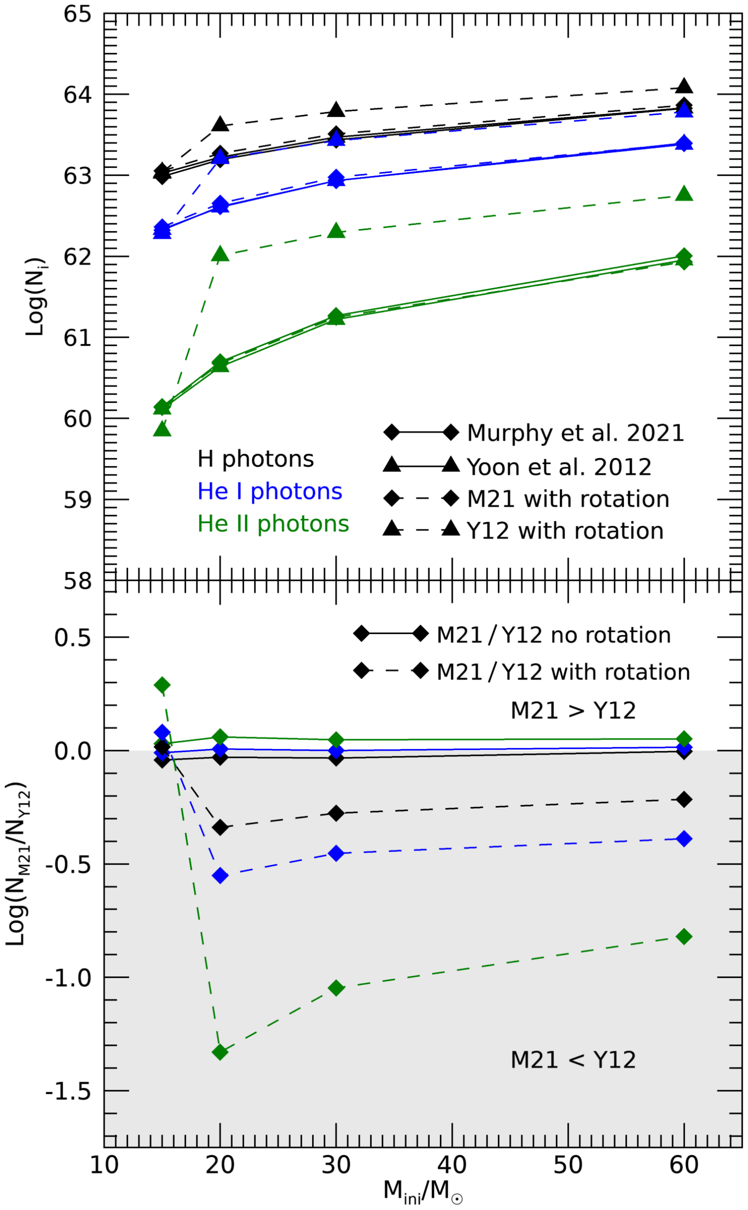

Figure 5.18: *Upper:* Comparison to ionizing photons produced over lifetime (N_i) by Yoon et al. (2012) (Y12) models to values in this work. Rotating models are shown by dashed lines, and selected for having similar initial rotational velocities to our rotating models in Murphy et al. (2021a) (M21), while solid lines show ionizing photons produced by non-rotating models. Triangle symbols indicate Y12 model values, and diamond symbols indicate ionizing photons produced by M21 models which are presented in this work. *Lower:* Ratio of N_i from this work to Y12 values. Colours indicate ionizing photon species as shown in the upper panel.

dominated envelopes is challenging to accurately model in 1-D. We encourage the development of 3-D radiation hydrodynamic simulations for Pop III stellar envelopes, similarly to the study of solar-metallicity models from Jiang et al. (2015).

5.5.5 Supernovae, Binaries and Supermassive Population III Stars

We note that in this work we have studied the ionizing photon production during the lifetime of individual stars, and integrated this to determine the ionizing photon production of a stellar population. We have therefore omitted the impact of explosive events such as SNe in the contribution to ionization of the first stellar populations. In addition, our models are based on single stars. Yet, we stress that the impact of the physical effects discussed here, such as rotation and convective overshooting, will also hold for binary stars. Berzin et al. (2021) discussed the contribution of stripped stars to reionization. These authors found that the contribution of stripped stars compared to single stars reduces moving towards lower metallicities, but stripped stars still have a noticeable effect in the spectral energy distribution of galaxies in the early Universe. The relative contribution of binary stars to the production of ionizing photons depend on their initial orbital separation. The statistics of Pop III binaries were investigated in Liu et al. (2021), which showed that relatively close binaries (semi major axis $< 100\,\mathrm{au}$) tend to be rare in Pop III systems. This is in contrast with many previous results (Kinugawa et al. 2014; Hartwig et al. 2016; Belczynski et al. 2017; Liu & Bromm 2020a) and tends to weaken the importance of close binary evolution for these Pop III stars. If close binary evolution is rare for Pop III stars, we expect our results for the ionizing photon production of Pop III stellar populations to be largely unchanged by the inclusion of binaries. Given the caveats associated with Pop III star formation, we encourage further research to investigate Pop III binaries and their impact on ionization.

As discussed in Section 1.3.4, recent studies have provided new insights into the nature of Pop III supermassive stars (SMSs) and their role in the formation of the first quasars (Hosokawa et al. 2013; Umeda et al. 2016; Woods et al. 2017; Haemmerlé et al. 2018, 2019; Haemmerlé 2021a). These objects are expected to contribute significantly to ionization, so should be included in further studies alongside the mass range of stars discussed in this work. The detectability of such objects with JWST has been investigated in Martins et al. (2020), showing that SMSs should be detectable if they are luminous and relatively cool. In Section 1.3.4 we also discussed that, for a narrow range of initial masses, it has been found that SMSs may explode as general relativity supernovae (GRSNe) (Chen et al. 2014a), with the detectability of these events by JWST and G-REX studied recently in Moriya et al. (2021). They found that GRSNe would have long plateau phases that appear as persistent sources at high redshifts, but would be distinguishable from high redshift galaxies. If SMSs and GRSNe are found with these new facilities in the coming years, then it is likely that they will significantly affect reionization at high redshifts.

5.5.6 Escape Rates of Ionizing Photons

The contribution of the first stars to cosmic reionization not only depends on ionizing photons produced, but also on the escape fraction (f_{esc}) of these photons from the minihalo or host galaxy. Simulations of the early Universe have been used to study the contribution of the first stellar populations to hydrogen reionization (Gnedin & Ostriker 1997; Sokasian et al. 2004; Whalen et al. 2004; Kitayama et al. 2004; McQuinn et al. 2007; Haardt & Madau 2012; Wise et al. 2014; Finlator et al. 2018; Katz et al. 2019) and can reproduce hydrogen reionization up to $z = 6$. However, to do so they require escape fractions of at least 20%. Some studies have shown that the first galaxies had high escape fractions with Whalen et al. (2004) suggesting $f_{\rm esc} > 0.95$, and Wise & Cen (2009) finding escape fractions of $0.25 < f_{\rm esc} < 0.8$ for galaxies of masses greater than $10^7\,{\rm M}_\odot$ with a top-heavy initial mass function (IMF). Alvarez et al. (2006) also showed high escape fractions of up to 90% when stars of masses $80{\rm M}_\odot < M_{\rm ini} < 500{\rm M}_\odot$ are included. More recent work (Wise et al. 2014) has shown that the escape fraction is inversely dependent on halo mass with $f_{\rm esc} \sim 0.5$ for halo masses $< 2\times10^7\,{\rm M}_\odot$ and escape fractions as low as $f_{\rm esc} \sim 0.05$ for halo masses $> 2\times10^8\,{\rm M}_\odot$, which is similar to results found in Kitayama et al. (2004) showing that halos of mass $< 10^6\,{\rm M}_\odot$ have escape fractions of more than 80% while the escape fraction for higher mass halos ($> 10^7\,{\rm M}_\odot$) is essentially zero. This inverse relationship of escape fraction and halo mass was further supported by the Renaissance simulations (Xu et al. 2016c). As work to constrain the escape fraction of ionizing photons continues, it is important to keep this limit in mind in determining how the first stars contributed to reionization. Through simultaneous efforts to predict the ionizing photon contribution of Pop III stars and the escape rates of photons from these populations we move closer to understanding the epoch of reionization, and prepare for prospective detections from facilities such as JWST.

5.6 Conclusions

In this chapter we have investigated the ionizing photon production rates and total ionizing photons produced by our Geneva Pop III stellar evolution grid. We have presented analytical fits for the ionizing photons produced by non-rotating zero-metallicity models in the mass range $1.7\,{\rm M}_\odot \leq M_{\rm ini} \leq 500\,{\rm M}_\odot$. We have discussed the results for individual models and explained the impact of initial mass, rotation, and convective overshooting. We have analysed the ionizing photon production of populations of these stars for a number of different IMFs, and showed how this evolves over time. We have also compared our results to previous works on ionizing photon production of Pop III stellar evolution models, Schaerer (2002) and Yoon et al. (2012). The following points summarise our findings from this chapter.

- The total number of ionizing photons produced over the lifetime of individual stars increases with increasing initial mass despite shorter lifetimes at higher initial masses. This is due to the higher luminosity and surface temperatures of more massive models which drive higher ionizing photon production rates.

- Rotation impacts the total ionizing photons produced by up to 25% for the initial rotational velocity considered here. The most significant impact is higher H ionizing photon production for less massive models and lower He II ionizing photon production for more massive models. The difference in rotational effects for different ionizing photon species reflects the dominant surface property in each case. H ionizing photons are dominated by changes in luminosity, while He II ionizing photons are dominated by changes in surface temperature.

- Higher convective overshooting increases the total number of ionizing photons produced for all species at all initial masses considered here. Increases in luminosity and surface temperature contribute to higher ionizing photon production rates but increased lifetimes is the dominant factor in increasing total ionizing photons produced with higher convective overshooting.
- Ionizing photon production increases with decreasing IMF slope, because more top-heavy IMFs are dominated by higher initial masses which produce more ionizing photons. This variation depends on the IMF slopes considered, with a decrease of 26% comparing the non-rotating $\alpha_{\rm ov} = 0.1$ SB13 IMF population to the Salpeter IMF population.
- Along with producing less ionizing photons than more top-heavy IMF populations, populations of higher IMF slope, α, take longer to produce ionizing photons since they are dominated by less massive models with longer lifetimes.
- Varying the minimum mass, $M_{\rm min}$, of the population decreases the total H ionizing photons produced for populations with IMF slopes of $\alpha \geq 1$, by up to $\sim$50% for $M_{\rm min} = 1.7\,{\rm M}_\odot$ compared to $M_{\rm min} = 9\,{\rm M}_\odot$ where $\alpha = 2.35$.
- Varying the maximum mass, $M_{\rm max}$, of the population increases the total H ionizing photons produced for all IMF slopes considered here, by up to $\sim$30% for $M_{\rm max} = 500\,{\rm M}_\odot$ compared to $M_{\rm max} = 120\,{\rm M}_\odot$ where $\alpha = 1$.
- Our modifications to the H abundance profile using the SNAPSHOT method impact the ionizing photon production rates of a $20\,{\rm M}_\odot$ model by up to 20% halfway through the MS and 30% at the end of the MS.
- Through comparing our results to Schaerer (2002), we have found that our approach of using a blackbody fit is a good approximation for H ionizing photons. While we find that a blackbody fitting overestimates He II ionizing photons at initial masses $\leq 40\,{\rm M}_\odot$, this is not expected to significantly impact our ionizing photon production results for the population since the He II ionizing photon production for all IMF slopes ≤ 2.35 is dominated by stars with $M_{\rm ini} > 40\,{\rm M}_\odot$.
- Through comparing our results to Yoon et al. (2012), we have found that models that achieve CHE produce significantly more ionizing photons with increases of up to 1.4 dex. This shows that massive rotators should produce more ionizing

photons if magnetic fields are included, which will impact top-heavy IMF populations significantly.

Chapter 6

Conclusions and Outlook

In this chapter we summarise our principal conclusions on the effects of rotation on the evolution of the first stars in the Universe (Section 6.1) and discuss the future prospects for understanding the evolution of the first stars. We outline further research that can be done to improve our knowledge of Pop III stellar evolution focusing on increased rotational velocity and mixing in Section 6.2.1, and understanding Pop III mass-loss mechanisms in Section 6.2.2. We then discuss next steps for our stellar evolution grid, specifically through radiative transfer modelling in Section 6.2.3.

6.1 Principal Thesis Results

In Chapters 4 and 5 we give our full conclusions for the results of this work. Here we summarise the three main findings of this thesis with respect to rotational effects on key evolutionary properties of Pop III stars. These are, the effect of rotation on surface properties and how that connects to interior structure; the effect of rotation on metal enrichment, specifically the final ^{14}N abundance; and the effect of rotation on the ionizing photon production of zero-metallicity stars.

6.1.1 Effect of Rotation on Surface Properties

The first key result of this work relates to how rotation impacts the surface properties of Pop III stars. This is discussed in Sections 4.2 and 4.3, based on the analysis of the massive models ($9\,\mathrm{M}_\odot \leq M_\mathrm{ini} \leq 120\,\mathrm{M}_\odot$) in our Geneva stellar evolution grid. Through a detailed investigation of how rotation impacts the internal structure of zero-metallicity stars, we have determined that there are a number of ways in which rotational mixing impacts stellar structure depending on the initial mass and rotational velocity of the star.

Despite the variety of behaviour for models of different initial masses, we have identified that, in general, rotation increases the luminosity and decreases the surface temperature of our models. The reasons for this are threefold.

- Firstly, rotational mixing increases the core size by mixing material from outside the core inwards. For example, supplying the H-burning core with additional hydrogen during the MS. This increases the energy generation, which subsequently increases the luminosity.
- Secondly, during the He-burning phase, rotational mixing brings He-burning products from the core to the H-burning shell. This increases the energy generation of the H shell, which impacts the stellar structure. The impact to stellar structure varies depending on the initial mass of the model, but generally we observe an increase to the stellar radius which is reflected by a decrease to surface temperature.
- Thirdly, models which approach critical rotation experience a decrease in surface temperature. This results from their decreased effective surface gravity as the centrifugal force of rotation counteracts their gravitational force.

Whether these effects are observed in a given model depends primarily on the relative core size. This is observed in our results as dependent on the initial mass of the model, given that models of different initial masses have different relative core sizes. We have found that models with smaller cores relative to their stellar mass tend to be dominated by increases to luminosity. This is likely because lower mass models tend to have lower relative core sizes (see Figure 4.4 in Section 4.2), and the luminosity of lower mass models is more sensitive to changes in energy generation (see Section 1.1.2). However, their stellar structure is also more sensitive to changes to the H shell in the He-burning phase, so they can experience a large decrease in surface temperature during He burning. By contrast, models with larger cores relative to their stellar mass are less sensitive to changes to the H-burning shell.

From Figure 4.4 in Section 4.2 we saw that models of higher initial masses tend to have larger relative core sizes, so they are less sensitive to changes to the H-burning shell. However, from Figure 4.8 in Section 4.3 we know that the most massive models are also most likely to approach critical rotation. Since the most massive models, $M_{\rm ini} = 60, 85, 120\,{\rm M}_\odot$, approach critical rotation, their effective surface gravity is decreased and they have relatively lower surface temperatures to non-rotating models of the same initial mass.

Therefore, for the majority of the evolution we have found that the impact of rotation on less massive models is dominated by increased luminosities, while for more massive models the dominant effect is a decrease to the surface temperature. During He burning the case is more complex and the H shell can play a dominant role in determining the surface properties. During this phase less massive models can see large decreases to their surface temperature depending on their relative core size and the initial rotational velocity considered.

6.1.2 Effect of Rotation on Metal Enrichment

The second principal result of this work is the effect of rotation on the metal enrichment of Pop III stars, for which we have focused on the enrichment of ^{14}N. This is discussed in Section 4.4, again based on the analysis of the massive models in our Geneva grid. In that section, we described our investigation of the ^{14}N production of our models, with and without rotation. We had expected that rotational mixing would increase ^{14}N abundance in all cases, however, we found that the effects of rotation on chemical enrichment were more complex than predicted. Ultimately, we have found that the impact of rotation on stellar structure is such that it can increase, but also hinder, ^{14}N enrichment. The nature with which rotational mixing impacts chemical enrichment depends on the initial structure of the star, i.e. the relative core size, and the initial rotational velocity.

We have shown that the interruption of ^{14}N production with rotation arises from sudden changes to the stellar structure, resulting from the 'CNO boost'. This event represents a sharp increase in energy generation in the H-burning shell when the CNO cycle becomes the dominant energy source following the introduction of ^{12}C and ^{16}O to the region. The strength of this boost in energy in the stellar envelope can cause the size of the stellar core to be reduced. If this happens during He burning it distances the He core from the H shell, making it more difficult for rotationally mixed He-burning products to reach the H-burning shell where they would form ^{14}N through the CNO cycle. For precise mass and initial velocity domains this behaviour occurs early in the He-burning phase, thus significantly impacting the final ^{14}N abundance of the star. The best example of this is the $20\,\mathrm{M}_\odot$ model with $\upsilon_{\mathrm{ini}} = 0.4\,\upsilon_{\mathrm{crit}}$ which produces $\sim$4.5 dex less ^{14}N than the $15\,\mathrm{M}_\odot$ model with $\upsilon_{\mathrm{ini}} = 0.4\,\upsilon_{\mathrm{crit}}$, due mainly to a strong CNO boost early in the He-burning phase.

We note also that the production of ^{14}N is not limited to the He-burning phase, and that it can be produced any time that He-burning products are in contact with a H-burning region. This occurs, for example, if a H-burning shell develops in a region where He burning previously took place. This is the case for the non-rotating $20\,\mathrm{M}_\odot$ model, which experiences a CNO boost in the post He-burning phase when the contraction of the star allows the H shell to move inwards to a region which had previously experienced He burning. The $20\,\mathrm{M}_\odot$ non-rotator thus ends its life with a relatively large ^{14}N abundance, comparable to that of the $120\,\mathrm{M}_\odot$ model with $\upsilon_{\mathrm{ini}} = 0.4\,\upsilon_{\mathrm{crit}}$.

In conclusion, what we have learned is that it is not enough to know the initial rotational velocity in order to predict how much ^{14}N will be produced by a Pop III star. Instead, we need to have a detailed understanding of the interior structure to accurately predict metal yields. This can be achieved through comparing the chemical yields of our models with future observations, to understand what initial parameter space could have led to a stellar structure capable of producing a given abundance.

6.1.3 Effect of Rotation on Ionizing Photon Production

The third major result of this work refers to the effect of rotation on the ionizing photon production of Pop III stars, both for individual models, and populations of zero-metallicity stars. The results of our work on the ionizing photon production of Pop III stars, based on our Geneva stellar evolution grid, are presented in Chapter 5. In that chapter we discuss the impact of rotation, convective overshooting, and the nature of the IMF on ionizing photon production. Here we will summarise how rotation in particular affects ionizing photon production, and how this compares to the effects of varying convective overshooting and the nature of the IMF.

For individual models of initial masses $9\,\mathrm{M}_\odot \leq M_{\mathrm{ini}} \leq 120\,\mathrm{M}_\odot$, rotation impacts the total ionizing photons produced by up to $\sim$25% for the initial rotational velocity considered here ($\upsilon_{\mathrm{ini}} = 0.4\,\upsilon_{\mathrm{crit}}$). The impact of rotation on ionizing photon production varies for different initial masses, which reflects the impact of rotation on the surface properties. The number of H ionizing photons produced is increased by up to $\sim$25% when rotation is included, while the more energetic He II ionizing photons are decreased by up to $\sim$25% when rotation is included. The difference in rotational effects for different ionizing photon species reflects the dominant surface property in each case. As explained in Section 2.8.2, H ionizing photons are dominated by changes in luminosity, while He II ionizing photons are dominated by changes in surface temperature. We describe in Section 6.1.1 that the main effect of rotation on models of different initial masses is that less massive models have increased luminosities and more massive models have decreased surface temperatures. Therefore, less massive models have a larger increase in H ionizing photons when rotation is included, while more massive models have a larger decrease in He II ionizing photons when rotation is included.

Convective overshooting, on the other hand, leads to an increase in the production of all ionizing photon species by roughly 20% for all initial masses considered, because increased convective overshooting increases luminosity and surface temperature. This further proves that the impact of rotation is more complex than increased core size alone, and shows that we need to accurately model rotation in stellar evolution codes to understand how rotation affects stellar structure.

To understand how rotation impacts the ionizing photon production of populations of zero-metallicity stars we used IMFs of the form $\xi(M) \propto M^{-\alpha}$ (Section 2.8.3) and varied the slope, α, with a fixed total stellar mass of the population. As the IMF slope changes, the dominant mass in the population also changes, i.e. higher values of α mean that lower mass stars dominate. Therefore, the effect of rotation on the population depends on the effect of rotation for the dominant initial mass. This explains why for lower values of α we see that the main effect of rotation is a decrease to the He II ionizing photons produced by the population, while for higher values of α we observe a larger increase to H ionizing photons with rotation.

We have also found that more massive models produce more ionizing photons than models of lower initial masses due to their higher luminosities and temperatures. Therefore, populations of lower IMF slopes, α, produce more ionizing photons. To understand how this effect compares to the impact of rotation and convective overshooting on the ionizing photon production of a population, we take the example of two IMF slopes in particular. These are the Salpeter IMF slope, $\alpha = 2.35$ (Salpeter 1955), and the Stacy & Bromm (2013) (SB13) IMF slope, $\alpha = 0.17$. Taking the non-rotating $\alpha_{\mathrm{ov}} = 0.1$ (lower convective overshooting) SB13 population as a reference, the value for total H ionizing photons produced per stellar mass of the population ($N_{\mathrm{pop}}/\mathrm{M}_{\mathrm{tot}}$) is 1.13×10^{62} photons $\mathrm{M}_{\odot}^{-1}$ (see Table 5.4). This value increases by 7.7% when rotation of $\upsilon_{\mathrm{ini}} = 0.4\,\upsilon_{\mathrm{crit}}$ is included, by 9.9% with higher overshooting of $\alpha_{\mathrm{ov}} = 0.3$, and decreases by 26% when we assume a Salpeter IMF slope. Therefore, if comparing between the SB13 and Salpeter IMF slopes, then the choice of IMF slope is relatively more impactful than the effect of rotation or convective overshooting for the values considered here. For more similar IMF slopes the effect of changing the IMF slope is more comparable to the impact of rotation.

6.2 Future Work in Studying the First Stars

As outlined in Section 6.1, in this work we have provided new insights into the effects of rotation on the evolution of the first stars. Specifically we have improved understanding of how rotation impacts the interior structure, metal enrichment, and ionizing photon production of zero-metallicity stars. However, many open questions about the evolution of Pop III stars remain and there are still evolutionary properties that could be further investigated. We are also limited in our stellar evolution modelling to computational power so we rely on 1-D models which limit resolution and require some assumptions for complex physics like convective mixing. Furthermore, we have had to enforce certain modifications to ease computations of Pop III models (see Section 2.7), whose unique structure can give rise to computational difficulties. Despite this, we have provided a state-of-the-art stellar evolution grid of Pop III stars with and without rotation. These models can act as the basis for numerous future studies such as radiative transfer modelling, population synthesis, and hydrodynamical simulations of the early Universe. In this section we will discuss some next steps for the study of the evolution of the first stars in the Universe. We focus on three main topics which would build on the results of this thesis and advance our understanding of Pop III stars.

6.2.1 Higher Rotational Velocity and Increased Mixing

As described in Section 1.2.1, many of the first stars are expected to form with rapid rotation near the critical limit (Stacy et al. 2011, 2013; Hirano & Bromm 2018). Rapid rotation is also predicted for the first stars based on the chemical abundance patterns of CEMP stars (Choplin et al. 2018, Section 1.3.1). The initial rotational velocity considered in this work is $\upsilon_{\rm ini} = 0.4\,\upsilon_{\rm crit}$ for consistency with the higher-metallicity Geneva stellar evolution grids (Section 2.6). To match the initial rotational velocity predicted by star formation and chemical enrichment works this value should likely be increased. Currently this research is being carried out by collaborators to study how the evolution of our Pop III models varies when an initial rotational velocity of $\upsilon_{\rm ini} = 0.7\,\upsilon_{\rm crit}$ is assumed (Tsiatsiou et al., 2021 in prep.). Given that our most massive models reach critical rotation on the MS with $\upsilon_{\rm ini} = 0.4\,\upsilon_{\rm crit}$, we expect that these new models with higher rotation will spend significant periods of their evolution at critical rotation. This increased rotational instability will have important consequences for the mass loss of these stars, and subsequently their final fates and impact on their environments.

Increased rotational velocity and interior mixing also poses interesting questions for the chemical enrichment of the models. Our work has shown that higher rotation can trigger earlier CNO boosts and may subsequently hinder chemical enrichment (Section 4.4). From our results we then expect that this behaviour would occur at lower initial masses due to the increased rotational mixing of models with $\upsilon_{\rm ini} = 0.7\,\upsilon_{\rm crit}$, e.g. the dip in ^{14}N abundance for the $20\,{\rm M}_{\odot}$ rotating model seen in Figure 4.10 would occur at a lower initial mass. Perhaps however, rotational mixing in models with $\upsilon_{\rm ini} = 0.7\,\upsilon_{\rm crit}$ would be so strong that, despite the suppression of the He core following a strong CNO boost, rotational mixing would be strong enough to continue supplying the H shell with ^{12}C and ^{16}O. As we have shown, the internal structure of zero-metallicity stars makes them very sensitive to changes in rotational mixing. Therefore, confidence in the effects of higher rotation on our models requires additional stellar evolution models. These new models with $\upsilon_{\rm ini} = 0.7\,\upsilon_{\rm crit}$ will develop our understanding of the mixing processes and chemical enrichment in Pop III stars and will help us to better understand their impact on the early Universe.

In Groh et al. (2019), the impact of higher rotation and magnetic fields are studied with consistent input physics for Geneva stellar evolution models with initial metallicity Z=0.0004. The results of this investigation are shown in Figure 6.1 (Figure 18 of Groh et al. 2019). Plotted in the figure are various rotating models with and without magnetic fields. In black are models from Groh et al. (2019), in red is a Z=0.0004 model rotating with $\upsilon_{\rm ini} = 0.4\,\upsilon_{\rm crit}$ from Szécsi et al. (2015), and in blue is a Z=0.0004 model rotating with $\upsilon_{\rm ini} = 0.4\,\upsilon_{\rm crit}$ from Choi et al. (2016), both of which include magnetic fields. It can be seen from Figure 6.1 that magnetic fields increase mixing in the models, and that mixing is further increased by increasing the initial rotational velocity from $\upsilon_{\rm ini} = 0.4\,\upsilon_{\rm crit}$

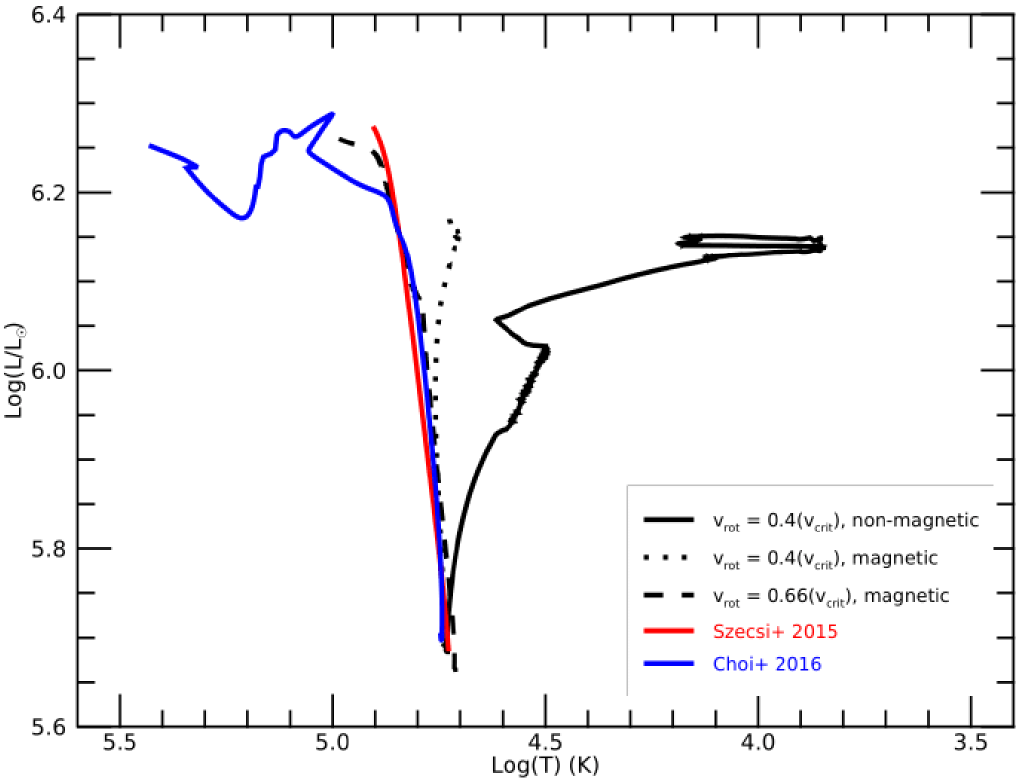

Figure 6.1: Evolutionary tracks in the HR diagram for Z=0.0004 models with initial mass $M_{\rm ini} = 60\,{\rm M}_\odot$ computed by different groups. The black lines indicate the models computed in Groh et al. (2019), while the blue and red lines correspond to MESA (Choi et al. 2016) and Bonn models (Szécsi et al. 2015). Taken from Groh et al. (2019), Figure 18.

to $\upsilon_{\rm ini} = 0.66\,\upsilon_{\rm crit}$. From Figure 6.1 we observe that this increased rotational mixing is required to match models with magnetic fields from other works, which shows that to understand the impact of magnetic fields properly we require consistent physics of the models. Therefore, while we can expect increased magnetic fields to increase mixing in zero-metallicity models, to isolate their impact we need to run new models with consistent physical inputs and including magnetic fields. We discussed in Section 1.2.6 that Yoon et al. (2012) modelled the evolution of Pop III stars with magnetic fields. That work found that magnetic fields gave rise to chemically homogeneous evolution (CHE) in massive rotating models. This greatly increases surface temperature and drastically changes the evolution along the HR diagram. In Section 5.5.3 we then showed how the high temperatures of models with CHE substantially increase the ionizing photon production of Pop III stars. Since the physics of our stellar evolution models varies somewhat from the Bonn stellar evolution models presented in Yoon et al. (2012), we cannot fully disentangle the effects of including magnetic fields. The inclusion of magnetic fields in our models is thus an additional prospect for future work in understanding the evolution of zero-metallicity models, and isolating the effects of various mixing properties.

6.2.2 Mass-Loss Mechanisms

In Section 1.2.3 we discuss how mass-loss mechanisms operate in zero-metallicity stars. Based on the negligible radiative winds of Pop III stars, episodic mass loss is the only mechanism for removing angular momentum from these stars. In our work we have shown that this leads to the spin up of our models with models of initial masses $M_{\rm ini} = 60, 85, 120\,{\rm M}_{\odot}$ reaching critical rotation on the MS (Section 4.3). For this we have found the mechanical mass-loss implementation in GENEC (Section 2.5.2) to be insufficient in evolving our models away from critical rotation, so instead we use an averaged mass-loss rate at the critical rotation limit (Section 2.7.1). This estimate has allowed our computation of these stars, however, more research is required to accurately model this phase. In reality, the instabilities induced approaching critical rotation could drive a form of pulsational mass loss or some other type of eruption. To understand this critical phase we therefore encourage 3-D hydrodynamic modelling of the behaviour of Pop III stars at the critical rotation limit. While such simulations are computationally expensive it could be feasible to use 3-D simulations to model brief periods of the evolution, for example, approaching the critical rotation limit towards the end of the MS.

Further modelling is also required to study other episodic mass-loss events in these stars. For instance in late phases we have seen that these stars can experience sudden changes in structure and energy generation which may trigger pulsations and lead to mass-loss events. Strong chemical gradients and increased compactness of zero-metallicity stars reduces their stability, thus warranting further research to investigate if these instabilities could drive episodic mass-loss events. To study these instabilities accurately requires 3-D simulations of the stellar interior. In work by Jiang et al. (2018), 3-D hydrodynamical simulations were used to study eruptive mass loss in solar-metallicity massive stars. More specifically they studied the LBV phase when these stars are close to the Eddington limit and were able to reproduce observed mass-loss rates and behaviour on the HR diagram for stars of initial masses $M_{\rm ini} = 35\,{\rm M}_{\odot}$ and $80\,{\rm M}_{\odot}$. A key finding of that work was that the helium opacity peak can drive oscillations in the envelopes of massive stars, which contribute significantly to the mass-loss rates found. Previous work based on 1-D simulations had not predicted that the helium opacity peak played an important role in LBV mass loss, and it was expected that the iron opacity peak would be predominantly responsible for pulsations at the Eddington limit. The novel importance of the helium opacity peak is particularly interesting for zero-metallicity stars since they are iron deficient, and infers that they may experience similar pulsations to solar-metallicity stars in the LBV phase. Therefore, work similar to that of Jiang et al. (2018) would provide new insights into the behaviour of Pop III stars near the Eddington limit and how continuum driven winds may develop in their envelopes.

In the coming years we expect to make great strides in understanding episodic mass loss of stars in the early Universe. Not only will we have new observational facitilies such as JWST and SKA, but there are also ongoing research projects such as the ASSESS project (Episodic MAss LoSS in Evolved MaSsive Stars). The ASSESS project focuses on topics such as the frequency of eruptive events like η Car and their metallicity dependence, the nature of LBV mass loss, and the nature of episodic mass loss in massive stars in the pre-SN stages. Recent works from this project have developed new ways to identify observations of mass-loss events in the SMC, LMC, and the dwarf galaxy NGC 6822 (Yang et al. 2019, 2020, 2021a,b). Their most recent paper (Yang et al. 2021b) presents a method to identify RSGs using a $\sim 1.6\,\mu$m 'H-bump' signature. These developing observational strategies, together with new observations of the early Universe in the coming years, are expected to greatly advance our knowledge of eruptive mass-loss events. Having detailed models of mass-loss events in low-metallicity and zero-metallicity stars will better help us to understand these observations, and will provide new insight into the evolution of the first galaxies.

6.2.3 Radiative Transfer Modelling

To predict the observed spectra of Pop III stars we can use radiative transfer modelling. This involves taking the predicted surface properties of our models and inputting them to a radiative transfer code, such as CMFGEN (Hillier & Miller 1998) for example. As explained in Chapter 5, modelling the stellar atmosphere would also improve the accuracy of our ionizing photon predictions. An example of the combined analysis of a star through stellar evolution and atmosphere modelling is the work of Groh et al. (2014). In that work the spectroscopic signatures of a non-rotating $60\,\mathrm{M}_\odot$ star at solar-metallicity (from Ekström et al. 2012) are calculated at 53 stages across the evolution from the ZAMS to the pre-SN stages, using CMFGEN. By doing so, the connection between interior structure and spectroscopic signatures provided a novel understanding of how solar-metallicity massive stars evolve through different spectroscopic phases based on changes to their energy generation and internal abundances.

This is illustrated in Figure 6.2 (Figure 9 of Groh et al. 2014) which shows the simultaneous duration of evolutionary and spectroscopic phases, as well as the corresponding evolution of magnitudes and ionizing photons produced. That work provided new insight into how observations of massive stars can be linked to evolutionary phases and the interior structure of the observed star. For instance it can be observed from Figure 6.2 that the $60\,\mathrm{M}_\odot$ model spends a significant period of its MS in the LBV phase. This is somewhat surprising given that observed LBVs are typically expected to be He-burning stars, and emphasises that we can better understand spectral observations when we have combined models of interior and spectroscopic evolution. Since evolution at zero metallicity is vastly different from evolution at solar metallicity, the corresponding evolution of spectroscopic and interior properties is likely to differ from that work. A similar approach of modelling the spectroscopic properties through radiative transfer across the evolution

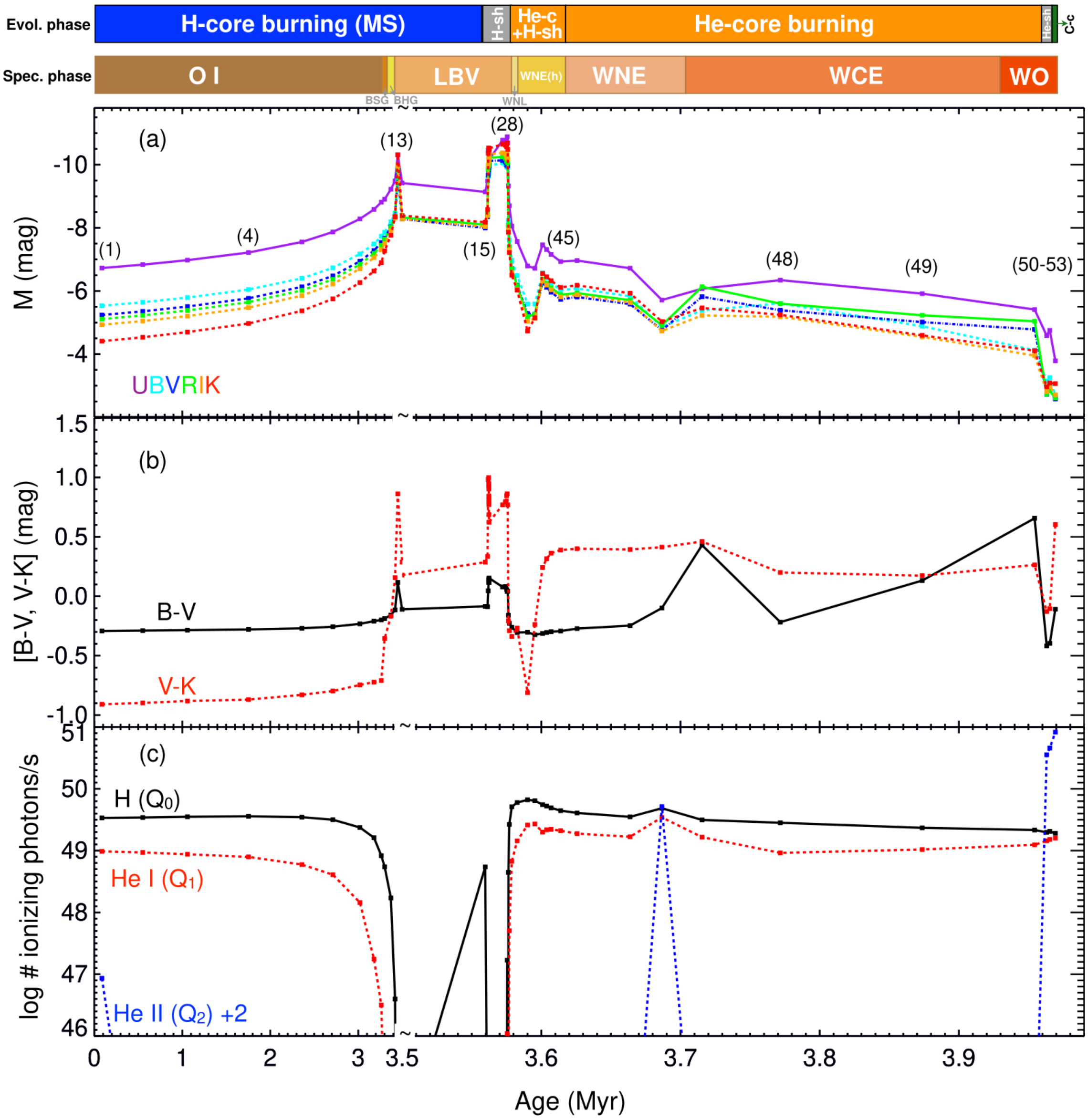

Figure 6.2: Evolution of absolute magnitudes (a), B - V and V - K colors (b), and number of H, He I, and He II ionizing photons emitted per second (c) throughout the lifetime of a non-rotating 60 $M_\odot$ star. At the top we indicate the duration of evolutionary and spectroscopic phases as reference. To make the post-MS evolution clearer, the ordinate scale was changed at 3.5 Myr. Taken from Groh et al. (2014), Figure 9.

of our Pop III models would prepare us for future observations of Pop III spectra. It would also develop our knowledge of the mass loss of the first stars by providing us with the specific duration of spectroscopic phases such as the LBV phase.

Radiative transfer modelling can also be used to model the spectra of explosions of our models and predict the nature of their SNe. The first stellar explosions are hugely important for understanding how the first stars impacted their environments through chemical enrichment and ionization, and may be our best chance for resolving individual

Pop III stars in future observations since their extreme luminosities should be detectable out to high redshifts. In Whalen et al. (2013a,b,c) predictions for the detectability of Pop III stellar explosions are presented based on 1-D stellar evolution models using the KEPLER stellar evolution code (Weaver et al. 1978), the radiation hydrodynamics code RAGE (Gittings et al. 2008), and the SPECTRUM code (Frey et al. 2013). From that work, our knowledge of what to expect from future observations of the first SNe has greatly improved. From models of initial masses $M_{\rm ini} = 150, 175, 200, 225, 250\,{\rm M}_\odot$ they predicted that Pop III PISNe could be detected out to $z \sim 30$ by deep-sky surveys with JWST, and out to $z \sim 20$ by all-sky surveys with WFIRST (Whalen et al. 2013a,b). From models of initial masses $M_{\rm ini} = 15, 25, 40\,{\rm M}_\odot$ they later predicted that Pop III CCSNe could be detected out to $z \sim 10-15$ by JWST (Whalen et al. 2013c). Our models can be used in a similar fashion to predict the nature of the first SNe, with the added advantage of studying the effects of rotation on SN spectra and lightcurves. Given the high rotation expected for Pop III stars it is crucial that we consider the impact of rotation on the first stellar explosions.

In addition to radiative transfer modelling our Geneva Pop III grid could be used for a myriad of simulations to further our understanding of the impact of the first stars on the early Universe. As we have discussed, observations from JWST, WFIRST, and similar facilities may be able to detect the explosive deaths of the first massive stars, but only if they are sufficiently bright. Therefore, it is important that we model what can be observed, such as populations of the first stars. This can be done using population synthesis of stellar evolution models. The Geneva group has developed a population synthesis code called SYCLIST (SYnthetic CLusters Isochrones and Stellar Tracks, Georgy et al. 2014), which presents an excellent opportunity to simulate zero-metallicity populations using our new Pop III stellar evolution grid.

Furthermore, much of what has been learned about the early Universe has been done through numerical simulations. Cosmological simulations have investigated the formation of the first stars, the chemical enrichment of the second generation of stars, the reionization of the Universe, and the development of the first galaxies. The accuracy of these simulations relies partially on the numerical resolution, but also on the certainty of our assumptions and input physics. For example, updated predictions for the nucleosynthetic yields of Pop III stars are crucial for modelling the chemical enrichment of the early Universe. An example of cosmological simulations that have been used to develop our understanding of the early Universe are the Renaissance simulations (O'Shea et al. 2015; Xu et al. 2016b,a,c; Barrow et al. 2017; Norman et al. 2018; Smith et al. 2018). These novel simulations studied the evolution of hundreds of well-resolved galaxies at redshifts of $z \simeq 25-8$, and in doing so have laid the groundwork for understanding the nature of the first galaxies ahead of future observations. The assumptions for Pop III formation and feedback used in these simulations are that of Wise et al. (2014), which took ionizing photon predictions from Schaerer (2002), and SN explosion energies and metal ejecta masses from Nomoto et al. (2006) and Heger et al. (2003). In this work we have presented new predictions for ionizing photon production for Pop III stars (Chapter 5), and recent work from Liu et al. (2021) has used our model grid to predict SNe chemical yields. Thus our grid is already well placed to be used to describe the Pop III feedback physics for future hydrodynamical simulations.

To conclude, we have presented novel results on the effects of rotation on the structural evolution, chemical enrichment, and ionizing photon production of the first stars. We have also shown how our findings can be used to advance future research on Pop III stars. We are constantly learning more and more about the earliest stars in our Universe, the findings presented here contribute to that knowledge and will hopefully aid future discoveries as we enter a new frontier of observational and theoretical research.

Appendix A

Appendix

A.1 Onset of He Burning

In Section 4.2 we discuss the distinctive feature at the onset of He burning for lower mass models, using the non-rotating $9\,M_\odot$ model to illustrate the evolutionary behaviour at this stage. Figure 4.2 shows the key stages in the evolution (stages 3-6) that were used to study this prominent effect on the surface properties. To understand the behaviour of the star during this period, the surface properties were compared with the central properties, Figure A.1, for stages 3-6 in the evolution of the loop. These points correspond to significant differences in the internal structure at this stage, see Figure A.3. From Figure A.1 we see that, while the central properties are similar to what we expect for the onset of He-core burning, the surface properties reveal that more complex behaviour is going on. This is illustrated by the comparison of the $60\,M_\odot$ model properties (Figure A.2) where the surface temperature, bottom left panel, increases sharply as the star contracts following H-core exhaustion then gradually decreases following He ignition as the stellar envelope expands during He-core burning.

By contrast, the $9\,M_\odot$ model shows a sharp decrease in surface temperature immediately after He ignition followed by a gradual increase in surface temperature. Since the central conditions of the star cannot illustrate why the surface is behaving in this manner the internal structure of the star needed to be investigated. Figure A.3 shows, for the four ages noted in Figure A.1 (stages 3-6), where a H-burning shell has formed following H-core exhaustion. This shell would have developed towards the end of H-core burning as the star is contracting. When hydrogen is depleted in the core the continuing contraction of the star ignites this H shell leading to a boost in luminosity at the surface, seen as the first luminosity bump in the bottom right panel of Figure A.1. He burning

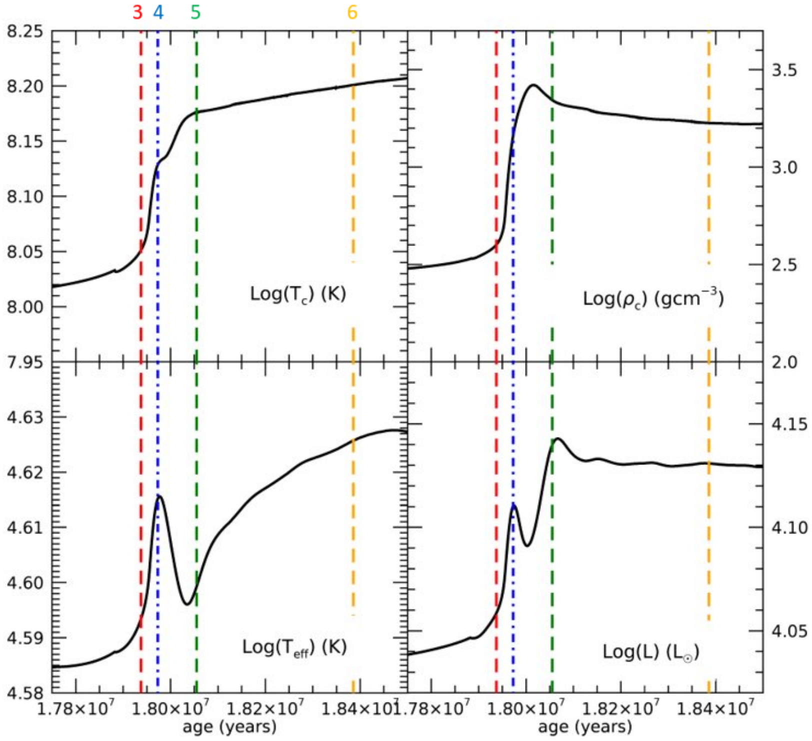

Figure A.1: Central and surface properties of the non-rotating $9\,M_\odot$ model, including central temperature (T_c), central density (ρ_c), effective temperature (T_{eff}), and luminosity (L). Indicated by the vertical dashed lines are the ages which correspond to stages 3-6 in Figure 4.2.

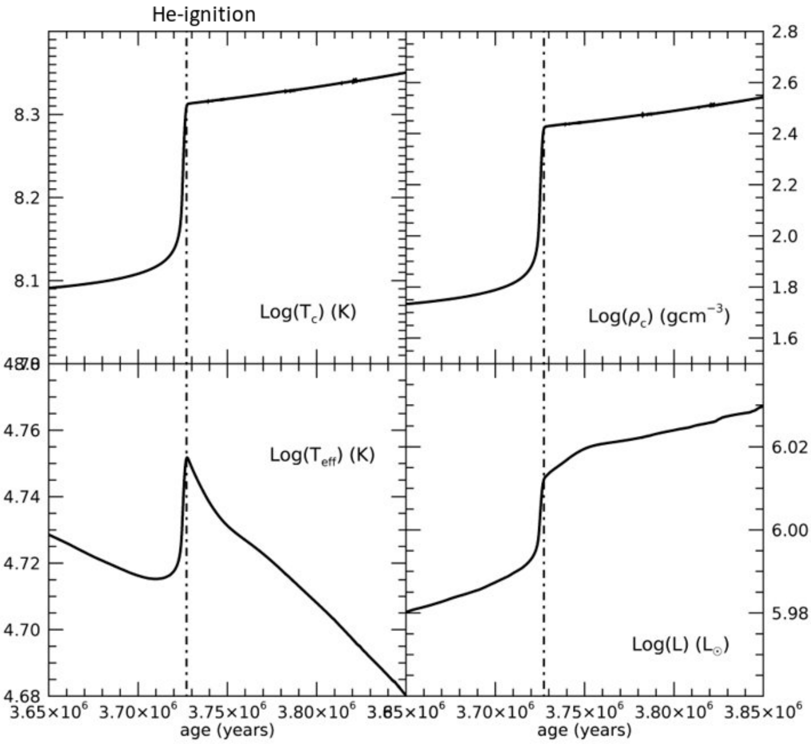

Figure A.2: Central and surface properties of the non-rotating $60\,M_\odot$ model, similarly to Figure A.1. The dashed line indicates He ignition.

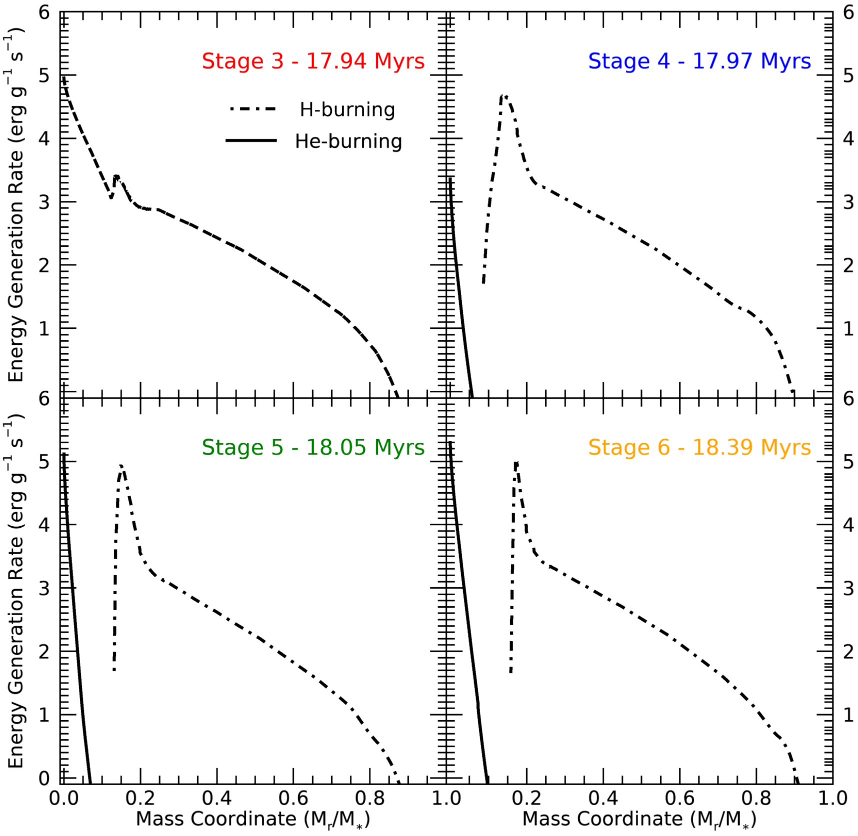

Figure A.3: Energy contribution of H burning and He burning for the 9 M$_\odot$ model at stages 3-6 in Figure 4.2. Mass coordinate illustrates how much mass lies within that region of the stellar interior with stellar centre at $M_r/M_* = 0$.

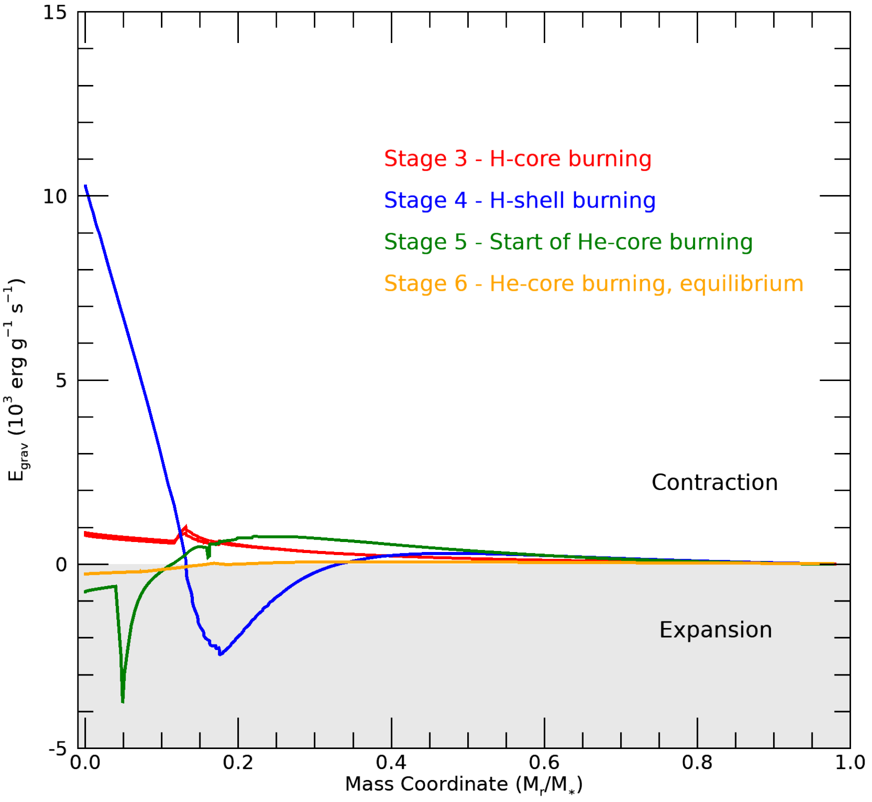

Figure A.4: Gravitational energy generation rates for the 9 M$_\odot$ non-rotating model, where positive values indicate contraction and negative values indicate expansion. Evolutionary stages 3-6 are indicated by the legend.

then begins in the core and we get a further boost to the luminosity. However, this still does not explain the effect on surface temperature. The surprising increase in surface temperature suggests that the stellar envelope may be contracting when He-core burning begins, to investigate this theory the gravitational energy contribution for the stellar interior structure was studied, plotted here as Figure A.4. When positive this indicates contraction, conversely negative values indicate expansion. This therefore allows us to visualise how the stellar core and envelope react to the varying nuclear burning conditions. What can be seen from Figure A.4, is that just prior to He-core ignition when the H-burning shell dominates (stage 4), the now inactive core is strongly contracting, while the envelope expands due to the energy boost from this H shell. This causes the star to lose its thermal equilibrium as the connection between core and envelope becomes unstable. At 18.05 Myrs into the star's evolution (stage 5) He-core burning has now begun and the star starts to regain this thermal equilibrium. As seen from Figure A.4 this leads to a sharp expansion of the outer core and a contraction of the envelope. The contraction of the envelope gives the surface temperature increase that we see in Figure A.1, until approximately 350'000 years later (stage 6) when the star is once again stable and can continue He burning as seen for higher mass models such as the $60\,\mathrm{M}_\odot$ example.

Bibliography

Abbott, B. P., Abbott, R., Abbott, T. D., et al. 2016, Physical Review X, 6, 041015

Abbott, B. P., Abbott, R., Abbott, T. D., et al. 2017, **ApJ**, 848, L12

Abbott, D. C. 1982, **ApJ**, 259, 282

Abbott, R., Abbott, T. D., Abraham, S., et al. 2020a, **ApJ**, 900, L13

Abbott, R., Abbott, T. D., Abraham, S., et al. 2020b, **Phys. Rev. Lett.**, 125, 101102

Abel, T., Bryan, G. L., & Norman, M. L. 2002, Science, 295, 93

Abramovici, A., Althouse, W. E., Drever, R. W. P., et al. 1992, Science, 256, 325

Alvarez, M. A., Bromm, V., & Shapiro, P. R. 2006, **ApJ**, 639, 621

Angulo, C., Arnould, M., Rayet, M., et al. 1999, **Nucl. Phys. A**, 656, 3

Aoki, W., Beers, T. C., Christlieb, N., et al. 2007, **ApJ**, 655, 492

Arnett, W. D., Hirschi, R., Campbell, S. W., et al. 2018, arXiv e-prints, arXiv:1810.04659

Arnett, W. D., Meakin, C., Hirschi, R., et al. 2019, **ApJ**, 882, 18

Asplund, M., Grevesse, N., & Sauval, A. J. 2005, in Astronomical Society of the Pacific Conference Series, Vol. 336, Cosmic Abundances as Records of Stellar Evolution and Nucleosynthesis, ed. I. Barnes, Thomas G. & F. N. Bash, 25

Bañados, E., Venemans, B. P., Mazzucchelli, C., et al. 2018, **Nature**, 553, 473

Barbon, R., Ciatti, F., & Rosino, L. 1979, **A&A**, 72, 287

Barkana, R. & Loeb, A. 2001, **Phys. Rep.**, 349, 125

Barrow, K. S. S., Wise, J. H., Norman, M. L., O'Shea, B. W., & Xu, H. 2017, **MNRAS**, 469, 4863

Becker, G. D. & Bolton, J. S. 2013, **MNRAS**, 436, 1023

Beers, T. C. & Christlieb, N. 2005, **ARA&A**, 43, 531

Beers, T. C., Preston, G. W., & Shectman, S. A. 1992, **AJ**, 103, 1987

Belczynski, K., Heger, A., Gladysz, W., et al. 2016, **A&A**, 594, A97

Belczynski, K., Ryu, T., Perna, R., et al. 2017, **MNRAS**, 471, 4702

Benson, A., Venkatesan, A., & Shull, J. M. 2013, **ApJ**, 770, 76

Berzin, E., Secunda, A., Cen, R., Menegas, A., & Götberg, Y. 2021, arXiv e-prints, arXiv:2102.08408

Böhm-Vitense, E. 1958, **ZAp**, 46, 108

Boian, I. & Groh, J. H. 2018, **A&A**, 617, A115

Boian, I. & Groh, J. H. 2019, **A&A**, 621, A109

Boian, I. & Groh, J. H. 2020, **MNRAS**, 496, 1325

Bouret, J. C., Lanz, T., Martins, F., et al. 2013, **A&A**, 555, A1

Bromm, V. 2012, The First Stars and Galaxies - Basic Principles

Bromm, V. 2013, Reports on Progress in Physics, 76, 112901

Bromm, V., Coppi, P. S., & Larson, R. B. 1999, **ApJ**, 527, L5

Bromm, V., Coppi, P. S., & Larson, R. B. 2002, The Astrophysical Journal, 564, 23

Bromm, V. & Loeb, A. 2003, **ApJ**, 596, 34

Bühler, R. & Blandford, R. 2014, Reports on Progress in Physics, 77, 066901

Burrows, A. & Goshy, J. 1993, **ApJ**, 416, L75

Castellani, V., Chieffi, A., & Tornambe, A. 1983, **ApJ**, 272, 249

Castor, J. I., Abbott, D. C., & Klein, R. I. 1975, **ApJ**, 195, 157

Castro, N., Fossati, L., Langer, N., et al. 2014, **A&A**, 570, L13

Cayrel, R., Depagne, E., Spite, M., et al. 2004, **A&A**, 416, 1117

Chaboyer, B. & Zahn, J. P. 1992, **A&A**, 253, 173

Chabrier, G. 2003, **PASP**, 115, 763

Chatzopoulos, E. & Wheeler, J. C. 2012, **ApJ**, 748, 42

Chen, K.-J., Heger, A., Woosley, S., et al. 2014a, **ApJ**, 790, 162

Chen, K.-J., Woosley, S., Heger, A., Almgren, A., & Whalen, D. J. 2014b, **ApJ**, 792, 28

Cherchneff, I. & Dwek, E. 2010, **ApJ**, 713, 1

Chevalier, R. A. 1977, **ARA&A**, 15, 175

Chevalier, R. A. & Fransson, C. 1985, Supernova Interaction with a Circumstellar Wind and the Distance to SN 1979c, Vol. 224, 123

Chiaki, G., Wise, J. H., Marassi, S., et al. 2020, **MNRAS**, 497, 3149

Chieffi, A. & Limongi, M. 2004, **ApJ**, 608, 405

Chieffi, A. & Tornambe, A. 1984, **ApJ**, 287, 745

Choi, J., Dotter, A., Conroy, C., et al. 2016, **ApJ**, 823, 102

Choplin, A. & Hirschi, R. 2020, arXiv e-prints, arXiv:2001.02341

Choplin, A., Hirschi, R., Meynet, G., & Ekström, S. 2017, **A&A**, 607, L3

Choplin, A., Hirschi, R., Meynet, G., et al. 2018, **A&A**, 618, A133

Choplin, A., Maeder, A., Meynet, G., & Chiappini, C. 2016, **A&A**, 593, A36

Christlieb, N., Schörck, T., Frebel, A., et al. 2008, **A&A**, 484, 721

Chugai, N. N. & Danziger, I. J. 1994, **MNRAS**, 268, 173

Clark, P. C., Glover, S. C. O., Klessen, R. S., & Bromm, V. 2011a, **ApJ**, 727, 110

Clark, P. C., Glover, S. C. O., Smith, R. J., et al. 2011b, Science, 331, 1040

Clarkson, O. & Herwig, F. 2020, arXiv e-prints, arXiv:2005.07748

Clarkson, O., Herwig, F., & Pignatari, M. 2018, **MNRAS**, 474, L37

Cooke, J., Sullivan, M., Gal-Yam, A., et al. 2012, **Nature**, 491, 228

Cooke, R. J. & Madau, P. 2014, **ApJ**, 791, 116

Cox, J. P. & Giuli, R. T. 1968, Principles of stellar structure

Cristini, A., Hirschi, R., Meakin, C., et al. 2019, **MNRAS**, 484, 4645

Cristini, A., Meakin, C., Hirschi, R., et al. 2017, **MNRAS**, 471, 279

Crowther, P. A. 2007, **ARA&A**, 45, 177

Crowther, P. A., Lennon, D. J., & Walborn, N. R. 2006, **A&A**, 446, 279 de Bennassuti, M., Salvadori, S., Schneider, R., Valiante, R., & Omukai, K. 2017, MNRAS, 465, 926

de Jager, C., Nieuwenhuijzen, H., & van der Hucht, K. A. 1988, A&AS, 72, 259

de Mink, S. E., Langer, N., Izzard, R. G., Sana, H., & de Koter, A. 2013, ApJ, 764, 166

de Souza, R. S., Ishida, E. E. O., Johnson, J. L., Whalen, D. J., & Mesinger, A. 2013, MNRAS, 436, 1555

de Souza, R. S., Ishida, E. E. O., Whalen, D. J., Johnson, J. L., & Ferrara, A. 2014, MNRAS, 442, 1640

Dessart, L., Audit, E., & Hillier, D. J. 2015, MNRAS, 449, 4304

Dessart, L., Waldman, R., Livne, E., Hillier, D. J., & Blondin, S. 2013, MNRAS, 428, 3227

Dijkstra, M., Haiman, Z., Mesinger, A., & Wyithe, J. S. B. 2008, MNRAS, 391, 1961

Dopcke, G., Glover, S. C. O., Clark, P. C., & Klessen, R. S. 2013, ApJ, 766, 103

Dwek, E. 2016, ApJ, 825, 136

Dwek, E. & Cherchneff, I. 2011, ApJ, 727, 63

Dwek, E., Staguhn, J., Arendt, R. G., et al. 2014, ApJ, 788, L30

Eggenberger, P., Meynet, G., Maeder, A., et al. 2008, Ap&SS, 316, 43

Ekström, S., Georgy, C., Eggenberger, P., et al. 2012, A&A, 537, A146

Ekström, S., Meynet, G., Chiappini, C., Hirschi, R., & Maeder, A. 2008, A&A, 489, 685

El Eid, M. F., Fricke, K. J., & Ober, W. W. 1983, A&A, 119, 54

Eldridge, J. J., Izzard, R. G., & Tout, C. A. 2008, MNRAS, 384, 1109

Fan, X., Hennawi, J. F., Richards, G. T., et al. 2004, AJ, 128, 515

Fan, X., Narayanan, V. K., Lupton, R. H., et al. 2001, AJ, 122, 2833

Fan, X., Strauss, M. A., Richards, G. T., et al. 2006, AJ, 131, 1203

Fan, X., Strauss, M. A., Schneider, D. P., et al. 2003, AJ, 125, 1649

Farrell, E., Groh, J., Meynet, G., & Eldridge, J. 2021a, arXiv e-prints, arXiv:2109.02488

Farrell, E., Groh, J. H., Hirschi, R., et al. 2021b, MNRAS, 502, L40

Farrell, E. J., Groh, J. H., Meynet, G., et al. 2020, MNRAS, 495, 4659

Farrell, E. J., Groh, J. H., Meynet, G., et al. 2019, A&A, 621, A22

Faucher-Giguère, C.-A., Lidz, A., Hernquist, L., & Zaldarriaga, M. 2008, ApJ, 688, 85

Faucher-Giguère, C.-A., Lidz, A., Zaldarriaga, M., & Hernquist, L. 2009, ApJ, 703, 1416

Ferguson, J. W., Alexander, D. R., Allard, F., et al. 2005, ApJ, 623, 585

Ferrarese, L. & Ford, H. 2005, Space Sci. Rev., 116, 523

Filippenko, A. V. 1997, ARA&A, 35, 309

Finlator, K., Keating, L., Oppenheimer, B. D., Davé, R., & Zackrisson, E. 2018, MNRAS, 480, 2628

Fowler, W. A. & Hoyle, F. 1964, ApJS, 9, 201

Frey, L. H., Even, W., Whalen, D. J., et al. 2013, ApJS, 204, 16

Fryer, C. L., Belczynski, K., Wiktorowicz, G., et al. 2012, ApJ, 749, 91

Fryer, C. L., Woosley, S. E., & Heger, A. 2001, ApJ, 550, 372

Fuller, J. 2017, MNRAS, 470, 1642

Gal-Yam, A., Mazzali, P., Ofek, E. O., et al. 2009, Nature, 462, 624

Gall, C., Andersen, A. C., & Hjorth, J. 2011, A&A, 528, A14

Georgy, C., Ekström, S., Eggenberger, P., et al. 2013a, A&A, 558, A103

Georgy, C., Ekström, S., Granada, A., et al. 2013b, A&A, 553, A24

Georgy, C., Granada, A., Ekström, S., et al. 2014, A&A, 566, A21

Gittings, M., Weaver, R., Clover, M., et al. 2008, Computational Science and Discovery, 1, 015005

Gnedin, N. Y. & Ostriker, J. P. 1997, ApJ, 486, 581

Gräfener, G. & Hamann, W. R. 2008, A&A, 482, 945

Gräfener, G., Owocki, S. P., & Vink, J. S. 2012, A&A, 538, A40

Gräfener, G., Vink, J. S., de Koter, A., & Langer, N. 2011, A&A, 535, A56

Greif, T. H., Bromm, V., Clark, P. C., et al. 2012, MNRAS, 424, 399

Greif, T. H., Glover, S. C. O., Bromm, V., & Klessen, R. S. 2010, ApJ, 716, 510

Greif, T. H., Johnson, J. L., Bromm, V., & Klessen, R. S. 2007, **ApJ**, 670, 1

Greif, T. H., Springel, V., White, S. D. M., et al. 2011, **ApJ**, 737, 75

Grevesse, N. & Noels, A. 1993, in Origin and Evolution of the Elements, ed. N. Prantzos, E. Vangioni-Flam, & M. Casse, 15–25

Groenewegen, M. A. T. & Lamers, H. J. G. L. M. 1989, **A&AS**, 79, 359

Groh, J. H., Ekström, S., Georgy, C., et al. 2019, **A&A**, 627, A24

Groh, J. H., Farrell, E. J., Meynet, G., et al. 2020, **ApJ**, 900, 98

Groh, J. H., Meynet, G., & Ekström, S. 2013a, **A&A**, 550, L7

Groh, J. H., Meynet, G., Ekström, S., & Georgy, C. 2014, **A&A**, 564, A30

Groh, J. H., Meynet, G., Georgy, C., & Ekström, S. 2013b, **A&A**, 558, A131

Haardt, F. & Madau, P. 2012, **ApJ**, 746, 125

Haehnelt, M. G., Madau, P., Kudritzki, R., & Haardt, F. 2001, **ApJ**, 549, L151

Haemmerlé, L. 2021a, **A&A**, 647, A83

Haemmerlé, L. 2021b, arXiv e-prints, arXiv:2104.11754

Haemmerlé, L., Eggenberger, P., Meynet, G., Maeder, A., & Charbonnel, C. 2013, **A&A**, 557, A112

Haemmerlé, L., Klessen, R. S., Mayer, L., & Zwick, L. 2021, arXiv e-prints, arXiv:2105.13373

Haemmerlé, L., Meynet, G., Mayer, L., et al. 2019, **A&A**, 632, L2

Haemmerlé, L., Woods, T. E., Klessen, R. S., Heger, A., & Whalen, D. J. 2018, **MNRAS**, 474, 2757

Hartwig, T., Agarwal, B., & Regan, J. A. 2018, **MNRAS**, 479, L23

Hartwig, T., Bromm, V., Klessen, R. S., & Glover, S. C. O. 2015, **MNRAS**, 447, 3892

Hartwig, T., Ishigaki, M. N., Klessen, R. S., & Yoshida, N. 2019, **MNRAS**, 482, 1204

Hartwig, T., Volonteri, M., Bromm, V., et al. 2016, **MNRAS**, 460, L74

Hartwig, T. & Yoshida, N. 2019, **ApJ**, 870, L3

Heger, A., Fryer, C. L., Woosley, S. E., Langer, N., & Hartmann, D. H. 2003, **ApJ**, 591, 288

Heger, A., Langer, N., & Woosley, S. E. 2000, **ApJ**, 528, 368

Heger, A. & Woosley, S. E. 2002, **ApJ**, 567, 532

Heger, A. & Woosley, S. E. 2010, **ApJ**, 724, 341

Hellings, P. 1983, **Ap&SS**, 96, 37

Henyey, L. G., Forbes, J. E., & Gould, N. L. 1964, **ApJ**, 139, 306

Herwig, F., Bloecker, T., Schoenberner, D., & El Eid, M. 1997, **A&A**, 324, L81

Hester, J. J. 2008, **ARA&A**, 46, 127

Hicks, W. M., Wells, A., Norman, M. L., et al. 2021, **ApJ**, 909, 70

Higgins, E. R. & Vink, J. S. 2019, **A&A**, 622, A50

Hillier, D. J. & Miller, D. L. 1998, **ApJ**, 496, 407

Hirano, S. & Bromm, V. 2018, **MNRAS**, 476, 3964

Hirano, S., Hosokawa, T., Yoshida, N., Omukai, K., & Yorke, H. W. 2015, **MNRAS**, 448, 568

Hirano, S., Hosokawa, T., Yoshida, N., et al. 2014, **ApJ**, 781, 60

Hirschi, R., Meynet, G., & Maeder, A. 2004, **A&A**, 425, 649

Hosokawa, T., Hirano, S., Kuiper, R., et al. 2016, **ApJ**, 824, 119

Hosokawa, T., Omukai, K., Yoshida, N., & Yorke, H. W. 2011, Science, 334, 1250

Hosokawa, T., Yorke, H. W., Inayoshi, K., Omukai, K., & Yoshida, N. 2013, **ApJ**, 778, 178

Howes, L. M., Asplund, M., Keller, S. C., et al. 2016, **MNRAS**, 460, 884

Huang, W. & Gies, D. R. 2006, **ApJ**, 648, 580

Huang, W., Gies, D. R., & McSwain, M. V. 2010a, **ApJ**, 722, 605

Huang, W., Gies, D. R., & McSwain, M. V. 2010b, **ApJ**, 722, 605

Humphreys, R. M. & Davidson, K. 1994, **PASP**, 106, 1025

Iglesias, C. A. & Rogers, F. J. 1996, **ApJ**, 464, 943

Iocco, F., Mangano, G., Miele, G., Pisanti, O., & Serpico, P. D. 2007, **Phys. Rev. D**, 75, 087304

Ishigaki, M. N., Tominaga, N., Kobayashi, C., & Nomoto, K. 2018, ApJ, 857, 46

Ishii, M., Ueno, M., & Kato, M. 1999, PASJ, 51, 417

Izotov, Y. I., Chaffee, F. H., Foltz, C. B., et al. 1999, ApJ, 527, 757

Janka, H.-T. 2012, Annual Review of Nuclear and Particle Science, 62, 407

Janka, H. T., Langanke, K., Marek, A., Martínez-Pinedo, G., & Müller, B. 2007, Phys. Rep., 442, 38

Jeon, M., Bromm, V., Besla, G., Yoon, J., & Choi, Y. 2021, MNRAS, 502, 1

Jeřábková, T., Hasani Zonoozi, A., Kroupa, P., et al. 2018, A&A, 620, A39

Jiang, Y.-F., Cantiello, M., Bildsten, L., Quataert, E., & Blaes, O. 2015, ApJ, 813, 74

Jiang, Y.-F., Cantiello, M., Bildsten, L., et al. 2018, Nature, 561, 498

Joggerst, C. C., Almgren, A., Bell, J., et al. 2010, ApJ, 709, 11

Johnson, J. A. 2019, Science, 363, 474

Johnson, J. L., Whalen, D. J., Fryer, C. L., & Li, H. 2012, ApJ, 750, 66

Johnson, J. L., Whalen, D. J., Li, H., & Holz, D. E. 2013, ApJ, 771, 116

Kaiser, E. A., Hirschi, R., Arnett, W. D., et al. 2020, MNRAS, 496, 1967

Karlsson, T., Johnson, J. L., & Bromm, V. 2008, ApJ, 679, 6

Kasen, D., Woosley, S. E., & Heger, A. 2011, ApJ, 734, 102

Katz, H., Kimm, T., Haehnelt, M. G., et al. 2019, MNRAS, 483, 1029

Kiminki, D. C. & Kobulnicky, H. A. 2012, ApJ, 751, 4

Kinugawa, T., Inayoshi, K., Hotokezaka, K., Nakauchi, D., & Nakamura, T. 2014, MNRAS, 442, 2963

Kinugawa, T., Nakamura, T., & Nakano, H. 2021, MNRAS, 501, L49

Kippenhahn, R. 1974, in Late Stages of Stellar Evolution, ed. R. J. Tayler & J. E. Hesser, Vol. 66, 20

Kippenhahn, R., Meyer-Hofmeister, E., & Thomas, H. C. 1970, A&A, 5, 155

Kippenhahn, R., Weigert, A., & Weiss, A. 2012, Stellar Structure and Evolution

Kitayama, T. & Yoshida, N. 2005, ApJ, 630, 675

Kitayama, T., Yoshida, N., Susa, H., & Umemura, M. 2004, **ApJ**, 613, 631

Klessen, R. 2019, Formation of the first stars, ed. M. Latif & D. Schleicher, 67–97

Kobayashi, C., Tominaga, N., & Nomoto, K. 2011, **ApJ**, 730, L14

Kobulnicky, H. A. & Fryer, C. L. 2007, **ApJ**, 670, 747

Kroupa, P. 2001, **MNRAS**, 322, 231

Krtička, J. & Kubát, J. 2006, **A&A**, 446, 1039

Krtička, J. & Kubát, J. 2009, **A&A**, 493, 585

Krtička, J., Owocki, S. P., & Meynet, G. 2011, **A&A**, 527, A84

Krumholz, M. R. 2015, The Formation of Very Massive Stars, ed. J. S. Vink, Vol. 412, 43

Kudritzki, R.-P. & Puls, J. 2000, **ARA&A**, 38, 613

Lamers, H. J. G. L. M. & Cassinelli, J. P. 1999, Introduction to Stellar Winds

Latif, M. A., Schleicher, D. R. G., Schmidt, W., & Niemeyer, J. C. 2013, **MNRAS**, 436, 2989

Lee, U., Osaki, Y., & Saio, H. 1991, **MNRAS**, 250, 432

Leśniewska, A. & Michałowski, M. J. 2019, **A&A**, 624, L13

Leung, S.-C. & Fuller, J. 2020, **ApJ**, 900, 99

Leung, S.-C., Nomoto, K., & Blinnikov, S. 2019, **ApJ**, 887, 72

Li, G.-W., Shi, J.-R., Yanny, B., et al. 2018, **ApJ**, 863, 70

Liddle, A. 2003, An Introduction to Modern Cosmology, Second Edition

LIGO Scientific Collaboration, Aasi, J., Abbott, B. P., et al. 2015, Classical and Quantum Gravity, 32, 074001

Limongi, M. & Chieffi, A. 2012, **ApJS**, 199, 38

Liu, B. & Bromm, V. 2020a, **MNRAS**, 495, 2475

Liu, B. & Bromm, V. 2020b, **ApJ**, 903, L40

Liu, B., Meynet, G., & Bromm, V. 2021, **MNRAS**, 501, 643

Liu, J., Zhang, H., Howard, A. W., et al. 2019, arXiv e-prints, arXiv:1911.11989

Lucy, L. B. & Solomon, P. M. 1970, **ApJ**, 159, 879

Mackey, J., Bromm, V., & Hernquist, L. 2003, **ApJ**, 586, 1

Maeder, A. 1987, **A&A**, 173, 247

Maeder, A. 1992, **A&A**, 264, 105

Maeder, A. 1995, **A&A**, 299, 84

Maeder, A. 1997, **A&A**, 321, 134

Maeder, A. 2009, Physics, Formation and Evolution of Rotating Stars

Maeder, A., Grebel, E. K., & Mermilliod, J.-C. 1999, **A&A**, 346, 459

Maeder, A. & Meynet, G. 1987, **A&A**, 182, 243

Maeder, A. & Meynet, G. 1989, **A&A**, 210, 155

Maeder, A. & Meynet, G. 2000a, **A&A**, 361, 159

Maeder, A. & Meynet, G. 2000b, **ARA&A**, 38, 143

Maeder, A. & Meynet, G. 2012, Reviews of Modern Physics, 84, 25

Maeder, A. & Zahn, J.-P. 1998, **A&A**, 334, 1000

Margolin, L. G., Rider, W. J., & Grinstein, F. F. 2006, Journal of Turbulence, 7, 15

Marigo, P., Chiosi, C., & Kudritzki, R. P. 2003, **A&A**, 399, 617

Marigo, P., Girardi, L., Chiosi, C., & Wood, P. R. 2001, **A&A**, 371, 152

Martayan, C., Frémat, Y., Hubert, A. M., et al. 2007, **A&A**, 462, 683

Martinet, S., Meynet, G., Ekström, S., et al. 2021, **A&A**, 648, A126

Martins, F., Schaerer, D., Haemmerlé, L., & Charbonnel, C. 2020, **A&A**, 633, A9

Mauron, N. & Josselin, E. 2011, **A&A**, 526, A156

McKee, C. F. & Ostriker, E. C. 2007, **ARA&A**, 45, 565

McKee, C. F. & Tan, J. C. 2008, **ApJ**, 681, 771

McQuinn, M. 2016, **ARA&A**, 54, 313

McQuinn, M., Lidz, A., Zahn, O., et al. 2007, **MNRAS**, 377, 1043

McWilliam, A., Preston, G. W., Sneden, C., & Searle, L. 1995, **AJ**, 109, 2757

Meakin, C. A. & Arnett, D. 2007, ApJ, 667, 448

Meynet, G., Ekström, S., & Maeder, A. 2006, A&A, 447, 623

Meynet, G. & Maeder, A. 1997, A&A, 321, 465

Meynet, G. & Maeder, A. 2002, A&A, 390, 561

Michałowski, M. J. 2015, A&A, 577, A80

Moe, M. & Di Stefano, R. 2017, ApJS, 230, 15

Montero, P. J., Janka, H.-T., & Müller, E. 2012, ApJ, 749, 37

Moriya, T. J., Chen, K.-J., Nakajima, K., Tominaga, N., & Blinnikov, S. I. 2021, MNRAS, 503, 1206

Moriya, T. J., Wong, K. C., Koyama, Y., et al. 2019, PASJ, 71, 59

Mortlock, D. J., Warren, S. J., Venemans, B. P., et al. 2011, Nature, 474, 616

Motte, F., Bontemps, S., & Louvet, F. 2018, ARA&A, 56, 41

Muijres, L. E., Vink, J. S., de Koter, A., Müller, P. E., & Langer, N. 2012, A&A, 537, A37

Mukhamedzhanov, A. M., Bém, P., Brown, B. A., et al. 2003, Phys. Rev. C, 67, 065804

Murphy, L. J., Groh, J. H., Ekström, S., et al. 2021a, MNRAS, 501, 2745

Murphy, L. J., Groh, J. H., Farrell, E., et al. 2021b, MNRAS, 506, 5731

Nomoto, K., Tominaga, N., Umeda, H., Kobayashi, C., & Maeda, K. 2006, Nucl. Phys. A, 777, 424

Norman, M. L., Chen, P., Wise, J. H., & Xu, H. 2018, ApJ, 867, 27

Nugis, T. & Lamers, H. J. G. L. M. 2000, A&A, 360, 227

Ofek, E. O., Cameron, P. B., Kasliwal, M. M., et al. 2007, ApJ, 659, L13

Omukai, K. & Palla, F. 2001, ApJ, 561, L55

Omukai, K. & Palla, F. 2003, ApJ, 589, 677

O'Shea, B. W. & Norman, M. L. 2007, ApJ, 654, 66

O'Shea, B. W., Wise, J. H., Xu, H., & Norman, M. L. 2015, ApJ, 807, L12

Owocki, S. 2005, in Astronomical Society of the Pacific Conference Series, Vol. 337, The Nature and Evolution of Disks Around Hot Stars, ed. R. Ignace & K. G. Gayley, 101

Paxton, B., Bildsten, L., Dotter, A., et al. 2011, ApJS, 192, 3

Paxton, B., Cantiello, M., Arras, P., et al. 2013, ApJS, 208, 4

Paxton, B., Marchant, P., Schwab, J., et al. 2015, ApJS, 220, 15

Petrovic, J., Pols, O., & Langer, N. 2006, A&A, 450, 219

Planck Collaboration, Ade, P. A. R., Aghanim, N., et al. 2016, A&A, 594, A13

Planck Collaboration, Aghanim, N., Akrami, Y., et al. 2020, A&A, 641, A6

Porter, J. M. & Rivinius, T. 2003, PASP, 115, 1153

Ramírez-Agudelo, O. H., Simón-Díaz, S., Sana, H., et al. 2013, A&A, 560, A29

Regan, J. A. & Downes, T. P. 2018, MNRAS, 478, 5037

Regan, J. A., Downes, T. P., Volonteri, M., et al. 2019, MNRAS, 486, 3892

Regan, J. A., Visbal, E., Wise, J. H., et al. 2017, Nature Astronomy, 1, 0075

Rivinius, T., Carciofi, A. C., & Martayan, C. 2013, A&A Rev., 21, 69

Roberts, L. F., Ott, C. D., Haas, R., et al. 2016, ApJ, 831, 98

Roederer, I. U., Preston, G. W., Thompson, I. B., et al. 2014, AJ, 147, 136

Ryan, S. G., Norris, J. E., & Beers, T. C. 1996, ApJ, 471, 254

Safarzadeh, M. & Haiman, Z. 2020, ApJ, 903, L21

Salpeter, E. E. 1955, ApJ, 121, 161

Sana, H., de Mink, S. E., de Koter, A., et al. 2012, Science, 337, 444

Sanyal, D., Langer, N., Szécsi, D., -C Yoon, S., & Grassitelli, L. 2017, A&A, 597, A71

Sarkar, S. 1996, Reports on Progress in Physics, 59, 1493

Sarmento, R., Scannapieco, E., & Côté, B. 2019, arXiv e-prints, arXiv:1901.03727

Scalo, J. M. 1986, Fund. Cosmic Phys., 11, 1

Schaerer, D. 2002, A&A, 382, 28

Schaerer, D. 2003, A&A, 397, 527

Schaller, G., Schaerer, D., Meynet, G., & Maeder, A. 1992, A&AS, 96, 269

Schneider, F. R. N., Ohlmann, S. T., Podsiadlowski, P., et al. 2019, Nature, 574, 211

Schneider, F. R. N., Podsiadlowski, P., Langer, N., Castro, N., & Fossati, L. 2016, MNRAS, 457, 2355

Schootemeijer, A., Langer, N., Grin, N. J., & Wang, C. 2019, arXiv e-prints, arXiv:1903.10423

Scott, L. J. A., Hirschi, R., Georgy, C., et al. 2021, MNRAS, 503, 4208

Searle, L. & Sargent, W. L. W. 1972, ApJ, 173, 25

Sharma, M., Theuns, T., Frenk, C. S., & Cooke, R. J. 2018, MNRAS, 473, 984

Skúladóttir, Á., Salvadori, S., Amarsi, A. M., et al. 2021, arXiv e-prints, arXiv:2106.11592

Smartt, S. J. 2009, ARA&A, 47, 63

Smith, B. D., Regan, J. A., Downes, T. P., et al. 2018, Monthly Notices of the Royal Astronomical Society, 480, 3762

Smith, B. D., Wise, J. H., O'Shea, B. W., Norman, M. L., & Khochfar, S. 2015, MNRAS, 452, 2822

Smith, N. 2014, ARA&A, 52, 487

Smith, N. & Owocki, S. P. 2006, ApJ, 645, L45

Smith, R. J., Glover, S. C. O., Clark, P. C., Greif, T., & Klessen, R. S. 2011, MNRAS, 414, 3633

Sodroski, T. J., Odegard, N., Arendt, R. G., et al. 1997, ApJ, 480, 173

Sokasian, A., Yoshida, N., Abel, T., Hernquist, L., & Springel, V. 2004, MNRAS, 350, 47

Spera, M. & Mapelli, M. 2017, MNRAS, 470, 4739

Spruit, H. C. 2002, A&A, 381, 923

Stacy, A. & Bromm, V. 2013, MNRAS, 433, 1094

Stacy, A. & Bromm, V. 2014, ApJ, 785, 73

Stacy, A., Bromm, V., & Lee, A. T. 2016, MNRAS, 462, 1307

Stacy, A., Bromm, V., & Loeb, A. 2011, MNRAS, 413, 543

Stacy, A., Greif, T. H., & Bromm, V. 2010, **MNRAS**, 403, 45

Stacy, A., Greif, T. H., & Bromm, V. 2012, **MNRAS**, 422, 290

Stacy, A., Greif, T. H., Klessen, R. S., Bromm, V., & Loeb, A. 2013, **MNRAS**, 431, 1470

Starkenburg, E., Martin, N., Youakim, K., et al. 2017, **MNRAS**, 471, 2587

Stothers, R. & Chin, C.-W. 1973, **ApJ**, 179, 555

Sukhbold, T. & Woosley, S. E. 2014, **ApJ**, 783, 10

Susa, H., Hasegawa, K., & Tominaga, N. 2014, **ApJ**, 792, 32

Szécsi, D., Langer, N., Yoon, S.-C., et al. 2015, **A&A**, 581, A15

Takahashi, K., Umeda, H., & Yoshida, T. 2014, **ApJ**, 794, 40

Tammann, G. A., Sandage, A., & Reindl, B. 2003, **A&A**, 404, 423

Tan, J. C., Beltrán, M. T., Caselli, P., et al. 2014, in Protostars and Planets VI, ed. H. Beuther, R. S. Klessen, C. P. Dullemond, & T. Henning, 149

Tanaka, M., Moriya, T. J., & Yoshida, N. 2013, **MNRAS**, 435, 2483

Tanikawa, A., Kinugawa, T., Yoshida, T., Hijikawa, K., & Umeda, H. 2021a, **MNRAS**, 505, 2170

Tanikawa, A., Susa, H., Yoshida, T., Trani, A. A., & Kinugawa, T. 2021b, **ApJ**, 910, 30

Tominaga, N., Iwamoto, N., & Nomoto, K. 2014, **ApJ**, 785, 98

Tominaga, N., Umeda, H., & Nomoto, K. 2007, **ApJ**, 660, 516

Topping, M. W. & Shull, J. M. 2015, **ApJ**, 800, 97

Tumlinson, J. & Shull, J. M. 2000, **ApJ**, 528, L65

Turk, M. J., Abel, T., & O'Shea, B. 2009, Science, 325, 601

Uchida, H., Shibata, M., Takahashi, K., & Yoshida, T. 2019, arXiv e-prints, arXiv:1901.08260

Umeda, H., Hosokawa, T., Omukai, K., & Yoshida, N. 2016, **ApJ**, 830, L34

Umeda, H. & Nomoto, K. 2002, **ApJ**, 565, 385

Umeda, H. & Nomoto, K. 2003, **Nature**, 422, 871

Umeda, H., Yoshida, T., Nagele, C., & Takahashi, K. 2020, **ApJ**, 905, L21

Valiante, R., Schneider, R., Salvadori, S., & Bianchi, S. 2011, **MNRAS**, 416, 1916

van Loon, J. T., Cioni, M. R. L., Zijlstra, A. A., & Loup, C. 2005, **A&A**, 438, 273

van Marle, A. J., Owocki, S. P., & Shaviv, N. J. 2008, **MNRAS**, 389, 1353

Vartanyan, D., Laplace, E., Renzo, M., et al. 2021, arXiv e-prints, arXiv:2104.03317

Vink, J. S., de Koter, A., & Lamers, H. J. G. L. M. 1999, **A&A**, 350, 181

Vink, J. S., de Koter, A., & Lamers, H. J. G. L. M. 2000, **A&A**, 362, 295

Vink, J. S., de Koter, A., & Lamers, H. J. G. L. M. 2001, **A&A**, 369, 574

Vink, J. S., Muijres, L. E., Anthonisse, B., et al. 2011, **A&A**, 531, A132

Vink, J. S. & Sander, A. A. C. 2021, **MNRAS**, 504, 2051

Volonteri, M. 2010, **A&A Rev.**, 18, 279

Wang, F., Yang, J., Fan, X., et al. 2021, **ApJ**, 907, L1

Weaver, T. A., Zimmerman, G. B., & Woosley, S. E. 1978, **ApJ**, 225, 1021

Weis, K. & Bomans, D. J. 2020, Galaxies, 8, 20

Welsh, L., Cooke, R., & Fumagalli, M. 2019, **MNRAS**, 487, 3363

Welsh, L., Cooke, R., & Fumagalli, M. 2021, **MNRAS**, 500, 5214

Whalen, D., Abel, T., & Norman, M. L. 2004, **ApJ**, 610, 14

Whalen, D., van Veelen, B., O'Shea, B. W., & Norman, M. L. 2008, **ApJ**, 682, 49

Whalen, D. J., Even, W., Frey, L. H., et al. 2013a, **ApJ**, 777, 110

Whalen, D. J., Fryer, C. L., Holz, D. E., et al. 2013b, **ApJ**, 762, L6

Whalen, D. J., Joggerst, C. C., Fryer, C. L., et al. 2013c, **ApJ**, 768, 95

Whalen, D. J., Smidt, J., Even, W., et al. 2014, **ApJ**, 781, 106

Whitworth, A. 1979, **MNRAS**, 186, 59

Windhorst, R. A., Timmes, F. X., Wyithe, J. S. B., et al. 2018, **ApJS**, 234, 41

Wise, J. H. & Cen, R. 2009, **ApJ**, 693, 984

Wise, J. H., Demchenko, V. G., Halicek, M. T., et al. 2014, **MNRAS**, 442, 2560

Wollenberg, K. M. J., Glover, S. C. O., Clark, P. C., & Klessen, R. S. 2020, **MNRAS**, 494, 1871

Woods, T. E., Heger, A., Whalen, D. J., Haemmerlé, L., & Klessen, R. S. 2017, **ApJ**, 842, L6

Woosley, S. E. 2017, **ApJ**, 836, 244

Woosley, S. E. & Weaver, T. A. 1995, The Astrophysical Journal Supplement Series, 101, 181

Worseck, G., Prochaska, J. X., Hennawi, J. F., & McQuinn, M. 2016, **ApJ**, 825, 144

Wu, S. & Fuller, J. 2021, **ApJ**, 906, 3

Wu, X.-B., Wang, F., Fan, X., et al. 2015, **Nature**, 518, 512

Xu, H., Ahn, K., Norman, M. L., Wise, J. H., & O'Shea, B. W. 2016a, **ApJ**, 832, L5

Xu, H., Norman, M. L., O'Shea, B. W., & Wise, J. H. 2016b, **ApJ**, 823, 140

Xu, H., Wise, J. H., Norman, M. L., Ahn, K., & O'Shea, B. W. 2016c, **ApJ**, 833, 84

Yamasawa, D., Habe, A., Kozasa, T., et al. 2011, **ApJ**, 735, 44

Yang, M., Bonanos, A. Z., Jiang, B., et al. 2021a, **A&A**, 646, A141

Yang, M., Bonanos, A. Z., Jiang, B., et al. 2021b, **A&A**, 647, A167

Yang, M., Bonanos, A. Z., Jiang, B.-W., et al. 2019, **A&A**, 629, A91

Yang, M., Bonanos, A. Z., Jiang, B.-W., et al. 2020, **A&A**, 639, A116

Yoon, S.-C. & Cantiello, M. 2010, **ApJ**, 717, L62

Yoon, S.-C., Dessart, L., & Clocchiatti, A. 2017, **ApJ**, 840, 10

Yoon, S. C., Dierks, A., & Langer, N. 2012, **A&A**, 542, A113

Yoshida, N., Omukai, K., Hernquist, L., & Abel, T. 2006, **ApJ**, 652, 6

Zackrisson, E., González, J., Eriksson, S., et al. 2015, **MNRAS**, 449, 3057

Zackrisson, E., Rydberg, C.-E., Schaerer, D., Östlin, G., & Tuli, M. 2011, **ApJ**, 740, 13

Zahn, J. P. 1992, **A&A**, 265, 115

Zwicky, F. 1966, **ApJ**, 143, 192